Fakultät für Physik
Chemische Physik fern vom Gleichgewicht

Symmetry Breaking in Networks of Globally Coupled Oscillators: From Clustering to Chimera State

Felix Peter Kemeth

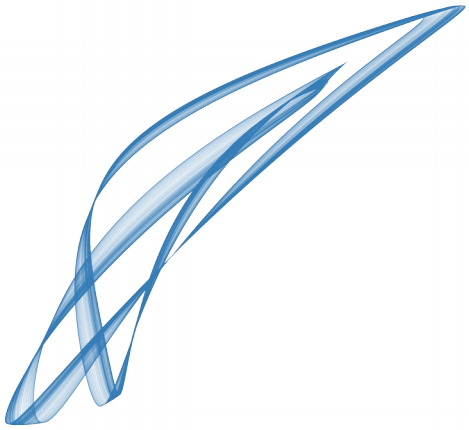

Vollständiger Abdruck der von der Fakultät für Physik der Technischen Universität München zur Erlangung des akademischen Grades eines Doktors der Naturwissenschaften (Dr. rer. nat.) genehmigten Dissertation.

Vorsitzender: Prof. Dr. Andreas Bausch

Prüfende der Dissertation:

1. Prof. Dr. Katharina Krischer

2. Prof. Dr. Oliver Junge

Die Dissertation wurde am 11.12.2018 bei der Technischen Universität München eingereicht und durch die Fakultät für Physik am 01.04.2019 angenommen.

Erstgutachterin (Themenstellerin): Prof. K. Krischer
Zweitgutachter: Prof. O. Junge

Abstract

Symmetry-broken states arise naturally in oscillatory networks. In particular, the ubiquitous occurrence of such symmetry-broken cluster patterns in nature still remains unclear. It is known that the dynamics of many such oscillatory systems is captured by ensembles of Stuart-Landau oscillators. Starting from small ensembles, we investigate clustering and chimera states in globally coupled Stuart-Landau systems. For just two oscillators, we show where in parameter space symmetry-broken states exist, and how they bifurcate. Doubling the number of oscillators, we further discuss how such cluster states bifurcate, and eventually turn into so-called chimera states, states of coexisting coherence and incoherence. We report that these states with partially broken symmetry, in which two oscillators remain synchronized, have different set-wise symmetries in the incoherent oscillators. In particular, some are and some are not invariant under a permutation symmetry on average. Using symmetry detectives, this allows for a classification of different chimera states in small networks. Adding more oscillators to the ensemble, we elaborate how the observed 2-cluster states crowd in phase space. Using persistence, we discuss how this crowding leads to a continuous transition from balanced cluster states to the synchronized solution via intermediate unbalanced 2-cluster states. These cascade-like transitions emerge from what we call cluster singularities. At these codimension-2 points, the bifurcations of all 2-cluster states collapse and the stable balanced cluster state bifurcates into the synchronized solution supercritically. We confirm our results using numerical simulations, and discuss how our conclusions apply to spatially extended systems.

In the thermodynamic limit, we present a universal characterization scheme for chimera states, applicable to both numerical and experimental data sets. The scheme is based on two correlation measures, also called order parameters, that enable a meaningful definition of chimera states as well as their classification into three categories: stationary, turbulent and breathing. We demonstrate that this approach is both consistent with previously recognized chimera states and enables us to not only classify but also to detect states as chimeras which have not been categorized as such before.

The idea of extracting order parameters can also be implemented in a data-driven way. We discuss this by using diffusion maps, a nonlinear manifold learning technique, and elaborate how comparing time series using diffusion maps yields what we call intrinsic variabilities. Using several examples, we show that such variabilities may be one-to-one with the spatial coordinate on which the dynamics are simu-

lated, or the heterogeneous parameters contained in the system. Tuning the kernel scale of the diffusion maps, coarse descriptions of dynamical phenomena can be obtained, and, in particular, we demonstrate that for chimera states one can employ this method to extract variabilities similar to order parameters. Taking overlapping time chunks, we outline how this approach can further be used to extract the attracting manifold from the data. All these extracted variabilities may be used as new coordinates, spanning an "emergent" or "equal" space in which the dynamics can be embedded or visualized, with an eye towards eventually creating reduced models in these variables.

Zusammenfassung

Symmetrie-gebrochene Zustände sind ein häufiges Phänomen in Netzwerken von gekoppelten Oszillatoren. Dennoch sind viele Fragen über das Auftreten solcher Zustände in der Natur immer noch unbeantwortet. Was man jedoch weiß ist, dass sich viele solcher oszillatorischer Systeme auf Ensembles von Stuart-Landau Oszillatoren abbilden lassen. Beginnend mit einer kleinen Anzahl Oszillatoren untersuchen wir Symmetrie-gebrochene Systeme wie Chimärenzustände und Clusterzustände in Systemen von global gekoppelten Stuart-Landau Oszillatoren. Anhand von zwei solcher Oszillatoren zeigen wir wo im Parameterraum Symmetrie-gebrochene Zustände existieren, und wie diese bifurkieren. In Systemen von doppelt so vielen Oszillatoren untersuchen wir anschließend wie solche Clusterzustände sich im Parameterraum verhalten. Insbesondere zeigen wir wie eine Sequenz von Bifurkationen zu Chimärenzuständen, Zuständen aus koexistierenden kohärenten und inkohärenten Oszillatoren, führt. Des Weiteren führen wir vor Augen dass diese Symmetrie-gebrochenen Zustände aus zwei synchronisierten und zwei desynchronisierten Oszillatoren verschiedene Symmetrien aufweisen können: Ihre Attraktoren können entweder invariant unter einer Vertauschung der beiden inkohärenten Oszillatoren sein, oder auch nicht. Deshalb ist es, mit Hilfe von so genannten Symmetrie Detektiven, möglich solche Zustände in kleinen Netzwerken zu klassifizieren.
Durch das Hinzufügen weiterer Oszillatoren untersuchen wir wie sich die Attraktoren von 2-Cluster Zuständen im Phasenraum verdichten. Mit Hilfe des Persistenz-Theorems diskutieren wir hierbei wie dieses Verdichten zu einem kontinuierlichen Übergang von balancierten Clusterzuständen zur synchronen Lösung via unbalancierter 2-Cluster Lösungen führt. Des Weiteren zeigen wir dass diese Kaskaden-artigen Übergänge aus einer ausgezeichneten Singularität entspringen. An diesem Kodimension-2 Punkt, welche wir Clustersingularität nennen, kollabieren die Bifurkationen aller 2-Cluster Zustände in einen Punkt, und der Übergang von der balancierten zur synchronen Lösung wird superkritisch. Ferner bestätigen wir unsere Ergebnisse durch numerische Simulationen, und diskutieren wie sich unsere Schlussfolgerungen auf räumlich ausgedehnte Systeme anwenden lassen.
Für Chimärenzustände im thermodynamischen Limit schlagen wir ein universelles Klassifizierungsschema vor, welches sowohl auf Simulations- als auch auf Messdaten anwendbar ist. Dieses Klassifizierung basiert auf zwei Korrelationsmaße, so genannten Ordnungsparametern, welche eine Einteilung solcher Zustände in drei Gruppen erlauben: Stationäre Chimären, turbulente Chimären und periodische Chimären. Anhand mehrerer Beispiele zeigen wir dass unser Ansatz konsistent ist mit früheren

Klassifizierungen. Überdies ermöglicht diese Klassifizierung nicht nur eine Einteilung bestehender Chimärenzustände, sonder ermöglicht auch Zustände, die bisher nicht als Chimären erkannt wurden, als solche zu kennzeichnen.
Die Extrahierung von Ordnungsparametern kann jedoch auch in einem rein Datengetriebenen Ansatz vollzogen werden. Insbesondere diskutieren wir ferner wie man Diffusion Maps, eine nichtlinear Datenreduktionsmethode, zu diesem Zweck heranziehen kann, und erörtern wie durch das Vergleichen von Zeitserien unter Verwendung dieser Methode intrinsische Variabilitäten in den Daten extrahiert werden können. An mehreren Beispielen legen wir dar wie solche Variabilitäten entweder mit den räumlichen Koordinaten des Systems korrelieren, oder, für dem Fall dass solche räumliche Koordinaten nicht existieren, mit den intrinsischen heterogenen Parametern übereinstimmen. Desweiteren können durch das variieren des Skalenparameters im Diffusion Maps Algorithmus gröbere Parametrisierungen des Systems gewonnen werden, was eine Extraktion von Ordnungsparametern für Chimärenzustände ermöglicht. All diese extrahierten Variabilitäten können schließlich als Koordinaten eines emergenten Raumes herangezogen werden, in dem die Dynamik eingebettet, visualisiert oder auch modelliert werden kann.

Acknowledgements

I would like to thank Prof. Katharina Krischer for the excellent supervision, the endless patience and the joy doing research she triggers. In addition, Prof. Yannis Kevrekidis provided inspiring ideas, passionate discussions and motivation, for which I am very thankful. I thank my Mentor Prof. Oliver Junge for always having an open ear and for all of his advice throughout my PhD. I thank Sindre Haugland, who is an excellent collaborator and friend, without whom many parts of my research would have not been possible. Thank you to Dr. Konrad Schönleber, Dr. Vladimir García-Morales, Dr. Matthias Wolfrum, Dr. Christian Bick, Prof. Ronen Talmon and Prof. Erik Bollt for inspiring and vivid discussions about nonlinear dynamics, which I enjoyed a lot. I am very thankful to Munir Salman and Max Patzauer, for many inspiring discussions about research even beyond physics, and Qi Li, Daniel Heger, Simon Filser and Anton Tosolini for being always supportive and positive. I also thank Kevin Höhlein for his excellent work and the joyful discussions. Thank you to the whole group E19a, for the amazing time and the wonderful atmosphere, that makes research a great experience. I am very thankful to my wife Julia and my family for their unconditional support.

Contents

Chapter 1

Introduction

Recent advances in aritificial intelligence allow us to get an impression of how the human brain is able to master tasks like face recognition, memorizing impressions and decision making [1–3]. The final goal of creating a mathematical model of the brain with its billions of brain cells and trillions of dendrites, however, still remains far out of reach [4, 5]. Even a detailed simulation of a single neuron with its different ion concentrations and membrane potentials requires a significant computational effort [4]. This complexity creates the need of simplified approaches which are easier to implement, simulate and interpret.
Using reduced models, however, creates the risk of missing out important features of the full system. Modeling the brain using networks of just thousands of neurons, one might obtain poor performance in the above mentioned tasks. Thus, one usually is anxious for finding a model small enough to be computationally treatable, but large enough to capture all the features of interest.
The human brain, however, is by no means homogeneous: all neurons differ from another by their physiological properties such as the number of links to other neurons or their intrinsic behavior when unperturbed. In particular, neurons in certain regions of the brain may show single spikes, separated by a larger window of quiescence, short bursts of spikes or periodic spiking. These observations led to several mathematical models describing such individual neurons, such as the Hodgkin-Huxley model [6], FitzHugh-Nagumo model [7, 8] or the Hindmarsh-Rose equations [9], which, among others, serve as building blocks for larger network architectures.
Networks of such neurons and animal brains in general may show a vast variety of dynamical patterns. In particular, during the sleep phase of animals, the brain tends to show less active behavior than during the awake state. However, there are also animals, such as dolphins, crocodiles and certain birds performing migration, which rest with only one half of the brain at a time, with the other half remaining awake [10]. Such behavior, so called uni-hemispheric sleep, and the respective patterns in brain activity, attracted much attention in recent years. Another phenomenon which remains an active field of research is the onset of epileptic seizures. There, a large part of the brain spontaneously synchronizes, leading to uncontrolled muscle contraction of the patient [11]. In both cases, the uni-hemispheric sleep and

the epileptic seizures, a part of the brain shows quiet or synchronous dynamics, whereas the other part remains irregular.
In the field of nonlinear dynamics, and in particular when considering networks of coupled oscillators, such patterns have been termed chimera states, in analogy of the creature in creek mythology consisting of different animal parts [12]. Hereby, the focus has been on large ensembles consisting of many oscillating units. Such high-dimensional systems, however, are hard to analyze in more detail, and much of the mechanisms behind chimera states still remain unsolved.
The splitting up of an ensemble of oscillators into two or more groups in general is also known as clustering [13]. Similar to chimera states, clustering appears in a large variety of networks, and a unifying theory of these states is still missing.
The investigation of such phenomena in the brain with its heterogeneity and different lobes is hardly possible. Therefore, we reduce the complexity by applying three basic assumptions: First, we assume that all neurons are oscillatory. This means, a single neuron without any input would perform periodic spiking. Second, all neurons are equal, that is, their spiking amplitude and frequency are identical. And third, the neurons form a dense network in the sense that each neuron is coupled to all other neuron symmetrically and with equal weights.
One thus eventually reduces the brain dynamics to that of a fully connected network of identical oscillators. In contrast to simulating the full, biological system, such a reduction indeed allows to model and hopefully understand the origins of clustering and chimera dynamics. More importantly, such normal forms of globally coupled oscillators serve as a good proxy for not only the brain, but for various physical systems showing oscillatory behavior. Examples range from coupled Josephson junctions, the flashing of fireflies and the chirping of crickets to coupled electrical circuits and electro-chemical cells [14–16]. Therefore, understanding the mechanisms behind symmetry broken states in networks of identical oscillators allows to not only draw conclusions about processes in the brain, but to also explain clustering and chimeras in many physical processes, e.g. electro-chemical systems. This means, results obtained from networks of globally coupled limit-cycle oscillators are applicable to any physical, chemical or biological system showing the qualitatively same dynamical phenomena.
Studying such normal forms, this thesis tries to add to the understanding of clustering and chimera dynamics using a two-fold approach. Starting from minimal ensembles of oscillators, we investigate the emerging dynamical phenomena with increasing system size. This facilitates a detailed analysis and understanding of clustering and chimeras in such small networks, and allows to draw connections to networks of even infinitely many neurons. In order to understand and differentiate chimeras in such large networks, however, we use data mining to reduce the dynamics to just one or a view variables, such as order parameters, allowing a classification of these high-dimensional hybrid states. Finally, we extend our analysis to not only chimera states but to high-dimensional dynamics in general, and pursue the task of

finding suitable embedding variables.
The main results of this two-fold approach, that is from low-dimensional chimeras and clusters in minimal networks to chimeras in the thermodynamic limit, and the reduction of high-dimensional chimera states and chaotic states in general to low-dimensional order-parameters, have been published in [17–20], and the respective sections in this thesis strictly follow the argumentation of these articles.
The thesis is structured as follows. First, a detailed bifurcation analysis of two mean-coupled limit cycle oscillators is given. Doing so, we investigate under which circumstances symmetry broken states, such as cluster states, can arise, and how they bifurcate. We subsequently extend the analysis to systems of four oscillators. There, we discuss the emergence of different kinds of chimera states. In particular, we find two chimeras, which differ in the symmetry properties of their incoherent oscillators, which led us to coin them symmetric and asymmetric chimera states [17]. The analysis of four oscillators also allows us to draw conclusions about so-called amplitude clusters, not only for four oscillators but for globally coupled limit-cycle systems in general. In the course of these investigations, we find certain co-dimension two points, which we dubbed cluster singularities [18]. There, the arrangement of cluster states becomes singular, and balanced cluster states directly bifurcate off the synchronized solution.
In Chapter 3, we turn our attention to chimera states in general. Due to the vast amount of chimeras reported in the literature, a thorough classification seems to be helpful for their understanding. Therefore, we propose two order parameters, g_0, describing the fraction of spatially coherent oscillators, and h_0, describing the fraction of temporally coherent oscillators, and classify diverse chimera states from the literature according to these variables [19].
In the last part of this thesis, we discuss how order parameters can be extracted in a data-driven way. To do so, we use a nonlinear manifold learning technique called diffusion maps, and discuss how the extracted variables may be suited for embedding, dimensionality reduction and attractor reconstruction [20]. Finally, we conclude with a detailed discussion of our results, and propose open question for future research.

Chapter 2

The Dynamics of Mean-Coupled Stuart-Landau Oscillators

We start our considerations with the investigation of ensembles of globally coupled limit cycle oscillators. Globally hereby means that the interaction between the oscillating units does not depend on their spatial respective location nor the distances between them.
This assumption of a global coupling is useful when there is, for example, a system with non-local interactions in a small container such that non-locality effectively becomes global. Another effective global coupling can be found in some parts of the brain, where the neurons are oscillatory and densly connected. Other examples include systems in which some variables diffuse much more slowly than other variables. Then, the fast diffusion can be approximated adiabatically, which effectively becomes a global coupling.
In addition, suppose that the oscillating units in such an example are close to the onset of oscillation. That means each isolated oscillator performs close to sinusoidal oscillations with a constant amplitude. Furthermore, we assume that the global coupling is linear. Then it can be shown that any such system can be mapped onto the globally coupled complex Ginzburg-Landau equation [21–23],

$$\begin{aligned}\partial_t W = W + (1 + ic_1)\,\nabla_x^2 W - (1 + ic_2)\,|W|^2\,W \\ + (\alpha + i\beta)\,\frac{1}{L}\int (W(s') - W(s))\,ds'.\end{aligned} \tag{2.1}$$

with the complex amplitude $W = W(\boldsymbol{x}, t)$ and the real parameters c_1, c_2, α and β. Hereby, c_1 specifies the linear dispersion through the diffusive coupling, and c_2, also referred to as shear [24], determines the effect of the amplitude on the phase dynamics. α and β are the real and imaginary parts of the complex coupling constant. The first term on the right sight of Eq. 2.1 can be regarded as a linear energy input, leading to an increase of the oscillation amplitude. In contrast, the nonlinear term, or dissipation term, acts as a damping, reducing amplitudes larger than one. The second term describes the diffusive coupling, whereas the integral term represents the linear global coupling.

Eq. 2.1 has been studied extensively in the literature. See for example Ref. [25] for the globally coupled complex Ginzburg-Landau equation with one spatial dimension and Ref. [26] for its dynamics with two spatial dimensions.
For some of the dynamical states observed in this equation, the diffusive coupling seems to be essential. Such states include, for example, localized turbulence [26]. For other dynamical phenomena, however, the diffusive coupling can be viewed as a perturbation, which leads to the spatial arrangement of the oscillators and possibly a ripening of diffusion boundaries between them [27, 28], but does not alter the essential features of the dynamical state. In other words, similar dynamics can also be observed when neglecting the diffusive coupling. Examples include cluster states, states in which the system breaks up into two or more clusters with each cluster being internally synchronized [15], and chimera states, cluster states in which at least one cluster breaks up and shows incoherent motion [29, 30].
In order to reduce the complexity, we therefore proceed this chapter with a discrete version of the complex Ginzburg-Landau equation with linear global coupling,

$$\begin{aligned}\partial_t W_k = W_k - (1+ic_2)\left|W_k\right|^2 W_k \\ + (\alpha+i\beta)\left(\frac{1}{N}\sum_j W_j - W_k\right)\end{aligned} \tag{2.2}$$

with $k = 1, \ldots, N$. In particular, Eq. 2.2 can be obtained from Eq. 2.1 by neglecting the diffusion term, which yields an ensemble of globally coupled limit cycle oscillators. The intrinsic dynamics of each unit of this ensemble, also called a Stuart-Landau oscillator [31], follows

$$\partial_t W_k = W_k - (1+ic_2)\left|W_k\right|^2 W_k, \tag{2.3}$$

with a real parameter c_2, the shear [24], and a complex variable $W = x + iy$. Transforming Eq. 2.3 into polar coordinates, $W = R\exp[i\phi]$, one can derive equations for the amplitude R and the phase ϕ, respectively, yielding

$$\begin{aligned}\partial_t R &= R - R^3 \\ \partial_t \phi &= -c_2 R^2.\end{aligned}$$

The stable attractor of this single nonlinear oscillator is thus a limit cycle oscillation with amplitude $R = 1$ and phase velocity $-c_2$.
Building on these intrinsic dynamics, we can investigate the effects of the global coupling in Eq. 2.2 by investigating the dynamics of many of such limit cycle oscillators.
This chapter is structured as follows: First, we restrict our analysis on the dynamics of just two oscillators, and show where stable symmetric and asymmetric fixed-point solutions exist in parameter space. Moreover, we also give a short overview of the

period orbits that appear in this system.
These considerations form the basis for our investigations of an ensemble of four oscillators. There, we show where balanced cluster states, states with two oscillators in each cluster, can be observed. In addition, we outline how those cluster states bifurcate in such a setting. An important part in this section will be the analysis of how chimera states originate from such balanced cluster states. We then give a detailed explanation of how these states further bifurcate into fully incoherent dynamics using Lyapunov exponents and classify the appearing chimeras using symmetry arguments.
In the last part of this chapter, we explain how the results obtained generalize to larger ensembles of globally coupled limit cycle oscillators. There, we also discuss the occurrence of a new co-dimension two-point, which we call a cluster singularity. At this point, the transition form balanced cluster states to synchronized motion becomes, in contrast to previously observed transitions, continuous. In the course of our considerations, we draw connections to the spatially extended system, Eq. 2.1, whenever possible. For a reproduction of the derivation of the complex Ginzburg-Landau equation with global coupling for general oscillatory systems close to the onset of oscillations, see Appendix A, where we strictly follow the arguments outlined in Refs. [21–23].
Some aspects of this chapter, in particular the differentiation of symmetric and asymmetric chimeras, and clustering as well as cluster singularities, we published in Refs. [17, 18], and thus some parts of Chapter 2 follow closely the content of these references.
In addition, this chapter contains parts explaining background necessary to follow the subsequent considerations, and thus these parts do not contain new findings. These parts include the derivation of the Benjamin-Feir instability, Sec. 2.1.11, the calculation of Lyapunov exponents, Secs. 2.2.4 and 2.2.8, and the derivation of symmetry detectives, Sec. 2.2.6.

2.1 The Dynamics of Two Coupled Oscillators

In this section, we take two oscillators of the form as shown in Eq. (2.3), and couple them through their respective mean. That is, we take the Stuart-Landau ensemble, Eq. (2.3), with $N = 2$ [24, 32]. Doing so, we obtain the following description for the two complex amplitudes W_1 and W_2,

$$\partial_t W_k = W_k - (1 + ic_2)\,|W_k|^2\,W_k + (\alpha + i\beta)\,(\langle W\rangle - W_k) \tag{2.4}$$

with $k \in \{1, 2\}$, the complex coupling constant $(\alpha + i\beta)$ and the real shear c_2. Hereby, the coupling is diffusive in the sense that it vanishes if $W_1 = W_2$ [24]. In

particular,

$$\begin{aligned}\partial_t W_1 &= W_1 - (1+ic_2)\left|W_1\right|^2 W_1 + \kappa\left(\frac{1}{2}\left(W_1+W_2\right) - W_1\right)\\ &= W_1 - (1+ic_2)\left|W_1\right|^2 W_1 + \frac{\alpha+i\beta}{2}\left(W_2 - W_1\right)\\ \partial_t W_2 &= W_2 - (1+ic_2)\left|W_2\right|^2 W_2 + \kappa\left(\frac{1}{2}\left(W_2+W_1\right) - W_2\right)\\ &= W_2 - (1+ic_2)\left|W_2\right|^2 W_2 + \frac{\alpha+i\beta}{2}\left(W_1 - W_2\right)\end{aligned}$$

holds. However, analysis simplifies using polar coordinates, transforming the equations into

$$\begin{aligned}\dot{R}_i e^{i\phi_i} + iR_i\dot{\phi}_i e^{i\phi_i} &= R_i e^{i\phi_i} - (1+ic_2)\,R_i^3 e^{i\phi_i} + \frac{\alpha+i\beta}{2}\left(R_j e^{i\phi_j} - R_i e^{i\phi_i}\right)\\ \dot{R}_i + iR_i\dot{\phi}_i &= R_i - (1+ic_2)\,R_i^3 + \frac{\alpha+i\beta}{2}\left(R_j e^{i(\phi_j-\phi_i)} - R_i\right)\end{aligned}$$

which can be separated into amplitude and phase equations for R_1, R_2, ϕ_1, ϕ_2, respectively, yielding

$$\begin{aligned}\partial_t R_1 &= R_1 - R_1^3 + \frac{\alpha}{2}\left(R_2\cos\left(\phi_2-\phi_1\right) - R_1\right) - \frac{\beta}{2}\left(R_2\sin\left(\phi_2-\phi_1\right)\right)\\ \partial_t R_2 &= R_2 - R_2^3 + \frac{\alpha}{2}\left(R_1\cos\left(\phi_1-\phi_2\right) - R_2\right) - \frac{\beta}{2}\left(R_1\sin\left(\phi_1-\phi_2\right)\right)\\ \partial_t \phi_1 &= -c_2 R_1^2 + \frac{\beta}{2R_1}\left(R_2\cos\left(\phi_2-\phi_1\right) - R_1\right) + \frac{\alpha}{2R_1}\left(R_2\sin\left(\phi_2-\phi_1\right)\right)\\ \partial_t \phi_2 &= -c_2 R_2^2 + \frac{\beta}{2R_2}\left(R_1\cos\left(\phi_1-\phi_2\right) - R_2\right) + \frac{\alpha}{2R_2}\left(R_1\sin\left(\phi_1-\phi_2\right)\right).\end{aligned}$$

Note that we explicitly exclude the solutions with $R_1 = 0$ and/or $R_2 = 0$, since at those points the phases of the respective oscillators are not defined. Therefore, we will not consider any solutions with either $R_1 = 0$ or $R_2 = 0$ in the course of this work.

Due to the rotational invariance of the system, the dynamics do not depend on the absolute values of the phases but only on the phase difference. Hence one can write $\Delta\phi = \phi_1 - \phi_2$, and reduce the equations to

$$\partial_t R_1 = R_1 - R_1^3 + \frac{\alpha}{2}\left(R_2\cos\left(\Delta\phi\right) - R_1\right) + \frac{\beta}{2}R_2\sin\left(\Delta\phi\right) \tag{2.5}$$

$$\partial_t R_2 = R_2 - R_2^3 + \frac{\alpha}{2}\left(R_1\cos\left(\Delta\phi\right) - R_2\right) - \frac{\beta}{2}R_1\sin\left(\Delta\phi\right) \tag{2.6}$$

$$\partial_t \Delta\phi = -c_2\left(R_1^2 - R_2^2\right)$$

$$+\frac{\beta}{2}\cos(\Delta\phi)\left(\frac{R_2}{R_1}-\frac{R_1}{R_2}\right)-\frac{\alpha}{2}\sin(\Delta\phi)\left(\frac{R_2}{R_1}+\frac{R_1}{R_2}\right). \tag{2.7}$$

Eqs. (2.5) to (2.7) describe the dynamics of the two mean coupled oscillators in a co-rotating frame. That is, oscillations with fixed amplitudes and phase differences in the original system, Eq. 2.4, correspond to fixed points in this three variable system.

With an eye towards obtaining fixed point solutions of Eqs. (2.5) to (2.7), it has proven useful to rewrite the equations by introducing the sum and the difference of the square amplitudes, $\gamma = R_1^2 + R_2^2$ and $\rho = R_1^2 - R_2^2$, with

$$\begin{aligned}\partial_t\gamma &= 2R_1\partial_t R1_1 + 2R_2\partial_t R1_2\\ \partial_t\rho &= 2R_1\partial_t R1_1 - 2R_2\partial_t R1_2.\end{aligned}$$

This transforms Eqs. (2.5) - (2.7) into

$$\begin{aligned}\partial_t\gamma &= (2-\alpha)\left(R_1^2+R_2^2\right) - 2\left(R_1^2+R_2^2\right)^2 + 4R_1^2R_2^2 + 2\alpha R_1R_2\cos(\Delta\phi)\\ \partial_t\rho &= (2-\alpha)\left(R_1^2-R_2^2\right) - 2\left(R_1^4-R_2^4\right) + 2\beta R_1R_2\sin(\Delta\phi)\\ \partial_t\Delta\phi &= -c_2\left(R_1^2-R_2^2\right) - \frac{\beta}{2}\cos(\Delta\phi)\frac{R_1^2-R_2^2}{R_1R_2} - \frac{\alpha}{2}\sin(\Delta\phi)\frac{R_1^2+R_2^2}{R_1R_2}\end{aligned}$$

and using $R_1R_2 = \sqrt{\gamma^2-\rho^2}/2$,

$$\partial_t\gamma = (2-\alpha-2\gamma)\gamma + \gamma^2 - \rho^2 + \alpha\sqrt{\gamma^2-\rho^2}\cos(\Delta\phi) \tag{2.8}$$

$$\partial_t\rho = (2-\alpha-2\gamma)\rho + \beta\sqrt{\gamma^2-\rho^2}\sin(\Delta\phi) \tag{2.9}$$

$$\partial_t\Delta\phi = -c_2\rho - \beta\cos(\Delta\phi)\frac{\rho}{\sqrt{\gamma^2-\rho^2}} - \alpha\sin(\Delta\phi)\frac{\gamma}{\sqrt{\gamma^2-\rho^2}}. \tag{2.10}$$

Note that fixed points of the transformed system, Eqs. (2.8) - (2.10), are also fixed points of the original system, Eqs. (2.5) - (2.7).

2.1.1 Symmetries

Considering the symmetries of an equation allows one to draw conclusions about the possible invariant sets of the system. Therefore, we briefly mention the apparent symmetries in the equations here.

An apparent symmetry in the system is that it stays invariant under the permutation of the two oscillators, that is, under the operation of the symmetry group $\mathbf{S}_2$ corresponding to an exchange of symbols. The full four-dimensional system, Eq. 2.4, is invariant under the rotations $W_k \to W_k e^{i\theta}$,

$$\partial_t W_k e^{i\theta} = W_k e^{i\theta} - (1+ic_2)\left|W_k e^{i\theta}\right|^2 W_k e^{i\theta} + (\alpha+i\beta)\left(\langle We^{i\theta}\rangle - W_k e^{i\theta}\right)$$

$$= W_k e^{i\theta} - (1+ic_2)\,|W_k|^2\,W_k e^{i\theta} + (\alpha+i\beta)\left(\langle W\rangle e^{i\theta} - W_k e^{i\theta}\right)$$
$$\rightarrow \partial_t W_k = W_k - (1+ic_2)\,|W_k|^2\,W_k + (\alpha+i\beta)\left(\langle W\rangle - W_k\right).$$

However, we removed this symmetry by just regarding the phase differences of the two oscillators, which yields the three-dimensional system described by Eqs. (2.8) - (2.10).
Since the original ensemble of N oscillators is $\mathbf{S}_N$-equivariant, every symmetry broken state must belong to a subgroup of $\mathbf{S}_N$. In particular, for any two-cluster states $\boldsymbol{u}_{\rm cl}$, the isotropy subgroup $\Sigma_{\boldsymbol{u}_{\rm cl}}$ has the form $\mathbf{S}_{N_1}\times\mathbf{S}_{N_2}\subseteq\mathbf{S}_N$. Furthermore, let $\{\gamma\in\mathbf{S}_N\backslash\Sigma_{\boldsymbol{u}_{\rm cl}}\}$ denote the set of operations not included in the isotropy subgroup of $\boldsymbol{u}_{\rm cl}$, then there exist $N_{\boldsymbol{u}_{\rm cl}} = \|\{\gamma\in\mathbf{S}_N\backslash\Sigma_{\boldsymbol{u}_{\rm cl}}\}\|$ cluster solutions related to $\boldsymbol{u}_{\rm cl}$ which form the so-called group orbit of $\boldsymbol{u}_{\rm cl}$ [33]. For example, considering the two-cluster solution $\boldsymbol{u}_{\rm cl} = (\gamma,\rho,\Delta\phi)$, then $\tilde{\boldsymbol{u}}_{\rm cl} = (\gamma,-\rho,-\Delta\phi)$ is also a 2-cluster solution and $\boldsymbol{u}_{\rm cl}$, $\tilde{\boldsymbol{u}}_{\rm cl}$ belong to the same group orbit.
Two more symmetries originate from the fact that the parameters c_2 and β appear complex in Eq. (2.2) and have an effect on the phase separation $\Delta\phi$ rather than the amplitude separations ρ. That is, a simultaneous change of the signs of c_2 and β corresponds to an exchange of the two oscillators. In particular, if $c_2 = 0$, bifurcations are symmetric with respect to $\beta\rightarrow-\beta$. In the original system, Eq. 2.4, this symmetry is expressed through

$$\beta\rightarrow-\beta,\ c_2\rightarrow-c_2,\ W_1\rightarrow W_1^*,\ W_2\rightarrow W_2^*,$$

which corresponds to an interchange of the two oscillators and shifting the phase by $\pi/2$, under which the system is invariant. Or, expressed through γ and ρ,

$$\beta\rightarrow-\beta,\ c_2\rightarrow-c_2,\ \rho\rightarrow-\rho,\ \Delta\phi\rightarrow-\Delta\phi.$$

2.1.2 Weak Coupling Limit

If the coupling is weak, that is if $\|\kappa=\alpha+i\beta\| << 1$, then the amplitudes relax to $R_1 = 1$, $R_2 = 1$ on a fast time scale, and the dynamics can be described, in a good approximation, by the phase equation only [21]. Therefore, with the adiabatic approximation $\rho = 0$ and $\gamma = 2$ the system, Eqs. (2.8) - (2.10), reduces to

$$\partial_t\Delta\phi = -\alpha\sin(\Delta\phi),$$

and thus to a sine-coupled system [15]. Notice that it has two fixed points at $\Delta\phi = 0$ and $\Delta\phi = \pm\pi$, and therefore only the in-phase and anti-phase invariant solutions exist for weak coupling. Important findings for larger ensembles of limit-cycle oscillators with weak coupling, that is, for globally coupled phase oscillator systems, are summarized in [34] and [35] and are beyond the scope of the considerations here.

2.1.3 Symmetric Fixed-Point Solutions

Fixed point solutions of the two coupled oscillator system, Eqs. (2.8) - (2.10), can be obtained by setting the transformed equations $\partial_t\gamma, \partial_t\rho$ and $\partial_t\Delta\phi$ equal to zero. Doing so, we focus in this Section on solutions with $\rho = 0$, that is for solutions that have $R_1 = R_2$ and which we call *symmetric* fixed point solutions.
From Eq. (2.10) then follows that

$$\alpha \sin(\Delta\phi) = 0 \ \rightarrow \Delta\phi \in \{0, \pm\pi\} \ \forall\alpha \neq 0$$

and thus for equal amplitudes, only in-phase solutions $\Delta\phi = 0$ and anti-phase fixed-point solutions $\Delta\phi = \pm\pi$ exist.
In case of the symmetric in-phase solution ($\rho = 0, \Delta\phi = 0$) it follows from Eq. (2.8) that

$$\begin{aligned} 0 &= (2 - \alpha - 2\gamma)\,\gamma + \gamma^2 + \alpha\gamma \\ 0 &= 2 - \alpha - \gamma + \alpha \\ \rightarrow \gamma &= 2 \end{aligned}$$

and with $\rho = R_1^2 - R_2^2 = 0$ it follows that $R_1 = R_2 = 1$. It is worth mentioning that this solution is, despite its stability, independent of the system parameters, and in the following, we will refer to it as the synchronized solution

$$\boldsymbol{u}_s = \begin{pmatrix} \gamma_s \\ \rho_s \\ \Delta\phi_s \end{pmatrix} = \begin{pmatrix} 2 \\ 0 \\ 0 \end{pmatrix}. \tag{2.11}$$

For the anti-phase solution ($\rho = 0, \Delta\phi = \pm\pi$), Eq. (2.8) turns into

$$\begin{aligned} 0 &= (2 - \alpha - 2\gamma)\,\gamma + \gamma^2 - \alpha\gamma \\ 0 &= 2 - \alpha - \gamma - \alpha \\ \rightarrow \gamma &= 2 - 2\alpha \end{aligned}$$

and thus, with $\gamma = R_1^2 + R_2^2$, $R_1 = R_2 = \sqrt{1-\alpha}$. We abbreviate this anti-phase solution with

$$\boldsymbol{u}_a = \begin{pmatrix} \gamma_a \\ \rho_a \\ \Delta\phi_a \end{pmatrix} = \begin{pmatrix} 2 - 2\alpha \\ 0 \\ \pm\pi \end{pmatrix}. \tag{2.12}$$

Due to the dependence of $\boldsymbol{u}_a$ on α, and since we require that the amplitudes are strictly positive, the solution only exists for $\alpha < 1$. In contrast to the synchronized solution $\boldsymbol{u}_s$, the anti-phase solution $\boldsymbol{u}_a$ does depend on the system parameters, i.e. it is a function of α.

In order to investigate the stability of the two symmetric solutions, it is useful to investigate the eigenvalues of the Jacobian,

$$
\begin{aligned}
J_{11} &= (2-\alpha-2\gamma)+\alpha\frac{\gamma}{\sqrt{\gamma^2-\rho^2}}\cos(\Delta\phi)\\
J_{12} &= -2\rho-\alpha\frac{\rho}{\sqrt{\gamma^2-\rho^2}}\cos(\Delta\phi)\\
J_{13} &= -\alpha\sqrt{\gamma^2-\rho^2}\sin(\Delta\phi)\\
J_{21} &= -2\rho+\beta\frac{\gamma}{\sqrt{\gamma^2-\rho^2}}\sin(\Delta\phi)\\
J_{22} &= (2-\alpha-2\gamma)-\beta\frac{\rho}{\sqrt{\gamma^2-\rho^2}}\sin(\Delta\phi)\\
J_{23} &= \beta\sqrt{\gamma^2-\rho^2}\cos(\Delta\phi)\\
J_{31} &= \beta\cos(\Delta\phi)\frac{\gamma\rho}{(\gamma^2-\rho^2)^{3/2}}+\alpha\sin(\Delta\phi)\left(\frac{\gamma^2}{(\gamma^2-\rho^2)^{3/2}}-\frac{1}{\sqrt{\gamma^2-\rho^2}}\right)\\
J_{32} &= -c_2-\beta\cos(\Delta\phi)\left(\frac{\rho^2}{(\gamma^2-\rho^2)^{3/2}}+\frac{1}{\sqrt{\gamma^2-\rho^2}}\right)\\
&\quad+\alpha\sin(\Delta\phi)\frac{\gamma\rho}{(\gamma^2-\rho^2)^{3/2}}\\
J_{33} &= \beta\sin(\Delta\phi)\frac{\rho}{\sqrt{\gamma^2-\rho^2}}-\alpha\cos(\Delta\phi)\frac{\gamma}{\sqrt{\gamma^2-\rho^2}}
\end{aligned}
\tag{2.13}
$$

evaluated at these fixed points. In particular, the eigenvalues reveal the stability depending on the parameters α, β and c_2.
At the synchronized solution $\boldsymbol{u}_s$, the Jacobian simplifies to

$$
\mathbf{J}|_{\boldsymbol{u}_s} = \begin{pmatrix} -2 & 0 & 0 \\ 0 & -2-\alpha & 2\beta \\ 0 & -c_2-\beta/2 & -\alpha \end{pmatrix}
$$

with the eigenvalues

$$
\begin{aligned}
\lambda_{s,1} &= -2\\
\lambda_{s,2} &= -1-\alpha-\sqrt{1-\beta^2-2\beta c_2}\\
\lambda_{s,3} &= -1-\alpha+\sqrt{1-\beta^2-2\beta c_2}.
\end{aligned}
$$

and eigenvectors

$$
\boldsymbol{v}_1 = \begin{pmatrix} 1 \\ 0 \\ 0 \end{pmatrix}\ ,\ \boldsymbol{v}_2 = \begin{pmatrix} 0 \\ \frac{1+\sqrt{1-\beta^2-2\beta c_2}}{c_2+\beta/2} \\ 1 \end{pmatrix}\ ,\ \boldsymbol{v}_3 = \begin{pmatrix} 0 \\ \frac{1-\sqrt{1-\beta^2-2\beta c_2}}{c_2+\beta/2} \\ 1 \end{pmatrix}.
$$

Note that the eigenvector corresponding to $\lambda_1 = -2$ is $\boldsymbol{v}_{s,1} = (1,0,0)^{\mathrm{T}}$, and thus points in the direction of γ and hence of the sum $R_1^2 + R_2^2$. Nevertheless, λ_1 is always negative, ensuring that this direction is always stable near the synchronous solution. The largest eigenvalue is λ_3, which is always positive for $\alpha < -1$. Thus, for this range of α, the synchronized solution is always unstable. For $\alpha > -1$, the stability of the synchronized solution depends on the parameters β and c_2 in the following way. For $\beta = 0$, $\boldsymbol{u}_s$ is unstable for $\alpha < 0$ and stable for $\alpha > 0$. If $c_2 = 0$, $\boldsymbol{u}_s$ is stable for all $\alpha > 0$ and for the range $-1 < \alpha < 0$ with the condition

$$\begin{aligned} \lambda_{s,3} &= -1 - \alpha + \sqrt{1-\beta^2} < 0 \\ \alpha &> -1 + \sqrt{1-\beta^2}\ \forall \beta^2 < 1, \end{aligned}$$

as indicated through the solid blue line in Fig. 2.1. In addition, one additional direction becomes unstable at

$$\begin{aligned} \lambda_{s,2} &= -1 - \alpha - \sqrt{1-\beta^2} = 0 \\ \alpha &= -1 - \sqrt{1-\beta^2}\ \forall \beta^2 < 1, \end{aligned}$$

indicated through a blue shaded line in Fig. 2.1.
For $c_2 \neq 0$, and values of β and c_2 with opposite signs, the square root in $\lambda_{s,3}$ is not necessarily smaller 1, decreasing the parameter space for which the synchronized state is stable. Nevertheless, increasing α has always a stabilizing effect.
Furthermore, it is worth mentioning that there is a special curve at $\alpha = -1$ and $\beta^2 + 2\beta c_2 > 1$. Then, the real parts of $\lambda_{s,2}$ and $\lambda_{s,3}$ are zero and their values are mutually complex conjugate, indicating a Hopf-bifurcation. Note that the parameter range for which the synchronized solution is stable is independent on the number of oscillators [36, 37]. This is due to the circulant structure of the Jacobi matrix evaluated at this solution, and is explained in more detail in Section 2.1.11.

Evaluated at the anti-phase solution $\boldsymbol{u}_a$, the Jacobian reads

$$\mathbf{J}|_{\boldsymbol{u}_a} = \begin{pmatrix} 2\alpha - 2 & 0 & 0 \\ 0 & -2 + 3\alpha & -\beta\,(2 - 2\alpha) \\ 0 & -c_2 + \beta/\,(2 - 2\alpha) & \alpha \end{pmatrix}$$

with the eigenvalues

$$\begin{aligned} \lambda_{a,1} &= 2\alpha - 2 \\ \lambda_{a,2} &= 2\alpha - 1 - \sqrt{(1-\alpha)^2 - \beta^2 + 2\,(1-\alpha)\,\beta c_2} \\ \lambda_{a,3} &= 2\alpha - 1 + \sqrt{(1-\alpha)^2 - \beta^2 + 2\,(1-\alpha)\,\beta c_2}. \end{aligned}$$

Note that $\boldsymbol{u}_a$ only exists for $\alpha < 1$, as indicate through the red dashed line in Fig. 2.1. Therefore, as for the synchronous solution, $\lambda_{a,1}$ is always negative and

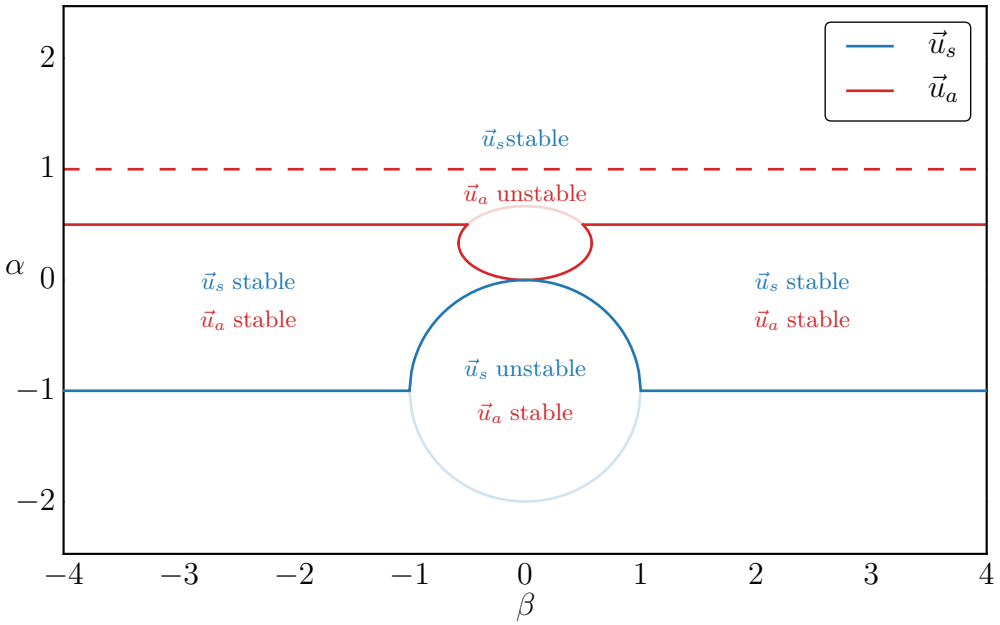

Figure 2.1: Stability of the symmetric solutions $\boldsymbol{u}_s$ and $\boldsymbol{u}_a$ for $c_2 = 0$. From positive to negative α, the stable synchronized solution $\boldsymbol{u}_s$ loses stability at the solid blue line. At the horizontal blue line, the real parts of a pair of complex conjugate eigenvalues cross the imaginary axis, indicating a Hopf bifurcation. On the other hand, at the curved solid blue line, it loses one stable direction, and another at the shaded blue curve. From negative to positive α, the stable anti-phase solution $\boldsymbol{u}_a$ looses two stable directions at the horizontal solid red line, whereas it looses one stable direction at the solid red curve and another at the shaded red curve. It disappears at $\alpha = 1$, indicated through the dashed red line, where the amplitudes vanish.

hence the direction $\boldsymbol{v}_{s,1} = (1, 0, 0)^{\mathrm{T}}$ is always stable. Again, the third eigenvalue is the largest eigenvalue, dictating the range of stability. In particular for $c_2 = 0$, $\boldsymbol{u}_a$ is stable for $\alpha < 1/2$ if the square root is complex, and changes stability at

$$\begin{aligned} \lambda_{a,3} &= 2\alpha - 1 + \sqrt{(1-\alpha)^2 - \beta^2} = 0 \\ 2\alpha - 1 &= -\sqrt{(1-\alpha)^2 - \beta^2} \\ (2\alpha - 1)^2 &= (1-\alpha)^2 - \beta^2 \\ \alpha_{1,2} &= \frac{1}{3} \pm \frac{1}{3}\sqrt{1 - 3\beta^2} \quad \Big| \; \beta < \frac{1}{\sqrt{3}} \,,\; \alpha < \frac{1}{2} \end{aligned}$$

if the square root is real. The boundaries of the stable regions for $c_2 = 0$ are depicted as a solid red line in Fig. 2.1. At the red shaded line, an additional direction of the

anti-phase solution changes stability. The asynchronous solution can be seen as a so-called splay state [38] or ponies on a merry-go-round [39]. This state has the property that all oscillators have the same amplitude and neighboring oscillators have a phase difference of $2\pi/N$. As for the synchronized solution, it can be shown that the boundaries of stability of this state is independent of the number of oscillators N [36]. As already mentioned, the amplitudes of the splay state depend on the coupling constant α. More negative α values lead to a more repulsive coupling, which in turn results in an increase of the respective amplitudes.
From Fig. 2.1 it becomes clear that for $\beta = 0$, the synchronized solution is unstable for negative values of α and becomes stable at $\alpha = 0$, whereas the anti-phase solution is stable for negative α and becomes unstable at $\alpha = 0$. For $\beta \neq 0$, however, the two states do not change anymore their stability at the same value of α, giving rise to the existence of patches in parameter space with a bistability of $\boldsymbol{u}_s$ and $\boldsymbol{u}_a$. In addition, it is worth mentioning that at the horizontal lines in Fig. 2.1 the real parts of two eigenvalues of the Jacobian are complex with zero real part, indicating a Hopf bifurcation. Furthermore, notice the symmetry $\beta \to -\beta$ in the parameter plane, as predicted by the symmetries explained in Section 2.1.1.

2.1.4 Asymmetric Fixed-Points in the Case of no Shear

To simplify the analysis of *asymmetric* solutions, that is solutions with $\rho \neq 0$, we first restrict our analysis to the case of no shear ($c_2 = 0$). This simplifies the equation for the angular velocity, Eq. (2.10), and at a fixed point $\partial_t \Delta\phi = 0$ with $\alpha \neq 0$ it becomes

$$\tan(\Delta\phi) = -\frac{\beta\rho}{\alpha\gamma}.$$

It is interesting to observe that if the absolute value of the real part of the coupling constant, α, is relatively large compared to the imaginary part, β, then the system tends to the symmetric solutions $\boldsymbol{u}_a, \boldsymbol{u}_s$. If, however, the magnitude β increases, the tangents of phase difference becomes non-zero and the phase difference thus accepts values different from 0 and $\pm\pi$. As shown in Section 2.1.5, solving Eqs. (2.8) and (2.9) yields as stationary solutions

$$\gamma_{1,2} = \frac{6 - 3\alpha \pm \sqrt{(2-\alpha)^2 - 8\beta^2}}{4} \tag{2.14}$$

$$\rho_{1,2}^2 = \left(1 + \frac{\alpha^2}{\beta^2}\right)(2 - \alpha - 2\gamma_{1,2})\,\gamma_{1,2} + \gamma_{1,2}^2. \tag{2.15}$$

Note that, by taking the square root of Eq. (2.15), one obtains two solutions, $\pm\rho$, for γ_1 and γ_2, respectively, and thus in total four solutions. However, through the definition of $\rho = R_1^2 - R_2^2$, a sign change in ρ corresponds to an interchange of the two oscillators, and thus the solutions $\pm\rho_{1,2}$ belong to the same group orbit

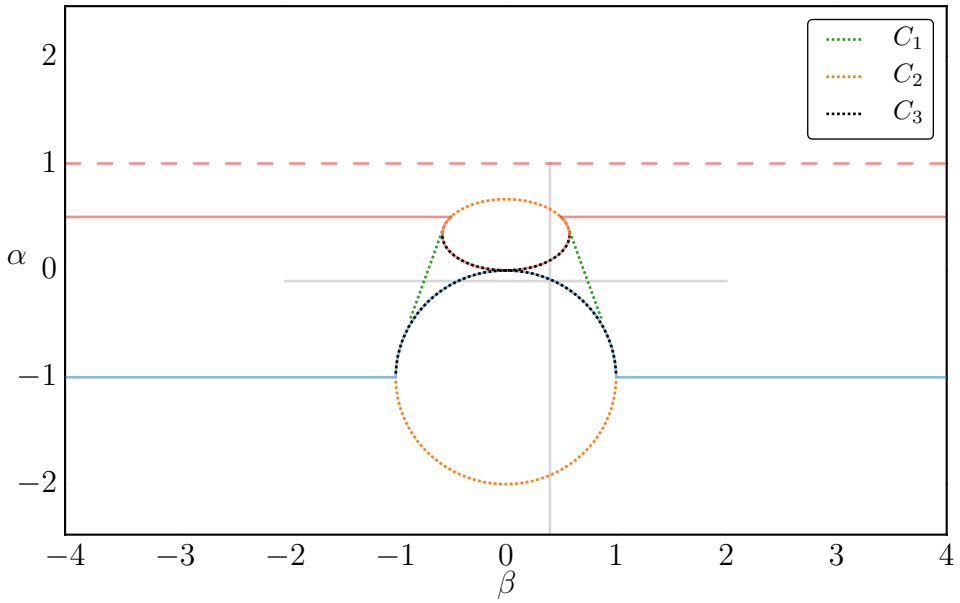

Figure 2.2: Parameter range in which the asymmetric solutions, Eqs. (2.14) and (2.15), exist for $c_2 = 0$. Hereby, solution γ_1 exists for parameter values between condition C_1, indicated through the dotted green lines, and between the dotted orange curves, condition C_2. The boundaries of two solutions γ_2 are again the dotted green lines, and condition C_3, indicated through the dotted black curves. Further bifurcation curves of the synchronized solutions $\boldsymbol{u}_s$ and $\boldsymbol{u}_a$ are shown as shaded blue and red curves. Notice the correspondence of C_2 and C_3 with the curved bifurcation lines of $\boldsymbol{u}_s$ and $\boldsymbol{u}_a$. The gray lines indicate the one-parameter continuation cuts shown in Fig. 2.3.

(c.f. Sec. 2.1.1). Therefore, we treat the solutions of Eqs. (2.14) and (2.15) as two independent solutions, and keep in mind that each solutions exist of two symmetric branches.

2.1.5 General Solution with Zero Shear

At a fixed point solution, Eqs. (2.8) to (2.10) read

$$\begin{aligned} 0 &= (2 - \alpha - 2\gamma)\,\gamma + \gamma^2 - \rho^2 + \alpha\sqrt{\gamma^2 - \rho^2}\cos(\Delta\phi) \\ 0 &= (2 - \alpha - 2\gamma)\,\rho + \beta\sqrt{\gamma^2 - \rho^2}\sin(\Delta\phi) \\ \cos(\Delta\phi) &= -\frac{\alpha\gamma}{\beta\rho}\sin(\Delta\phi)\,. \end{aligned}$$

Assuming the non-trivial case $\alpha \neq 0$, the angular equation yields

$$\tan(\Delta\phi) = -\frac{\beta\rho}{\alpha\gamma}.$$

Using the trigonometric identities

$$\cos\arctan(x) = 1/\sqrt{1+x^2}$$
$$\sin\arctan(x) = x/\sqrt{1+x^2}$$

one obtains

$$0 = (2-\alpha-2\gamma)\gamma + \gamma^2 - \rho^2 + \alpha\frac{\sqrt{\gamma^2-\rho^2}}{\sqrt{1+\left(\frac{\beta\rho}{\alpha\gamma}\right)^2}}$$
$$0 = (2-\alpha-2\gamma)\rho - \beta\frac{\beta\rho}{\alpha\gamma}\frac{\sqrt{\gamma^2-\rho^2}}{\sqrt{1+\left(\frac{\beta\rho}{\alpha\gamma}\right)^2}}$$

which can be simplified into

$$0 = (2-\alpha-2\gamma)\gamma + \gamma^2 - \rho^2 + \alpha\gamma\sqrt{\alpha^2}\frac{\sqrt{\gamma^2-\rho^2}}{\sqrt{\alpha^2\gamma^2+\beta^2\rho^2}}$$
$$0 = (2-\alpha-2\gamma) - \frac{\beta^2}{\alpha}\sqrt{\alpha^2}\frac{\sqrt{\gamma^2-\rho^2}}{\sqrt{\alpha^2\gamma^2+\beta^2\rho^2}}.$$

Substituting

$$\frac{\sqrt{\alpha^2\gamma^2-\alpha^2\rho^2}}{\sqrt{\alpha^2\gamma^2+\beta^2\rho^2}} = -\frac{1}{\alpha\gamma}\left[(2-\alpha-2\gamma)\gamma + \gamma^2 - \rho^2\right]$$

yields

$$0 = (2-\alpha-2\gamma)\gamma + \frac{\beta^2}{\alpha^2}\left[(2-\alpha-2\gamma)\gamma + \gamma^2 - \rho^2\right]$$
$$\rho^2 = \left(1+\frac{\alpha^2}{\beta^2}\right)(2-\alpha-2\gamma)\gamma + \gamma^2.$$

This solution plugged into one of the equations above yields, using Mathematica,

$$\gamma_{1,2} = \frac{6-3\alpha \pm \sqrt{(2-\alpha)^2-8\beta^2}}{4}$$
$$\rho^2 = \left(1+\frac{\alpha^2}{\beta^2}\right)(2-\alpha-2\gamma_{1,2})\gamma_{1,2} + \gamma_{1,2}^2,$$

which are exactly Eqs. (2.14)-(2.15) from above.

2.1.6 Boundaries of the Existence of the Asymmetric Solutions

Since the solutions must be real, Eq. (2.14) requires

$$\begin{aligned}(2-\alpha)^2 - 8\beta^2 &> 0\\ \alpha^2 - 4\alpha + 4 - 8\beta^2 &> 0\\ \alpha_{1,2} &< 2 \pm \sqrt{8\beta^2}.\end{aligned}$$

We dub this condition C_1. The border $\alpha_{1,2} = 2 \pm \sqrt{8\beta^2}$ is indicated through the dotted green line in Fig. 2.2. However, this is only one of the necessary conditions. The second condition requires that $\rho^2 > 0$, i.e. that ρ is real. Therefore, from Eq. (2.15),

$$\begin{aligned}&\left(1 + \frac{\alpha^2}{\beta^2}\right)(2 - \alpha - 2\gamma)\,\gamma + \gamma^2 > 0\\ \Rightarrow &\left(1 + \frac{\alpha^2}{\beta^2}\right)(2 - \alpha - 2\gamma) + \gamma > 0.\end{aligned}$$

This inequality must remain true for both solutions, γ_1 and γ_2, respectively, and thus gives us two sets of conditions. Solving this expression using software such as Mathematica we obtain a first set of conditions, namely

$$\begin{aligned}\alpha &> -1 - \sqrt{1-\beta^2}\\ \alpha &< \frac{1 + \sqrt{1-3\beta^2}}{3}\end{aligned}$$

for the range of α values for which γ_1 exists. This condition we call C_2, and the borders $\alpha = -1 - \sqrt{1-\beta^2}$ and $\alpha = \frac{1+\sqrt{1-3\beta^2}}{3}$ are indicated as dotted orange curves in Fig. 2.2. The second set, conditions C_3 for γ_2, read

$$\begin{aligned}\alpha &> -1 + \sqrt{1-\beta^2}\\ \alpha &< \frac{1 - \sqrt{1-3\beta^2}}{3},\end{aligned}$$

which are indicated as a dotted black curve in Fig. 2.2.
These conditions indicate that the asymmetric solutions only exist for relatively small values of the coupling strength $\|\alpha + i\beta\|$. This has also been observed in networks of many relaxational oscillators, where asymmetric solutions (i. e. cluster solutions) can only be observed for small to medium coupling strengths. [40].

2.1.7 Bifurcations of the Asymmetric Fixed Point Solutions

From the considerations above, we conclude that for parameter values between condition C_1, indicated through the dotted green lines, and between the dotted orange curves, condition C_2, the asymmetric solution $\boldsymbol{u}_1 = (\gamma_1, \pm\rho_1, \Delta\phi_1)$ exists. In addition, the boundaries of solution $\boldsymbol{u}_2 = (\gamma_2, \pm\rho_2, \Delta\phi_2)$ are the dotted green lines, and condition C_3, indicated through the dotted black curves. In total, this means that one asymmetric solution only exists in the ranges between the dotted black lines and the dotted green lines, whereas the other asymmetric solution exists in the range between the dotted orange curves and the dotted green lines. Note that the dotted black and orange curves coincide with bifurcation curves of the symmetric solutions $\boldsymbol{u}_s$ and $\boldsymbol{u}_a$, see Fig. 2.1. This leads to the following conclusions: Since both of the asymmetric solutions, $\boldsymbol{u}_1$ and $\boldsymbol{u}_2$, consist of two branches each, $\pm\rho_{1,2}$, the dotted orange curves and the dotted black curves can be identified as pitchfork bifurcations.
Starting from negative α values, the two branches of the $\boldsymbol{u}_1$ solution emerge at the dotted orange curve from synchronized solution. In addition, the two branches of the $\boldsymbol{u}_2$ solution are born through a pitchfork at the lower dotted black curve, which subsequently get destroyed at the upper dotted black curve at the anti-phase solution. There, the anti-phase solution looses one stable direction. Solutions $\boldsymbol{u}_1$ finally merge through a pitchfork at the upper dotted orange curve, adding another unstable direction to the anti-phase solution. However, changing the parameter β, the (in fact) four solutions $\boldsymbol{u}_1$ and $\boldsymbol{u}_2$ are either born or destroyed through two simultaneous saddle node bifurcations at each of the dotted orange curves.
The continuation of the different solutions along one-parameter cuts (as indicated by the gray lines in Fig. 2.2) is shown in Fig. 2.3, where each solution is represented by its $\Delta\phi$ variable. This means that the synchronized solution is located at $\Delta\phi = 0$ and the anti-phase solution at $\pm\pi$. In Fig. 2.3(a), $\beta = 0.4$ is held fixed and the synchronous solution is continued with increasing α. There, one observes a subcritical pitchfork at which the solution branches of $\boldsymbol{u}_1$ are created and $\boldsymbol{u}_s$ gains an additional stable direction. After another pitchfork the synchronized solution becomes stable and the two branches of $\boldsymbol{u}_2$ are born. Those two branches then reach the anti-phase solution $\boldsymbol{u}_a$ where they get destroyed in a pitchfork bifurcation, rendering $\boldsymbol{u}_a$ unstable. Finally, the branches of $\boldsymbol{u}_1$ merge with $\boldsymbol{u}_a$ in another pitchfork, adding the second unstable direction to $\boldsymbol{u}_a$.
Fixing α at $\alpha = -0.1$ and starting from negative β values (Fig. 2.3(b)), we observe two saddle-node bifurcations, each involving one branch of $\boldsymbol{u}_1$ and $\boldsymbol{u}_2$, respectively. The branches of $\boldsymbol{u}_2$ are annihilated through a subcritical pitchfork at the synchronized solution. Due to the invariance upon a change in the sign of $\beta \to -\beta$, this scenario holds also for positive β values. Note that there is no bifurcation at $\beta = 0$. The crossing of the two branches of $\boldsymbol{u}_1$ is no real crossing but is a consequence of

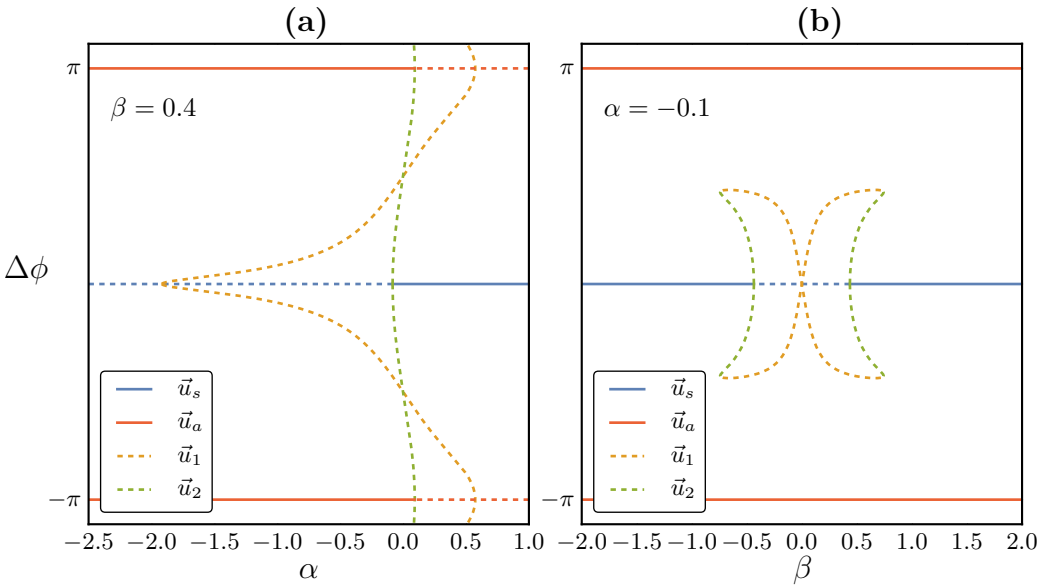

Figure 2.3: Continuation of the fixed point solutions in the reduced model of four mean-coupled oscillators with AUTO, (a) along the vertical cut shown in Fig. 2.2 with $\beta = 0.4$, (b) along the horizontal cut in Fig. 2.2 with $\alpha = -0.1$. Stable solutions are shown as solid curves, whereas unstable branches are indicated by dashed curves. Note that the branches at $\pm\pi$ symbolize the same solution $\boldsymbol{u}_a$.

the projection of the solutions onto the $\Delta\phi$ variable.

Degenerate Pitchfork Points

When the different bifurcation curves meet, a set of co-dimension two points can be identified. First, one observes in Fig. 2.2 that there are in total four points at which the two saddle node curves (dotted green lines) hit the pitchfork curves (dotted black and dotted orange curves). One can obtain their parameter values by setting the conditions $C_1 = C_3$, that is

$$\begin{aligned} 2 \pm \sqrt{8\beta^2} &= \frac{1 + \sqrt{1 - 3\beta^2}}{3} \\ \Rightarrow 5 \pm 6\sqrt{2}\beta &= \sqrt{1 - 3\beta^2} \\ \Rightarrow 24 \pm 60\sqrt{2}\beta + 75\beta^2 &= 0 \\ \Rightarrow \beta_{1,2} &= \mp\frac{2\sqrt{2}}{5} \end{aligned}$$

and thus yielding

$$\alpha = \frac{1 + \sqrt{1 - 3\beta_{1,2}^2}}{3} = \frac{2}{5}$$

and the second pair

$$\begin{aligned} 2 \pm \sqrt{8\beta^2} &= -1 + \sqrt{1 - \beta^2} \\ \Rightarrow 9 \pm 6\sqrt{8}\beta + 8\beta^2 &= 1 - \beta^2 \\ \Rightarrow \beta_{1,2} &= \mp\frac{2\sqrt{2}}{3} \end{aligned}$$

with

$$\alpha = -1 + \sqrt{1 - \beta_{1,2}^2} = -\frac{2}{3}.$$

So in total, where the $\mathcal{SN}$ curves meet the $\mathcal{P}$ curves, there are two times two special points $\Lambda = (\alpha, \beta)$,

$${}_1\Lambda_{\mathcal{SN}}^{\mathcal{P}} = \left(\frac{2}{5}, \pm\frac{2\sqrt{2}}{5}\right) \qquad {}_2\Lambda_{\mathcal{SN}}^{\mathcal{P}} = \left(-\frac{2}{3}, \pm\frac{2\sqrt{2}}{3}\right).$$

At these points, the two saddle node curves hit the pitchfork curves, thereby forming the degenerate pitchfork bifurcation points ${}_1\Lambda_{\mathcal{SN}}^{\mathcal{P}}$ and ${}_2\Lambda_{\mathcal{SN}}^{\mathcal{P}}$, with the latter shown in Fig. 2.4 and the former being depicted in Fig. 2.5.

Takens-Bogdanov Points

At the parameter points ${}_1\Lambda_{\mathcal{TB}} = (1/2, -1/2)$ and ${}_2\Lambda_{\mathcal{TB}} = (-1, -1)$ Hopf bifurcations end and hit pitchfork curves $\mathcal{P}$. In particular, the variables $R_1, R_2, \Delta\phi$ are

$${}_1\boldsymbol{u}_{\mathcal{TB}} = \begin{pmatrix} \sqrt{1/2} \\ \sqrt{1/2} \\ \pi \end{pmatrix} \qquad {}_2\boldsymbol{u}_{\mathcal{TB}} = \begin{pmatrix} 1 \\ 1 \\ 0 \end{pmatrix}$$

with the eigenvalues at the asynchronous solution,

$$\begin{aligned} \lambda_{a,1} &= 2\alpha - 2 \\ \lambda_{a,2} &= 2\alpha - 1 - \sqrt{(1-\alpha)^2 - \beta^2 + 2(1-\alpha)\beta c_2} \\ \lambda_{a,3} &= 2\alpha - 1 + \sqrt{(1-\alpha)^2 - \beta^2 + 2(1-\alpha)\beta c_2}. \end{aligned}$$

yielding at ${}_1\Lambda_{\mathcal{TB}}$, ${}_1\boldsymbol{u}_{\mathcal{TB}}$

$${}_1\lambda_{\mathcal{TB}} = \begin{pmatrix} -1 \\ 0 \\ 0 \end{pmatrix}.$$

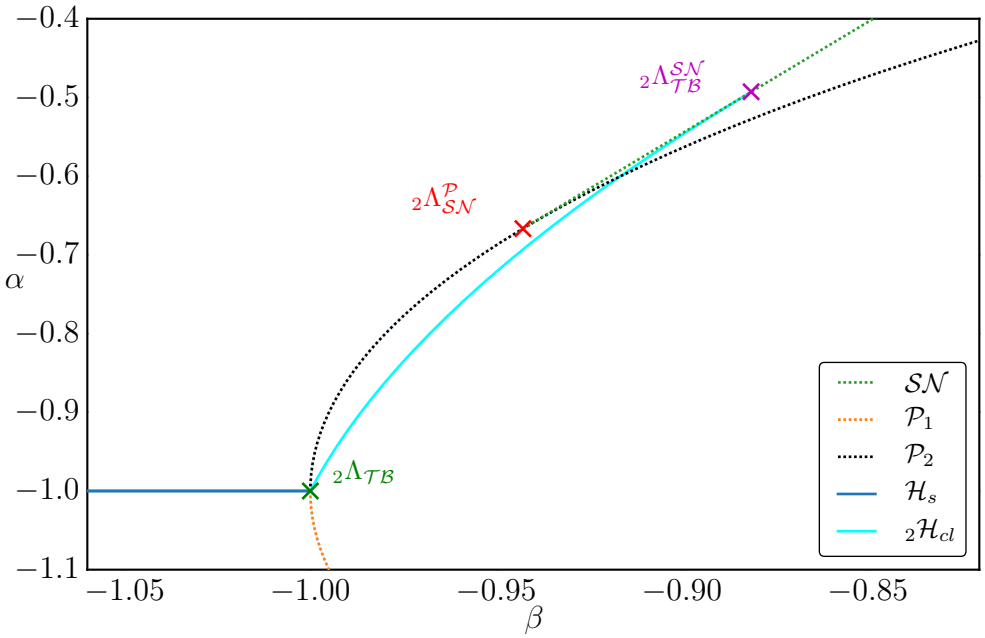

Figure 2.4: Bifurcation diagram with the saddle node curve $\mathcal{SN}$ (dotted green), where two simultaneous saddle node bifurcations between the γ_1 and γ_2 solutions occur. The two pitchfork curves $\mathcal{P}_1$ and $\mathcal{P}_2$ are indicated through dotted orange and black curves, whereas the Hopf bifurcation from the synchronous solution, $\mathcal{H}_s$, is drawn as a solid blue line. In addition, the Takens-Bogdanov point, $_2\Lambda_{\mathcal{TB}} = (-1,-1)$, and the degenerate Pitchfork point, $_2\Lambda^{\mathcal{P}}_{\mathcal{SN}} = \left(-2\sqrt{2}/3, -2/3\right)$, are indicated. The Hopf curve $\mathcal{H}_{cl}$ from the asymmetric solutions was obtained numerically using *PyDSTool* [41, 42], and the numerical results are indicated as cyan dots.

For $_2\Lambda_{\mathcal{TB}}$, $_2\boldsymbol{u}_{\mathcal{TB}}$, one obtains with the eigenvalues at the synchronized solution,

$$\begin{aligned}\lambda_{s,1} &= -2\\ \lambda_{s,2} &= -1-\alpha-\sqrt{1-\beta^2-2\beta c_2}\\ \lambda_{s,3} &= -1-\alpha+\sqrt{1-\beta^2-2\beta c_2}.\end{aligned}$$

the eigenvalues

$$_2\lambda_{\mathcal{TB}} = \begin{pmatrix}-2\\0\\0\end{pmatrix}$$

with two eigenvalues being zero, indicative of Takens-Bogdanov points[1]. The former is shown in Fig. 2.5, and latter Takens-Bogdanov point, $_2\Lambda_{\mathcal{TB}} = (-1,-1)$, is

[1] Close to a Takens-Bogdanov point, there must also be a saddle loop bifurcation curve, which we will discuss in Sections 2.1.8 and 2.1.9

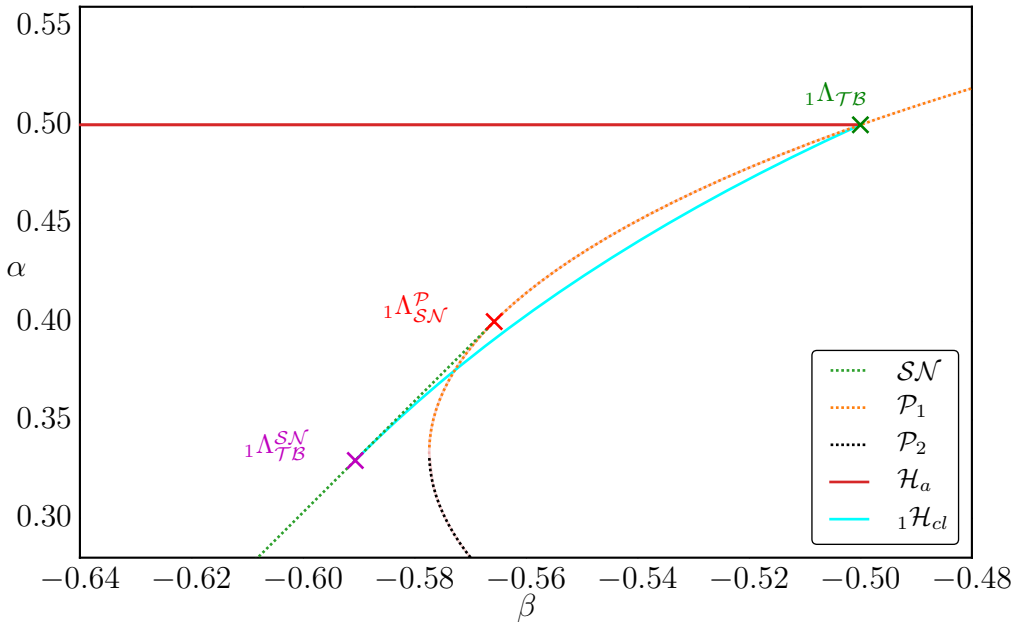

Figure 2.5: Bifurcation diagram with the saddle node curve $\mathcal{SN}$ (dotted green), where two simultaneous saddle node bifurcations between the γ_1 and γ_2 solutions occur. The two pitchfork curves $\mathcal{P}_1$ and $\mathcal{P}_2$ are indicated through dotted orange and black curves, whereas the Hopf bifurcation from the anti-phase solution, $\mathcal{H}_a$, is drawn as a solid red line. In addition, the Takens-Bogdanov point, $_1\Lambda_{\mathcal{TB}} = (-0.5, 0.5)$, and the degenerate Pitchfork point, $_1\Lambda^{\mathcal{P}}_{\mathcal{SN}} = \left(-2\sqrt{2}/5, 2/5\right)$, are indicated. The Hopf curve $_1\mathcal{H}_{cl}$ from the asymmetric solutions was obtained numerically using *PyDSTool* [41, 42], and the numerical results are indicated as cyan dots.

depicted in Fig. 2.4.
Between the co-dimension two bifurcation points shown in Fig. 2.4, $_2\Lambda_{\mathcal{TB}} = (-1, -1)$ and $_2\Lambda^{\mathcal{P}}_{\mathcal{SN}} = \left(-2/3, -2\sqrt{2}/3\right)$, there is a range of parameters for which a supercritical pitchfork bifurcation occurs from the stable synchronized solution $\boldsymbol{u}_s$. Therefore, the asymmetric solutions, which emerge through this pitchfork, must be stable, too. By evaluating the eigenvalues of the Jacobian for these parameter values, this can indeed be verified numerically. Note that to the right of the stable region, see Figs. 2.4 and 2.5, γ_1 has two unstable directions, indicating that the stable region looses its stability through a Hopf bifurcation[2]. Furthermore, the shape of the stable region suggests that this Hopf curve hits the saddle node line at larger values of α. In order to estimate the exact parameter set of this co-dimension two point, one can evaluate the eigenvalues of the Jacobian along the $\mathcal{SN}$ curve,

$$\mathbf{J}\big|_{\boldsymbol{u}_1=\boldsymbol{u}_2}$$

[2] A supercritical Hopf, as verified through simulations.

and investigate when two of these eigenvalues become zero. Numerically, we find that this is the case for

$$ {}_1\Lambda_{\mathcal{TB}}^{\mathcal{SN}} = (0.3294, \pm 0.5906) \qquad {}_2\Lambda_{\mathcal{TB}}^{\mathcal{SN}} = (-0.4928, \pm 0.8814)\,. $$

The former is shown in Fig. 2.5, and the latter, ${}_2\Lambda_{\mathcal{TB}}^{\mathcal{SN}}$, is depicted in Fig. 2.4. Using this information we can conclude that the parameter regimes for which the asymmetric solution is stable, either close to the anti-phase solution (Fig. 2.5) or to the synchronized solution (Fig. 2.4), are bounded on the one side by a supercritical Hopf bifurcation curve (indicated through a cyan curve in both figures). On the other side, it is confined by a supercritical pitchfork and a saddle node bifurcation curve. There are two Takens-Bogdanov points at both ends of the Hopf bifurcation curve, and a degenerate pitchfork point where the saddle node hits the pitchfork bifurcation curve. These stable regimes are rather thin in parameter space, c.f. Figs. 2.4 and 2.5, but grow when increasing the shear c_2, as will be discussed later.

2.1.8 Periodic Orbits Near the Synchronized Solution

For $\beta < 0$, there are four different Hopf bifurcations. In particular, one Hopf bifurcation from the synchronized solution, $\mathcal{H}_s$, one from the anti-phase solution, $\mathcal{H}_a$, and two from the asymmetric solutions, ${}_1\mathcal{H}_{cl}$ (c.f. Fig. 2.4) and ${}_2\mathcal{H}_{cl}$ (c.f. Fig. 2.5), both of which have a multiplicity of two. The periodic invariant sets originating from these bifurcations can be continued using numerical continuation software such as *AUTO*. Close to the synchronized solution, the resulting bifurcation curves are summarized in Fig. 2.6, with a schematic including phase portraits shown in Fig. 2.7.

For small α and β values, the synchronized solution $\boldsymbol{u}_s$ is the only fixed point solution besides the anti-phase solution $\boldsymbol{u}_a$, which we omit here in this section. In particular, the synchronized solution is unstable for these parameter values, see bottom-left corner in Figs. 2.6 and 2.7. The Hopf bifurcation at the synchronized solution, $\mathcal{H}_s$, can be identified as a subcritical Hopf bifurcation for the parameter values considered here. Coming from the negative α values, unstable limit cycles with two unstable directions are born at $\alpha = -1$ for $\beta < -1$, c.f. the blue curve in Figs. 2.6 and 2.7, rendering $\boldsymbol{u}_s$ stable (top-left region in Figs. 2.6 and 2.7). These limit cycles then grow in amplitude with increasing α. For $\alpha \to 0^-$, the limit cycles become relaxational, with the property that they approach the two points $\gamma = \rho$ and $\gamma = -\rho$. Note that we explicitly excluded these two points, which correspond to solutions with one of the two amplitudes, R_1 or R_2, being zero. It is worth mentioning that the period of the orbits does not diverge when $\alpha \to 0^-$, but the numerical continuation fails when converging to these nonphysical solutions.

The stable synchronized solution undergoes a supercritical pitchfork bifurcation when increasing β ($\mathcal{P}_1$, dashed black curve in Figs. 2.6 and 2.7), creating the two symmetric branches of the stable asymmetric solution $\boldsymbol{u}_1$ (the two filled dots in the

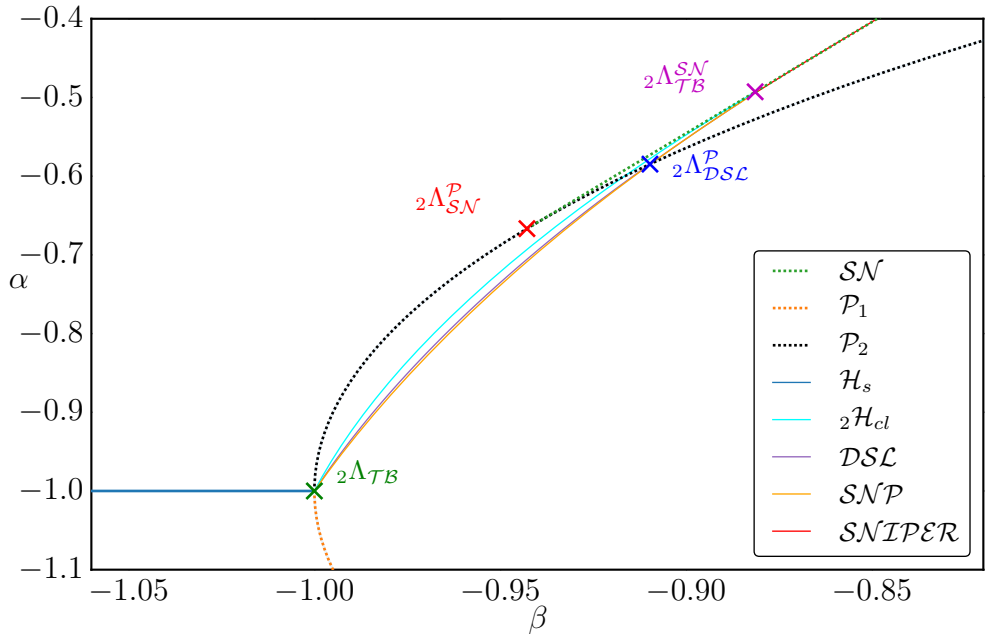

Figure 2.6: Bifurcation diagram with the saddle node curve $\mathcal{SN}$ (dotted green), where two simultaneous saddle node bifurcations between the γ_1 and γ_2 solutions occur. The two pitchfork curves $\mathcal{P}_1$ and $\mathcal{P}_2$ are indicated through dotted orange and black curves, whereas the Hopf bifurcation from the synchronous solution, $\mathcal{H}_s$, is drawn as a solid blue line. The Hopf curve $_1\mathcal{H}_{cl}$ from the asymmetric solutions (cyan), the double saddle loop bifurcation curve $\mathcal{DSL}$ (either normal or forked, magenta) and the saddle node of periodic orbits curve $\mathcal{SNP}$ were obtained numerically using *PyDSTool* and *AUTO*. See Fig. 2.7 for a sketch of the bifurcation curves and detailed phase portraits.

middle top part in Fig. 2.7), and turning $\boldsymbol{u}_s$ into a saddle with one unstable direction. This supercritical pitchfork, however, becomes subcritical at the degenerate pitchfork point $_2\Lambda^{\mathcal{P}}_{\mathcal{SN}}$. From the resulting subcritical pitchfork curve, the two unstable branches of the asymmetric solution $\boldsymbol{u}_2$ emerge, thus adding two more fixed point solutions to the system, yielding in total the five fixed point solutions $\boldsymbol{u}_s$ (stable), $\boldsymbol{u}_1$ (stable) and $\boldsymbol{u}_2$ (unstable). All asymmetric solutions get destroyed through two simultaneous saddle node bifurcations (dotted green line in Figs. 2.6 and 2.7), each involving one branch of $\boldsymbol{u}_1$ and $\boldsymbol{u}_2$, respectively.
On the other hand, the stable $\boldsymbol{u}_1$ solutions undergo two simultaneous supercritical Hopf bifurcations $_2\mathcal{H}_{cl}$ for smaller values of α (cyan curve in Figs. 2.6 and 2.7), creating two stable limit cycles. These two limit cycles subsequently either form an 8-shaped figure and undergo a double saddle loop bifurcation (DSL, lower part of the magenta curve in Figs. 2.6 and 2.7), or form two simultaneous saddle loops with the two solutions of $\boldsymbol{u}_2$ and undergo a forked double saddle loop (fDSL, upper part

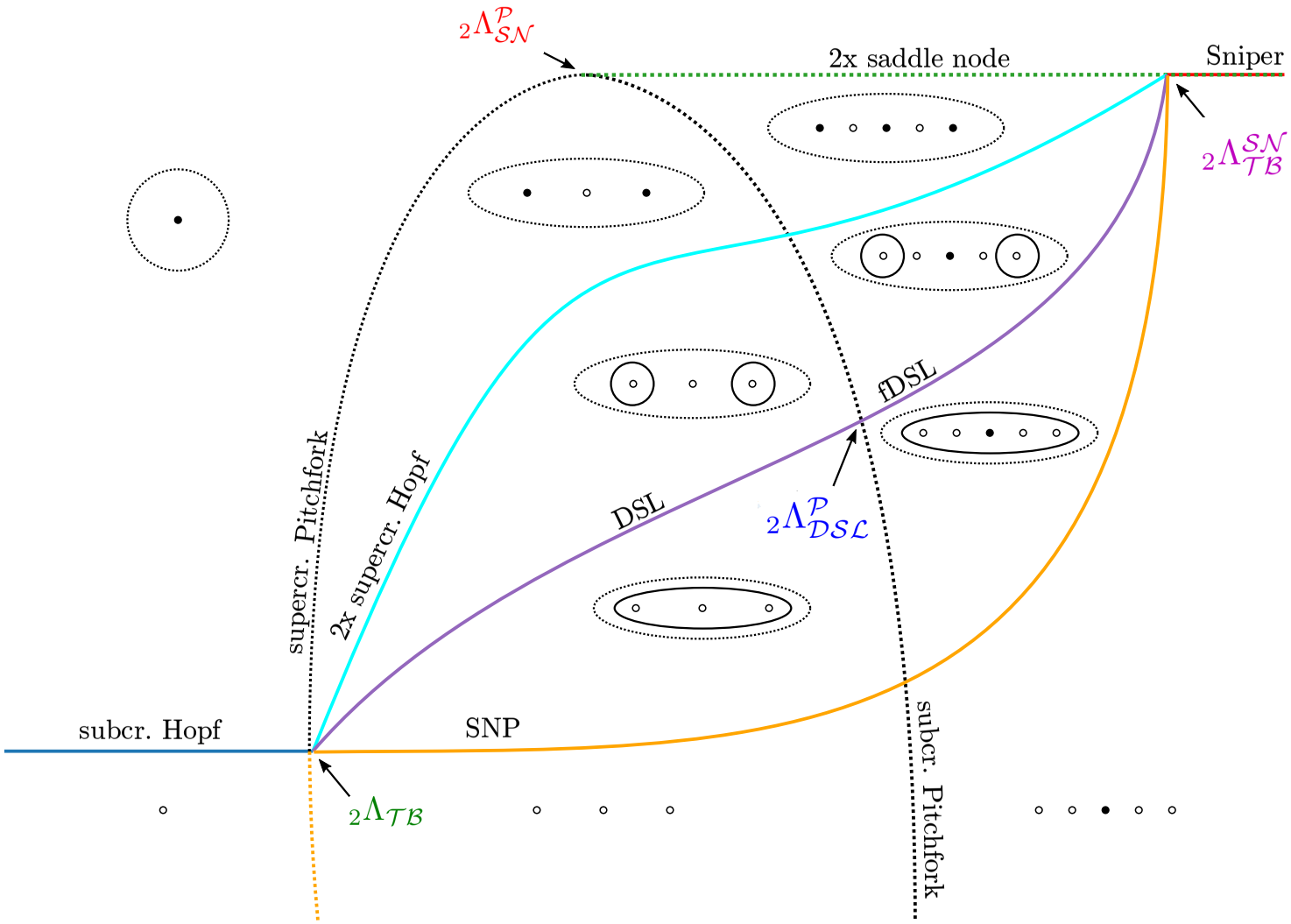

Figure 2.7: Sketch of the bifurcation diagram near of periodic orbits near the synchronized solution. Filled circles indicate stable fixed point solutions, empty circles represent unstable or saddle fixed points, solid closed orbits indicate stable limit cycles, and dashed closed orbits symbolize unstable or saddle limit cycles. See Fig. 2.6 for the actual location of the bifurcation curves in parameter space. The codimension-2 points $_2\Lambda_{\mathcal{TB}}$ and $_2\Lambda^{\mathcal{SN}}_{\mathcal{TB}}$ are Taken-Bogdanov points, $_2\Lambda^{\mathcal{P}}_{\mathcal{SN}}$ is a degenerate Pitchfork point and at $_2\Lambda^{\mathcal{P}}_{\mathcal{DSL}}$ the double saddle loop (DSL) turns into a forked double saddle loop (fDSL). The fixed point of the anti-phase solution has been omitted.

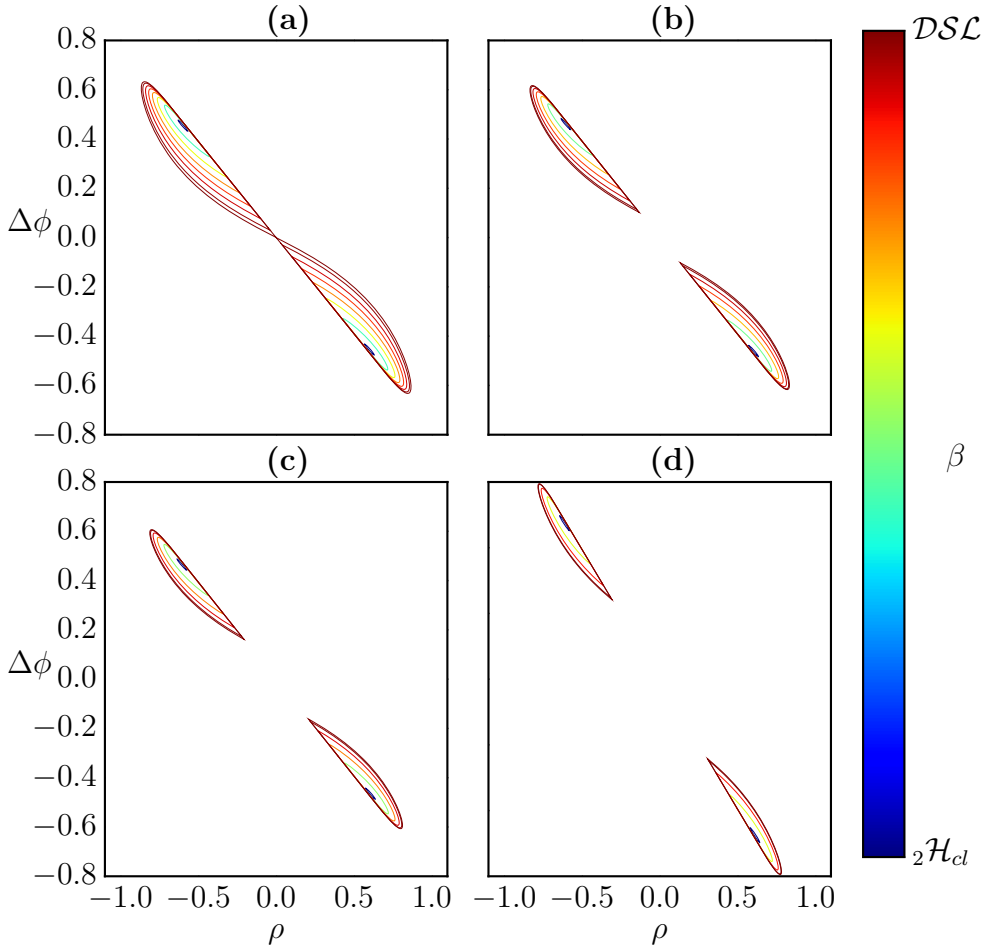

Figure 2.8: Stable limit cycles from the supercritical Hopf ${}_2\mathcal{H}_{cl}$ in the $\Delta\phi$-ρ plane, with the color encoding the respective β values for β between the ${}_2\mathcal{H}_{cl}$ (dark blue) and the $\mathcal{DSL}$ (either normal or forked, dark red). The respective α values are (a) $\alpha = -0.59$, (b) $\alpha = -0.584$, (c) $\alpha = -0.58$ and (d) $\alpha = -0.57$.

of the magenta curve in Figs. 2.6 and 2.7). After any of these two cases, the two smaller limit cycles transformed into a single stable limit, revolving around the three (or five) fixed point solutions. See Ref. [43] for a discussion of this bifurcation[3].
In Ref. [43], the double saddle loop is a codimension-2 bifurcation. In the system considered here, the two oscillators are interchangeable, leading to symmetric bifurcations (e.g. the two simultaneous saddle node and Hopf bifurcations of the asymmetric solutions). This symmetry translates the codimension-2 bifurcation considered in Ref. [43] into a codimension-1 bifurcation here.
At the codimension-2 point ${}_2\Lambda^{\mathcal{P}}_{\mathcal{DSL}}$, when the double saddle loop bifurcation crosses the subcritical pitchfork curve $\mathcal{P}_1$, the double saddle loop curve turns into what we call a forked double saddle loop bifurcation (for an illustration, see Fig. 2.8). The two remaining limit cycles, the stable one from the double saddle loop, and the unstable one from the subcritical Hopf at the synchronized solution, disappear through a saddle node of periodic orbits (SNP, solid orange curve in Figs. 2.6 and 2.7). For larger values of β, the unstable limit cycle stemming from ${}_2\mathcal{H}_s$ gets destroyed through a saddle node of infinite period bifurcation (Sniper, red line with green dashes in Figs. 2.6 and 2.7), at which two saddle node bifurcations simultaneously occur on the unstable periodic orbit. The saddle node of periodic orbits curve and the supercritical Hopf both end in the Takens-Bogdanov points ${}_2\Lambda_{\mathcal{TB}}$ and ${}_2\Lambda^{\mathcal{SN}}_{\mathcal{TB}}$. These Takens-Bogdanov points with symmetry are reminiscent to those reported in a system of two nonlinearily-coupled Stuart-Landau oscillators [44].
The stable limit cycles between the supercritical Hopf curve ${}_2\mathcal{H}_{cl}$ and the double saddle loop curve in the $\Delta\phi$-ρ plane are depicted in Fig. 2.8. For $\alpha = -0.59$ (Fig. 2.8(a)), the limit cycles grow with increasing β (encoded through the coloring, from dark blue to dark red), and eventually form an 8-shaped figure at the double saddle loop bifurcation. However, for larger values of α (Figs. 2.8(b-d)), the limit cycles bifurcate in what we call a forked double saddle loop, at which the two respective limit cycles form homoclinic orbits with two different saddles (the two solutions of $\boldsymbol{u}_2$).
Note that the double saddle loop is also called gluing bifurcation in systems with symmetries [45, 46]. In particular, a gluing bifurcation in a system of two coupled oscillators is also described in more detail in Ref. [47].

2.1.9 Periodic Orbits Near the Anti-Phase Solution

For values of positive α, the bifurcations of the periodic orbits are qualitatively similar to the ones described in the previous section, and are depicted in Fig. 2.9. Starting from the subcritical Hopf at the anti-phase solution, $\mathcal{H}_a$ (red in Fig. 2.9), unstable periodic orbits grow with decreasing α and hit at $\alpha = 0$ nonphysical solutions with vanishing amplitudes. Increasing β, the periodic solutions get destroyed

[3]There seem to be errors in the unfolding of the double saddle loop in this article.

either through a saddle node of infinite period or a saddle node of periodic orbits (the latter not shown in Fig. 2.9). At the supercritical Hopf ${}_1\mathcal{H}_{cl}$ (cyan) stable periodic orbits are born which bifurcate in a double saddle loop (magenta curve in Fig. 2.9), with the resulting periodic orbits disappearing in a saddle node of periodic orbits. Note that, due to the symmetry in the system, the same bifurcations happen for positive β.

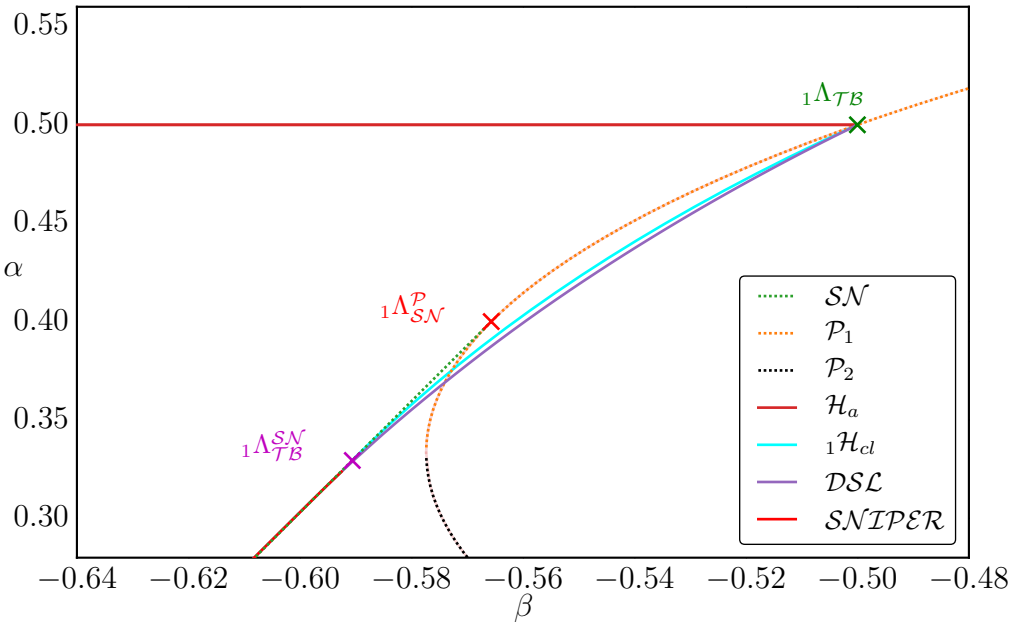

Figure 2.9: Bifurcation diagram with the saddle node curve $\mathcal{SN}$ (dotted green), where two simultaneous saddle node bifurcations between the γ_1 and γ_2 solutions occur. The two pitchfork curves $\mathcal{P}_1$ and $\mathcal{P}_2$ are indicated through dotted orange and black curves, whereas the Hopf bifurcation from the anti-phase solution, $\mathcal{H}_a$, is drawn as a solid red line. The Hopf curve ${}_1\mathcal{H}_{cl}$ from the asymmetric solutions (cyan) and the double saddle loop bifurcation curves $\mathcal{DSL}$ (either normal or forked, magenta) were obtained numerically using *PyDSTool* and *AUTO*.

2.1.10 Bifurcation Diagram with Non-Zero Shear

The analysis can also be extended to the case of non-zero shear c_2. From the analytic expression of the eigenvalues at the synchronized solution

$$\begin{aligned}\lambda_{s,1} &= -2\\ \lambda_{s,2} &= -1-\alpha-\sqrt{1-\beta^2-2\beta c_2}\\ \lambda_{s,3} &= -1-\alpha+\sqrt{1-\beta^2-2\beta c_2}.\end{aligned}$$

and anti-phase solutions,

$$\begin{aligned}\lambda_{a,1} &= 2\alpha - 2\\ \lambda_{a,2} &= 2\alpha - 1 - \sqrt{(1-\alpha)^2 - \beta^2 + 2(1-\alpha)\beta c_2}\\ \lambda_{a,3} &= 2\alpha - 1 + \sqrt{(1-\alpha)^2 - \beta^2 + 2(1-\alpha)\beta c_2}.\end{aligned}$$

we can determine bifurcations for all values of α, β and c_2. For $\boldsymbol{u}_s$, the real parts of the eigenvalues changes sign when

$$\alpha = -1 \pm \sqrt{1 - \beta^2 - 2\beta c_2},$$

or, in an implicit form,

$$\begin{aligned}\alpha + 1 &= \pm\sqrt{1 - \beta^2 - 2\beta c_2}\\ \alpha^2 + 2\alpha + 1 &= 1 - \beta^2 - 2\beta c_2\\ \alpha^2 + \beta^2 + 2\alpha + 2\beta c_2 &= 0.\end{aligned}$$

and with $\kappa = \alpha + i\beta$,

$$\|\kappa\|^2 + 2(\operatorname{Re}\kappa + \operatorname{Im}\kappa c_2) = 0. \tag{2.16}$$

In literature, one usually writes the coupling constant κ as $\kappa = K(1 + ic_1)$ (recall that we use $\kappa = \alpha + i\beta$ here). Expressing the condition above through K and c_1 yields

$$\left(1 + c_1^2\right) K + 2(1 + c_1 c_2) = 0$$

which coincides with Eqs. (2) to (5) of Ref. [48] and is also referred to as Benjamin-Feir instability [36, 49]. Boundaries of stability of the synchronized solution for different c_2 values are shown in Fig. 2.10. The asynchronous solution $\boldsymbol{u}_a$ undergoes stability changes when the real part of $\lambda_{a,3}$ becomes zero. This happens when α satisfies the following condition

$$\alpha = -\frac{1}{3}\left(2\beta c_2 - 1 \pm \sqrt{(2\beta c_2 - 1)^2 - \beta^2 + \beta c_2}\right).$$

As for the case with zero shear, these parameter ranges are independent of the number of oscillators [36, 37]. In particular, the condition for $\lambda_{a,3} = 0$,

$$2\alpha - 1 + \sqrt{(1-\alpha)^2 - \beta^2 + 2(1-\alpha)\beta c_2} = 0$$

can be rewritten as

$$\alpha^2 + \beta^2 - 2(1-\alpha)(\alpha + \beta c_2) = 0$$

and with $\kappa = \alpha + i\beta$,

$$\|\kappa\|^2 - 2(1 - \operatorname{Re}\kappa)(\operatorname{Re}\kappa + \operatorname{Im}\kappa c_2) = 0. \tag{2.17}$$

This stability boundary of the asynchronous solution again coincides with earlier results, see for example Ref. [48]: The stability boundaries of $\boldsymbol{u}_a$ for different values of c_2 are depicted in Fig. 2.11.

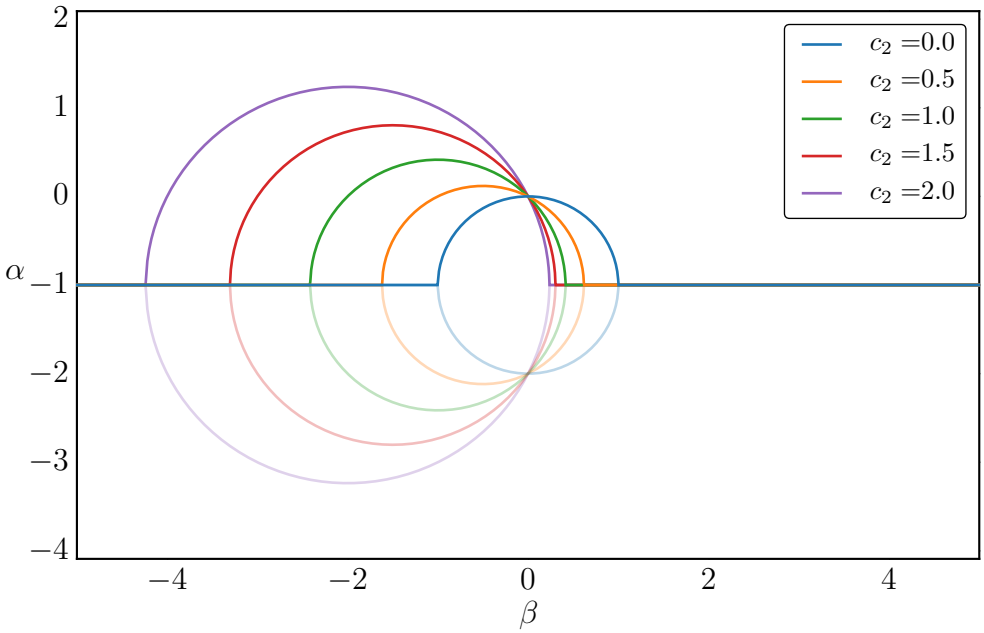

Figure 2.10: Stability boundaries of the synchronized solution $\boldsymbol{u}_s$ for different values of the shear c_2. The shaded lines indicate where a second direction of $\boldsymbol{u}_s$ becomes unstable.

Asymmetric Solutions for Non-Zero Shear

Even for the case of non-zero shear, it is possible to obtain an analytic expression for the two asymmetric solutions $\gamma_{1,2}$, $\rho_{1,2}$. In particular, using the transformed equations, Eqs. (2.8) to (2.10), evaluated at a fixed point solution, gives

$$\begin{aligned}
0 &= (2-\alpha-2\gamma)\,\gamma + \gamma^2 - \rho^2 + \alpha\sqrt{\gamma^2-\rho^2}\cos(\Delta\phi) \\
0 &= (2-\alpha-2\gamma)\,\rho + \beta\sqrt{\gamma^2-\rho^2}\sin(\Delta\phi) \\
0 &= -c_2\rho - \beta\cos(\Delta\phi)\frac{\rho}{\sqrt{\gamma^2-\rho^2}} - \alpha\sin(\Delta\phi)\frac{\gamma}{\sqrt{\gamma^2-\rho^2}}.
\end{aligned}$$

Solving the first two equations for $\cos(\Delta\phi)$ and $\sin(\Delta\phi)$ yields

$$\begin{aligned}
\sqrt{\gamma^2-\rho^2}\cos(\Delta\phi) &= -(2-\alpha-2\gamma)\frac{\gamma}{\alpha} - \frac{\gamma^2-\rho^2}{\alpha} \\
\sqrt{\gamma^2-\rho^2}\sin(\Delta\phi) &= -(2-\alpha-2\gamma)\frac{\rho}{\beta}
\end{aligned}$$

and inserted into the last equation,

$$0 = -c_2\rho + \frac{\beta}{\alpha}\frac{\rho}{\gamma^2-\rho^2}\left[(2-\alpha-2\gamma)\,\gamma + \gamma^2 - \rho^2\right] + \frac{\alpha}{\beta}\frac{\gamma}{\gamma^2-\rho^2}(2-\alpha-2\gamma)\,\rho$$

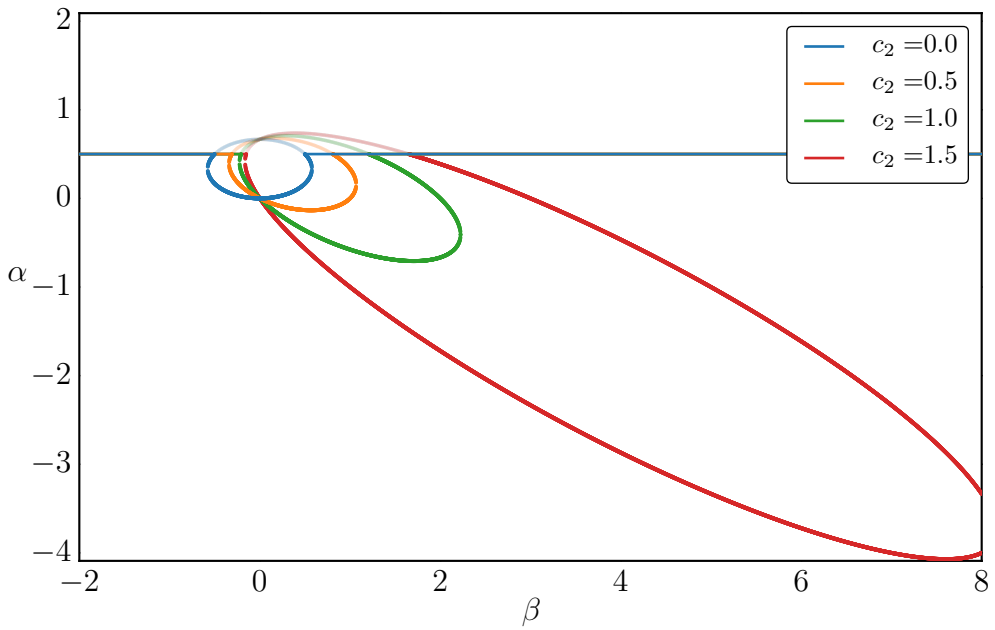

Figure 2.11: Stability boundaries of the anti-phase solution $\boldsymbol{u}_a$ for different values of c_2. The shaded lines indicate where a second direction of $\boldsymbol{u}_a$ becomes unstable.

$$
\begin{aligned}
0 &= -c_2\left(\gamma^2-\rho^2\right)+\frac{\beta}{\alpha}\left[(2-\alpha-2\gamma)\,\gamma+\gamma^2-\rho^2\right]+\frac{\alpha}{\beta}(2-\alpha-2\gamma)\,\gamma\\
0 &= -c_2\alpha\beta\left(\gamma^2-\rho^2\right)+\beta^2(2-\alpha-2\gamma)\,\gamma+\beta^2\left(\gamma^2-\rho^2\right)+\alpha^2(2-\alpha-2\gamma)\,\gamma\\
0 &= \left(\beta^2-c_2\alpha\beta\right)\left(\gamma^2-\rho^2\right)+\left(\alpha^2+\beta^2\right)(2-\alpha-2\gamma)\,\gamma
\end{aligned}
$$

and solving for ρ^2

$$\rho^2=\frac{\alpha^2+\beta^2}{\beta^2-c_2\alpha\beta}(2-\alpha-2\gamma)\,\gamma+\gamma^2. \tag{2.18}$$

Using $1=\sin^2+\cos^2$, we can write

$$
\begin{aligned}
\gamma^2-\rho^2 &= (2-\alpha-2\gamma)^2\frac{\rho^2}{\beta^2}+\left(-(2-\alpha-2\gamma)\frac{\gamma}{\alpha}-\frac{\gamma^2-\rho^2}{\alpha}\right)^2\\
\gamma^2-\rho^2 &= (2-\alpha-2\gamma)^2\frac{\rho^2}{\beta^2}+\frac{1}{\alpha^2}\left(\gamma^2-\rho^2+(2-\alpha-2\gamma)\,\gamma\right)^2.
\end{aligned}
$$

Together with Eq. (2.18) this can be solved using Mathematica, yielding

$$
\begin{aligned}
\rho^2 &= \frac{\alpha^2+\beta^2}{\beta^2-c_2\alpha\beta}(2-\alpha-2\gamma)\,\gamma+\gamma^2, \qquad (2.19)\\
\gamma_{1,2} &= \frac{(2-\alpha)\left(3\beta-4\alpha c_2-\beta c_2^2\right)}{4\beta-8\alpha c_2-4\beta c_2^2}
\end{aligned}
$$

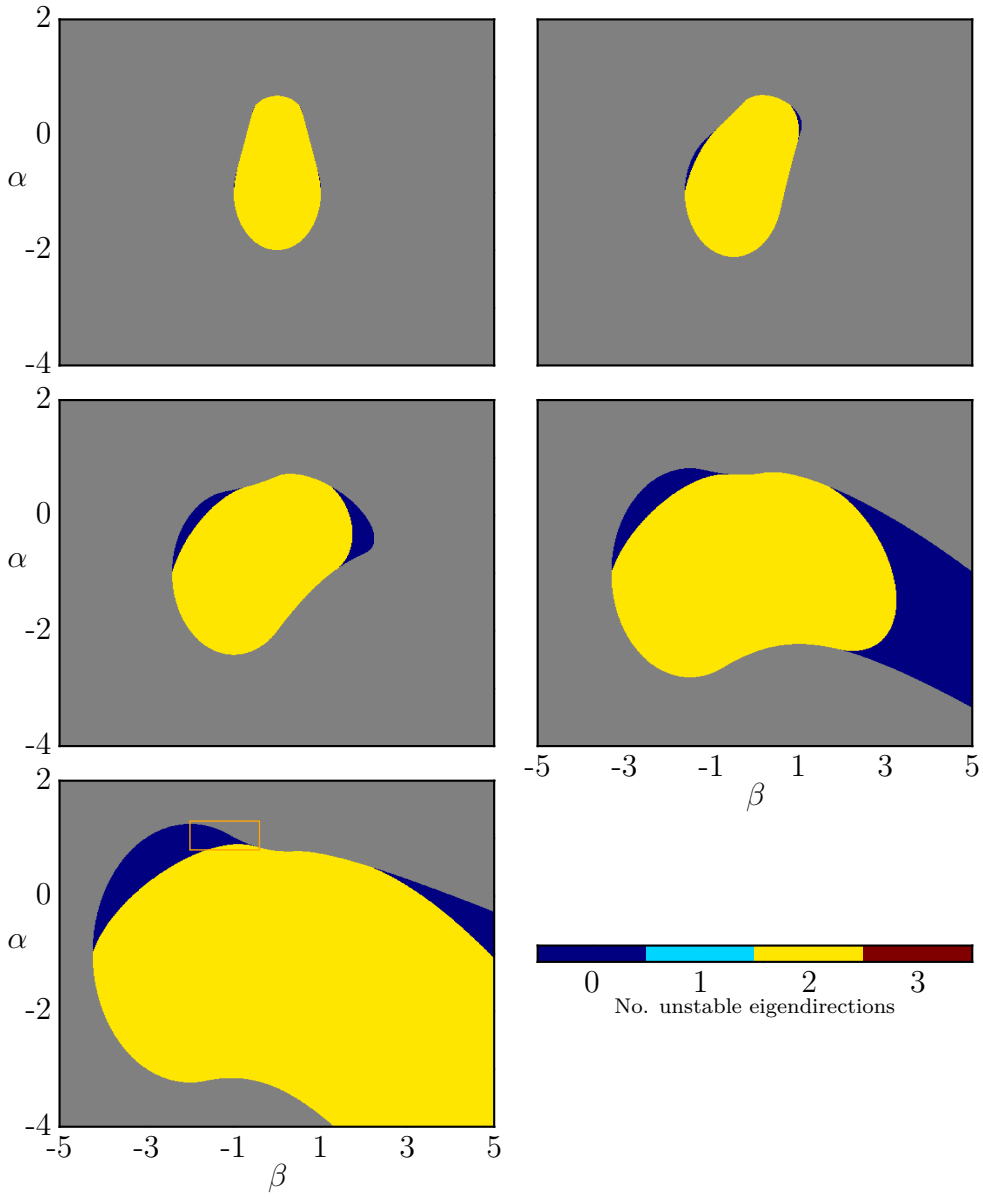

Figure 2.12: Stability of the asymmetric solution in an ensemble of two mean-coupled Stuart-Landau oscillators for $c_2 = 0, 0.5, 1, 1.5, 2$ (from top left to bottom). The color encodes the number of unstable eigendirections, and gray indicates that the asymmetric solution does not exist for this set of parameters. Note the correspondence of the upper left image with Fig. 2.2.

$$\pm \frac{\beta\sqrt{(2-\alpha)^2(1+c_2^2)^2 - 8\beta^2\,(1-c_2^2) + 8\alpha c_2\,(3\beta - 2\alpha c_2 - \beta c_2^2)}}{4\beta - 8\alpha c_2 - 4\beta c_2^2}. \tag{2.20}$$

Note that these equations reduce to the solutions (2.14) and (2.15) for $c_2 = 0$, which are

$$\gamma_{1,2} = \frac{6 - 3\alpha \pm \sqrt{(2-\alpha)^2 - 8\beta^2}}{4},$$
$$\rho_{1,2}^2 = \left(1 + \frac{\alpha^2}{\beta^2}\right)(2 - \alpha - 2\gamma_{1,2})\,\gamma_{1,2} + \gamma_{1,2}^2.$$

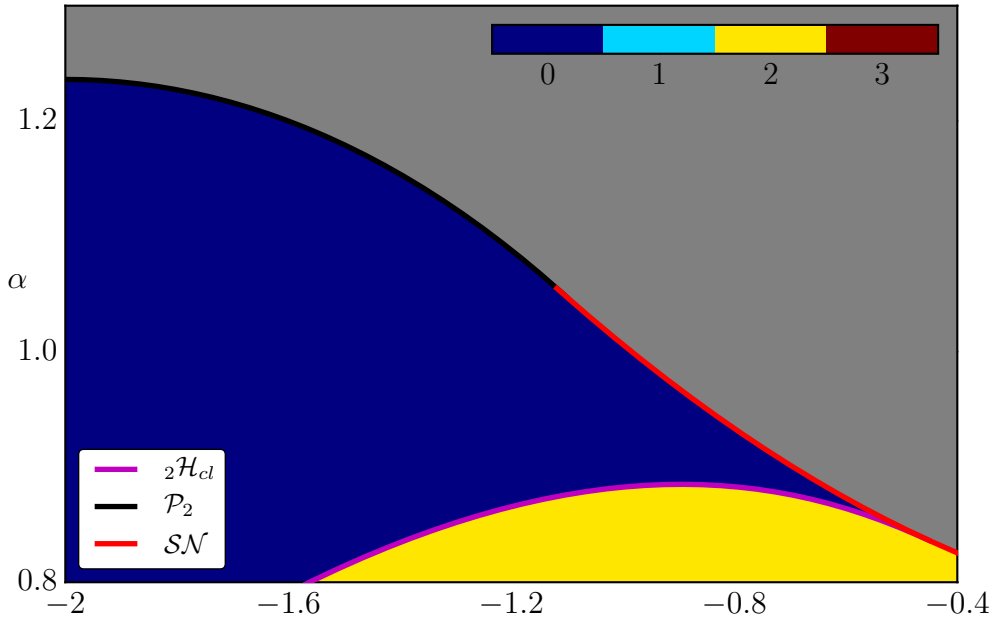

Figure 2.13: Stability of the asymmetric solution in an ensemble of two mean-coupled Stuart-Landau oscillators for $c_2 = 2$. The parameter range corresponds to the orange window indicated in Fig. 2.12 (bottom). As in Fig. 2.12, the color encodes the number unstable eigendirections, and gray indicates that the asymmetric solution does not exist for this set of parameters. The bifurcation curves plotted were obtained using AUTO and symbolize a supercritical Hopf bifurcation curve (magenta), the pitchfork bifurcation curve (black) and a saddle node bifurcation curve (red).

Stability of the Asymmetric Solutions for Non-Zero Shear

The stability of these asymmetric solutions can again be investigated through the eigenvalues of the Jacobian. There, we find that the solution $\boldsymbol{u}_2 = (\gamma_2, \pm\rho_2, \Delta\phi_2)$

is always unstable in the regarded parameter regimes, but $\boldsymbol{u}_1 = (\gamma_1, \pm\rho_1, \Delta\phi_1)$ is stable for certain ranges of α, β and c_2. In particular, the number of unstable eigendirections of $\boldsymbol{u}_1$ in the $\alpha-\beta$ parameter plane are shown in Fig. 2.12 for different values of c_2. Note that the stable windows of the asymmetric solution for $c_2 = 0$ are barely visible, but grow with increasing shear c_2. Furthermore, recall that the shear relates the dynamics of the amplitudes of the individual oscillators to their respective phase dynamics. This, in turn, means that oscillators with larger amplitudes seek to have larger phase velocities. On the other hand, the coupling prevents that the oscillators drift apart. This counterplay of the non-zero shear and the coupling may thus explain why one observes larger regions in parameter space at which asymmetric solutions are stable.
A parameter window in the $\alpha - \beta$ plane for $c_2 = 2$, as indicated through the orange box in Fig. 2.12, is shown enlarged in Fig. 2.13. There, the Hopf bifurcation curve (magenta), the saddle node bifurcation curve between the two asymmetric solutions (red) and the pitchfork with the synchronized solution (black) are shown. This window serves as a starting point for future considerations, as in Section. 2.2.

2.1.11 Stability of the Synchronized Solution

As already outlined, the region for which the synchronized solution is stable is independent of the number of oscillators in the system [48]. The same is true for the anti-phase solution (splay state), although the proof is more cumbersome. Therefore, we redraw the proof for the synchronized solution, and refer the reader to Ref. [36] for the case of the splay state.
Following Ref. [36], we linearize around the synchronous solution of an ensemble of N oscillators by writing $W_k = (1 + \epsilon_k) \exp(-ic_2 t)$. Then Eq. 2.2 turns into

$$\begin{aligned}
\partial_t W_k &= e^{-ic_2 t}\partial_t \epsilon_k - ic_2 (1+\epsilon_k) e^{-ic_2 t} \\
&= (1+\epsilon_k) e^{-ic_2 t} - (1+ic_2) \|1+\epsilon_k\|^2 (1+\epsilon_k) e^{-ic_2 t} \\
&+ \kappa \left(\langle 1+\epsilon \rangle e^{-ic_2 t} - (1+\epsilon_k) e^{-ic_2 t} \right)
\end{aligned}$$

with $\langle \cdot \rangle$ denoting the ensemble mean. This can be rewritten as

$$\begin{aligned}
\partial_t \epsilon_k - ic_2 (1+\epsilon_k) &= (1+\epsilon_k) - (1+ic_2)\|1+\epsilon_k\|^2 (1+\epsilon_k) \\
&\quad + \kappa (\langle 1+\epsilon \rangle - (1+\epsilon_k)) \\
\rightarrow \partial_t \epsilon_k &= (1+ic_2)(1+\epsilon_k) \\
&\quad - (1+ic_2)\left(1+\epsilon_k+\epsilon_k^* + \|\epsilon_k\|^2\right)(1+\epsilon_k) + \kappa(\langle\epsilon\rangle - \epsilon_k) \\
\rightarrow \partial_t \epsilon_k &\approx (1+ic_2)(1+\epsilon_k) \\
&\quad - (1+ic_2)(1+\epsilon_k+\epsilon_k^*)(1+\epsilon_k) + \kappa(\langle\epsilon\rangle - \epsilon_k) \\
\rightarrow \partial_t \epsilon_k &\approx (1+ic_2)(1+\epsilon_k) \\
&\quad - (1+ic_2)(1+2\epsilon_k+\epsilon_k^*) + \kappa(\langle\epsilon\rangle - \epsilon_k)
\end{aligned}$$

$$\rightarrow \partial_t \epsilon_k \approx -(1+ic_2)(\epsilon_k + \epsilon_k^*) + \kappa(\langle\epsilon\rangle - \epsilon_k)$$

with ϵ_k^* being the complex conjugate of ϵ_k. Writing $\epsilon_k = x_k + iy_k$, then

$$\partial_t x_k + i\partial_t y_k = -(1+ic_2)(2x_k) - (\alpha+i\beta)(x_k+iy_k) + \frac{\alpha+i\beta}{N}\sum_j (x_j+iy_j),$$

and when separating real and imaginary parts

$$\partial_t x_k = -2x_k - \alpha x_k + \beta y_k + \frac{1}{N}\sum_j (\alpha x_j - \beta y_j)$$
$$\partial_t y_k = -2c_2 x_k - \beta x_k - \alpha y_k + \frac{1}{N}\sum_j (\beta x_j + \alpha y_j)$$

holds. This linear system has the Jacobian of the form

$$J = \begin{pmatrix} E+K & K & \dots & K \\ K & E+K & K & \dots \\ \dots & \dots & \dots & K \\ K & \dots & K & E+K \end{pmatrix}$$

with

$$E = \begin{pmatrix} -2-\alpha & \beta \\ -\beta-2c_2 & -\alpha \end{pmatrix}$$

and

$$K = \begin{pmatrix} \frac{\alpha}{N} & -\frac{\beta}{N} \\ \frac{\beta}{N} & \frac{\alpha}{N} \end{pmatrix}$$

This is a circulant matrix, and its eigenvalues are given by

$$\lambda_0 = \mathrm{Eig}\,[E + N * K]$$
$$\lambda_{1,\dots,N} = \mathrm{Eig}\,[E]$$

Note that

$$\mathrm{Eig}\,[E+N*K] = \mathrm{Eig}\begin{pmatrix} -2 & 0 \\ -2c_2 & 0 \end{pmatrix}$$
$$\rightarrow (-2-\lambda_0)(-\lambda_0) = 0$$
$$\rightarrow \lambda_0 = \{0, -2\}$$

whereas

$$\lambda_{1,\dots,N} = \mathrm{Eig}\,[E]$$

$$= \mathrm{Eig}\begin{pmatrix} -2-\alpha & \beta \\ -\beta-2c_2 & -\alpha \end{pmatrix}$$
$$= -1-\alpha \pm \sqrt{1-\beta^2-2\beta c_2}$$

This ansatz is analogous the envelope equation employed by Benjamin and Fair [49]. Notice that $\lambda_0 = \{0, -2\}$ and $\lambda_{1,\ldots,N} = -1-\alpha \pm \sqrt{1-\beta^2-2\beta c_2}$ coincide with the eigenvalues obtained from the transformed system, see Sec. 2.1.10, except $\lambda_0 = 0$, the neutral direction, which we excluded by introducing the phase difference $\Delta\phi$.

2.2 The Dynamics of Four Coupled Oscillators

In the previous section, we investigated the dynamics of just two coupled Stuart-Landau oscillators. There, we also discussed that the bifurcation boundaries obtained for the synchronized and anti-phase solutions are independent of the number of oscillators in the ensemble. But this does not hold for the respective stability boundaries of the two symmetry broken solutions, $\boldsymbol{u}_1 = (\gamma_1, \rho_1, \Delta\phi_1)$ and $\boldsymbol{u}_2 = (\gamma_2, \rho_2, \Delta\phi_2)$. This becomes obvious when considering the different ways in which two-cluster solutions can become unstable for larger ensembles of oscillators: either on or transverse to the cluster manifold. That is, either the two cluster clumps remain clumped but their relative locations change, or one of the two clusters splits up into an arbitrary number of subclusters. The stability properties of the former is fully captured by the reduced equations, but since the latter cannot happen in an ensemble of just two oscillators, we can draw no conclusions about stability transverse to the cluster manifold.

This motivates this section, where we investigate the dynamics of four coupled oscillators. We start our considerations with examinations of where in parameter space balanced two-cluster solutions are stable in this ensemble. Using symmetry arguments, we then show that these regions in parameter space remain unchanged for larger ensembles of oscillators.

We then investigate how balanced cluster states in the four oscillator ensemble, so-called 2-2 clusters, bifurcate. In doing so, we discuss where 3-1 cluster states exist and where they are stable.

Furthermore, we find that one way in which stable 2-2 cluster states can get destroyed is through a supercritical Hopf bifurcation. Using *AUTO*, we show how the limit cycles born in this Hopf bifurcation further bifurcate, and discuss the transitions into chaotic motion via the Feigenbaum scenario [50–52] or the Ruelle-Takens-Newhouse route [52, 53]. In this parameter regime, however, two oscillators are still synchronized, and thus the chaotic attractor can be identified as a chimera attractor, similar to the ones observed in Refs. [29, 30], also called type-I chimeras [54].

The chaotic behavior of such chimera states can indeed be verified using Lyapunov

exponents. In particular, we additionally investigate Lyapunov exponents transverse to the manifold on which the chimeras live, that is, directions orthogonal to the manifold of the two synchronized oscillators. Doing so, we show where chimera states are stable in parameter space, and discuss how they further bifurcate.
Focusing on the detailed transition to chaotic motion in the Feigenbaum scenario mentioned above, we find that there exist qualitatively different chaotic attractors, some are symmetric under the exchange of the incoherent oscillators, and some are not. Using symmetry detectives, we analyze these chimera attractors in more detail, and classify them as *symmetric* and *asymmetric* chimera states, which we published in Ref. [17].

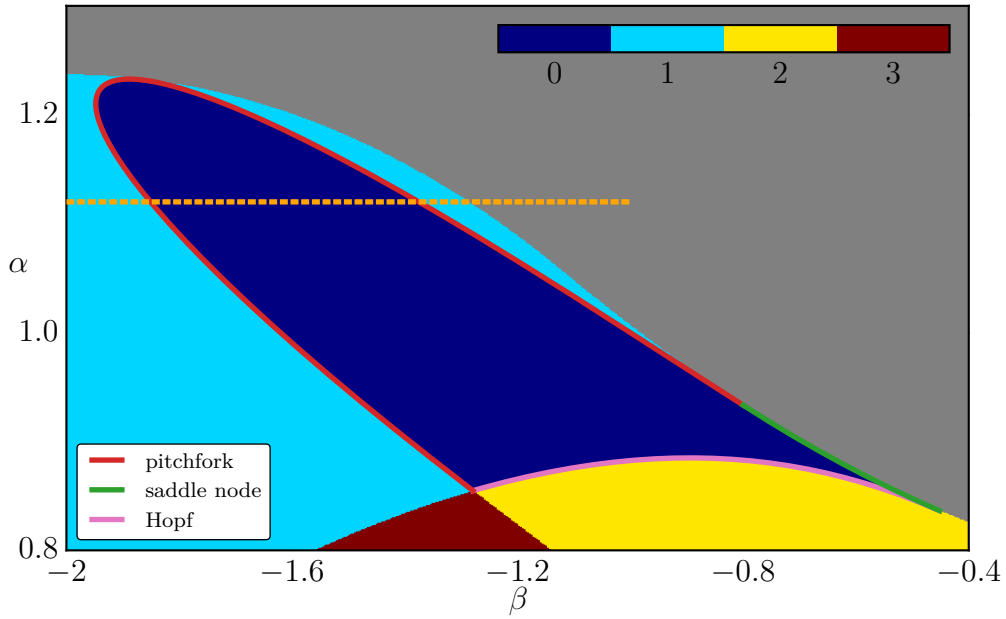

Figure 2.14: Stability of the balanced 2-2 cluster solution in an ensemble of four mean-coupled Stuart-Landau oscillators for $c_2 = 2$. The parameter range corresponds to the orange window indicated in Fig. 2.12 and shown in Fig. 2.13 for two oscillators. As in Fig. 2.12, the color encodes the number unstable eigendirections, and gray indicates that the balanced cluster solution does not exist for this set of parameters. The bifurcation curves were obtained using *AUTO* and symbolize a supercritical Hopf bifurcation curve (magenta), a pitchfork bifurcation curve (red) and a saddle node bifurcation curve (green).

2.2.1 Clustering in an Ensemble of Four Oscillators

As already outlined in the previous paragraph, the stability properties of the asymmetric solutions in the two oscillator ensemble (c.f. Figs. 2.12 and 2.13), offer only limited information about their stability in larger ensembles of mean-coupled Stuart-Landau oscillators. This is due to the fact that the individual clusters cannot break up in such a minimal ensemble.
In order to rephrase this more accurately, we follow Ref. [37] and describe the stability of 2-cluster states by two kinds of Lyapunov exponents, the *cluster integrity exponents* λ^{σ}_{CI}, and the *cluster system orbit stability exponents* λ_{SO}. The latter describe the stability along the 2-cluster manifold and are composed of 3 real numbers. The former, the cluster integrity exponents λ^{σ}_{CI}, describe the internal stability of each cluster σ. Due to the symmetries of the oscillator ensemble, the λ^{σ}_{CI} are degenerate in the sense that they consist of $2N_{\sigma}-2$ equal real values, with N_{σ} being the number of oscillators in cluster σ.
Extending our considerations by regarding four oscillators instead of two, and by

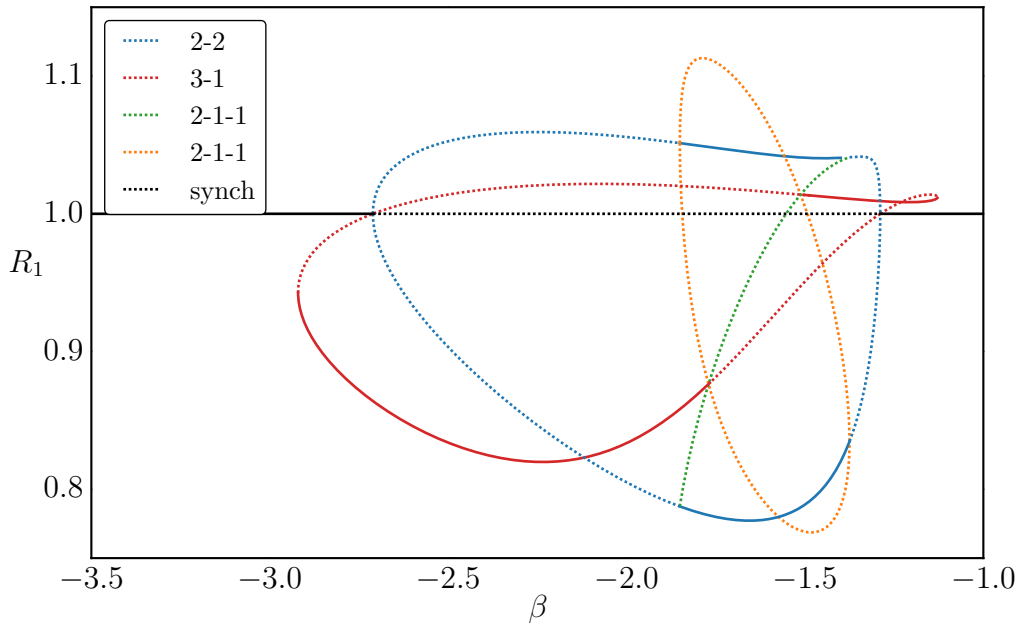

Figure 2.15: Continuation of the cluster solutions in ensemble of four coupled Stuart-Landau oscillators for $\alpha = 1.12$ and $c_2 = 2$, as indicated through the dashed orange line in Figs. 2.14 and 2.16, using *AUTO*. Dotted curves indicate saddles, whereas solid lines represent attracting solutions.

introducing polar coordinates, we obtain the dynamics of the four amplitudes R_k, $k = 1, \ldots, 4$, and three phase differences $\Delta\phi_{k1} = \phi_k - \phi_1$, $k = 1, \ldots, 3$ (see Appendix B for the equations). One thus has dynamics in a seven-dimensional phase

space $\mathbb{R}^4_+ \times \mathbf{T}^3$. Note that the asymmetric solutions $\boldsymbol{u}_{1,2}$ now correspond to cluster solutions with two oscillators in each cluster.

Through the new dimensions in phase space, however, the stability of those 2-2

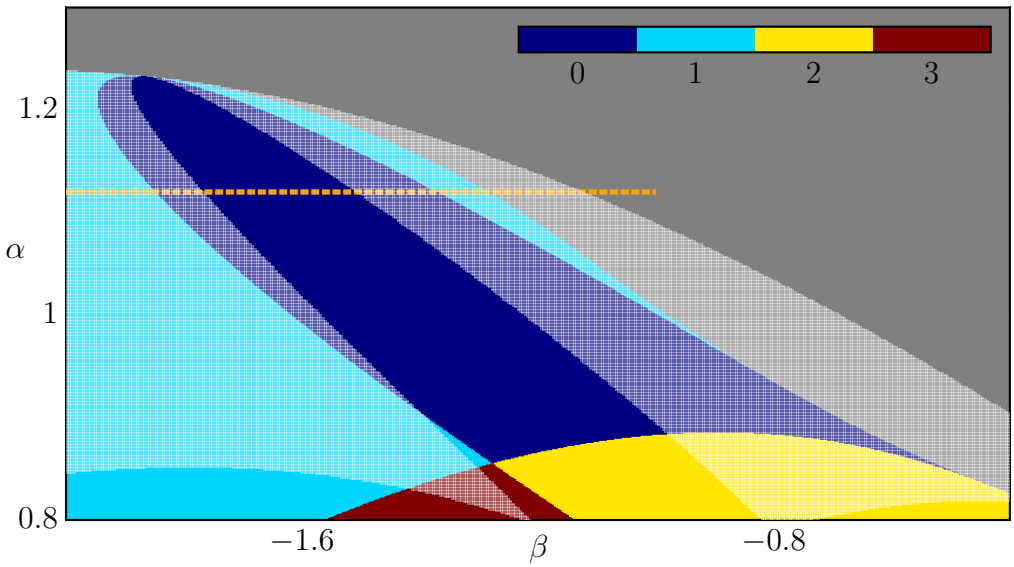

Figure 2.16: Stability of the balanced 2-2 cluster solution in an ensemble of four mean-coupled Stuart-Landau oscillators for $c_2 = 2$, as in Fig. 2.14. In addition, the regions in which the 3-1 cluster solution is stable are shown as transparent-white patches.

cluster solutions might differ from the stability of the $\boldsymbol{u}_{1,2}$ solutions in the two-oscillator ensemble. This can be visualized by evaluating the Jacobian of the four oscillator system at the 2-2 cluster solutions and investigating the number of positive eigenvalues. For the parameter window shown in Fig. 2.13 (corresponding to the orange window in Fig. 2.12 for $c_2 = 2$), the stability of the 2-2 cluster solution in the four oscillator system is shown in Fig. 2.14.

There, one can observe that the parameter range for which the balanced cluster solution is stable is smaller than the one for the two oscillator system. In addition, the balanced 2-2 cluster state gets destroyed either through a pitchfork (red curve in Fig. 2.14), a saddle node (green curve in Fig. 2.14) or a Hopf bifurcation (pink curve in Fig. 2.14). Furthermore, the stable 2-2 cluster solution no longer bifurcates off the synchronized solution except at one point ($\alpha \approx 0.62$ and $\beta \approx -1.85$). This point, which we dub a cluster singularity, is discussed in more detail in Sec. 2.3.1. To the right of this point, that is for large values of β, the pitchfork breaks up the cluster with the smaller amplitude, and to the left of this point, that is for smaller β values, the pitchfork breaks up the cluster with the larger amplitude.

The bifurcation scenario along a one-dimensional cut in parameter space, as indicated through the dashed orange line in Fig. 2.14, is shown in Fig. 2.15. There, the balanced 2-2 cluster solution and the resulting branches are continuated using *AUTO*, and the resulting amplitude of one of the oscillators is plotted as a function of β. The balanced 2-2 cluster solution is shown as a blue curve, with the stable regions solid and the unstable regions dashed. Note that the two stable regions belong to the same group orbit. Emanating from these stable patches, unstable 2-1-1 solutions can be observed (green and orange curves in Fig. 2.15), indicating that the balanced cluster solutions become unstable through subcritical pitchforks. It is worth mentioning that the green curve are in fact two branches lying over each other. Furthermore, the 3-1 cluster solution is depicted as a red curve in Fig. 2.15. Two stable regions of this solutions exist, which, in contrast to the 2-2 cluster solution, do not belong to the same group orbit. For the stable 3-1 cluster state at small values of β, the cluster with three oscillator has the smaller amplitude, whereas for the stable cluster state at larger values of β, the cluster with three oscillators has an amplitude larger than one. Note that the 2-2 cluster solution bifurcates off the synchronized solution via an equivariant pitchfork bifurcation, whereas the 3-1 cluster bifurcates with the synchronized solution in a transcritical, as predicted in Ref. [55]. In addition, the stable patches of the 2-2 and 3-1 cluster states overlap in parameter space, and also the stable regions of the 3-1 cluster and the synchronized solution (black line in Fig. 2.15).
This bifurcation scenario thus confirms that the transition between balanced cluster states and the synchronized solution is hysteretic [37]. Starting from the balanced cluster and increasing β, the cluster with the smaller amplitude breaks up and the 2-2 cluster state becomes unstable. Lying in the basin of attraction of the 3-1 cluster state, one of the two former synchronized oscillators joins the cluster with the larger amplitude. This 3-1 cluster then finally becomes unstable through a saddle node and the system settles on the synchronized solution, being the only remaining stable solution for this set of parameters. When then decreasing β again, the system remains on the synchronized motion, until it becomes unstable and the dynamics settle on the 3-1 cluster state. Further decreasing β destroys the 3-1 cluster state and the system converges again to the balanced cluster state.
On the other hand, when decreasing β from the balanced cluster solution, the cluster state with the larger amplitude breaks up. After the bifurcation, the dynamics again converge to the 3-1 cluster state, where one of the two former synchronized oscillators joins the cluster with the smaller amplitude. For reasons of clarity and comprehensibility, the amplitude of only one of the oscillators is depicted in Fig. 2.15.
As for the 2-2 cluster state, the regions in which the 3-1 cluster state is stable can be obtained by evaluating the Jacobian and investigating its eigenvalues. The parameter regimes for which the 3-1 cluster is stable is shown as white-shaded patches in Fig. 2.16, together with the stability diagram of the 2-2 cluster states. Again, the

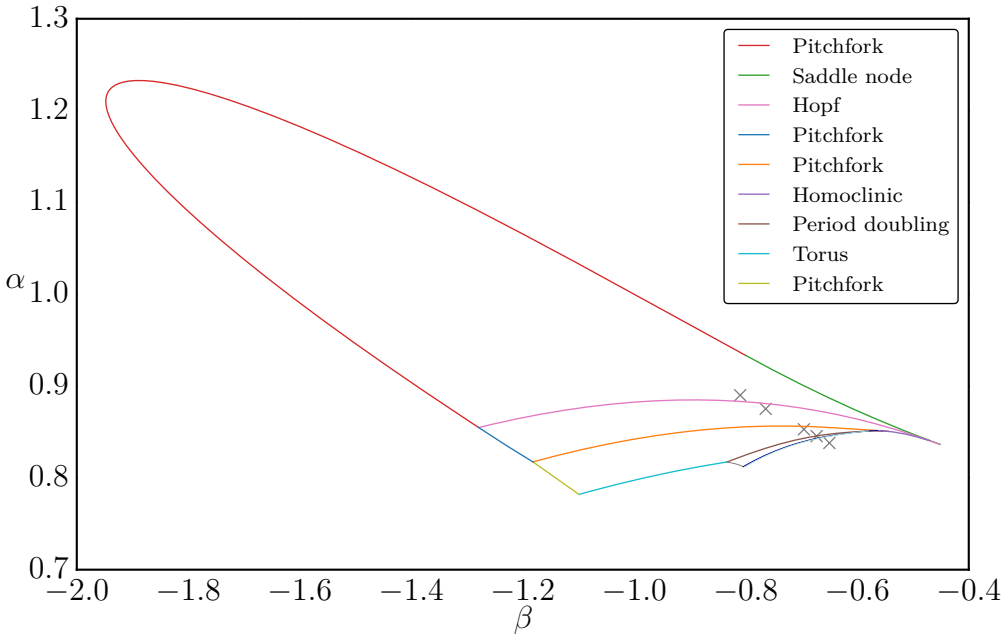

Figure 2.17: Bifurcations from the 2-2 clustered solution to a chimera state in an ensemble of four mean-coupled Stuart-Landau oscillators for $c_2 = 2$. Exemplary time series for the parameter sets indicated through the gray crosses are shown in Fig. 2.18.

orange line indicates part of where the parameter continuation of the cluster states, as shown in Fig. 2.15, is performed.

2.2.2 Symmetry-Broken Periodic Orbits and Chaos

The Hopf bifurcation at the 2-2 cluster solution (pink curve in Fig. 2.14) can be identified as supercritical in this parameter regime, and thus stable periodic orbits emanate from it. These orbits have the property that two and two oscillators are still synchronized, respectively, but with the amplitudes of and the phase difference between the two clusters oscillating. See Fig. 2.18(a) for exemplary time series of the 2-2 cluster fixed point and Fig. 2.18(b) for time series of the periodic orbits after the Hopf bifurcation.

Using *AUTO*, it is possible to continue these limit cycles in the $\alpha - \beta$ parameter plane. Doing so we find that those states get destroyed either through pitchfork bifurcations or homoclinic bifurcations, see Fig. 2.17. One of the pitchforks (dark blue curve in Fig. 2.17) breaks up the cluster with the larger mean-amplitude, whereas the other (orange curve in Fig. 2.17) breaks up the cluster with the smaller mean-amplitude, leading to periodic orbits with time series as shown in Fig. 2.18(c). Further continuing these 2-1-1 periodic orbits leads to another pitchfork (light green

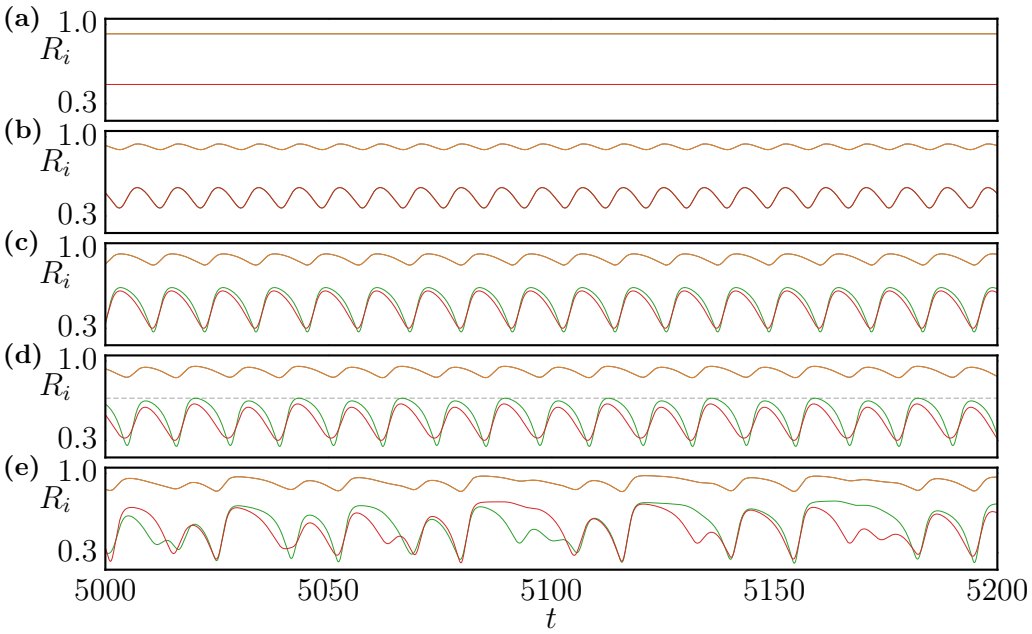

Figure 2.18: Amplitudes of the four oscillators from exemplary time series of (a) a two-cluster fixed point at $\alpha = 0.89$, $\beta = -0.81$, (b) a periodic 2-2 cluster state at $\alpha \approx 0.875$, $\beta \approx -0.764$, (c) a periodic 2-1-1 cluster state at $\alpha \approx 0.853$, $\beta \approx -0.696$, (d) a period-doubled 2-1-1 cluster state at $\alpha \approx 0.845$, $\beta \approx -0.673$, and (e) a chimera state with chaotic time series and two oscillators still synchronized. The individual parameter sets are indicated as gray crosses in Fig. 2.17. The dashed gray line in (d) shall provide better visibility of the period-two motion.

curve in Fig. 2.17), at which the remaining cluster breaks up, creating a periodic orbit where each of the oscillators follows its own orbit. In addition, the 2-1-1 orbits may also undergo a torus bifurcation (light blue curve in Fig. 2.17) or a period-doubling bifurcation (brown curve in Fig. 2.17). See Fig. 2.18(d) for exemplary time series of the period-doubled orbit. Using numerical simulations, we find that shortly after the torus bifurcation, the dynamics become chaotic, indicating a Ruelle-Takens-Newhouse route to chaos [52, 53]. Furthermore, we detect a cascade of period-doubling bifurcations (the second and third are indicated in Fig. 2.17), typical of a Feigenbaum route to chaos [50–52].

2.2.3 Bifurcations to Chimera States

Periodic solutions are best visualized using a Poincaré section, recording the dynamical states at discrete points in time [56]. In particular, we can analyze the period-doubling cascade to chaos in more detail by using so-called orbit diagrams. There, we plot the maximal values of the amplitudes of each oscillator as a func-

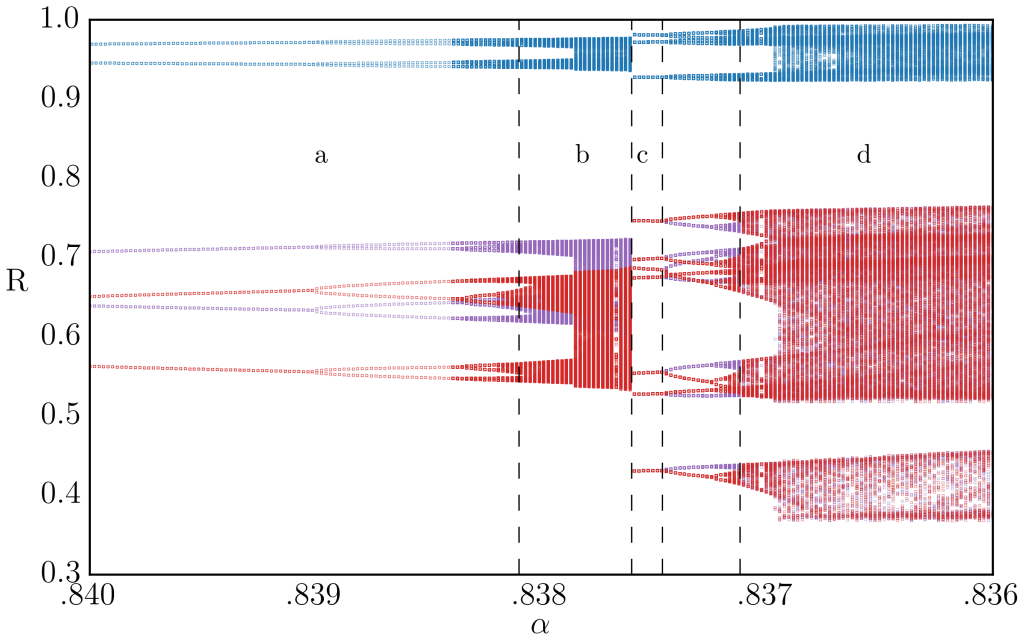

Figure 2.19: Poincaré map recording the maxima of the amplitudes of the individual oscillators for $0.84 \geq \alpha \geq 0.836$ and $\beta = -0.7$. Region (a) marks the parameter range in which periodic orbits are observed, starting with a period-doubled state, (b) indicates the existence of asymmetric chimera states, (c) denotes the region in which periodic orbits with discrete rotating wave symmetry exist, and for α values in region (d) symmetric chimera states are observed. The corresponding time series of the amplitudes are shown in Fig. 2.20. Note that the blue dots in fact correspond to the amplitudes of two oscillators.

tion of the bifurcation parameter. For the period-doubling cascade observed in this system, the orbit diagram for $\beta = -0.7$ is shown in Fig. 2.19. In particular, as can be seen in this figure, the period-2 orbit bifurcates into a period-4 orbit when α is reduced[4]. This subsequently bifurcates into a period-8 orbit and so forth. In other words, one observes a cascade of infinitely many period-doubling bifurcations [50], leading to a chaotic state (region b in Fig. 2.19). The time series of the amplitudes of such a chaotic attractor are depicted in Fig. 2.20(b). It is important to notice that the phase and the amplitude difference of two of the oscillators is zero, indicating that, although the total dynamics are chaotic, they are synchronized. Furthermore, this chimera state is not invariant under a permutation of the third and fourth oscillator. In other words, the two incoherent oscillators are not symmetric. Such an asymmetry can be verified using symmetry detectives, as explained in more detail in Sec. 2.2.6.

[4]Note that α in Fig. 2.19 decreases when going to the right.

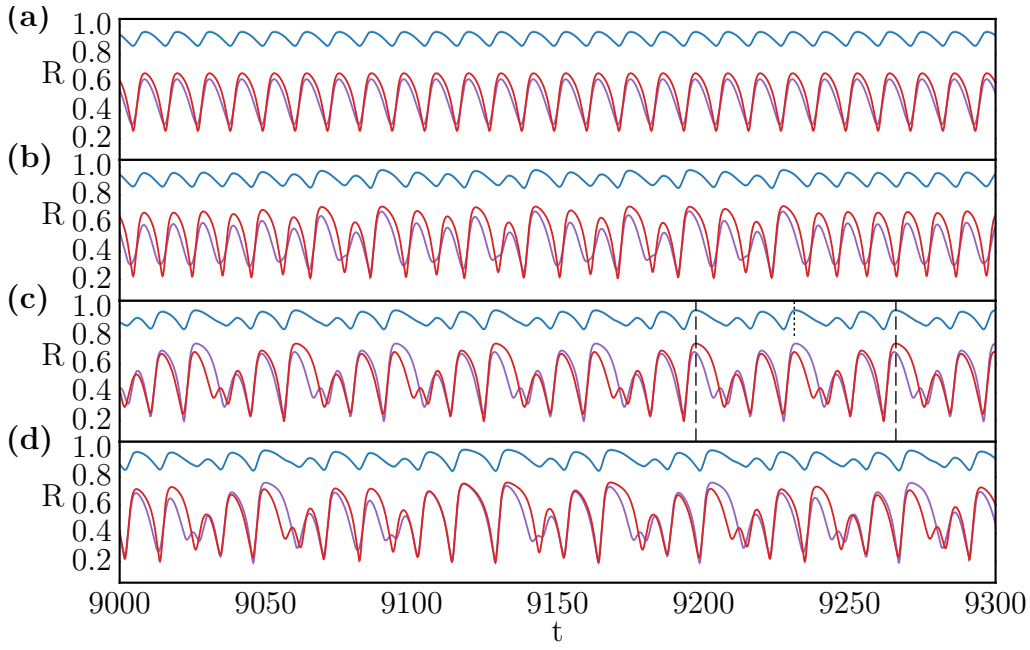

Figure 2.20: Time series of the amplitudes of the four oscillators of (a) a periodic orbit for $\alpha = 0.85$, (b) an asymmetric chimera state at $\alpha = 0.83764$, (c) a periodic orbit with phase shift symmetry at $\alpha = 0.8376$ and (d) a symmetric chimera state at $\alpha = 0.8365$. The other parameters are $\beta = -0.7$ and $c_2 = 2.0$. Note that two oscillators (here green and blue) are always synchronized for these parameter values and thus form only one curve. The vertical lines in (c) indicate the period of the desynchronized oscillators (dashed) and synchronized oscillators (dotted), respectively.

2.2.4 Lyapunov Exponents

As already mentioned when discussing the stability of two-cluster states, Sec. 2.2.1, the stability of a solution of a dynamical system can be described by so-called Lyapunov exponents [57]. Consider the trajectory $\boldsymbol{x}(t)$ of such a solution. Then its stability can be obtained by evaluating the temporal behavior of an infinitesimal perturbation $\delta\boldsymbol{x}$ added to this trajectory at a given time t_0. If the distance between the trajectory $(\boldsymbol{x} + \delta\boldsymbol{x})(t)$ and the original trajectory $\boldsymbol{x}(t)$ grows in time, then the manifold on which $\boldsymbol{x}(t)$ lives is either unstable or may be chaotic, and if the two trajectories converge, then the manifold is stable and non-chaotic. Linearizing around the solution $\boldsymbol{x}(t)$, such a distance can be expressed through

$$\|\delta\boldsymbol{x}(t)\| \approx e^{\lambda t}\|\delta\boldsymbol{x}(t_0)\|$$

and the maximal Lyapunov exponent λ can thus be defined as

$$\lambda = \lim_{t\to\infty} \frac{1}{t} \log \frac{\|\delta \boldsymbol{x}(t)\|}{\|\delta \boldsymbol{x}(t_0)\|}. \tag{2.21}$$

If λ is positive, then the initial disturbance grows in time, if λ is negative, then the manifold is attracting, and λ equal to zero indicates that the invariant manifold has a direction which is neither attracting nor repelling. Furthermore, a positive Lyapunov exponent serves as an indicator of a strange attractor, that is, chaotic dynamics.

Note that the actual number of Lyapunov exponents is equal to the number of dimensions of the system. The largest exponent, as defined in Eq. (2.21), describes just the divergence of the fastest growing direction, or the slowest decaying direction if it is negative. One can, however, estimate the second largest exponent by investigating the subspace orthogonal to the direction of maximum divergence (for a positive exponent) or minimal contraction (if the largest exponent is negative). The growth/decay rate in this subspace then yields the second exponent. Repeating this process, all exponents can be obtained iteratively [58].

In more detail, one uses an orthogonal basis $\delta\mathbf{X}(t_0)$ centered on the unperturbed trajectory $\boldsymbol{x}_0$, and subsequently evolves this vector frame using, for example, the Jacobian $\mathbf{J}$ centered at this trajectory,

$$\begin{aligned}
\delta\mathbf{X}(t_1) &= \mathbf{J}_{\boldsymbol{x}_0}\delta\mathbf{X}(t_0),\\
\delta\mathbf{X}(t_k) &= \mathbf{J}_{\boldsymbol{x}_k}\mathbf{J}_{\boldsymbol{x}_{k-1}}\cdots\mathbf{J}_{\boldsymbol{x}_0}\delta\mathbf{X}(t_0).
\end{aligned}$$

The initial "sphere" of perturbations then gets deformed, with the most prominent axis pointing into the direction of the largest Lyapunov exponent. One thus looks at the dilation/contraction of the principal axis of this deformed sphere. This can be obtained using QR decomposition [59] or Gram-Schmidt orthogonalization [60–62]. Let $\boldsymbol{v}_1$ be the principal axis corresponding to the largest exponent. Then the principal direction corresponding to the second largest exponent, $\boldsymbol{v}_2$, can be obtained via

$$\begin{aligned}
\boldsymbol{v}_2 &= \boldsymbol{v}_2 - \langle \boldsymbol{v}_2, \boldsymbol{v}_1{}' \rangle \boldsymbol{v}_1{}'\\
&\vdots\\
\boldsymbol{v}_k &= \boldsymbol{v}_k - \langle \boldsymbol{v}_k, \boldsymbol{v}_{k-1}{}' \rangle \boldsymbol{v}_{k-1}{}' - \cdots - \langle \boldsymbol{v}_k, \boldsymbol{v}_1{}' \rangle \boldsymbol{v}_1{}',
\end{aligned}$$

with $\boldsymbol{v}_i{}' = \boldsymbol{v}_i/\|\boldsymbol{v}_i\|$ and $\langle\cdot,\cdot\rangle$ indicating the inner product. Although it is sufficient to reorthogonalize the initial vector frame once every orbital period, one has to visit every region of the attractor to fulfill the requirement of ergodicity [58]. The Lyapunov spectrum λ_k can then be obtained by

$$\lambda_k = \frac{1}{T}\sum_{i=1}^{n} \log\|\boldsymbol{v}_k\|,$$

with T being the period over which the attractor is sampled and n being the number of reorthogonalizations performed.
It is worth mentioning that there are ways to estimate the largest Lyapunov exponent and also the full spectrum from time series only, that is, without knowing the underlying dynamical equations. See, for example, Ref. [63] for the approximation of the largest exponent, and Ref. [64] for the estimation of the Lyapunov spectrum. Here, we stick with the approach discussed above.

2.2.5 Feigenbaum Route to Chimera States

In order to verify that the chimera states discussed in Sec. 2.2.7 are indeed chaotic, we estimate the largest exponent along the period doubling cascade. The orbit diagram along the period doubling route for the two synchronized oscillators, and the corresponding maximal Lyapunov exponent are shown in Fig. 2.21. Note that there is a range of α values for which the maximal Lyapunov exponent is zero, indicating non-chaotic dynamics. Since in this region one observes period-n orbits, one of the Lyapunov exponents has to be zero. For the regions were no periodic orbits are observed, the largest Lyapunov exponent becomes positive. Recall that a positive maximal Lyapunov exponent of an attracting manifold indicates chaotic dynamics. Comparing Fig. 2.21 and Fig. 2.19, one can see from the Lyapunov exponents that the symmetric and also the asymmetric chimera states are indeed chaotic

2.2.6 Symmetry Detectives

In this section, different states along the period-doubling cascade, Fig. 2.19, are distinguished using the set-wise symmetries of the attracting manifold, which can be determined with symmetry detectives [17, 65, 66]. We apply this method to such states observed in the ensemble of four mean-coupled Stuart-Landau oscillators, and relate those states to different chimera states reported in recent literature. At the end of this section, we also show and discuss how our results extend to larger networks and spatially extended systems.
Given a dynamical system

$$\dot{\boldsymbol{x}} = \boldsymbol{f}(\boldsymbol{x}), \tag{2.22}$$

then this system is invariant under the operation γ if

$$\boldsymbol{f}(\gamma\boldsymbol{x}) = \gamma\boldsymbol{f}(\boldsymbol{x}). \tag{2.23}$$

The group $\{\gamma\}$ fulfilling Eq. (2.23) is called the symmetry group Γ and system (2.22) is said be be Γ-equivariant [33]. However, as mentioned above, solutions of Eq. (2.22) are not necessarily invariant under the same symmetry group Γ, i.e. the symmetry

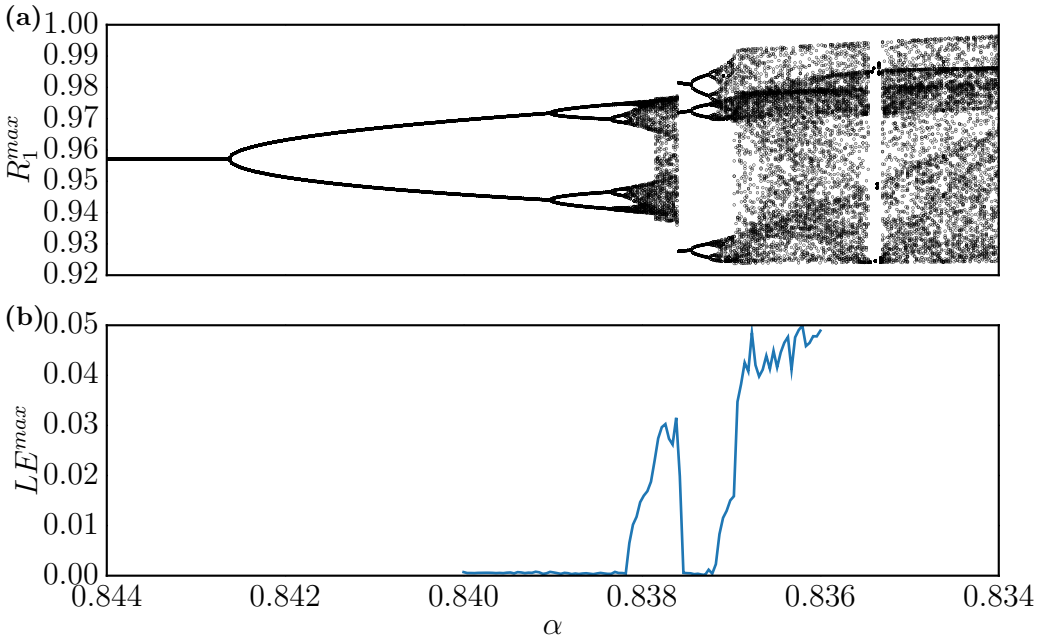

Figure 2.21: (a) Orbit diagram of the amplitude of synchronized cluster and (b) largest Lyapunov exponents along the period doubling route to chaos as a function of α. See also Fig. 2.19 for the full orbit diagram. Other parameter values are $c_2 = 2$ and $\beta = -0.7$. Note that due to the numerical effort, the Lyapunov exponent were calculated for a smaller α window only.

of solutions can be broken. Let $\boldsymbol{x}$ be a solution of system (2.22), then the group of transformations that leave $\boldsymbol{x}$ invariant,

$$\Sigma_{\boldsymbol{x}} = \{\gamma \in \Gamma : \gamma\boldsymbol{x} = \boldsymbol{x}\},$$

is called the isotropy subgroup of $\boldsymbol{x}$. Note that $\Sigma_{\boldsymbol{x}} \subseteq \Gamma$. Even turbulent or spatio-temporally chaotic states may exhibit some symmetries in their time-averaged dynamics [67–69]. Examples range from so-called soft turbulence in the Taylor-Couette experiment [70–74] to Faraday wave instabilities [68] and Rayleigh-Bernard convection [69]. Such symmetries are related to the set-wise symmetry of the attractor, that is, the group of symmetry operations that leave the whole attractor invariant. If the dimension of the phase space is three or less, such symmetries can be observed visually, see for example Ref. [75]. For higher-dimensional systems, Barany et al. proposed so-called symmetry detectives [65]. The idea is to transform the task of finding the symmetry group of a set A in space V to finding the symmetries of a single point K_A in some auxiliary space $\tilde{V}$ [33, 65]. This can be achieved by projecting

the set A through a Γ-equivariant map $\phi : V \to \tilde{V}$. Then, K_A can be expressed as

$$K_A = \lim_{T\to\infty} \frac{1}{T} \int_0^T \phi\left(x\left(t\right)\right) dt$$

for continuous dynamical systems [66]. $\phi : V \to \tilde{V}$ is called a detective with

$$\Sigma_{\phi(A)} = \Sigma_A,$$

if ϕ is Γ-equivariant and $\tilde{V}$ large enough, as explained in Ref. [33]. Once we mapped a trajectory of the dynamical system into the vector space $\tilde{V}$ using a detective function ϕ as described above, we can estimate the symmetry Σ_A of an attracting set by examining the isotropy subgroup $\Sigma(\omega)$ of $\omega = K_A \in \tilde{V}$ [76]. This can be achieved by taking $\omega_\gamma = K_{\gamma A}$ and computing the distances

$$t_\gamma = \|\omega_\gamma - \omega\|$$

for each symmetry operation $\gamma \in \Gamma$. The isotropy group $\Sigma(\omega)$ is thus the set of all γ for which $t_\gamma \approx 0$. This is in contrast to the instantaneous symmetry of a solution, which is the intersection of the isotropy groups $\Sigma(x)$ at every position of the attractor,

$$\Sigma_{\text{instant}} = \bigcap_{x\in A} \Sigma(x).$$

Using these two estimates, one can calculate the instantaneous and set-wise symmetries of an attracting manifold.
As an example taken from Ref. [67], consider the odd logistic map

$$x_{n+1} = \lambda x_n - x_n^3, \tag{2.24}$$

which is invariant under the identity transformation $e : x \to x$ and the reflection κ,

$$x \to -x \Rightarrow f(-x) = -rx + x^3 = -f(x),$$

that is, Eq. (2.24) is Γ-equivariant with $\Gamma = \{e, \kappa\}$. For $\lambda < 1$, the fixed point $x = 0$ is stable (c.f. Fig. 2.22). At $\lambda = 1$, this fixed point looses stability and a conjugate pair of fixed point emerges. Each of these fixed points subsequently undergoes a period doubling cascade to chaos. Finally, the individual chaotic attractors (only one of the two is shown in Fig. 2.22) merge in a symmetry increasing bifurcation at $\lambda = 3\sqrt{3}/2 \approx 2.6$, creating a strange attracting set invariant under reflections at $x = 0$.

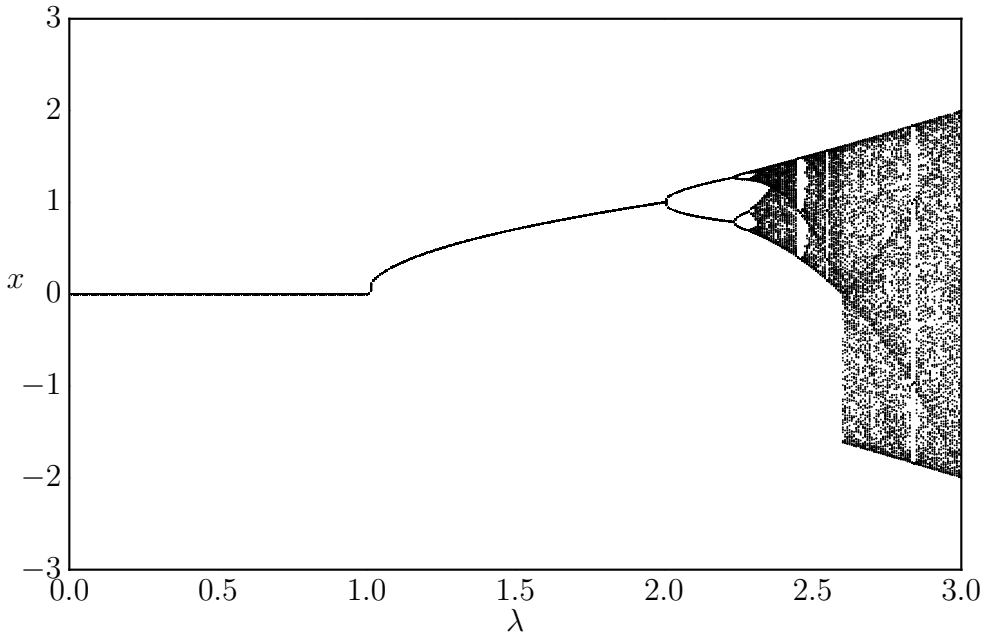

Figure 2.22: The variable x of the odd logistic equation plotted over 150 iterations for each value of the parameter λ.

2.2.7 Symmetric and Asymmetric Chimera States

Turning back for coupled Stuart-Landau oscillators, notice that the full model, Eq. (2.2), for $N = 4$, is invariant under a permutation of the indices, $\mathbf{S}_4$, and a phase shift $W \to W\exp(i\theta)$. As already discussed, the latter can be eliminated using the transformed variables $R_k = |W_k|$, $k = 1, \ldots, 4$, and $\Delta\theta_{k+1,k} = \theta_{k+1} - \theta_k = \angle W_{k+1} - \angle W_k$, $k = 1, \ldots, 3$, describing the dynamics in a seven-dimensional phase space ($\mathbb{R}_+^4 \times \mathbf{T}^3$, with $\mathbf{T} = \mathbb{R}/2\pi\mathbb{Z}$). Thus, a limit cycle in the original variables, Eq. (2.2), corresponds to a fixed point in the new amplitude and phase-difference variables.

As shown in Ref. [77] for systems with the symbol permutation symmetry $\mathbf{S}_N$, one can use the ring group $\mathbf{R}_\Gamma$ as auxiliary space $\tilde{V}$ with the polynomial detective

$$\phi_k(\boldsymbol{x}) = p\left(\gamma_k^{-1}\boldsymbol{x}\right) \ , \ p = x_1 x_2^2 \ldots x_{N-1}^{N-1},$$

with $k = 1, \ldots, |\mathbf{S}_N|$ and γ_k^{-1} being the inverse of $\gamma_k \in \mathbf{S}_N$. That is, for four globally coupled oscillators with $\mathbf{S}_4$ symmetry of order $|\mathbf{S}_4| = 24$, a possible choice for a symmetry detective is

$$\phi_k(\boldsymbol{x}) = p\left(\gamma_k^{-1}\boldsymbol{x}\right) \ , \ p = x_1 x_2^2 x_3^3 \ \to \ \boldsymbol{\phi}(\boldsymbol{x}) = \begin{pmatrix} x_1 x_2^2 x_3^3 \\ x_2 x_1^2 x_3^3 \\ \vdots \\ x_4 x_3^2 x_2^3 \end{pmatrix},$$

which we adopt in this section, although other choices of ϕ are also possible [76]. Here, we take the real parts of our complex time series W_k as input x_k.

Turning back to the chaotic states observed in Fig. 2.19, region b, with time series

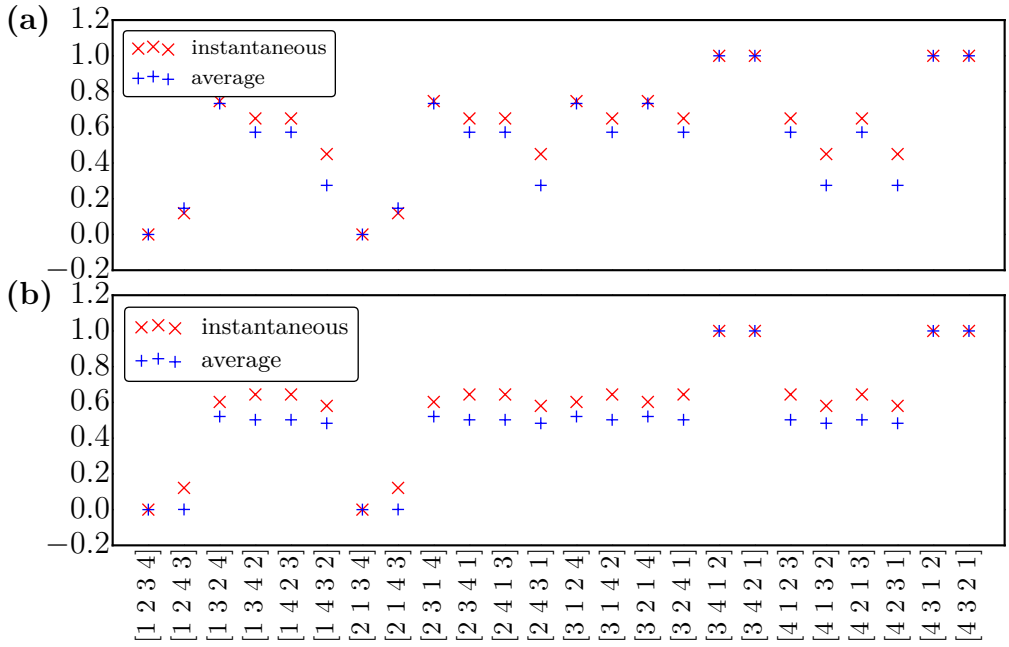

Figure 2.23: The distances t_γ for the symmetry operations $\gamma \in \mathbf{S}_4$. $t_\gamma \approx 0$ indicates the instantaneous and average symmetries of (a) the asymmetric chimera states at $\alpha = 0.83764$ and (b) the symmetric chimera state at $\alpha = 0.8365$, suggesting that the asymmetric chimera is invariant under the actions of $\mathbf{S}_2^i$, and the symmetric chimera under the actions of $\mathbf{S}_2^i \times \mathbf{S}_2^a$.

of the amplitudes depicted in Fig. 2.20 (b), where we argued that the corresponding chaotic attractor is not invariant under a permutation of the two incoherent, third and fourth, oscillators. This can be verified using symmetry detectives, as shown in Fig. 2.23 (a). There, one can see that the distances t_γ are non-zero when γ involves a permutation of the two incoherent oscillators. In other words, the underlying chaotic attractor has an $\mathbf{S}_2^i$ symmetry in the two synchronized oscillators only, with the superscript i indicating that the symmetry is instantaneous.

Further reducing α destroys the chimera state, yielding again a periodic state (region c in Fig. 2.19), with the time series shown in Fig. 2.20 (c). From the amplitude time series one can observe that the two desynchronized oscillators perform the same oscillations but with a constant phase shift. Such symmetry is called a phase-shift symmetry or discrete rotating wave [33, 78], reminiscent of the rotating waves observed in Ref. [30]. Denoting the phase-shift symmetry of the two nonsynchronized oscillators with $\mathbf{\Xi}_2$, this state has an isotropy subgroup $\mathbf{S}_2^i \times \mathbf{\Xi}_2$. Furthermore, it is worth mentioning that, due to the rotating-wave symmetry, the frequency of the

State	α-range	Symmetry	Index
2-2 FP	> 0.8760	$\mathbf{S}_2^i \times \mathbf{S}_2^i$	
2-2 PO	0.8760 to 0.8562	$\mathbf{S}_2^i \times \mathbf{S}_2^i$	
2-1-1 PO	0.8562 to 0.8381	$\mathbf{S}_2^i$	a
2-1-1 Chaos	0.8381 to 0.8376	$\mathbf{S}_2^i$	b
2-1-1 P6O	0.8376 to 0.8374	$\mathbf{S}_2^i \times \mathbf{\Xi}_2$	c
2-1-1 Chaos	< 0.8372	$\mathbf{S}_2^i \times \mathbf{S}_2^a$	d

Table 2.1: Different states observed in the system of four mean-coupled Stuart-Landau oscillators for $\beta = -0.7$ and $c_2 = 2$. FP denotes fixed point solution in the amplitude and phase difference variables, PO periodic orbits, Chaos indicates chaotic dynamics (chimeras) and P6O a period-6 orbit. The numbers indicate the number of synchronized oscillators, and the indices a-d correspond to the regions in Fig. 2.19 and the time series in Fig. 2.20.

oscillation in the amplitudes of the synchronized oscillators is twice the frequency of the desynchronized oscillators. This is reminiscent of the weak chimera states reported in Ref. [79], which are periodic but have different mean frequencies in the individual oscillators.

Further decreasing α first leads to a pitchfork bifurcation in which orbits with reduced symmetries are born, similar to the symmetry-decreasing bifurcations reported in Ref. [80]. After another cascade of period-doubling bifurcations, one again obtains chaotic dynamics, see the time series in Fig. 2.20 (d). Surprisingly, and opposed to the chimera state described above, this attractor is symmetric under a permutation of the two desynchronized oscillators. That the attracting manifold is indeed invariant under such a symmetry operation can be verified using the symmetry detectives mentioned above, with the distances t_γ shown in Fig. 2.23 (b). Note that a distance close to zero indicates an invariance under the respective group action, whereas $t_\gamma \neq 0$ indicates the absence of such a symmetry. Thus the symmetric chimera state has an $\mathbf{S}_2^i \times \mathbf{S}_2^a$ symmetry, different from asymmetric chimera states with sole $\mathbf{S}_2^i$ symmetry. For a summary of the states discussed so far, see table 2.1.

Calculating the symmetry detectives of the four coupled opto-electronic oscillators reported in Ref. [81], we find that also those states have an $\mathbf{S}_2^i \times \mathbf{S}_2^a$ symmetry, and can thus be identified as symmetric chimera states. In order to see if the states discussed above persist for larger ensembles of oscillators and under the influence of diffusion, we take the globally coupled version of the complex Ginzburg-Landau equation, Eq. (2.1), with one spatial dimension x and linear global coupling, indicated through the spatial integral [25, 31]. Numerically solving this system on a domain of length $L = 400$ and periodic boundary conditions, one obtains chaotic states resembling the asymmetric chimera (see Fig. 2.24 (a)), and the symmetric chimera (see Fig. 2.24(b)) for different parameter values.

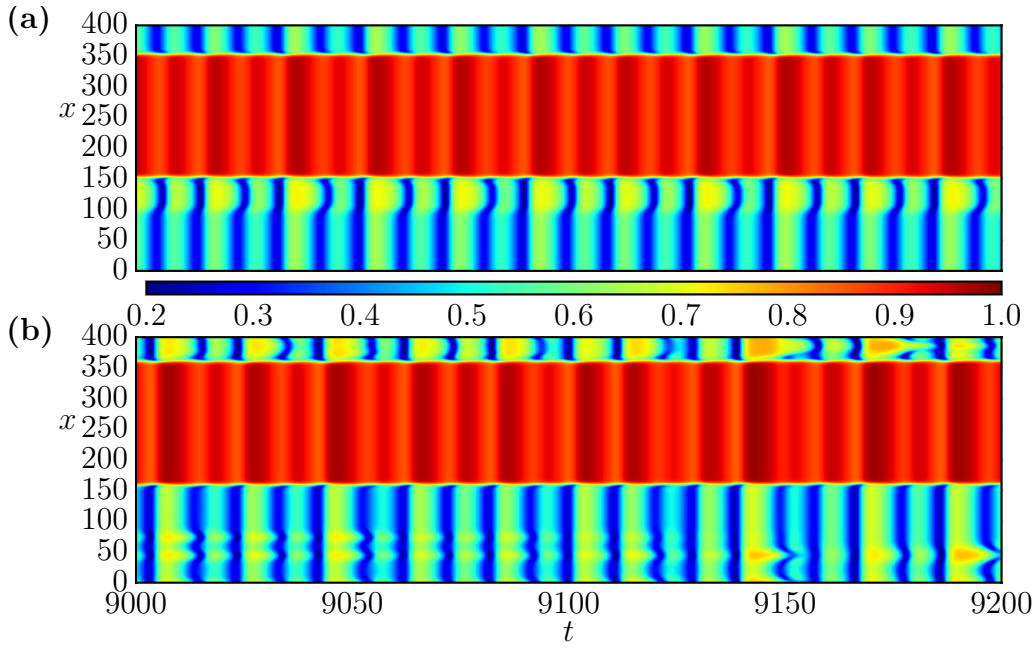

Figure 2.24: Space-time plot of the (a) asymmetric chimera in the spatially extended system with $L = 400$, $\alpha = 0.8304$, $\beta = -0.7$ and $c_2 = 2$. The asymmetry arises through the two clusters with small but different amplitudes (blue-ish and yellow-ish color in plot (a)). (b) Symmetric chimera in the spatially extended system with $L = 400$, $\alpha = 0.828$, $\beta = -0.7$ and $c_2 = 2$. The color encodes the absolute value of W.

Interestingly, in the spatially extended system the asymmetric chimera state of the four-oscillator network conserves its low-dimensional dynamics, manifesting itself in a three-cluster state with temporally chaotic behavior. A comparison of time-series recorded at a position within each of the three clusters and those shown in Fig. 2.20(b) is given in Fig. 2.25 and substantiates the correspondence of these states. In contrast, the symmetric chimera state transforms into a spatio-temporal chimera state with a synchronized, temporally chaotic cluster and a spatially incoherent, temporally chaotic region, as can be seen in Fig. 2.24(b). Corresponding time series of this apparently *extensive chimera state* are again displayed together with its low-dimensional counterparts in Fig. 2.26. Note that the α values at which those states arise are slightly shifted compared to the corresponding states observed in the four-oscillator system. This is an effect of the diffusion and the different sizes of the clusters.
That means we find different kinds of symmetry-broken states in a system of four globally coupled oscillators. In particular, there are chaotic states with $\mathbf{S}_2^i$ symmetry, which we dub asymmetric chimera states, states with $\mathbf{S}_2^i \times \mathbf{S}_2^a$ symmetry, which we call symmetric chimera states, and deterministic periodic orbits with $\mathbf{S}_2^i \times \mathbf{\Xi}_2$ sym-

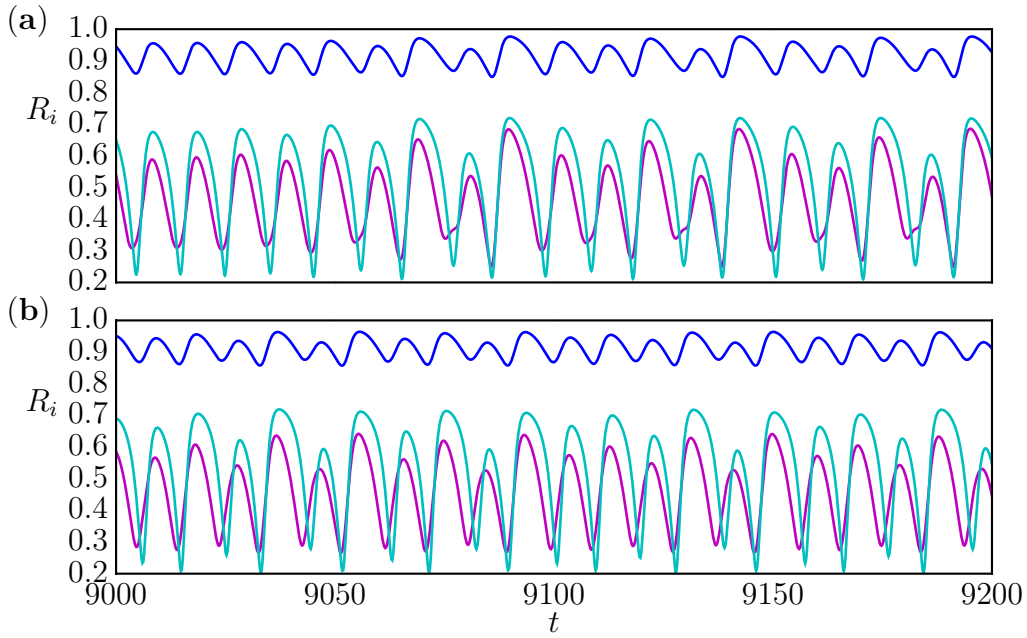

Figure 2.25: (a) Time series of the absolute value of W of the asymmetric chimera state in the four oscillator network, as shown in Fig. 2.20(b). (b) Exemplary time series of the absolute value of W of the asymmetric chimera state in the spatially extended system, at $x = 0$ (magenta), $x = 200$ (blue) and $x = 125$ (cyan), obtained from the data as shown in Fig. 2.24.

metry. The latter resemble weak chimeras as defined for phase oscillators, whereas the symmetric chimera states seems to exist also in other systems, such as the one reported in Ref. [81]. The discrimination based on the symmetries of the incoherent oscillators may facilitate our understanding of intricate dynamics such as chimera states, and may help to further classify them. In addition, such minimal chimera states in small networks may further reveal insights into dynamics of larger, and even spatially extended, systems of oscillators, which, as we have seen, maintain certain properties of their minimal relatives. Note that these chimeras are minimal in the sense that they consist of two coherent and two incoherent oscillators, fulfilling the condition of coexistence of coherence and incoherence, as required for chimera states [82]. There are, however, authors that claim chimeras can exist in ensembles of just three oscillators, see, for example, Ref. [83].

2.2.8 Stability of Chimera States

So far, we have investigated how chimera states are born when changing parameters, i.e. the coupling strength, in the system of four mean-coupled Stuart-Landau oscillators. In addition, we observed that the chimera states, the symmetric and

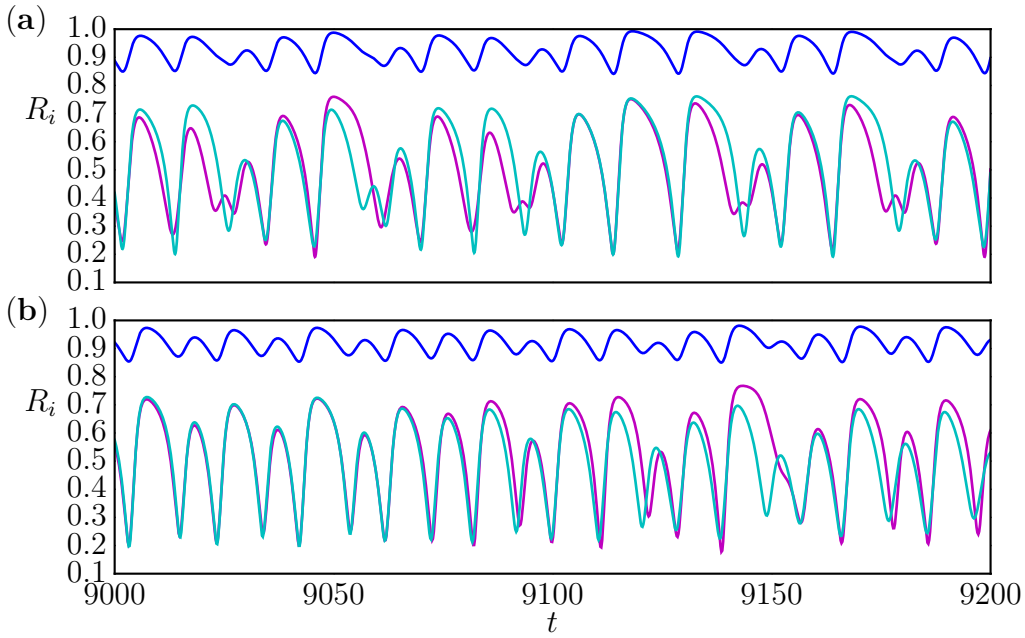

Figure 2.26: (a) Time series of the absolute value of W of the symmetric chimera state in the four oscillator network, as shown in Fig. 2.20(d). (b) Exemplary time series of the absolute value of W of the symmetric chimera state in the spatially extended system, at $x = 0$ (magenta), $x = 200$ (blue) and $x = 75$ (cyan), obtained from the data as shown in Fig. 2.24.

asymmetric ones, are indeed chaotic. The asymmetric chimera, however, seems to exist only in a small band in parameter space, c.f. Fig. 2.19. In contrast, the symmetric chimera seems to be stable in a larger parameter regime. The question then arises how such chimera states bifurcate in more detail.

Transversal Lyapunov Exponents

In order to estimate the stability of the chimera state, we follow Ref. [37] and calculate the variational equations of the mean coupled system, Eq. (2.2). In particular, we perturb $W_i(t_0) \to W_i(t_0) + \delta W_i$, and investigate the temporal evolution of the δW_i. If δW_i grows with time, the system is unstable, and if it decays, then the system state is stable. If δW_i is small, then we can, as in Ref. [37], rewrite Eq. (2.2) as

$$\begin{aligned}\partial_t W_i + \partial_t \delta W_i = (1-\kappa)\,(W_i + \delta W_i) \\ - (1 + ic_2)\,|W_i + \delta W_i|^2\,(W_i + \delta W_i) + \kappa\langle W_i + \delta W_i\rangle.\end{aligned}$$

Using

$$|W_i + \delta W_i|^2 = (W_i + \delta W_i)\,(W_i^* + \delta W_i^*)$$

$$
\begin{aligned}
&= |W_i|^2 + |\delta W_i|^2 + W_i \delta W_i^* + W_i^* \delta W_i \\
&\approx |W_i|^2 + W_i \delta W_i^* + W_i^* \delta W_i,
\end{aligned}
$$

we get

$$
\begin{aligned}
|W_i + \delta W_i|^2 (W_i + \delta W_i) &\approx \left(|W_i|^2 + W_i \delta W_i^* + W_i^* \delta W_i\right)(W_i + \delta W_i) \\
&\approx |W_i|^2 W_i + W_i^2 \delta W_i^* + 2 |W_i|^2 \delta W_i.
\end{aligned}
$$

We can separate the equation for the temporal evolution of our perturbation, yielding

$$
\begin{aligned}
\partial_t \delta W_i &= \left[1 - 2(1 + ic_2)|W_i(t_0)| - (\alpha + \beta)\right] \delta W_i \\
&= -(1 + ic_2) W_i(t_0)^2 \delta W_i^* + (\alpha + \beta) \langle \delta W_i \rangle. \qquad (2.25)
\end{aligned}
$$

To obtain the stability of chimera states, it is sufficient to investigate when the synchronized cluster breaks up, that is, when it becomes unstable with respect to perturbations transverse to the synchronization manifold. Without loss of generality, assume that oscillator W_1 and W_2 constitute the synchronized cluster, W_s. Then, following Refs. [81, 84], one can investigate the stability of this cluster by transforming the system of equations, Eqs. (2.25), as

$$
\begin{aligned}
\delta W_\perp &= \boldsymbol{v}_\perp^T \delta \boldsymbol{W} \\
&= \left(1/\sqrt{2}, -1/\sqrt{2}, 0, 0\right) \delta \boldsymbol{W}.
\end{aligned}
$$

Using the fact that $W_1(t) = W_2(t) = W_s(t)$, the considerations above lead to

$$
\partial_t \delta W_\perp = \left[1 - \kappa - 2(1 + ic_2)|W_s(t_0)|^2\right] \delta W_\perp - (1 + ic_2) W_s(t_0)^2 \delta W_\perp^*. \qquad (2.26)
$$

Together with

$$
\partial_t \delta W_\perp^* = -(1 - ic_2)\left(W_s(t_0)^2\right)^* \delta W_\perp + \left[1 - \kappa^* - 2(1 - ic_2)|W_s(t_0)|^2\right] \delta W_\perp^*
$$

Eq. (2.26) forms a linear dynamical system, defining the stability of W_s.
This approach can easily be tested at the synchronized solution Γ_s. Assume $\kappa = \alpha + i\beta$, with $\beta = 0$ and $c_2 = 0$. Then the variational equations read

$$
\begin{pmatrix} \partial_t \delta W_\perp \\ \partial_t \delta W_\perp^* \end{pmatrix} = \begin{pmatrix} 1 - \alpha - 2|W_s(t_0)|^2 & -W_s(t_0)^2 \\ -\left(W_s(t_0)^2\right)^* & 1 - \alpha - 2|W_s(t_0)|^2 \end{pmatrix} \begin{pmatrix} \delta W_\perp \\ \delta W_\perp^* \end{pmatrix},
$$

with the characteristic equation of the Jacobian,

$$
\begin{aligned}
\left(1 - \alpha - 2|W_s(t_0)|^2 - \lambda_i\right)^2 - W_s(t_0)^2 \left(W_s(t_0)^2\right)^* &= 0 \\
\left(1 - \alpha - 2R(t_0)^2 - \lambda_i\right)^2 - R(t_0)^4 &= 0
\end{aligned}
$$

$$(-1-\alpha-\lambda_i)^2 - 1 = 0$$
$$\lambda_1 = -\alpha \ , \ \lambda_2 = -2-\alpha.$$

Hereby, we use that for the amplitude of the synchronous oscillations, $R = 1\,\forall t$. Note that the resulting eigenvalues correspond to the eigenvalues in Sec. 2.1.3. This makes sense, since the synchronized oscillator pairs become unstable at $\alpha = 0$, and the system turns into a splay state. It is worth mentioning that in the general case for non-vanishing β and c_2, the eigenvalues of the variational equations do not necessarily correspond to the eigenvalues of the Jacobian as shown in Sec. 2.1.3. The reason is that the synchronized solution may become unstable and bifurcate into a state with two oscillators remaining synchronized, which would result in negative real parts of the eigenvalues obtained here, but not in the original system. In general, the Lyapunov spectrum for any state with two synchronized oscillators can be obtained using Eq. (2.26) and the procedures for the Lyapunov exponent estimations described in Sec. 2.2.4.

Lyapunov Exponents and Bifurcations of the Chimera State in the Four Oscillator System

Next, we use this concept to investigate how symmetric chimera states further bifurcate. In particular, we take parameters $\kappa = \alpha + i\beta$, with $\beta = -1.0$ and $c_2 = 2.0$ fixed, and use α as our bifurcation parameter. For the first run, we take a chimera state as starting point, with $\alpha = 0.8$, and subsequently reduce α to lower values. The two Lyapunov exponents obtained for the synchronized cluster, calculated using Eq. (2.26), are shown in Fig. 2.27. There, one can notice that the larger exponent increases while decreasing α, and eventually vanishes slightly below $\alpha \approx 0.752$. This indicates that the synchronized cluster, and thus the chimera state, becomes unstable at this point. These results can be confirmed using the Lyapunov spectrum of the full system, that is the eight-dimensional system with four complex oscillators. The results are depicted in Fig. 2.28. Note that, due to the rotational symmetry of the equations, and the rotational symmetry along the attractor, two Lyapunov exponents have to be zero. This can indeed be verified, up to numerical accuracy, in Fig. 2.28 (bottom). In addition, one exponent, indicated in blue, is always positive, indicating that the chimera state is indeed chaotic. Furthermore, the fourth-largest exponent, colored in red, increases with decreasing α, and becomes zero slightly below $\alpha \approx 0.752$, which coincides with the calculations of the reduced system, c.f. Fig. 2.27. Exemplary time series for the values of $\alpha = 0.752$, $\alpha = 0.7488$ and $\alpha = 0.74$ are plotted in Fig. 2.29. Note that above the bifurcation point indicated in Fig. 2.28, that is for $\alpha > 0.75$, the dynamics are chimera-like, whereas for $\alpha = 0.7488$, one can observe fully incoherent dynamics with intermittent behavior, c.f. the seemingly chimera-like windows with two oscillators almost synchronized in Fig. 2.29 (middle). There, one also can observe the week instability of the former

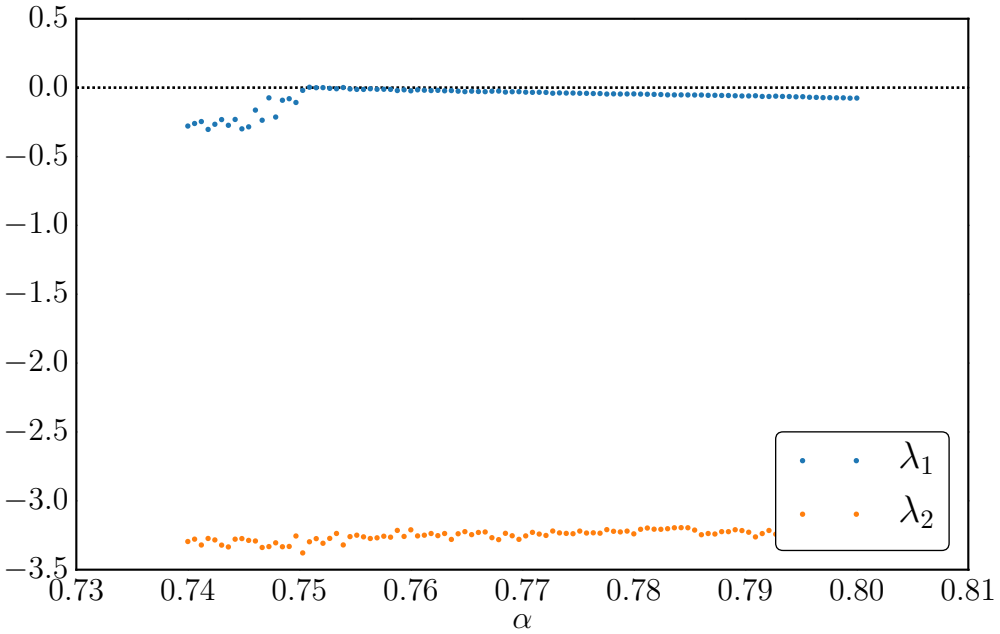

Figure 2.27: Lyapunov exponents of the synchronized cluster of a chimera state with $0.74 \leq \alpha \leq 0.8$, $\beta = -1.0$ and $c_2 = 2.0$, obtained using the reduced system, Eq. (2.26). Note that at $\alpha \approx 0.75$, the larger exponent approaches zero, indicating that the synchronized cluster of the chimera state becomes unstable.

synchronized cluster.
Note that, as indicated through just one positive Lyapunov exponent in Fig. 2.28, the chimera state and the fully incoherent state do not show hyperchaotic behavior. In particular, for the fully incoherent state, that is for $\alpha < 0.75$, the fourth-largest Lyapunov exponent is again negative. This indicates that the system does not get a second unstable direction. but rather that the unstable direction changed and now also points in the $(1, -1, 0.0)$ direction.
This can be verified by investigating the eigendirections corresponding to the individual Lyapunov exponents. Therefore, we investigate the Lyapunov spectrum for a chimera state at $\alpha = 0.752$ and for the fully incoherent state at $\alpha = 0.748$, with the β and c_2 values from above. For the chimera state, the direction to the largest Lyapunov exponent at a particular point in time is

$$\boldsymbol{v}_1 = \begin{pmatrix} -0.17027620 + 0.49383942i \\ -0.17027620 + 0.49383942i \\ -0.04649049 + 0.34967166i \\ 0.32689376 + 0.47219289i \end{pmatrix}.$$

Note that the first two entries, corresponding to the two synchronized oscillators, are identical. That means, the unstable direction involves a perturbation of the two

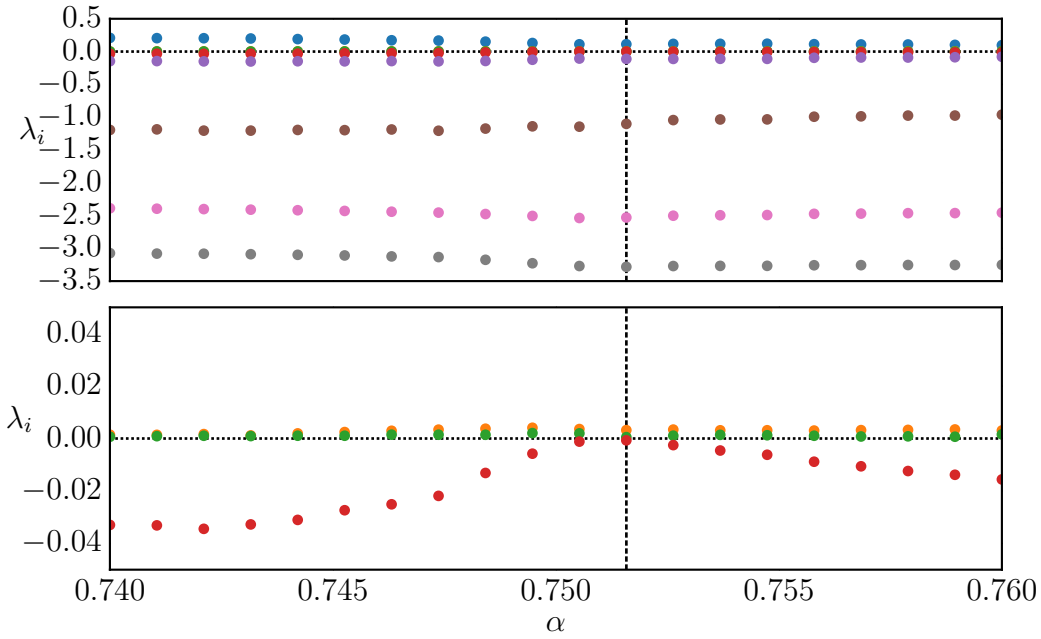

Figure 2.28: Top: Full Lyapunov spectrum of the chimera state/chaotic state, for the parameter values $0.74 \leq \alpha \leq 0.76$, $\beta = -1.0$ and $c_2 = 2.0$. Bottom: The same Lyapunov exponents in Top, but with different y-scale. There, one can observe that one exponent (indicated in red) vanishes at $\alpha \approx 0.752$ (indicated by the vertical dashed black line).

oscillators simultaneously. This can be viewed as a perturbation along the synchronized manifold of the two oscillators. The eigendirection of the fourth Lyapunov exponent (indicated as red in Fig. 2.28) is

$$\boldsymbol{v}_4 = \begin{pmatrix} -4.34747723 \cdot 10^{-01} + 5.57668735 \cdot 10^{-01} i \\ 4.34747723 \cdot 10^{-01} - 5.57668735 \cdot 10^{-01} i \\ -4.06237544 \cdot 10^{-14} + 2.11886064 \cdot 10^{-13} i \\ -2.28608799 \cdot 10^{-13} + 2.03226325 \cdot 10^{-13} i \end{pmatrix},$$

which is approximately zero in the third and fourth entry and has opposite sign in the first two entries, indicating a direction which is perpendicular to the synchronized manifold of the first two oscillators. For the chimera state, however, this direction is stable, represented through the negative Lyapunov exponent, and becomes less stable while decreasing α. However, note that all the directions are time dependent, although their qualitative structure seems to remain.
For the fully incoherent state the direction corresponding to the positive exponents

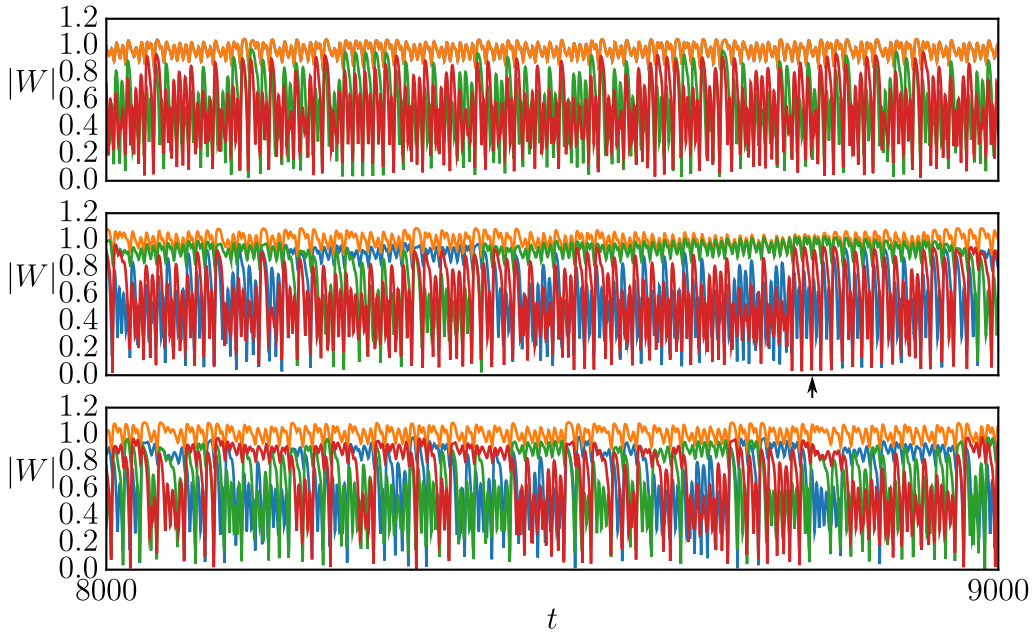

Figure 2.29: Exemplary time series of the amplitudes for $\alpha = 0.752$ (top), $\alpha = 0.7488$ (middle) and $\alpha = 0.74$ (bottom). The black arrow indicates the intermittent region with seemingly chimera-like behavior.

at a particular instance in time reads for example

$$\boldsymbol{v}_1 = \begin{pmatrix} -0.05777069 + 0.50732968i \\ -0.15750599 + 0.28431224i \\ -0.38217442 + 0.33854349i \\ -0.53907092 + 0.28700369i \end{pmatrix}.$$

All entries are very different, and the unstable direction does not seem to have any obvious structure. If one, on the other hand, investigates the unstable direction during an intermittent window (c.f. Fig. 2.29 (middle)), then the direction reads

$$\boldsymbol{v}_1 = \begin{pmatrix} -0.10624796 + 0.39264279i \\ -0.11866924 + 0.38571033i \\ -0.31020171 + 0.36260937i \\ -0.15492438 + 0.64805551i \end{pmatrix},$$

which shifts the first two oscillators similarly, and is reminiscent of the unstable direction observed for the chimera state. Also, the direction corresponding to the fourth largest exponent for the fully incoherent state during the intermittent dy-

namics,

$$\boldsymbol{v}_4 = \begin{pmatrix} -0.48968901 + 0.50281624i \\ 0.52680995 - 0.47934244i \\ -0.00499017 + 0.00283934i \\ 0.00274998 - 0.00648657i \end{pmatrix},$$

does posses a similar structure as in the case for the chimera state, but again only in the temporal regions where the first two oscillators become very close.

2.2.9 Blowout Bifurcation

The scenario described in the previous section can be identified as a so-called blowout bifurcation [85]. Blowout bifurcations occur when a Lyapunov exponent perpendicular to the invariant manifold on which a chaotic attractor lives, approaches zero. Two types of blowout bifurcations have been reported, a subcritical blowout, where the phase space close to the invariant manifold is riddled and the transition is hysteretic, and a supercritical blowout, characterized by on-off intermittency beyond the bifurcation point. Such bursts can also be observed at the onset of the fully

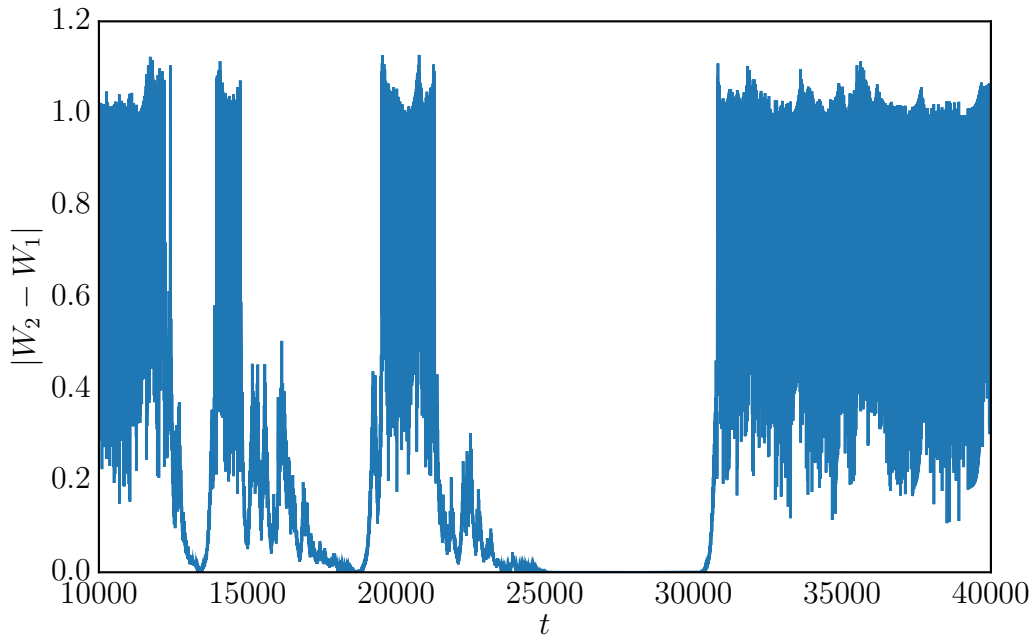

Figure 2.30: Time series of the absolute value of the difference between the second and first oscillator, obtained from numerical simulations of a four oscillator ensemble with the parameters $\alpha = 0.7504$, $\beta = -1.0$ and $c_2 = 2.0$.

incoherent dynamics in the system of four coupled Stuart-Landau oscillators, see Fig. 2.30. There, the modulus of the difference between the values of the second

and first oscillator (which where synchronized in the chimera state) is shown, with large irregular bursts and coherent plateaus interchanging in an irregular manner. Interestingly, the qualitatively same behavior of this on-off intermittency can be observed in the differences of all pairs of oscillators. This can be interpreted as a symmetry breaking from the fully incoherent state to one of the possible six chimera states (belonging to the same group orbit), where one pair of the four oscillators becomes synchronized. In the fully incoherent state, these six chimera states remain as unstable 'saddles', nearby which the chaotic states remains some period of time, as in Fig. 2.30. As explained in Ref. [85], the duration of the time period of these intermittent windows diverges at the bifurcation point, and the Lyapunov exponent transversal to this synchronized manifold subsequently decreases linearly with the bifurcation parameter. This is in accordance with our observations, see Fig. 2.27. The numerical approximations of the maximal transversal Lyapunov exponents in the β-α plane are shown in Fig 2.31. Starting from the chimera state and for

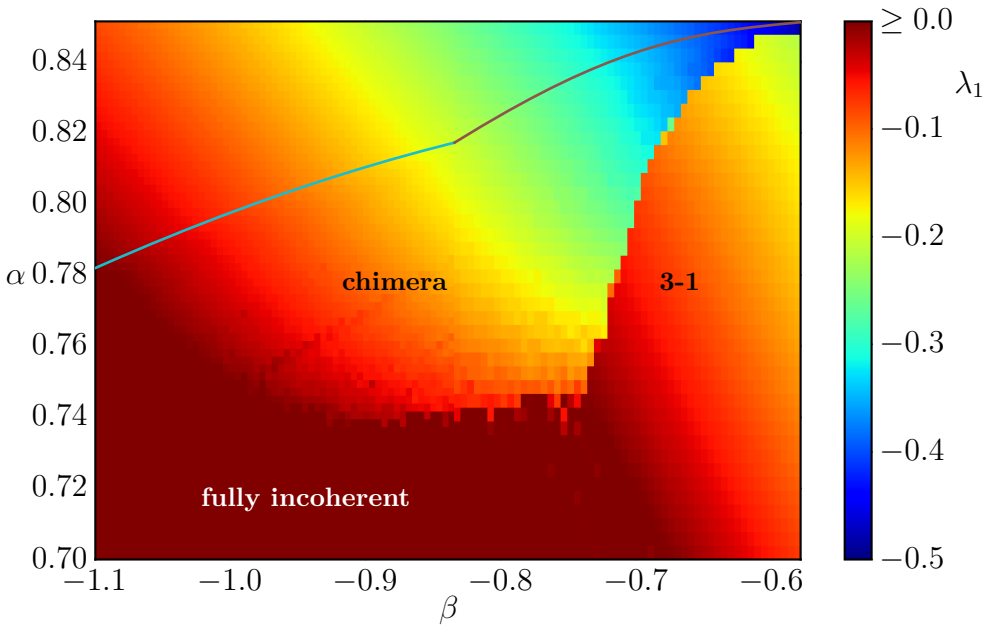

Figure 2.31: The maximal transversal Lyapunov exponent in the β-α plane for $c_2 = 2.0$. The numerical approximations are obtained by starting close to the torus bifurcation curve (blue) and the period doubling curve (magenta), using the method as explained in Sec. 2.2.8.

$\beta < -0.92$, one can observe that the maximal transversal Lyapunov exponent λ_1 grows continously until it becomes zero, indicating a blowout bifurcation. After the blowout, the dynamics is fully incoherent, without any pair of oscillators remaining synchronized. For β values slightly above $\beta = -0.92$, the transition from the chimera state to the fully incoherent state is non-continuous in the maximal transversal Lya-

punov exponent, indicating a bifurcation different from the blowout bifurcation. On the other hand, for $\beta > -0.74$, the chimera attractor gets destroyed and the system settles onto a stable 3-1 amplitude cluster state. This latter transition is hysteretic, indicating that this bifurcation possibly is a saddle node of unstable periodic orbits or a homoclinic bifurcation, destroying the chaotic attractor.

2.2.10 Non-Blowout Destruction of the Chimera State

Besides the continuous transition to fully incoherent dynamics by a linear convergence of transversal Lyapunov exponent to zero, there are also bifurcations of the chimera state which are characterized by a discontinuous transition, see Fig. 2.31. First, the chimera state can become unstable and converge to a stable 3-1 cluster state. This bifurcation occurs for parameter values $-0.74 \leq \beta \leq -0.6$. Furthermore, there is a discontinuous bifurcation curve between $-0.92 \leq \beta \leq -0.74$. An exemplary time series for parameter values below but close to the bifurcation curve, that is for $\alpha = 0.744$ and $\beta = -0.8$ are depicted in Fig. 2.32. Note that during the temporal evolution of the four oscillators in this example, a non-synchronized oscillator obtains a larger amplitude then the synchronized cluster. Following this

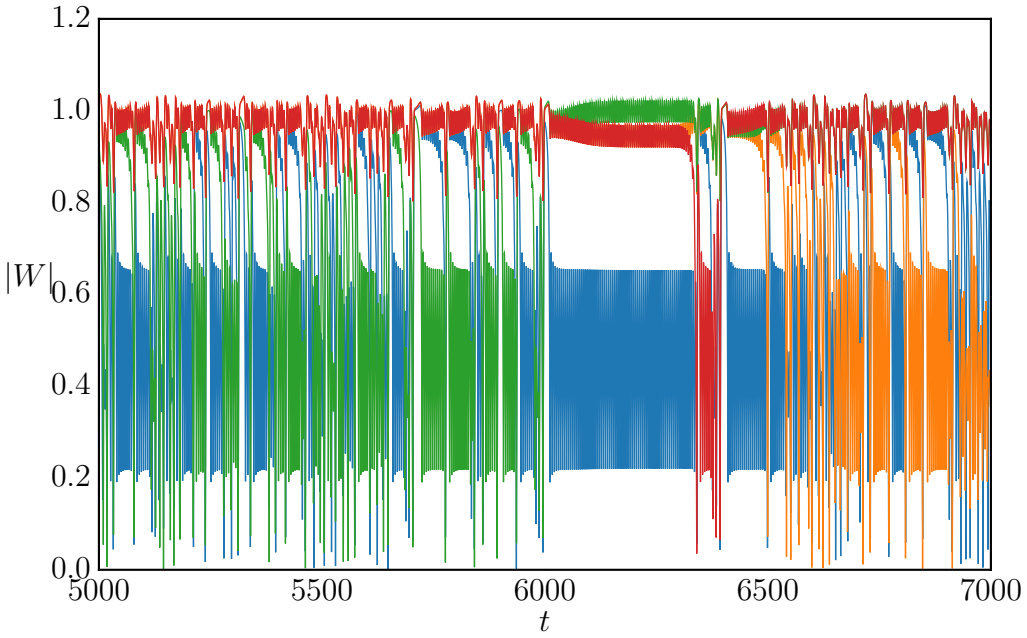

Figure 2.32: Exemplary time series of the amplitudes of the four complex variable W, obtained from a simulation below the non-blowout bifurcation to full incoherence at $\alpha = 0.744$, $\beta = -0.8$ and $c_2 = 2$.

event, the dynamics become seemingly periodic for a short period of time, which eventually ends in a break up of the synchronized cluster and the synchronization

of the two oscillators with the largest amplitudes. That means that the symmetry breaking inherited from the original 2-2 amplitude cluster state got lost, and all pairs of oscillators eventually become temporally synchronized. Surprising, however, is the fact that the transversal Lyapunov exponent is non-zero close to the bifurcation. This may be due to the fact that one has to choose one oscillator at which to evaluate the Jacobian, and the choice in this particular example is no longer unique. One can, in principle, evaluate the Jacobian always at the oscillator with the largest amplitude, which then yields negative transversal exponent above and below the bifurcation curve, or one can evaluate the linearized system at the first oscillator (blue in Fig. 2.32), which then yields the discontinuity shown in Fig. 2.31.
Furthermore note that the dynamics as shown in Fig. 2.32 are reminiscent of a non-stationary chimera state, that is, the cluster assignment of the individual oscillators changes in time. However, the mean time periods during which the synchronized oscillators remain synchronized seemingly reduce when departing from the bifurcation curve, with the dynamics becoming rather fully incoherent and non-chimera like. This is in contrast to the blowout bifurcation, after which one of the two former synchronized oscillators remains distinct with the largest amplitude, while the other oscillator joins the oscillators in the non-synchronized cluster, c.f. Fig. 2.29. However, in both scenarios, temporarily periodic or quasi-period windows are apparent. The set of all bifurcations from and to the chimera state is depicted in Fig. 2.33. Hereby, the blowout and non-blowout bifurcation curves are obtained through quadratic fits, and the hysteretic bifurcation through an exponential fit, to the data of the largest transversal Lyapunov exponent when it becomes zero or discontinous in the parameter plane, cf. Fig. 2.31. In addition, only one of the period doubling bifurcation curves are shown.

2.3 The Dynamics of Larger Ensembles

The analysis of the clustering behavior in the ensemble of four oscillators, c.f. Sec. 2.2.1, can easily be extended to larger ensembles of oscillators. In particular, we now consider 16 oscillators and investigate the clustering behavior along the parameter cut indicated by the dashed orange line in Fig. 2.16. That is, we fix $c_2 = 2$ and $\alpha = 1.12$ and vary β. We do this by simulating the full model, Eq. 2.2, starting from the balanced 8-8 cluster solution, and increasing β step-wise. Over the course of this increase, the system goes from a stable 8-8 solution to a stable 9-7 solution, 10-6 solution and so forth until it settles on the synchronized solution. In this way we obtain solutions for every cluster distribution, which we then use for continuation with AUTO. The continuation curves we obtain this way are depicted in Fig. 2.34(a), where again the amplitude of the cluster with the larger number of oscillators, R_{C_1}, is shown as a function of the continuation parameter β. The amplitudes of the smaller cluster for the same parameter window are shown in

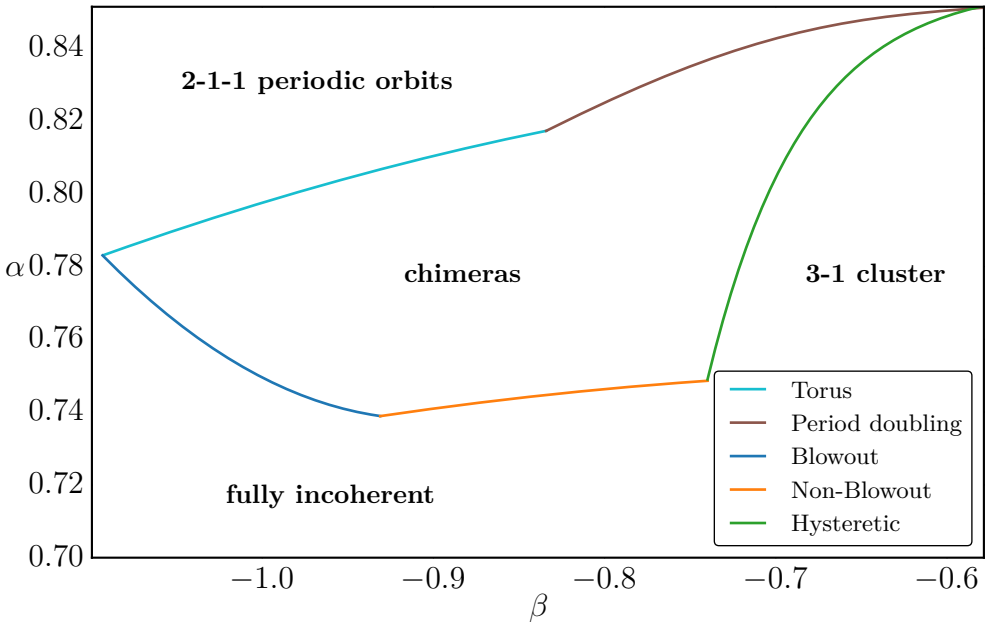

Figure 2.33: Bifurcations from and to the chimera state at $c_2 = 2$. The term hysteretic shall indicate that the transition from chimeras to 3-1 cluster states and vice versa is hysteretic, without being specific in what the actual bifurcation is.

Fig. 2.34(b). Note the correspondence of the 8-8 cluster solution, shown in blue, with the 2-2 cluster solution in Fig. 2.15.
There are two β values, β_1 and β_2, between which the synchronized solution is unstable, see Fig. 2.34. At the bifurcation points, there are also transcritical bifurcations of all unbalanced cluster states and pitchfork bifurcations of the balanced state. The two solution branches of each transcritical and of the pitchfork bifurcations, respectively, connect the two bifurcation points at β_1 and β_2. Each of the unbalanced clusters is born respectively destroyed in a saddle-node bifurcation, the most outer one corresponding to the $(N-1)$-1 cluster state being the only one that posses a stable branch. The other cluster states, as well as the balanced one, are stabilized through further (equivariant) pitchfork bifurcations (not shown), compare Fig. 2.15. In this way, two staircases of overlapping stable cluster states are generated, whereby the cluster distribution of the cluster states in subsequent steps differ by just one oscillator. This leads to two cascades of transitions between the two synchronized regions.
If we start from the stable synchronized solution for $\beta < \beta_1$ and slowly increase β, the system goes from the synchronized solution to a 15-1 cluster state, and then two a 14-2 state and so forth, traversing a cascade up to the balanced 8-8 cluster and back, until it settles again on the synchronized solution, see the blue curve in Fig. 2.35. Thereby, the originally larger cluster with amplitude R_{C_1} (cf. Fig. 2.34(a))

becomes the smaller one with amplitude R_{C_2} (cf. Fig. 2.34(b)) beyond the balanced cluster state. The second staircase, and with it the hysteretic behavior, can be seen when we subsequently reduce β again, cf. the orange curve in Fig. 2.35.

As mentioned above, all unbalanced cluster solutions, that is all cluster solutions except the 8-8 cluster, bifurcate with the synchronized solution in a transcritical bifurcation. In particular, the unbalanced cluster states exist on both sides of both bifurcation points where the synchronized solution changes stability. However, all cluster solutions lose stability through equivariant pitchfork bifurcations (the resulting branches are not shown in Fig. 2.34(a)), in which either the cluster with the larger or smaller amplitude breaks up. This is true except for the most unbalanced, the 15-1, cluster, for which the smallest cluster cannot break up. There we find that this stable state is destroyed in a saddle-node bifurcation instead. In addition, each kind of unbalanced cluster solution is stable in two different regions in parameter space. Each of these stable regions lies close but slightly shifted to the stable regions of neighboring cluster states.

2.3.1 Cluster Singularities

The observed phenomena of slightly shifted bifurcations can be explained with the concept of persistence. Loosely speaking, if two attractors are hyperbolic and close in phase space, then bifurcations of those attractors are also close in parameter space [55]. In addition, one can infer that between the cluster states shown in Fig. 2.34, which must also exist for larger ensembles, there lie many more cluster states in larger networks, and using persistence, their stability must be similar to that of the ones seen in Fig. 2.34.

This explains the cascade-like transition from balanced cluster states to the homogeneous solution in large ensembles, where, when changing a parameter, one oscillator after another joins the other cluster until the synchronized solution is reached. We conjecture that for infinitely large ensembles, the cluster attractors are infinitesimal close, and thus this process becomes continuous. This is similar to the Eckhaus instability, where the distances between subsequent bifurcations shrink with increasing system size [86].

Turning back to Fig. 2.16, we observe that there is a codimension-2 point (pink point in Fig. 2.16) where the stable 2-2 cluster bifurcates into the synchronized solution in a pitchfork bifurcation. This is in contrast to the phenomena observed in the literature, where the transition to the synchronized solution occurs via the unbalanced cluster solutions [37]. For the Stuart-Landau ensemble, Eq. (2.2), this point can be found analytically as

$$\alpha_{\mathrm{CS}} = -\frac{1 \pm \sqrt{3} c_2}{2}, \tag{2.27}$$

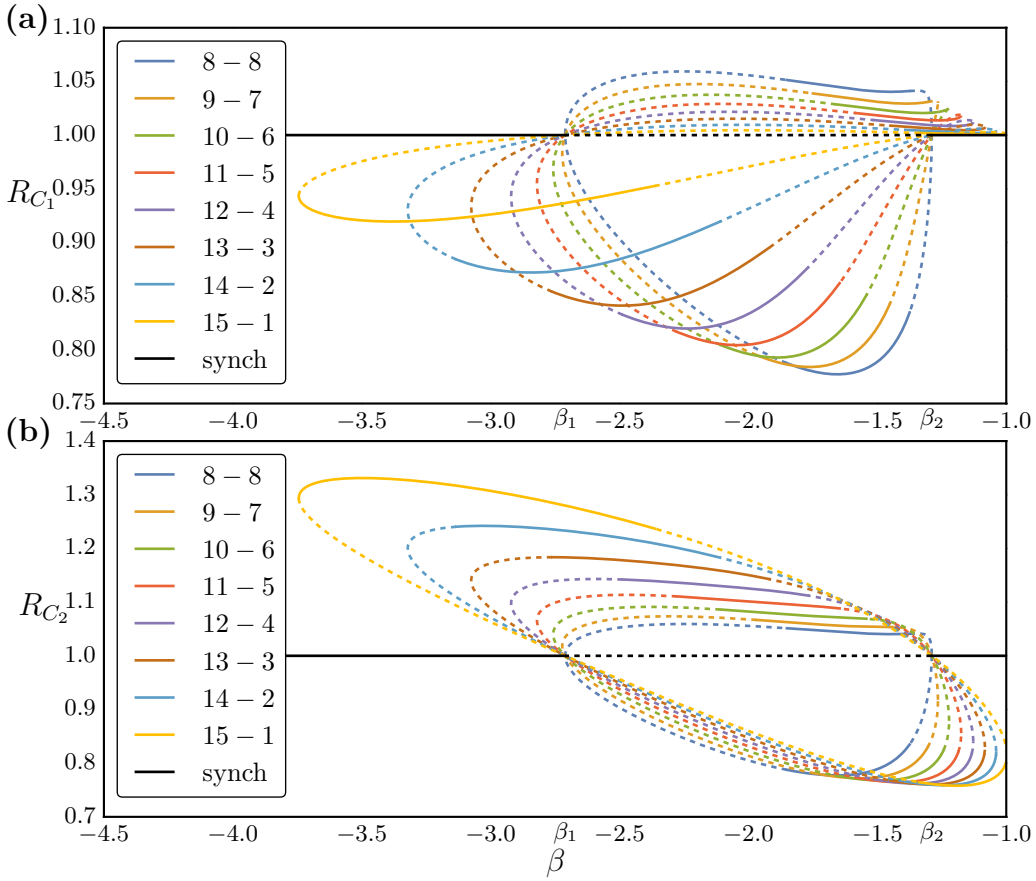

Figure 2.34: Cluster solutions in an ensemble of 16 coupled Stuart-Landau oscillators obtained using AUTO. Shown is (a) the amplitude of the larger cluster, R_{C_1}, as a function of the bifurcation parameter β, as indicated by the dashed orange line in Figs. 2.14 and 2.16, and (b) the amplitude of the smaller cluster, R_{C_2}. Other parameter values are $c_2 = 2$ and $\alpha = 1.12$. β_1 and β_2 indicate when the synchronized solution bifurcates.

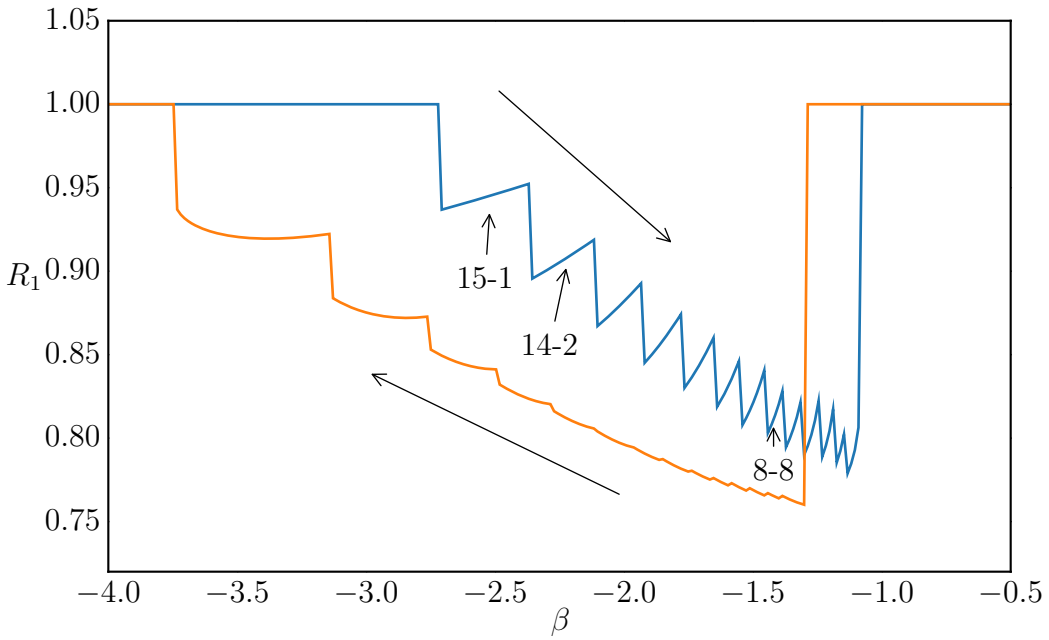

Figure 2.35: The amplitude of one of 16 oscillators as a function of the parameter β starting from the stable synchronized solution and increasing β (blue curve) and when subsequently reducing β (orange curve). Due to the addition of finite noise in the numerical simulations when increasing β, not all of the densely located cluster states close to β_2 are resolved.

$$\beta_{\mathrm{CS}} = \frac{-c_2 \pm \sqrt{3}}{2}, \tag{2.28}$$

with the derivation shown in Sec. 2.3.2.
The characteristics of such a point is that, when starting from a balanced 2-cluster solution and changing the parameters over this bifurcation point, the two clusters approach each other and finally merge and form the synchronized solution. This is what we call a **cluster singularity**. However, when varying the parameters such that one turns around the codimension-2 point either clock- or anticlockwise (that is, changing α and β along a path which circumvents the singularity on the left or on the right), either of the clusters shrinks and single oscillators join the other cluster until all oscillators finally form the synchronized solution. This scenario can be verified using numerical simulations and is shown in Fig. 2.36. There, simulations of $N = 20$ Stuart-Landau oscillators are shown when avoiding the cluster singularity clockwise (Fig. 2.36(a)), when directly crossing over the cluster singularity (Fig. 2.36(b)) and when avoiding the cluster singularity in an anticlockwise manner (Fig. 2.36(c)).
The cluster singularity serves as an organizing center for nearby unbalanced cluster solutions. Recall that all unbalanced 2-cluster solutions get destroyed in saddle-node bifurcations, cf. Fig. 2.34. In the cluster singularity, all these saddle-node

bifurcations as well as the pitchfork bifurcations that alter the stability properties of the cluster states collapse to a single point in phase space, suggesting the name cluster singularity. Note that when crossing the singularity, the stable balanced cluster solution directly bifurcates into the synchronized solution. However, the complete unfolding of this co-dimension 2 point still remains subject for future research.

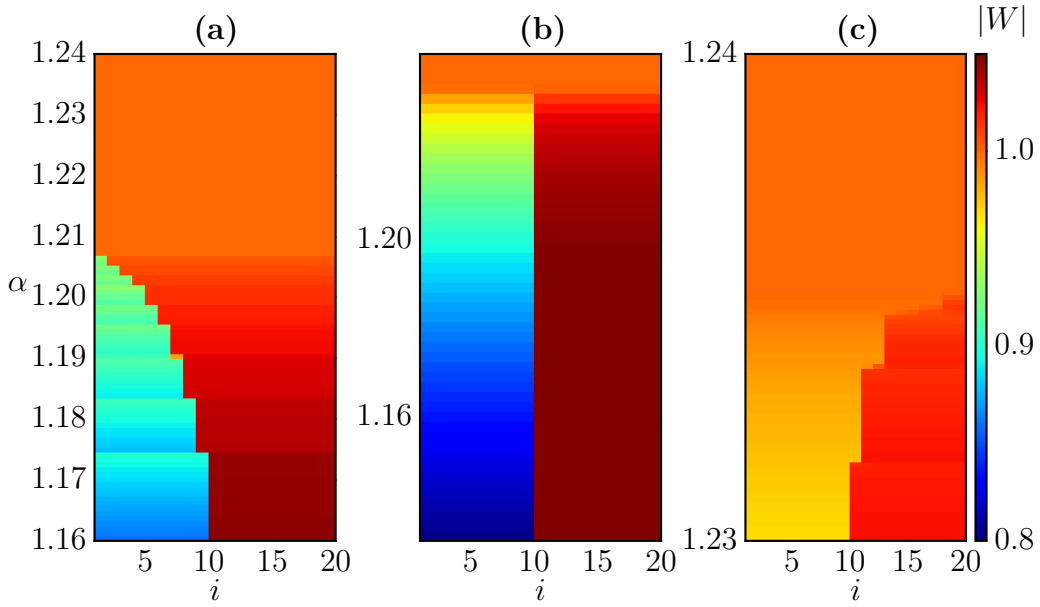

Figure 2.36: Simulations of the globally coupled Stuart-Landau ensemble close to the cluster singularity for $N = 20$ oscillators and $c_2 = 2$, (a) $\beta = \beta_{\mathrm{CS}} + 0.3 > \beta_{\mathrm{CS}}$, (b) $\beta = \beta_{\mathrm{CS}}$ and (c) $\beta = \beta_{\mathrm{CS}} - 0.05 < \beta_{\mathrm{CS}}$. The direction in which α is changed is from small to large values.

2.3.2 Derivation of the Cluster Singularities

The idea is that at the cluster singularity, the saddle-node bifurcations of all unbalanced 2-cluster solutions hit the pitchfork at which the synchronous solution becomes unstable. This must be true for any $\epsilon = N_1/N$. Therefore, for simplicity, we take the limit $\epsilon \to 0$ in system Eqs. (2.5) to (2.7), yielding

$$
\begin{aligned}
0 &= R_1 - R_1^3 \\
0 &= R_2 - R_2^3 + \alpha\left(R_1\cos\left(\Delta\phi\right) - R_2\right) - \beta R_1 \sin\left(\Delta\phi\right) \\
0 &= -c_2\left(R_1^2 - R_2^2\right) + \beta - \beta\cos\left(\Delta\phi\right)\left(\frac{R_1}{R_2}\right) - \alpha\sin\left(\Delta\phi\right)\left(\frac{R_1}{R_2}\right).
\end{aligned}
$$

This means $R_1 = 1$ and thus leaves

$$\begin{aligned} 0 &= R_2 - R_2^3 - \alpha R_2 + \alpha\cos(\Delta\phi) - \beta\sin(\Delta\phi) \\ 0 &= -c_2\left(R_2 - R_2^3\right) + \beta R_2 - \beta\cos(\Delta\phi) - \alpha\sin(\Delta\phi), \end{aligned}$$

and solving for R_2^2,

$$\begin{aligned} R_2^2 = &-\frac{2\alpha + 2\beta c_2 - 1 - c_2^2}{2\left(1 + c_2^2\right)} \\ &\pm \frac{\sqrt{\left(2\alpha + 2\beta c_2 - 1 - c_2^2\right)^2 - 4\left(\alpha^2 + \beta^2\right)\left(1 + c_2^2\right)}}{2\left(1 + c_2^2\right)}. \end{aligned}$$

Setting $R_2^2 = 1$ means we are at the point where the cluster solution meets the synchronous solution ($\Delta\phi = 0$ follows from $R_2 = R_1 = 1$), and from this the previous expression turns into

$$\begin{aligned} 1 &= -\frac{2\alpha + 2\beta c_2 - 1 - c_2^2}{2\left(1 + c_2^2\right)} \\ &\quad \pm \frac{\sqrt{\left(2\alpha + 2\beta c_2 - 1 - c_2^2\right)^2 - 4\left(\alpha^2 + \beta^2\right)\left(1 + c_2^2\right)}}{2\left(1 + c_2^2\right)} \\ \rightarrow 2\left(1 + c_2^2\right) &= -\left(2\alpha + 2\beta c_2 - 1 - c_2^2\right) \\ &\quad \pm \sqrt{\left(2\alpha + 2\beta c_2 - 1 - c_2^2\right)^2 - 4\left(\alpha^2 + \beta^2\right)\left(1 + c_2^2\right)} \end{aligned}$$

$$\begin{aligned} \rightarrow \left(2\alpha + 2\beta c_2 + 1 + c_2^2\right) &= \pm\sqrt{\left(2\alpha + 2\beta c_2 - 1 - c_2^2\right)^2 - 4\left(\alpha^2 + \beta^2\right)\left(1 + c_2^2\right)} \\ \rightarrow \left(2\alpha + 2\beta c_2 + 1 + c_2^2\right)^2 &= \left(2\alpha + 2\beta c_2 - 1 - c_2^2\right)^2 - 4\left(\alpha^2 + \beta^2\right)\left(1 + c_2^2\right) \\ \rightarrow (2\alpha + 2\beta c_2)^2 + \left(1 + c_2^2\right)^2 &+ 2\left(2\alpha + 2\beta c_2\right)\left(1 + c_2^2\right) \\ &= (2\alpha + 2\beta c_2)^2 \\ &\quad + \left(1 + c_2^2\right)^2 - 2\left(2\alpha + 2\beta c_2\right)\left(1 + c_2^2\right) \\ &\quad - 4\left(\alpha^2 + \beta^2\right)\left(1 + c_2^2\right) \\ \rightarrow 4\left(2\alpha + 2\beta c_2\right)\left(1 + c_2^2\right) &= -4\left(\alpha^2 + \beta^2\right)\left(1 + c_2^2\right) \\ \rightarrow \alpha^2 + \beta^2 + 2\left(\alpha + \beta c_2\right) &= 0 \end{aligned} \tag{2.29}$$

which coincides with the curve at which the homogeneous solution becomes unstable. For the saddle-node curve of the cluster solutions, the two solutions of R_2^2 must equal, and thus the discriminant must equal zero

$$0 = \left(2\alpha + 2\beta c_2 - 1 - c_2^2\right)^2 - 4\left(\alpha^2 + \beta^2\right)\left(1 + c_2^2\right)$$

$$
\begin{aligned}
4\left(\alpha^2+\beta^2\right)\left(1+c_2^2\right) &= \left(2\alpha+2\beta c_2-1-c_2^2\right)^2 \\
4\left(\alpha^2+\beta^2\right)\left(1+c_2^2\right) &= \left(2\alpha+2\beta c_2\right)^2+\left(1+c_2^2\right)^2-2\left(2\alpha+2\beta c_2\right)\left(1+c_2^2\right) \\
4\left(\alpha^2+\beta^2\right)\left(1+c_2^2\right) &= 4\left(\alpha+\beta c_2\right)^2+\left(1+c_2^2\right)^2-4\left(\alpha+\beta c_2\right)\left(1+c_2^2\right).
\end{aligned}
$$

Now use that $-2\left(\alpha+\beta c_2\right)=\alpha^2+\beta^2$ from Eq. (2.29) above,

$$
\begin{aligned}
4\left(\alpha^2+\beta^2\right)\left(1+c_2^2\right) &= 4\left(\alpha+\beta c_2\right)^2+\left(1+c_2^2\right)^2-4\left(\alpha+\beta c_2\right)\left(1+c_2^2\right) \\
4\left(\alpha^2+\beta^2\right)\left(1+c_2^2\right) &= \left(\alpha^2+\beta^2\right)^2+\left(1+c_2^2\right)^2+2\left(\alpha^2+\beta^2\right)\left(1+c_2^2\right) \\
0 &= \left(\alpha^2+\beta^2\right)^2+\left(1+c_2^2\right)^2-2\left(\alpha^2+\beta^2\right)\left(1+c_2^2\right) \\
0 &= \left(\alpha^2+\beta^2-1-c_2^2\right)^2 \\
0 &= \alpha^2+\beta^2-1-c_2^2. \qquad (2.30)
\end{aligned}
$$

Eq. (2.30) gives the saddle-node curve of the cluster with $\epsilon=0$. So for the cluster singularity, this saddle-node bifurcation coincides with the point at which the homogeneous solution becomes unstable, as given by Eq. (2.29), which yields in total the two conditions

$$
\begin{aligned}
0 &= \alpha^2+\beta^2+2\left(\alpha+\beta c_2\right) \\
0 &= \alpha^2+\beta^2-1-c_2^2.
\end{aligned}
$$

Subtraction of these two equations yields

$$
\begin{aligned}
0 &= 2\left(\alpha+\beta c_2\right)+1+c_2^2 \\
\alpha &= -\beta c_2-\frac{1}{2}\left(1+c_2^2\right) \qquad (2.31)
\end{aligned}
$$

and thus

$$
\begin{aligned}
0 &= \left(\beta c_2+\frac{1+c_2^2}{2}\right)^2+\beta^2-\left(1+c_2^2\right) \\
0 &= \left(2\beta c_2+1+c_2^2\right)^2+4\beta^2-4\left(1+c_2^2\right) \\
0 &= 4\beta^2c_2^2+\left(1+c_2^2\right)^2+4\beta c_2\left(1+c_2^2\right)+4\beta^2-4\left(1+c_2^2\right) \\
0 &= 4\beta^2\left(1+c_2^2\right)+\left(1+c_2^2\right)^2+4\beta c_2\left(1+c_2^2\right)-4\left(1+c_2^2\right) \\
0 &= 4\beta^2+\left(1+c_2^2\right)+4\beta c_2-4 \\
0 &= \beta^2+\beta c_2+\frac{-3+c_2^2}{4} \\
\beta &= \frac{-c_2\pm\sqrt{3}}{2}.
\end{aligned}
$$

This solution plugged into Eq. (2.31) yields

$$\begin{aligned}\alpha &= -\frac{-c_2 \pm \sqrt{3}}{2}c_2 - \frac{1}{2}\left(1 + c_2^2\right) \\ &= \frac{c_2 \mp \sqrt{3}}{2}c_2 - \frac{1}{2}\left(1 + c_2^2\right) \\ &= -\frac{1 \pm \sqrt{3}c_2}{2}.\end{aligned}$$

So, in total, we have at the cluster singularity

$$\alpha = -\frac{1 \pm \sqrt{3}c_2}{2} \tag{2.32}$$

$$\beta = \frac{-c_2 \pm \sqrt{3}}{2}. \tag{2.33}$$

This indicates two possible solutions for the cluster singularity. Furthermore, it is worth mentioning that it seems to exist for all c_2 values.

2.3.3 Clustering in Spatially Extended Systems

Adding a diffusive coupling in addition to the global coupling, one obtains a globally coupled version of the complex Ginzburg-Landau equation [25], see Eq. 2.1. In a sense, such a system can be viewed as an ensemble of infinitely many oscillators, coupled locally and globally. If the local coupling is weak or the spatial domain is very large, then we expect the solutions of the Stuart-Landau ensemble to exist also in the spatially extended system. For infinitely many oscillators, however, the 2-cluster solutions become infinitesimally close in phase space (cf. Fig. 2.34 for 16 oscillators) and thus infinitesimally small perturbations are sufficient to drive the solution from one cluster state to another. This is also what we observe in numerical simulations: the diffusive coupling leads to the selection of a particular cluster distribution, and the multi-stability of different cluster solutions, as apparent in Fig. 2.34 for Stuart-Landau oscillators, seems no longer to exist. What is special about the then globally stable 2-cluster solution, however, still remains unknown.

2.4 Conclusions

To summarize the results of this chapter, we investigated the dynamics of two and four coupled Stuart-Landau oscillators. There, we observed symmetry broken states which can be viewed as so-called cluster states. Starting from such cluster states, we discussed how chimera states are born in systems of four coupled oscillators. We

investigated how such chimera states further bifurcate using transversal Lyapunov exponent, and found different bifurcation scenarios, including the destruction via blowout bifurcations. After these bifurcations, fully incoherent dynamics can be observed, in which there are no pairs oscillators that remain synchronized.
Using symmetry detectives, we could distinguish two qualitatively different types of chimera states, which we dubbed symmetric and asymmetric chimeras. Hereby, the attractor of symmetric chimera states is invariant under the exchange the two incoherent oscillators, whereas the attracting manifold of asymmetric chimera states is not invariant under such a transformation. In addition, we have shown ways how clustering can occur in globally coupled ensembles of Stuart-Landau oscillators. In particular, starting from small ensembles, we described how 2-cluster branches bifurcate, and extended this analysis to larger ensembles of oscillators. Doing so, we found a codimension-2 point which we dubbed a cluster singularity: at this point, the stable balanced cluster solution bifurcates directly into the synchronized solution. In addition, all saddle-node bifurcations generating unbalanced cluster solutions collapse in this point. Using numerical simulations, we showed how ensembles of Stuart-Landau oscillators behave close to this cluster singularity. Since any oscillatory system close to the onset of oscillations can be mapped onto the dynamics of the Stuart-Landau oscillator, we believe that cluster singularities are common in oscillatory systems with global coupling, and that an experimental observation of these should be possible. Finally, we discussed how our results extend to spatially extended systems, where the diffusive coupling seems to destroy the multi-stability. We believe that our considerations may serve as a further step towards a better understanding of clustering behavior in coupled oscillators. In particular, the complete unfolding of the cluster singularity point is still topic of ongoing research. In addition, 2-cluster solutions in the regarded parameter windows may also become unstable through supercritical Hopf bifurcations for smaller α values, and even bifurcate into chimera states [17, 48]. How this transition occurs for different cluster distributions is still an open question. Furthermore, how the results obtained in this chapter extend to systems of coupled relaxational oscillators or weakly inhomogeneous systems still remains unanswered.

Chapter 3

Classification of Chimera States

In the previous chapter, we investigated chimera states in minimal networks of just four oscillators. There, we briefly discussed how such minimal chimeras manifest themselves in larger ensembles. In particular, symmetric chimeras seem to show spatiotemporal incoherent motion, whereas asymmetric chimera states seem to form spatially coherent clusters. The increasing number of reported chimeras, however, reveals that this classification into symmetric and asymmetric chimeras in larger ensembles of oscillators is by no means complete, and other measures are desirable. In this chapter, we present a universal characterization scheme for chimera states applicable to both numerical and experimental data sets which we published in Ref. [19]. The scheme is based on two correlation measures that enable a meaningful definition of chimera states as well as their classification into three categories: *stationary*, *turbulent* and *breathing*. In addition, these categories can be further subdivided according to the time-stationarity of these two measures. We demonstrate that this approach both is consistent with previously recognized chimera states and enables us to classify states as chimeras which have not been categorized as such before. Furthermore, the scheme allows for a qualitative and quantitative comparison of experimental chimeras with chimeras obtained through numerical simulations.
Before developing the classification theme, it is useful to recapitulate the emergence of so-called chimera states. In particular, the paper "Coexistence of Coherence and Incoherence in Nonlocally Coupled Phase Oscillators" by Kuramoto and Battogtokh published in 2002 [82] marks the commencement of intense research activities on a counter-intuitive phenomenon that has come to be known as a chimera state [12], i.e., the coexistence of coherent and incoherent dynamics in a network of symmetrically coupled identical oscillators. For a long time, the coexistence of coherence and incoherence had been believed to be bound to heterogeneous networks of oscillators, in which oscillators with a similar frequency might mutually synchronize, while those with larger deviations of their frequencies from the mean frequency keep on drifting incoherently. The discovery that an array of identical oscillators, all coupled in an identical way to their neighbors, can also be split into synchronized and drifting groups was likewise surprising as fundamental. The chimera state, being a novel type of dynamic state, can broaden our understanding of transitions from syn-

chrony to "turbulence" and vice versa, and has possible realizations and applications in nature, e.g. in neuroscience [87, 88] or hydrodynamics [89, 90]. Since the pioneering works in the early years of this millennium, chimera states have been observed in many different systems, ranging from systems with non-local coupling [91–96], via two-group approximations [97, 98] to global all-to-all coupling [54, 99]. Due to their robustness to noise, chimera states have also been observed experimentally, e.g. in networks of coupled chemical oscillators [98], arrays of coupled spatial light modulators [93], networks of mechanical oscillators [100] and electrochemical systems [54]. However, the various systems differ strongly in the visual attributes of their dynamic behavior, asking for a systematic categorization. In this chapter, we propose a classification scheme based on linear methods, which we believe fulfills the requirements of being universal and simple in its application.

Most early studies on chimera states dealt with non-locally coupled phase oscillators, where coherence refers to phase- and frequency-locked oscillators and incoherence to drifting oscillators, respectively [82]. Lately, more and more chimera patterns were discovered, wherein coherence and incoherence is of a different nature. One example is the so-called amplitude chimera, where the incoherent group is characterized by disorder in the amplitude of the oscillators while all the oscillators in the entire ensemble oscillate with the same frequency [96]. Other coherence/incoherence coexistence patterns differ from the classical chimera state by the variability of coherent and incoherent regions, which might both change their sizes and move in space [26, 30]. Furthermore, the stability properties of these diverse chimera states vary greatly. Many chimeras, among them the original one in systems of nonlocally coupled phase oscillators, are transient for a finite number of oscillators, but have a diverging transient time in the continuum limit $N \to \infty$ [101]. Others are stable already from small ensemble sizes on [79, 102], and still others have finite transient times even in the continuum limit [96].

These examples illustrate that the original definition of a chimera state as "a spatio-temporal pattern in which a system of identical oscillators is split into coexisting regions of coherent and incoherent oscillators" [103] does not cope with recent developments but calls for a more distinct characterization and refinement. There already exist two approaches towards characterization schemes in minimal networks [79] and for chimeras with non-local coupling [104], but they are both restricted to a small class of systems.

In this chapter we propose two measures for characterizing chimera states. Although based on linear methods, these quantities provide what we believe to be a clear and simple definition of chimera states, and, furthermore, they allow for an easy distinction between chimera states with different coherence properties and thus provide a useful classification scheme. In addition, our approach is independent of the coupling scheme and the spatial dimension of the system, and not restricted to phase oscillators, such as the (local) Kuramoto order parameter [82].

The chapter is structured as follows: In Sec. 3.1 we introduce a spatial and a tempo-

ral correlation measure applicable to arbitrary data sets and define chimera states with the help of these measures. In Sec. 3.2, these criteria are applied to experimental and simulated data of different chimera states, and in Sec. 3.3 a detailed characterization scheme on the basis of the measures is discussed.

3.1 Correlation Measures for Spatial and Temporal Coherence

3.1.1 A Measure for Correlation in Space

For systems with a spatial extent, that is, systems with a local or non-local coupling topology, we employ the local curvature as a measure for the spatial coherence. Hereby the local curvature of the observable is quantified by the second derivative with respect to space for spatially one-dimensional systems, or, more generally, by the Laplacian for any number of spatial dimensions. Therefore, we calculate the local curvature at each point in space by re-scaling and applying the discrete Laplacian $\mathbf{D}$ on each snapshot containing the spatial data f. For one snapshot at time t with one spatial dimension, this operation reads

$$\begin{aligned}\hat{\mathbf{D}}f &= \Delta x^2 \mathbf{D} f \\ &= f\left(x+\Delta x,t\right) - 2f\left(x,t\right) + f\left(x-\Delta x,t\right),\end{aligned} \tag{3.1}$$

where each data point in f can be either real, complex or of any higher dimension. In order to clarify this concept, consider the chimera state observed by Kuramoto and Battogtokh in a ring of non-locally coupled phase oscillators [82]. The evolution of the phases in the Kuramoto model is described by

$$\partial_t \theta\left(x,t\right) = \omega - \int G\left(x-x'\right) \sin\left(\theta\left(x,t\right) - \theta\left(x',t\right) + \alpha\right) dx' \tag{3.2}$$

with the coupling kernel

$$G\left(x-x'\right) = \frac{\kappa}{2} e^{-\kappa|x-x'|}.$$

We numerically integrate the Kuramoto model, Eq. (3.2), using the fourth-order Runge-Kutta method with fixed time step $dt = 0.025$ and $N = 3000$ oscillators. As initial conditions, random numbers σ with a Gaussian envelope

$$\theta\left(x,t=0\right) = 6.0 e^{-30.0(x-L/2)^2} \cdot \sigma\left(x\right) \tag{3.3}$$

are taken. Further parameters are $\alpha = 1.457$, $\kappa = 4.0$, $L = 1$. As boundary conditions periodic conditions are chosen.
One realization of the chimera state is depicted in Fig. 3.1(a). Through the applica-

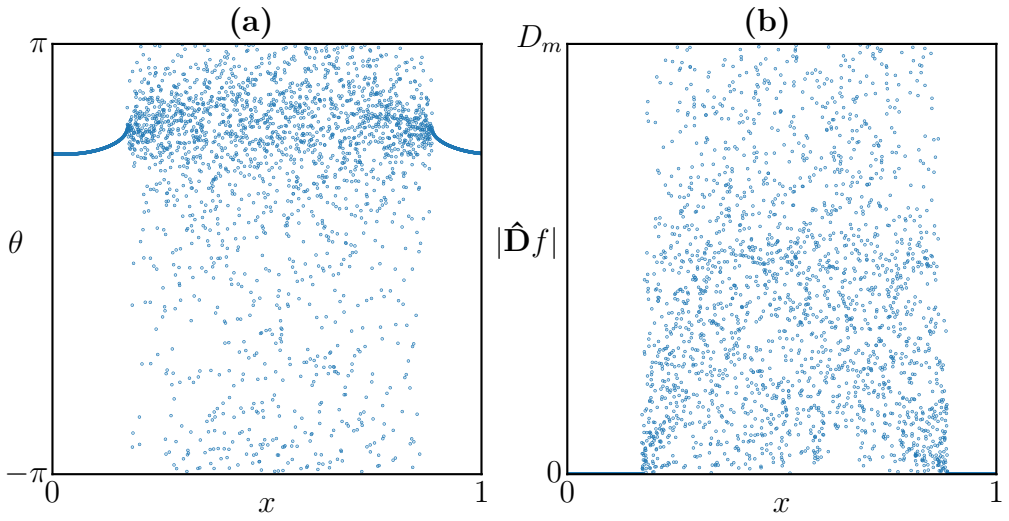

Figure 3.1: (a) Snapshot of the Kuramoto model[82], after the initial conditions decayed. (b) Absolute value of the local curvature obtained by applying the discrete Laplace operator on the data set shown in (a).

tion of the discrete Laplace operator, this snapshot is mapped onto a new function as shown in Fig. 3.1(b), with D_m indicating the maximal value of $|\hat{\mathbf{D}}f|$. Note that for phase oscillator systems, we apply this operator on the data in the complex plane, that is the phase oscillators are located on a ring with constant amplitude A. Then, D_m corresponds to the curvature at an oscillator whose two neighbors are shifted 180° in phase, i.e., whose neighboring oscillators are located on opposite positions on the circle. With the re-scaling obtained by multiplying the Laplacian with Δx^2 in Eq. (3.1), D_m converges to $4A$ in the continuum limit. In the synchronous regime $\lim_{N\to\infty} |\hat{\mathbf{D}}f| = 0$. This means that the synchronous regime is projected onto the x-axis through this transformation, while in the incoherent regime $|\hat{\mathbf{D}}|$ is finite and exhibits pronounced fluctuations. Consequently, when we consider the normalized probability density function g of $|\hat{\mathbf{D}}f|$, $g(|\hat{\mathbf{D}}f| = 0)$ measures the relative size of spatially coherent regions in each temporal realization. For a fully synchronized system $g(|\hat{\mathbf{D}}f| = 0) = 1$, while a totally incoherent system gives a value $g(|\hat{\mathbf{D}}f| = 0) = 0$. A value between 0 and 1 of $g(|\hat{\mathbf{D}}f| = 0)$ indicates coexistence of synchrony and incoherence.

Given this discussion, two important aspects have to be considered. First, the definition of spatial coherence and incoherence is not absolute, but has to be compared to the maximal curvature in each system. Thus, we argue that the characterization of coherence and incoherence is relative and depends on the individual system. Second, even in the coherent region, there might be some minor change in state (cf. Fig. 3.1(a) above) leading to a non-zero curvature. Hence, we are convinced

that in order to characterize something as coherent or incoherent, a threshold value is inevitable, although, as will be shown later, the exact position of the threshold does not change the qualitative outcome.
Considering the two arguments above, we propose that for spatially extended systems, a point for which the absolute local curvature is less than one percent of the maximum curvature present in the system should be characterized as coherent, and as incoherent otherwise.
With the threshold $\delta = 0.01 D_m$ our first correlation measure

$$g_0(t) := \int_0^\delta g(t, |\hat{D}|) d|\hat{D}|$$

can be used to describe the spatial extent occupied by coherent oscillators, even for systems beyond coupled phase oscillators. An example of g for the Kuramoto model is shown in Fig. 3.2(a). Note that, in general, g is time dependent. Fig. 3.2(b) shows $g_0(t)$ as a function of time. The value of $g_0(t)$ of about 0.3 confirms the interpretation of the state as a chimera state, while its time-independence reveals that the degree of coherence is stationary.
For systems without a spatial dimension, i.e., systems with solely global coupling,

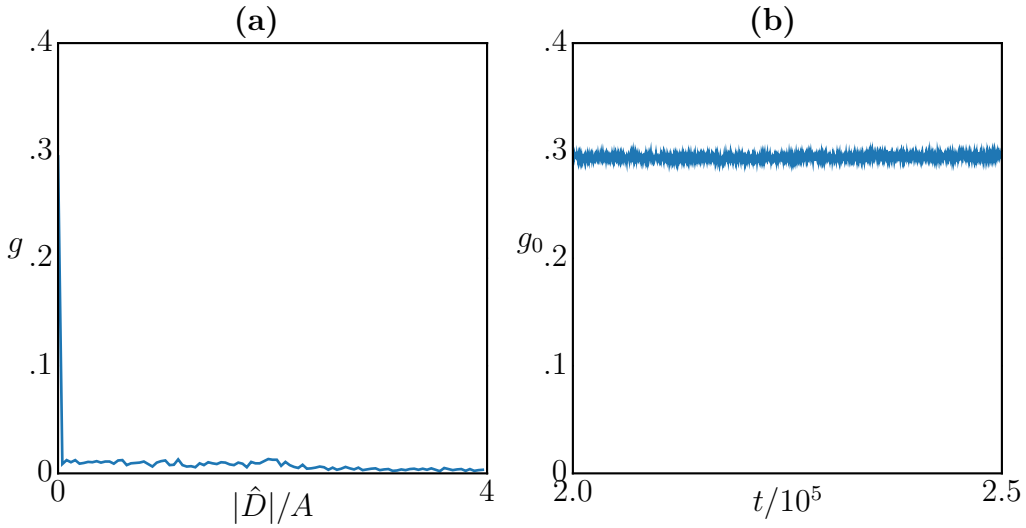

Figure 3.2: (a) Probability distribution function g of the discrete Laplace operator applied on the snapshot of Fig. 3.1(a). (b) Temporal evolution of $g_0(t)$ for a longer time series of the Kuramoto model.

curvature is not defined. Nevertheless, we argue that the pairwise Euclidean distances between the values of all oscillators, f_i,

$$\tilde{\mathbf{D}} f = \{\tilde{D}_{ij}\} = \|f_i - f_j\|, \; i \neq j,$$

are a good measure for synchrony/asynchrony. Again, from the normalized probability density function g of $\tilde{\mathbf{D}}f$, a variable

$$\tilde{g}_0(t) := \sqrt{\int_0^\delta g(t, |\tilde{\mathbf{D}}f|) d|\tilde{\mathbf{D}}f|},$$

can be obtained that is a measure for the relative amount of correlated oscillators. Here, the square root arises due to the fact that by taking all pairwise distances, the probability of oscillators i and j both being in the synchronous cluster equals $(N_0/N)^2$, with N_0 being the number of the synchronous oscillators. Since both measures, $g_0(t)$ and $\tilde{g}_0(t)$, describe the same property, that is, the degree of spatial synchronization of the system, we only use $g_0(t)$ as notation in the following.
As an illustration, consider the two groups of globally coupled phase oscillators investigated by Abrams et al [97]. The dynamics in the two-group approximation follow

$$\frac{d\theta_i^\sigma}{dt} = \omega + \sum_{\sigma'=1}^{2} \frac{K_{\sigma\sigma'}}{N_{\sigma'}} \sum_{j=1}^{N_{\sigma'}} \sin\left(\theta_j^{\sigma'} - \theta_i^\sigma - \alpha\right)$$

with the two groups $\sigma \in \{1, 2\}$ and the number of oscillators in each group N_σ, which are set to $N_1 = N_2 = 512$. The coupling-strengths $K_{\sigma\sigma'}$ are taken as $K_{11} = K_{22} = 0.675$ and $K_{12} = K_{21} = 0.325$. The phase lag $\alpha = \pi/2 - 0.1$ and the frequencies $\omega = 0$ are identical for all oscillators. Initial conditions are random phases with small variance (< 0.1) for group one and large variance ($= 2.0$) in group two. The system is integrated using a fourth-order Runge-Kutta method with a fixed time step of $dt = 0.01$.
An exemplary snapshot is depicted in Fig. 3.3(a), where oscillators $1, \ldots, N/2$ belong to group 1 and oscillators $N/2+1, \ldots, N$ constitute group 2. Clearly, group 1 is synchronous while the oscillators in group 2 behave incoherently. In the parameter region considered, a breathing of the chimera as expressed through an oscillation of the variance of the incoherent cluster was reported [97]. The temporal evolution of $g_0(t)$ is shown in Fig. 3.3(b). It can be observed that $g_0(t)$, i.e., the relative amount of partially synchronized oscillators, evolves periodically and "breathes" over time. Therefore, the temporal evolution of $g_0(t)$ allows for the discrimination between chimeras with constant and oscillating partial synchronization. We term these *stationary* and *breathing* chimeras, respectively. The latter term has been adapted from the literature, since the Kuramoto order parameter r exhibits the qualitatively same temporal behavior as g_0 [97]. Note that the two approaches above are independent of the spatial dimension and the number of variables of the different systems. This makes $g_0(t)$ a versatile tool for the classification of multifaceted data sets such as those obtained from chimera states.

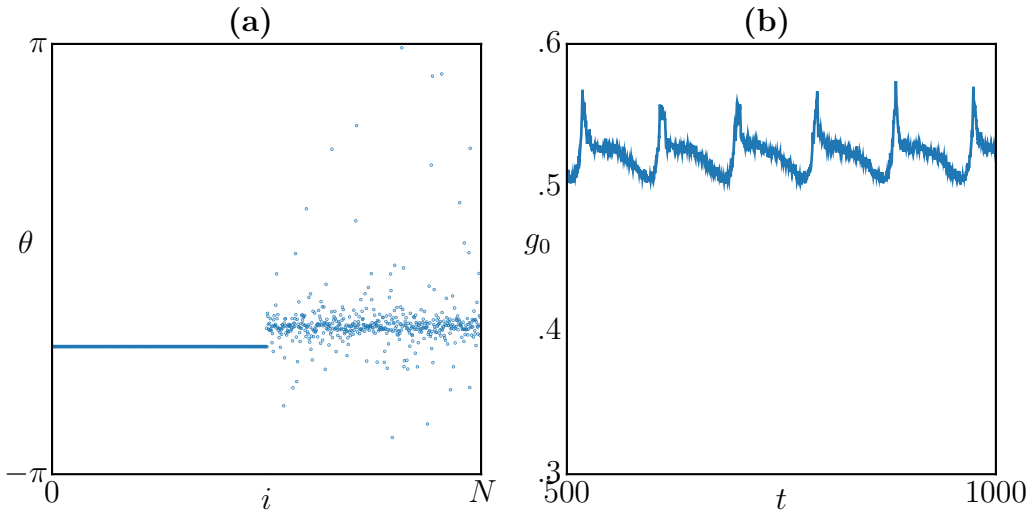

Figure 3.3: (a) Snapshot of a realization of the chimera state observed in the two-group model [97]. (b) Temporal evolution of $g_0(t)$.

3.1.2 A Measure for Correlation in Time

In addition to the measure for the spatial correlation discussed in the previous section, the temporal correlation of the individual oscillators provides valuable information for a distinction between different chimera dynamics as well. Suppose X_i and X_j are the real or complex time series of two individual oscillators with μ_i, μ_j and σ_i, σ_j their respective means and standard deviations. Then, consider the pairwise correlation coefficients

$$\rho_{ij} = \frac{\langle (X_i - \mu_i)^* (X_j - \mu_j) \rangle}{\sigma_i \sigma_j}$$

with $\langle \cdot \rangle$ indicating the temporal mean and $*$ complex conjugation. Note that $\rho_{ij} = 1$ for linearly correlated time series, $\rho_{ij} = -1$ for linearly anti-correlated time series and $|\rho_{ij}| = 1, \angle\rho_{ij} = \alpha$ for complex time series with a constant phase shift of α. That means, the normalized distribution function h of

$$\hat{\mathbf{R}} = \{|\rho_{ij}|\}, \, i \neq j$$

is a measure for the correlation in time. For static chimera states, where the coherent cluster is localized at the same position over time, $h(|\rho_{ij}| \approx 1)$ is non-zero. In practice, we consider two oscillators as correlated if $|\rho_{ij}| > 0.99 = \gamma$. As an example, consider the Kuramoto model mentioned above. Again, we map the system onto the complex plane with arbitrary constant amplitude A for all oscillators. Then, for the chimera state depicted in Fig. 3.4(a), we calculate the correlation matrix

$\hat{\mathbf{R}}$ and its probability distribution function h. The first row of $\hat{\mathbf{R}}$, $\{\rho_{0x}\}$, is shown in Fig. 3.4(b). Note that this approach maps the temporally coherent part onto 1, cf. Fig. 3.4(b). The distribution function h is depicted in Fig. 3.5(a). It exhibits

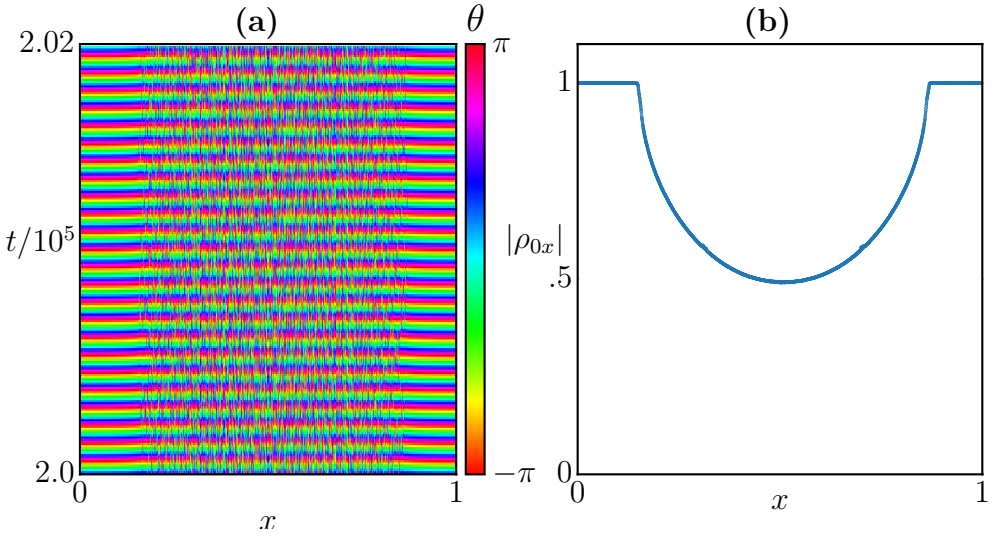

Figure 3.4: (a) Temporal evolution of the phase θ in the Kuramoto model [82]. (b) Pairwise correlation coefficients ρ_{0x} between the oscillator at $x = 0$ and the remaining oscillators.

a distinct peak at $|\rho| = 1$, indicating that the chimera state is static, i.e., that the majority of oscillators does not change its "group affiliation". We suggest to term this kind of chimera state a *static* chimera. The peak at $|\rho| \approx 0.5$ arises due to the partial linear correlation between oscillators at $x \approx 0.5$ and synchronous oscillators, cf. Fig. 3.4(b). The percentage of the time-correlated oscillators can now be quantified with

$$h_0 := \sqrt{\int_\gamma^1 h(|\rho|) d|\rho|},$$

e.g. $h_0 \approx \sqrt{0.08} \approx 0.28$ for the Kuramoto model, see Fig. 3.5(b).
Note that h_0 does not always reflect the size of the synchronized cluster. This is especially the case when coherent and incoherent regimes are non-static and perform spatial movements over time. Then, h_0 is much smaller than $g_0(t)$ and may vanish for large enough time windows. h_0 coincides with g_0, cf. Fig. 3.5(b), if and only if the chimera is static and no spatial coherence is present in the incoherent cluster.

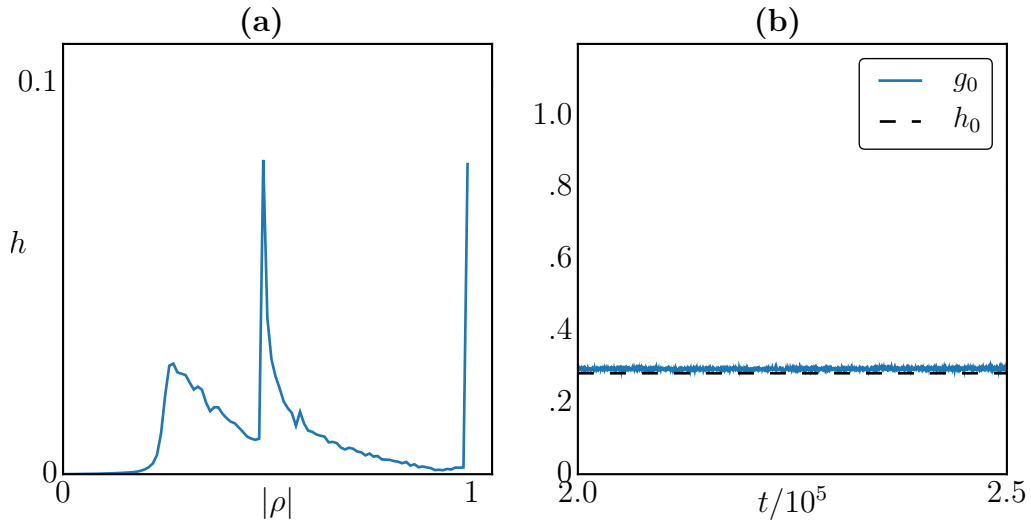

Figure 3.5: (a) Distribution function h. (b) Temporal evolution of $g_0(t)$ and the value of h_0, obtained from the same time interval. Note that h_0 is not a function of time and is shown here only for comparison with $g_0(t)$.

3.2 Examples of Chimera States and their Characterization

As shown in the previous section, $g_0(t)$ of the Kuramoto model remains constant in time and, in addition, coincides with h_0. This indicates the constant phase relation between the coherent and incoherent part and their spatial stationarity in time. The same qualitative behavior can be observed in many different non-locally coupled dynamical systems, such as in non-locally coupled Stuart-Landau oscillators investigated by Bordyugov et al. [91] and in chimera states observed by Sethia and Sen in a non-locally coupled version of the complex Ginzburg-Landau equation [95]. Sethia and Sen observed chimera states in the one-dimensional, nonlocal complex Ginzburg-Landau equation,

$$\frac{\partial W}{\partial t} = W - (1 + ic_2)\,|W|^2\,W + K\,(1 + ic_1)\left(\bar{W} - W\right),$$

with $c_1 = 0.5$, $c_2 = 2.0$, $K = 0.4$, $N = 2001$ and the spatial extension $-1 \leq x \leq 1$. The coupling $\bar{W}$ is chosen as

$$\bar{W}(x,t) = \int_{-1}^{1} G(x - x')W(x - x', t)dx'$$

with

$$G(x) = \frac{\kappa}{2\,(1 - e^{-\kappa})} e^{-\kappa|x|}$$

and $\kappa = 2$. As boundary conditions periodic boundaries are taken, and the initial conditions were taken similar to Eq. (3.3) with amplitude $A = 1$. As integrator, fourth-order Runge-Kutta with a fixed time-step of $dt = 0.01$ is used. A snapshot and the observables $g_0(t)$ and h_0 of the latter are depicted in Fig. 3.6(a) and (b), respectively. If h_0 is larger than 0, independent of the size of the regarded time

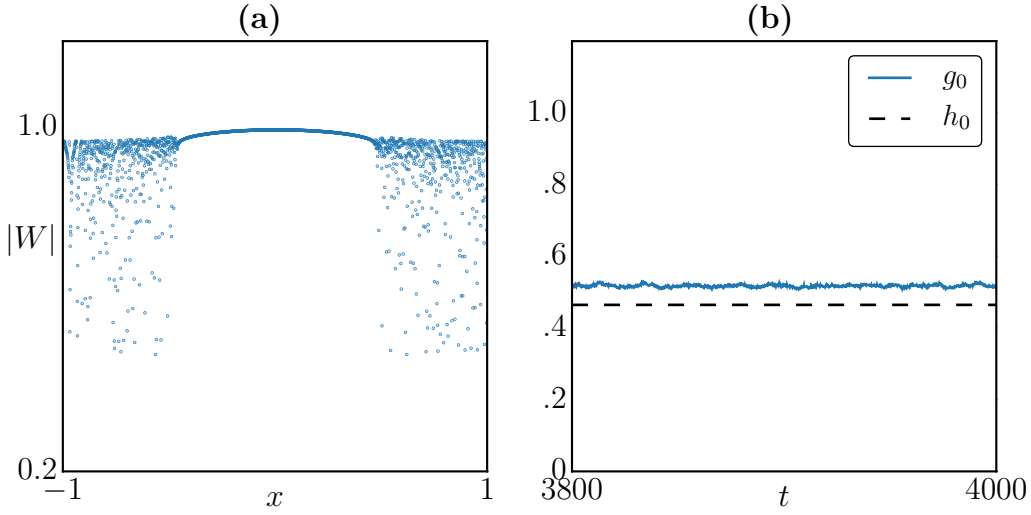

Figure 3.6: (a) Snapshot of the amplitude of the amplitude-mediated chimera [95]. (b) $g_0(t)$ and h_0 of the amplitude-mediated chimera state.

frame, then one can conclude that the chimera state is stationary in the sense that the incoherent and synchronous patches do not move. According to our definition above, this chimera state is a *static* chimera. Moreover, the finite values of $g_0(t)$ and h_0 indicate that the desynchronized dynamics are both *spatially* and *temporally* incoherent.

An example of a static chimera state not exhibiting temporal incoherence was examined by Omelchenko et al. in a system of non-locally coupled maps with a period-2 orbit [92], and subsequently experimentally realized in Ref. [93]. In particular, they used a lattice of local maps

$$\phi^{n+1} = 2\pi a I(\phi^n)$$

with $I(\phi) = (1 - \cos(\phi))/2$. The maps are coupled nonlocally, resulting in the underlying equation for ϕ on site i,

$$\phi_i^{n+1} = 2\pi a \left\{ I(\phi_1^n) + \frac{\epsilon}{2R} \sum_{j=-R}^{R} \left[I(\phi_{i+j}^n) - I(\phi_i^n) \right] \right\}.$$

Parameters are chosen as $N = 1024$, $a = 0.85$, $\epsilon = 0.4$ and $R = 420$.

As depicted in Fig. 3.7(a), the individual realizations are located on two stable

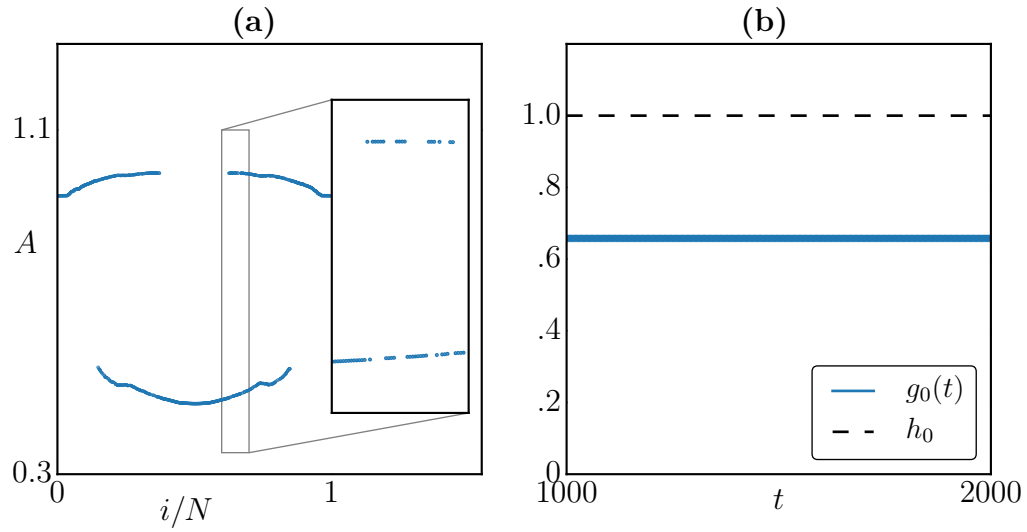

Figure 3.7: (a) Snapshot of the chimera state observed by Omelchenko et al. [92]. In the right part a magnification of the dynamics in the indicated rectangle is shown. (b) $g_0(t)$ and h_0 of the chimera state in (a). Note that h_0 does not depend on time.

branches. As evident from Fig. 3.7(b), for these chimeras $g_0(t)$ is constant and smaller than 1, while h_0 equals 1. The value of $g_0(t)$ between 0 and 1 affirms that we are dealing with a chimera state, while the fact that $h_0 = 1$ attests to the absence of any temporal incoherence.
As already mentioned in the previous section, the temporal evolution of $g_0(t)$ can be used to identify different dynamic behaviors of chimera states. Apart from being constant, $g_0(t)$ can oscillate in time for a *breathing* chimera state, as already shown in Fig. 3.3(b) for the two-groups approximation.
Another example is the so-called type II chimera, which was reported in the complex Ginzburg-Landau equation with nonlinear global coupling [54]. In particular, the equations read

$$\partial_t W = -i\nu W + (1 + ic_1)\,\nabla^2 W - (1 + i\nu)\,(\langle W\rangle - W)$$

$$+ (1 + ic_2)\left(\langle |W|^2 W\rangle - |W|^2 W\right) \tag{3.4}$$

and this system has the property that for the uniform mode,

$$\partial_t \langle W\rangle = -i\nu\langle W\rangle \;\rightarrow\; \langle W\rangle = \eta e^{-i\nu t}$$

holds. Thus, the mean $\langle W\rangle$ is confined on a circle with frequency ν and amplitude η [54]. This system shows type II chimeras for $c_1 = 0.2$, $c_2 = -0.63$, $\nu = 0.1$ and $\eta = 0.65$, with random initial conditions. As system size $L = 1000$ and $N = 4096$

grid points are taken. For integration a pseudo-spectral method with exponential time-stepping [105] and fixed time step of $dt = 0.01$ was used.

The temporal evolution of the absolute value of the complex amplitude and the

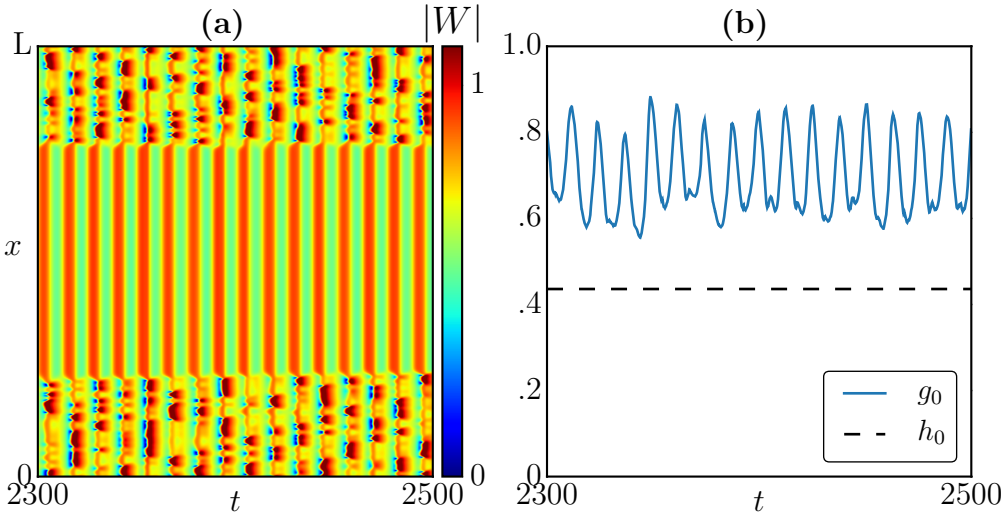

Figure 3.8: (a) Temporal evolution of the modulus of a one-dimensional simulation of the type II chimera state observed in the modified complex Ginzburg-Landau equation [54], with $L = 1000$. (b) $g_0(t)$ and h_0 calculated from the data shown in (a).

observables $g_0(t)$, together with the time independent value of h_0, are depicted in Fig. 3.8(a) and (b), respectively. In Fig. 3.8(b), the oscillatory behavior of $g_0(t)$ is evident, indicating partial synchronization also in the incoherent regime. Note that within the incoherent cluster, there are always homogeneous patches, leading to the offset between $g_0(t)$ and h_0.

Besides oscillating in time, the observable $g_0(t)$ can also vary irregularly. Such a behavior can be observed in the so-called type I chimera in the complex Ginzburg-Landau equation with linear global coupling [30], see Eq. (2.1). This system is integrated on a spatial domain of length $L = 200$ and $N = 2048$ grid points with periodic boundaries and parameters $c_1 = 1.2$, $c_2 = 1.7$, $\alpha = 0.67$ and $\beta = -0.8375$ using a pseudo-spectral integration method with exponential time-stepping [105] with $dt = 0.01$. A representative evolution of the modulus of the complex amplitude W and the corresponding measures $g_0(t)$ and h_0 are depicted in Fig. 3.9(a) and (b), respectively. Note that h_0 is significantly larger than 0, indicating that the chimera state is static. The irregularity in $g_0(t)$ arises from spatio-temporal intermittency, which appears spontaneously in the turbulent regime, leading to the emergence of patches of oscillators that are synchronous with the coherent region and shrink and disappear with time. Non-stationary chimera states with irregular phase bound-

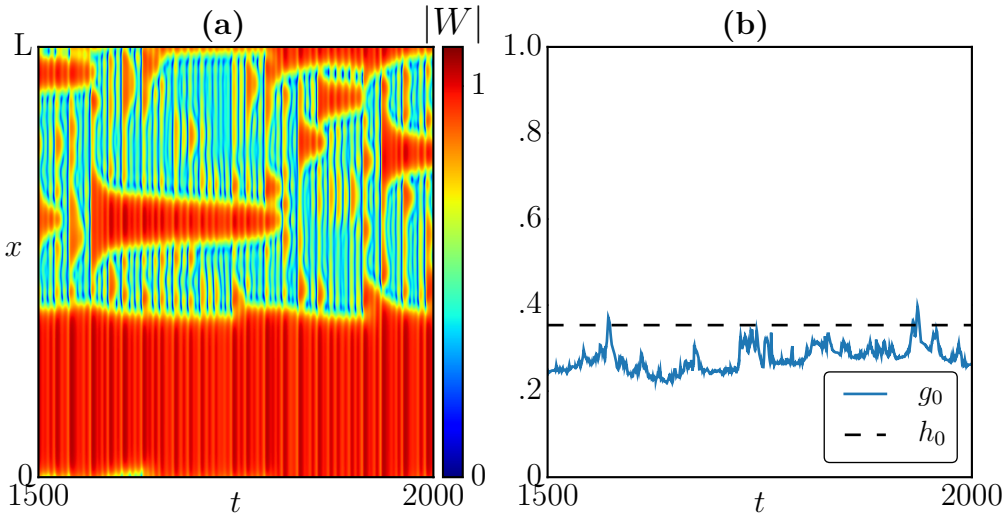

Figure 3.9: (a) Temporal evolution of the modulus of the complex amplitude of the type I chimera state observed in the CGLE with linear global coupling [30], with $L = 200$. (b) $g_0(t)$ and h_0 calculated from the data shown in (a).

aries were also reported by Bordyugov et al. [91], who named this state a *turbulent* chimera. We adapt this expression for general chimera states with irregular variation of the partial synchronization, $g_0(t)$.

Dynamics resembling the type I chimera in some aspects is the spatio-temporal intermittency as observed in the complex Ginzburg-Landau equation [106]. A realization of the spatio-temporal intermittency in the one-dimensional complex Ginzburg-Landau equation, Eq. (2.1), with $c_1 = 0$, $c_2 = -3$ and $K = 0$ is shown in Fig. 3.10(a) with fixed time step $dt = 0.01$, system size $L = 1000$ and $N = 2048$. In Fig. 3.10(b), the irregular evolution of $g_0(t)$ is apparent. However, in contrast to the type I chimera discussed above, $g_0(t)$ drops to zero at different points in time. This means that the coherent part, and with it the coexistence between synchrony and incoherence, vanishes completely from time to time. Therefore, spatio-temporal intermittency should not be considered to represent a chimera state. h_0 is also small (< 0.05), and results from the correlation of neighboring points due to diffusion.

Dynamics with reversed roles, that is turbulent patches appearing in an otherwise homogeneous regime, are found in the complex Ginzburg-Landau equation with linear [26], Eq. (2.1), and non-linear global coupling [30], Eq. 3.4, and is called localized turbulence. This dynamical state appears for $c_1 = 2$, $c_2 = -1.2$, $\alpha = 0.3$ and $\beta = 0$ in Eq. (2.1). An example is shown in Fig. 3.11, with a snapshot of the modulus of a two-dimensional simulation in (a) and the temporal evolution of a one-dimensional cut in (b). The corresponding correlation measures $g_0(t)$ and h_0, calculated from the two-dimensional spatio-temporal data with system size $L = 200$ are depicted in

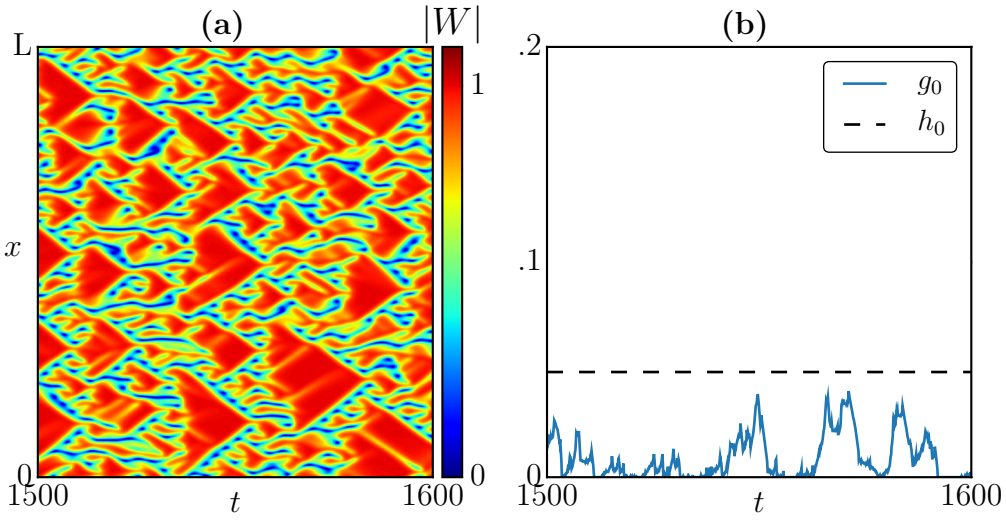

Figure 3.10: (a) Temporal evolution of the modulus of the complex amplitude of the one-dimensional complex Ginzburg-Landau equation showing spatio-temporal intermittency [106]. (b) $g_0(t)$ and h_0 calculated from the data shown in (a).

Fig. 3.12(a). The fluctuating value of $g_0(t)$ suggests that the degree of coherence changes with time. A strong increase of the synchronous part occurs at $t \approx 1350$, indicating a strong non-stationarity. However, calculations with larger system sizes suggest that the variations vanish in the thermodynamic limit $N \to \infty$. An illustration is depicted in Fig. 3.12(b), where $g_0(t)$ was calculated from two-dimensional simulations of systems with $L = 2000$.
A characteristic feature of localized turbulence, as compared to all chimera states discussed above, is that the turbulent islands are composed of several incoherent "bubble-like" structures, which move erratically in the spatial domain. Bubbles disappear or pop up through division of existing bubbles. Due to this steady motion of the turbulent islands, the fraction of the coherent time series, as measured by h_0 is small, and vanishes if the time window is chosen large enough. The same holds for the alternating chimeras observed by Haugland et al. [107], where the turbulent part alternates with the homogeneous regime in time (not shown).

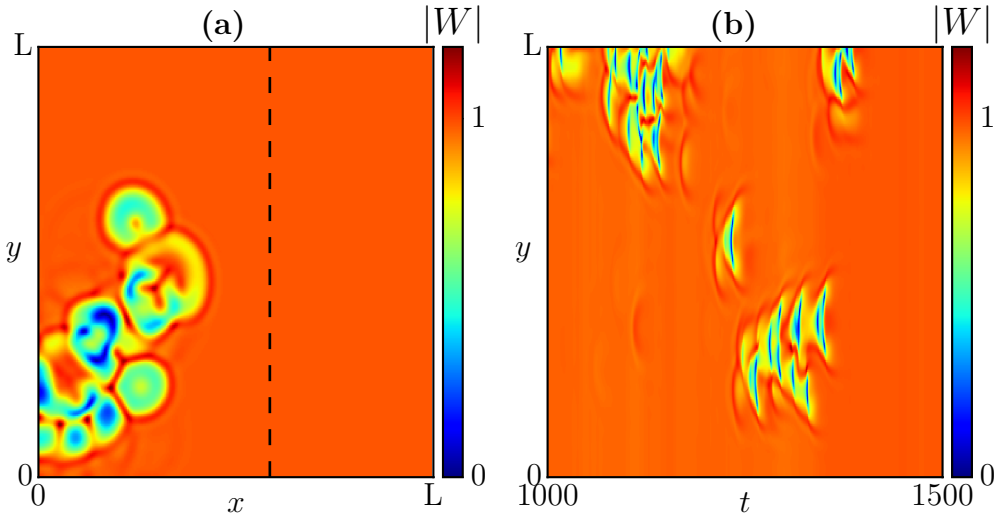

Figure 3.11: (a) Snapshot of the amplitude of the localized turbulence [26] at $t = 1500$ with $L = 200$. (b) Temporal evolution of a one-dimensional cut at the x-value indicated by the dashed line in (a).

3.2.1 Transient Chimeras

So far, we did not consider the long-term stability of the chimera states yet. However, especially in the context of chimera states, defining a stability concept is an important issue. While various chimera states, as the type I and type II chimeras mentioned above, are the only attractors for a specific parameter region, and as such are stable, many other chimera states including those of the Kuramoto model, are long-term transients with infinite transient time in the continuum limit $N \to \infty$ [101]. Then, there exist states encompassing coexistence of coherence and incoherence that collapse to the homogeneous state after a finite time even for $N \to \infty$. An example thereof is the so-called amplitude chimera [96]. The amplitude chimera states are found in a system of nonlocally coupled Stuart-Landau oscillators,

$$\dot{z}_j = \left(\lambda + i\omega - |z|^2\right) z + \frac{\sigma}{2P} \sum_{k=j-P}^{j+P} \left(\mathrm{Re} z_k - \mathrm{Re} z_j\right),$$

with $j = 1, 2, \ldots, N$, $z \in \mathbb{C}$, $\lambda = 1$, $\omega = 2$, $\sigma = 40$, $P = 60$ and $N = 3000$. Special care has to be taken when choosing the initial conditions, which is explained in more detail by Loos et al. [108]. For integration, an implicit Adams method with a fixed time step of $dt = 0.002$ is used. The space-time realization of such a state is depicted in Fig. 3.13(a), Fig. 3.13(b) showing the evolution of $g_0(t)$. Amplitude chimeras resemble the chimeras found in coupled period-2 maps (cf. Fig. 3.7) insofar as they are composed of two coherent domains with anti-phase behavior that are separated

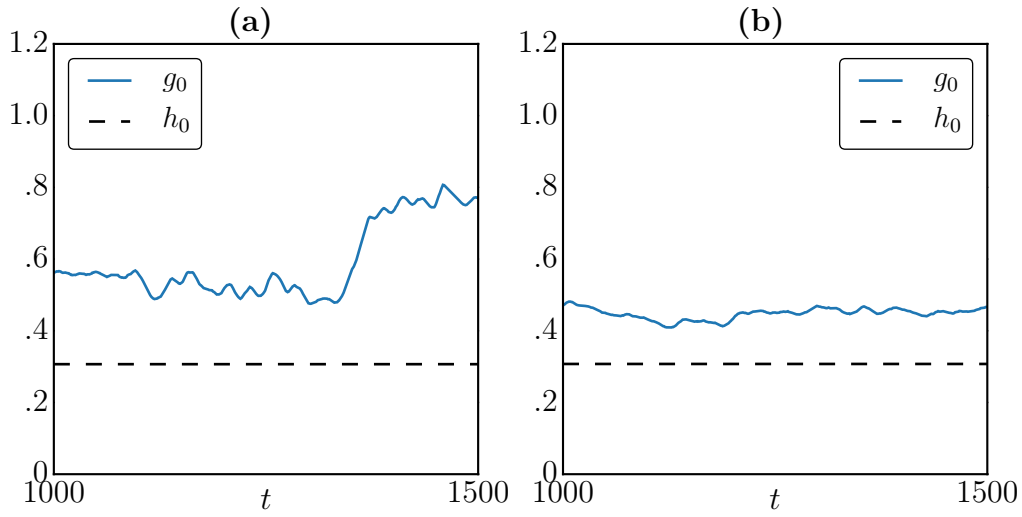

Figure 3.12: (a) $g_0(t)$ and h_0 of the localized turbulence with $L = 200$. (b) $g_0(t)$ and h_0 of the localized turbulence with domain length $L = 2000$.

by a spatially incoherent interfacial region. In the latter region, the absolute values of the amplitudes vary erratically in space but each oscillator is strictly periodic with a frequency equal to the frequency of the synchronous regions. The spatial incoherence renders $g_0(t)$ smaller than 1. However, as investigated in detail by Loos et al. [108] and also evident from Fig. 3.13, the chimera-like dynamics are not stable. A transition to full synchronization can be observed, i.e. $g_0(t) = 1$ after a finite time interval. In this case, the lifetime of the chimera state strongly depends on the choice of the initial conditions and asymptotically approaches a constant value in the continuum limit [108].
We consider it meaningful to discriminate between transient chimeras and chimera states which are attractive in the continuum limit. Therefore we suggest to introduce a separate class *transient* chimeras for states with $0 < g_0(t) < 1 \forall t < t_0$ and $g_0(t) = 1 \vee g_0(t) = 0$ at some transient time t_0.

Another remarkable case that created controversy as to its characterization as a chimera was reported by Falcke and Engel in a globally coupled version of the CO-oxidation model [109–111]. There, turbulent patches appeared in an otherwise homogeneously oscillating background, similar to the localized turbulence discussed above. But, in contrast to the behavior in the localized turbulence, no turbulent bubbles ever disappear. Details on the exact model are presented in Appendix C. A one-dimensional simulation is depicted in Fig. 3.14(a), with the corresponding measure $g_0(t)$ plotted in Fig. 3.14(b). There, the incoherent region expands into the synchronously oscillating domains with an approximately constant velocity that is strongly dependent on the diffusion coefficient D. This non-stationarity manifests

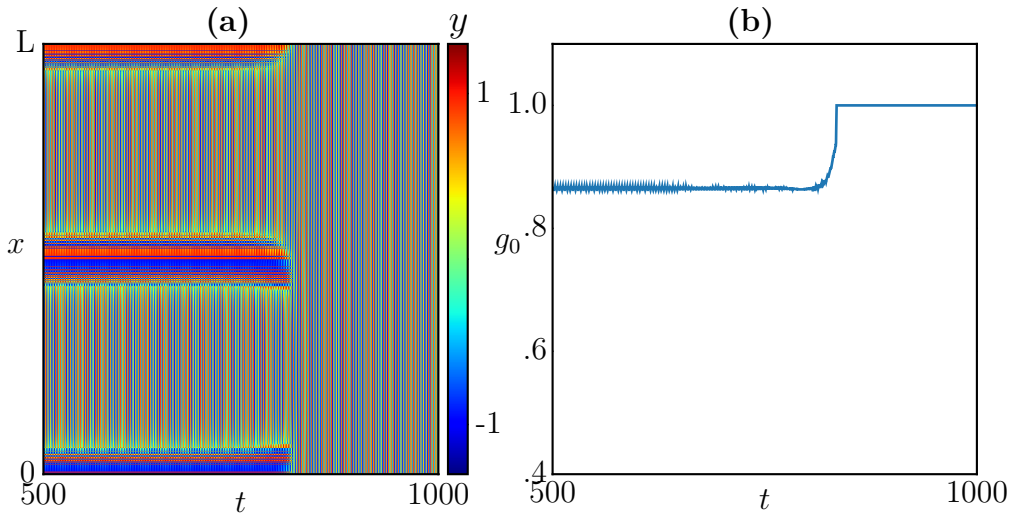

Figure 3.13: (a) Temporal evolution of the imaginary part, y, of the so-called amplitude chimera observed by Zakharova et al. [96]. (b) $g_0(t)$ of the chimera shown in (a).

itself in the overall systematically declining behavior of $g_0(t)$. In such a case a longer simulation time is necessary in order to verify that $g_0(t)$ vanishes after a finite time interval, which was confirmed for the present case. Since it mediates a transition from an unstable to a stable state, it fulfills the above defined criteria for a *transient* chimera state. We thus classify it accordingly.

3.2.2 Experimental Observation of Chimeras

Chimeras have also been observed in experimental setups [54, 93, 98]. In this section, we apply our approach to experimental data as described by Schönleber et al [112]. In this system, the thickness of a SiO_2 layer on a Si-electrode oscillates due to simultaneous electrochemical oxidation and etching. Changes of the SiO_2 thickness are measured via ellipsometric imaging. A snapshot of a measurement is depicted in Fig. 3.15(a), with the color indicating the thickness of the oxide layer. The experimental data was processed using a moving average over the last 10 time frames. The temporal evolution of a one-dimensional cut is shown in Fig. 3.15(b), where the homogeneous oscillation of a small region in an otherwise inhomogeneously oscillating background can be observed. Fig. 3.16(a) shows the pairwise correlation coefficients of the cross-section with a point inside the coherent cluster (here $y = 80$): a strong linear correlation within this cluster and the diminishing correlation with the remaining oscillators is evident. In Fig. 3.16(b), the behavior of $g_0(t)$ with time and the value of h_0 are shown. They are remarkably similar to the type II dynamics as depicted in Fig. 3.8. Hence we can conclude that the observed experimental

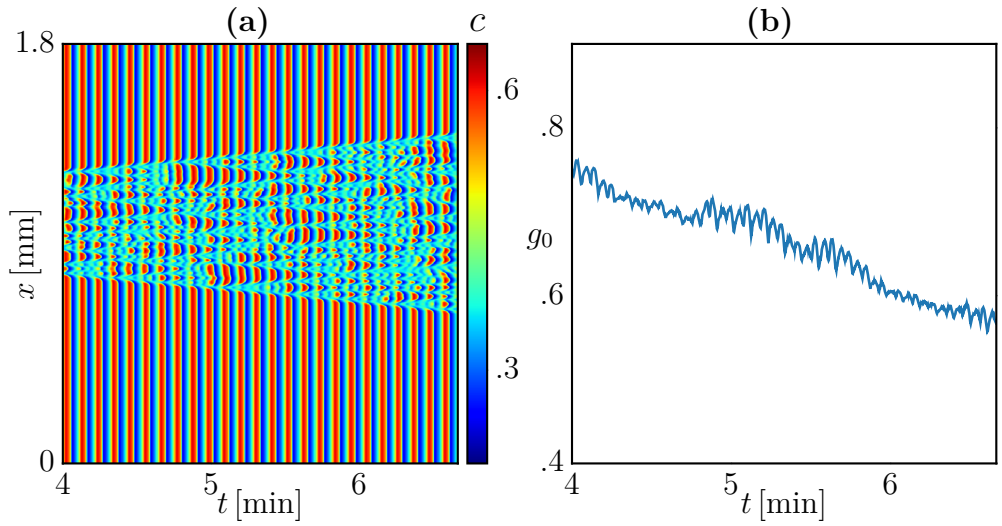

Figure 3.14: (a) Temporal evolution of the CO-coverage c. (b) $g_0(t)$ of the dynamics shown in (a).

chimera is of the *breathing* type. The smallness of h_0 originates from the fact that the coherent cluster is relatively small.

3.3 Classification Scheme

Above, we introduced two correlation measures, $g_0(t)$ and h_0, which allow a quantification of coherence and incoherence in dynamical systems. For phase oscillators, the local Kuramoto order parameter already quantifies the degree of incoherence as a function of space and time. In contrast, our global measure $g_0(t)$ yields information about the total relative sizes of the coherent and incoherent parts of the system, but does not contain information about local properties within the incoherent group. Nevertheless, it exhibits distinct qualitative types of temporal behavior for chimera states with visibly different dynamic features, and thus, like the local order parameter, can be used to discriminate between chimeras, transient chimeras and other types of dynamics. Its main advantage is its unrestricted applicability, not only to ensembles of phase oscillators, but to any type of dynamical system. Thus, $g_0(t)$ allows for a simple and straightforward classification of general chimera states.

For $g_0(t)$ equal to 0 or 1, one of the two phases, the coherent ($g_0(t) = 0$) or incoherent one ($g_0(t) = 1$), does not exist. This contradicts the requirement of "coexistence", and we argue that dynamical states where this occurs should be differentiated from chimera states. This includes spatio-temporal intermittency, the turbulent patterns in the CO model and the amplitude-chimera states. Yet, for the latter two, $0 < g_0(t) < 1$ is valid for a long time interval. Therefore, we suggest

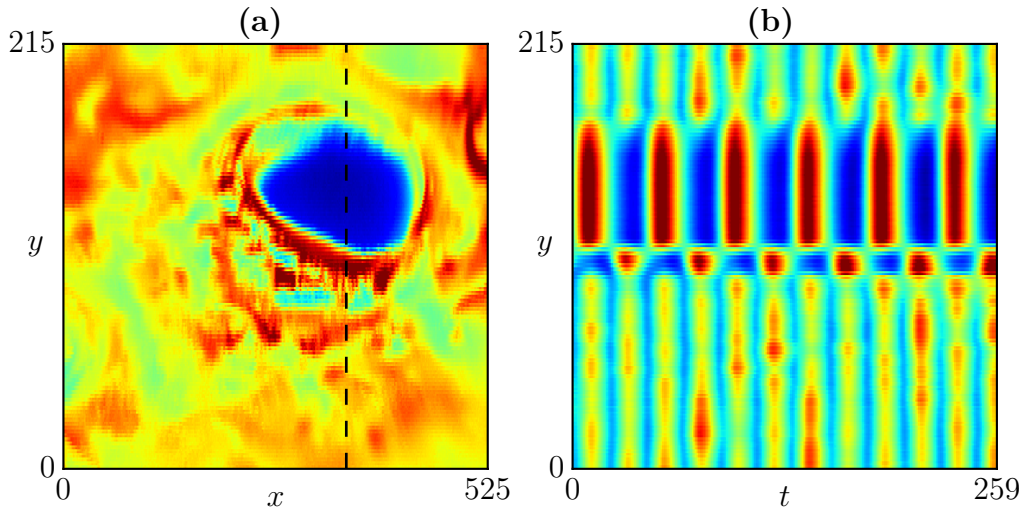

Figure 3.15: (a) Snapshot of the SiO_2 thickness on a Si-electrode in pseudo-colors. (b) Temporal evolution of a one-dimensional cut as shown in (a).

that these states are categorized as *transient* chimeras. In the case of intermittency, $g_0(t)$ fluctuates constantly, thereby attaining a value of 0 after arbitrary periods of time. It is therefore differentiated from chimera states.
Chimera states, i.e. states with $0 < g_0(t) < 1$, can then be classified into three groups:

1. **Stationary chimeras**: Chimera states with constant coherent cluster size $g_0(t)$,

2. **Turbulent chimeras**: Chimera states where the temporal evolution of $g_0(t)$ is irregular,

3. **Breathing chimeras**: States in which the behavior of $g_0(t)$ is periodic.

Note that there might be some ambiguity in the assignment to these sub-categories, since the boundaries between stationary/turbulent and turbulent/oscillatory are rather fluent.
Based on the temporal correlation measure h_0, these groups can be further divided into three subclasses:

1. *Static chimeras*, in which the coherent cluster is confined to the same position in space over time. That means, h_0 is non-zero and independent of the time window evaluated.

2. *Moving chimeras*, where h_0 vanishes if the regarded time window is taken sufficiently large.

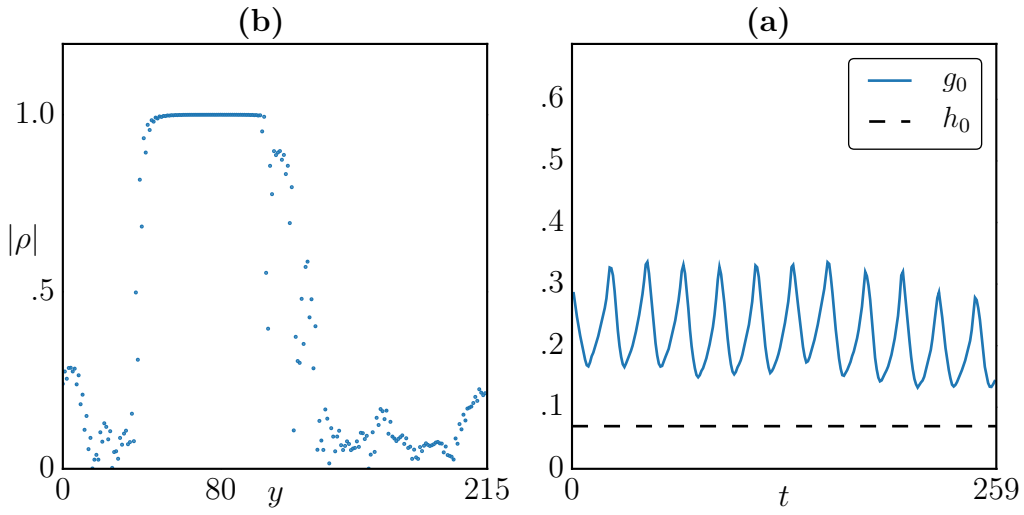

Figure 3.16: (a) Correlation coefficients for $y = 80$ for the one-dimensional cut shown in Fig. 3.15(b). (b) $g_0(t)$ and h_0 for the whole data set.

3. *Time-coherent chimeras*, that is chimera states with no temporal incoherence and thus $h_0 = 1$.

These criteria are summarized in a chimera classification scheme shown in Fig. 3.17. The examples discussed in the last two sections are assigned accordingly in the classification tree.
In conclusion, we have introduced two observables in this chapter, $g_0(t)$ and h_0, that are a measure for the degree of spatial and temporal coherence, respectively, and allow for a discrimination between different types of chimeras from simulated or experimental spatio-temporal data sets. All examples from literature considered here could be assigned to one of the classes. We verified the generality of the approach with additional examples, such as the FitzHugh-Nagumo model reported in Ref. [94] and the Rössler model discussed in Ref. [113]. Note, however, that the scheme does not distinguish between single- and multi-headed chimeras. Furthermore, it is likely that future studies will reveal additional phenomena which the method does not account for at the current stage. However, even in this case, the classification scheme should present a useful base skeleton that can be expanded as new discoveries will dictate.

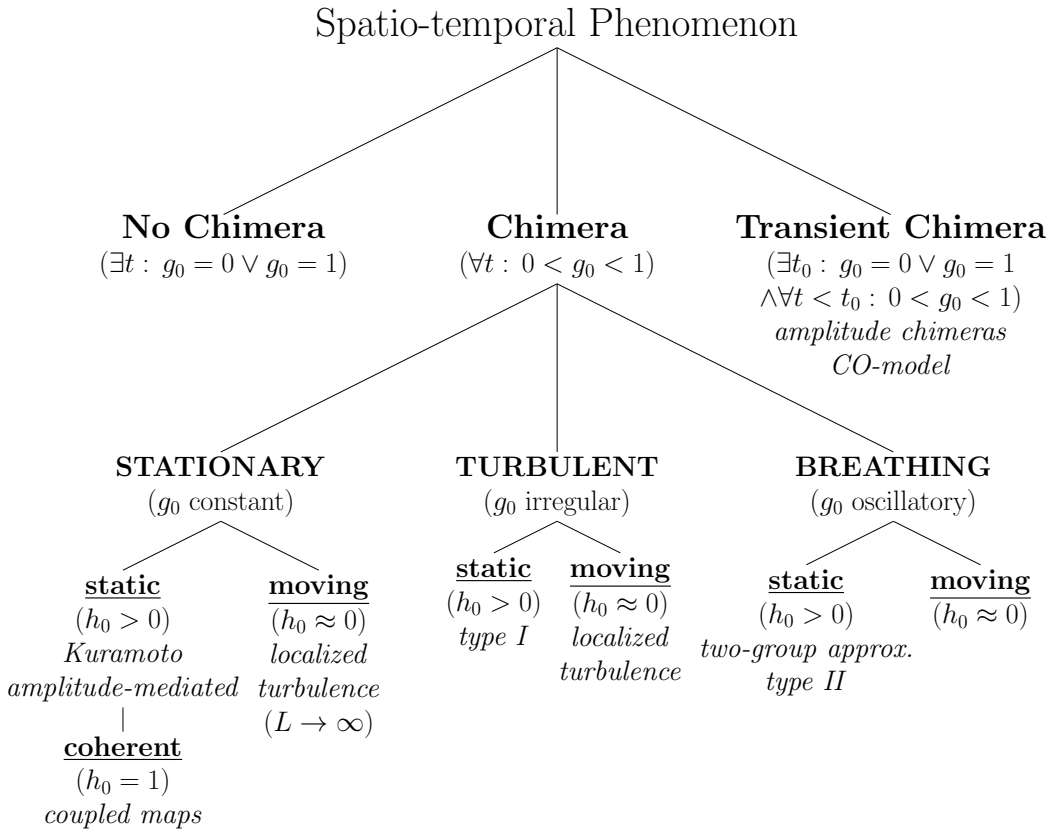

Figure 3.17: Characterization of chimera states by means of $g_0(t)$ and h_0. The different examples of chimera states discussed in this chapter are given in italics. In order to distinguish between no chimera and transient chimera, the transient time t_0 has to be much larger than the characteristic time of the uncoupled dynamics.

Chapter 4

Diffusion Maps Embedding of Complex Dynamics

In the previous chapter, we have seen how we can extract meaningful order parameters in order to classify chimera states. The definition of such order parameters were motivated by the goal to find a suitable classification of coexistence phenomena with coherent and incoherent dynamics. The discrete Laplace operator yielding the curvature at each point in space has proven to be a suitable tool.
In this chapter we discuss how one can obtain a suitable embedding of general complex dynamics using nonlinear manifold learning techniques. The goal is that one no longer has to come up with an educated guess of coarse grained variables which may be useful to embed the dynamics, but to use mathematical tools instead to find such variables, c.f. Fig. 4.1.
In recent years, many nonlinear manifold learning techniques have been proposed to embed nonlinear phenomena in a low-dimensional space. Examples include isomap [114], locally linear embedding [115] and Laplacian eigenmaps [116].
In this chapter, we use diffusion maps as the method of choice, and use it to compare and subsequently embed sets of time series obtained from a variety of qualitatively different dynamical systems. Thus, we begin this chapter with a brief introduction of diffusion maps, and illustrate the potential of this method on some intuitive examples. We then turn to complex dynamics, i.e. chaotic solutions of partial-differential equations, and discuss why the spatial coordinates form a set of suitable variables in which to embed the dynamics. Using diffusion maps, we show that the spatial coordinate in a sense emerges from the data. This directly links to the example of coupled heterogeneous neuronal oscillators, where there is no apparent space. There, we discuss how the heterogeneous parameters in the system can be used as a coarse parametrization of the dynamics. In especially, we discuss how emerging coordinates can be used to embed the dynamics in what we call an "emergent space". This emergent space, however, is not unique. Therefore, we turn to the role of the kernel scale in the diffusion maps approach, and discuss in more detail how a variation of the scale effects the embedding. Using overlapping time chunks in contrast to whole time series, we then discuss how one can use the diffusion maps embedding to

reconstruct the attracting manifold. At the end of this chapter, we conclude with a discussion of our results, and in particular, of the idea of the emergent space. For a published version of the core ideas of this chapter, see Ref. [20].

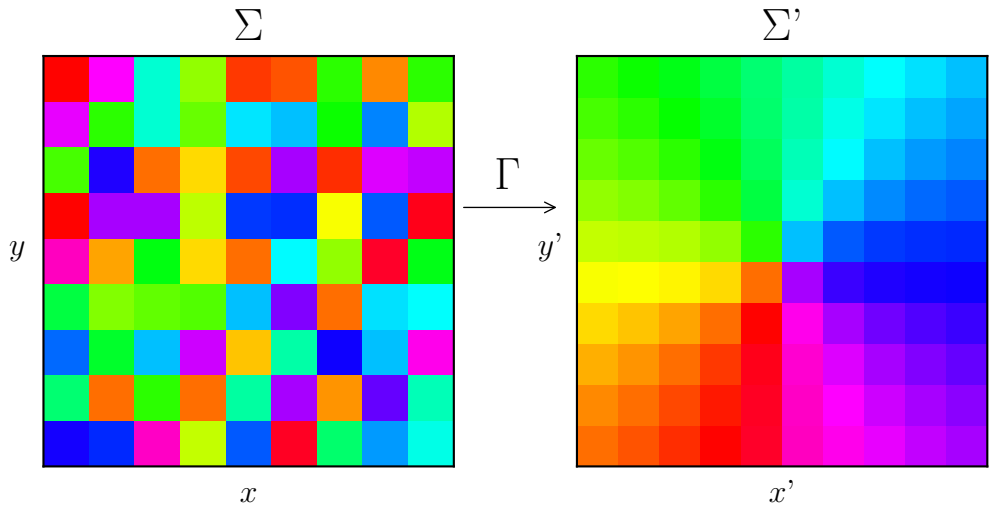

Figure 4.1: Dynamical systems may be irrgular and difficult to interprete in their original representation Σ, but may become more insightful when using suitable embeddings, for example when viewed in some space Σ'.

4.1 Diffusion Maps

In this chapter, we exploit the diffusion maps algorithm to find intrinsic variabilities contained in a data set. Suppose you have a collection of N time series $\{a_i\}$, $i = 1, \ldots, N$. Each time series a_i is a T-dimensional vector, containing the value of one or more recorded variables at T discrete points in time, with T depending on the sampling rate and regarded time window. Thus, each (time series) vector can be regarded as a point in a T-dimensional space, with all time series together forming a T-dimensional point cloud in this space. By calculating all pairwise Euclidean distances $d_{i,i'}$ between the points, the diffusion maps algorithm is able to reveal structures in the cloud [117–119]. For further analysis, it is useful to write these pairwise distances as a symmetric $N \times N$ distance matrix.
An important feature of diffusion maps is that it weights the distances between points that are close in T-dimensional space, i.e., time series which are similar, stronger than pairs of points at larger distances. This is similar to a diffusion process or random walk on the data, where the probability of jumping from point a_i to $a_{i'}$ is large if their distance is small, and vice versa. We achieve this property

by using a unimodal Gaussian kernel

$$k\left(a_i, a_{i'}\right) = e^{-\frac{\|a_i - a_{i'}\|^2}{2\epsilon}} .$$

The scale parameter ϵ is used to tune the weighting of the distances. For values of ϵ large compared to the order of the Euclidean distances, the Gaussian kernel decays very slowly. Thus, both small and large distances between points are given similar weights ≈ 1. For very small ϵ, the kernel decays very fast, and only the distances between close or similar points are significantly weighted.
Accordingly, the tuning of ϵ allows for very different representations of the same data, as described in more detail in Sec. 4.4. For convenience, we write $\epsilon = \text{const} \cdot D_{\max}$, with $D_{\max}$ being the maximal distance in the data.
By evaluating all distances with the Gaussian kernel, we obtain from the distance matrix a $N \times N$ kernel matrix $\mathbf{K}$. Row normalizing this kernel matrix yields a Markov or diffusion matrix $\mathbf{D}$ containing the probabilities for a random walk on the data, as described above. Decomposing the diffusion matrix, one obtains eigenvectors, so-called diffusion modes, which parameterize the data. Note that due to the properties of Markov matrices, the largest eigenvalue of the diffusion matrix equals one and corresponds to a constant eigenvector [120]. The eigenvectors corresponding to the other eigenvalues with absolute values closest to one can be viewed as representations of the most important structures, or variabilities, in the data.
Although we restrict our analysis using a simple Euclidean distance kernel, many extensions exist, such as vector diffusion maps [121] or diffusion maps using more refined distance metrics, e.g. the Mahalanobis distance [122]. Recent research in this direction involves a broad range of topics and applications, including intrinsic modeling [123], reduction in dynamical systems [124], multimodal data analysis [125, 126], and data organization [127], just to name a few.

As an illustrative example, we record the sunrise and sunset times at seven randomly chosen cities in Germany. We then structure our measurements as minutely time series, where each entry is either 1 if at the given minute the sun is above the horizon, while it is 0 if the sun has not yet risen or already set. In short, we have a $60 \cdot 24 \times 7$ data matrix, as shown in Fig. 4.2(a), which can be seen as a very crude exemplary measurement. The geographic locations of these arbitrary cities are shown on the map of Germany, Fig. 4.2(b). Due to their different geographic locations, it is obvious that the sunrise and sunset times are different for the individual cities. The sun rises earlier in the most eastern cities, e.g. in Berlin, and later in the western cities, as in Düsseldorf and Cologne. Also in winter the days are shorter in the northern cities, as in Hamburg and Bremen, and longer in Stuttgart in the South. Due to these facts, the geographic locations are implicitly contained in the data. However, a human might still not be able geographically locate the cities just by visually examining the time series in Fig. 4.2(a).

Diffusion maps, in contrast, are able to obtain their relative arrangement by cal-

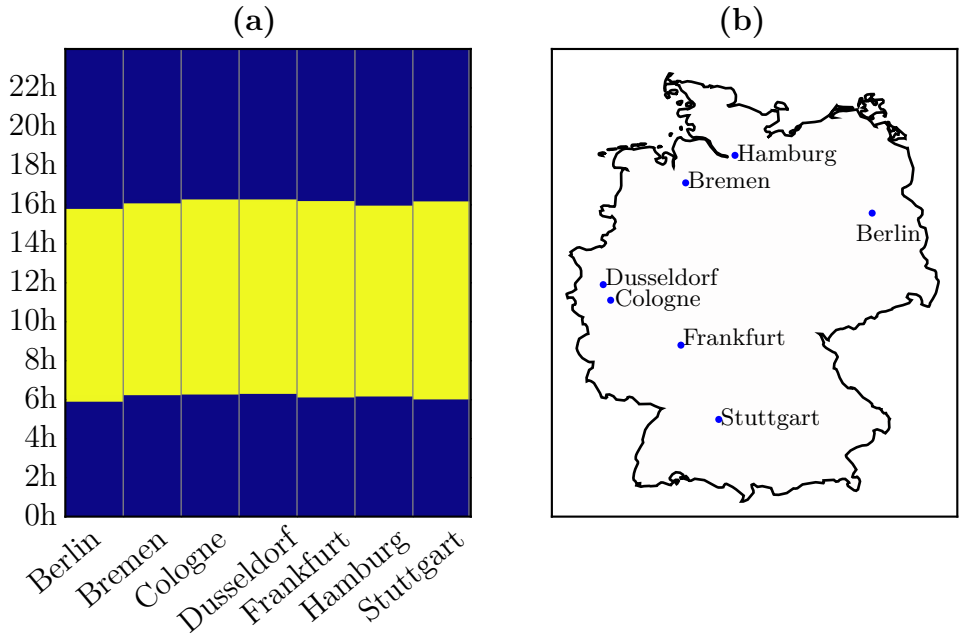

Figure 4.2: (a) Minutes of daytime, marked as 1 (yellow), and nighttime, marked as 0 (black), of seven arbitrary cities in Germany for the 27th of October 2016 in GMT [128]. (b) Map of Germany with the location of the chosen cities [129].

culating the distances between the Boolean vectors. Cities which are close to each other on the map have similar sunrise and sunset times compared to cities far away. Hence, by calculating and decomposing the diffusion matrix, as described above, one obtains eigenvectors that parameterize their relative arrangement. This is visually verified in Fig. 4.3, where the space spanned by the two modes ϕ_1 and ϕ_2 shows a one-to-one correspondence with the geographic positions of the cities, that is, their respective longitudinal and latitudinal degrees. Note that the modes following ϕ_2 are just harmonics of ϕ_1 and ϕ_2. That means diffusion maps also find that the cities are arranged on a two-dimensional manifold.
We conclude that the physical west-east and north-south locations can be viewed as variabilities inherent in the data. These variabilities lead to different time series of the individual points. Due to these differences, diffusion maps are able to find the number and directions of these variabilities. However, it is worth mentioning that the algorithm is able to find the right relative arrangement, but not the actual positions of the cities.
The idea of finding variabilities in the data can be generalized to systems such as partial differential equations and networks, where information on the location in physical space or the location in parameter space is implicitly contained in some temporal observation of these systems.

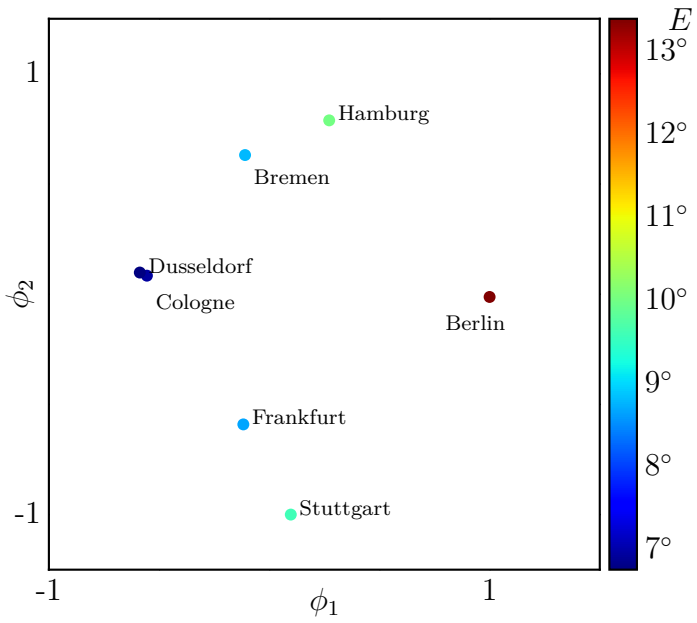

Figure 4.3: The first two independent diffusion modes, ϕ_1 and ϕ_2 for $\epsilon = e^{10} \approx 3.0 \cdot 10^3 D_{\max}$ of the data shown in Fig. 4.2(a), colored with their longitudinal geographic position. By comparing with the actual locations in Fig. 4.2(b), it becomes obvious that ϕ_1 and ϕ_2 span a space in which the mutual arrangements of the cities reflect their actual positions. Additionally, due to the correspondence between the coloring and ϕ_1, one can visually verify that ϕ_1 parameterizes the west-east direction.

4.2 Recovering Space from Spatiotemporal Data

As discussed above, the idea of finding the variabilities in the data can be generalized to systems such as partial differential equations and networks. In this section, we start by investigating a spatiotemporal chaotic phenomenon in a system with one spatial dimension. In particular, we consider spatiotemporal intermittency, see also Fig. 3.10, in the complex Ginzburg-Landau equation, a general reaction-diffusion equation for oscillatory systems with a spatial extension [31, 106, 130], c.f. Eq. 2.1 with $\alpha = \beta = 0$. Characteristic for these chaotic dynamics is the repeated appearance of synchronous patches at seemingly random places in space and time. Following their emergence, these patches shrink with a constant rate due to diffusion, giving rise to triangular patterns, see Fig. 4.4(a) for simulation data with zero-flux boundaries. Note that due to the incoherent nature of the dynamics, the individual time series of a discretized version of this dynamical system are mutually different. Nevertheless, due to the diffusion in the system, trajectories located close

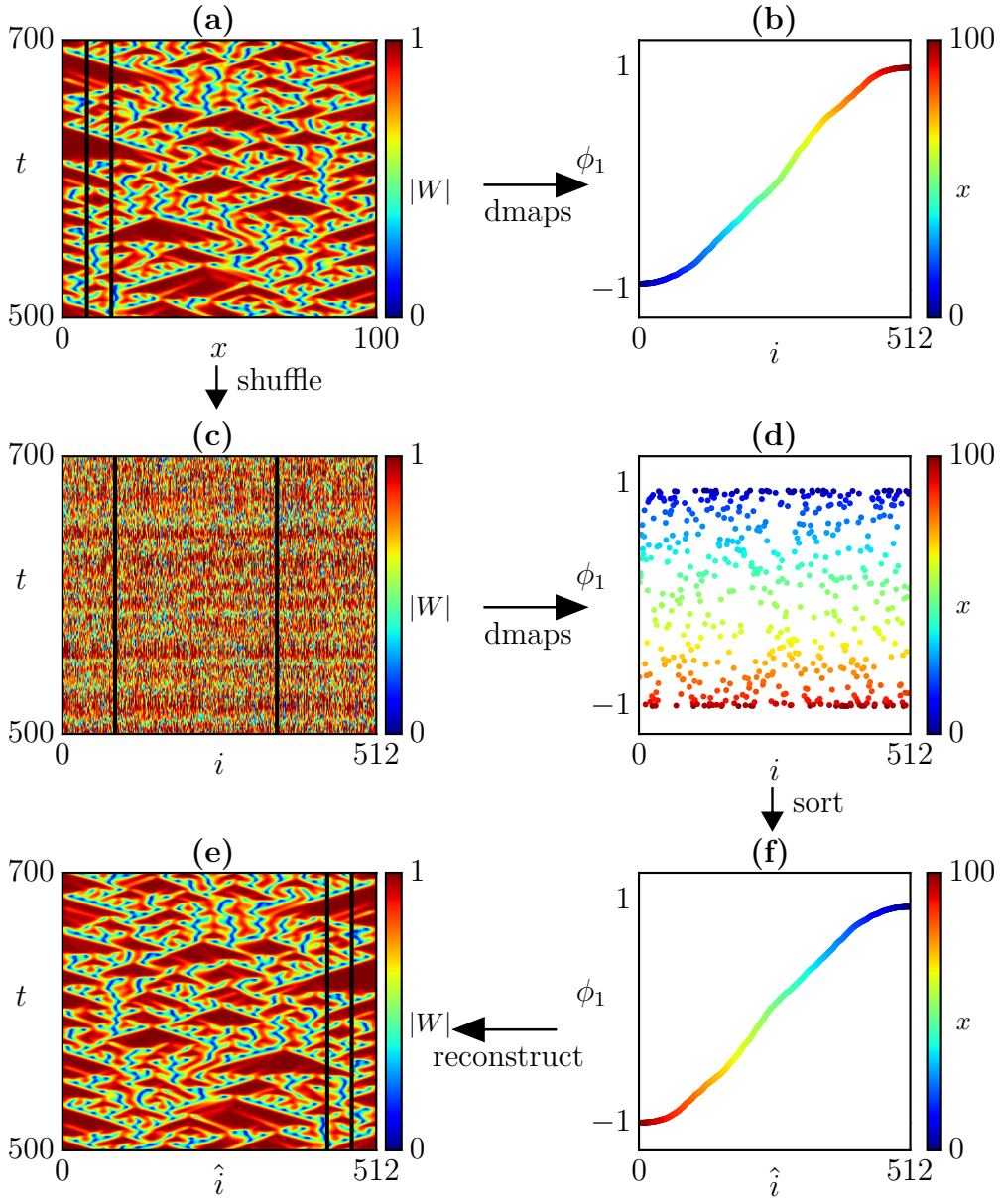

Figure 4.4: Left: Data of spatiotemporal intermittency. Right: First diffusion mode or the spatiotemporal data shown on the left. For details, see text.

to each other in space tend to be similar. This fact can be exploited in the diffusion maps approach, where the Euclidean distance between neighboring time series is expected to be small compared to the distances between time series separated by a larger distance in physical space.
By calculating the diffusion matrix, it can be shown that the first diffusion mode ϕ_1 correlates with the spatial dimension x: each entry of ϕ_1 corresponds to a particular time series, and if any one entry is large, the corresponding time series is located at large x, while for small entries, the trajectories are located towards the left end of the spatial axis, see Fig. 4.4(b).
Note that here, the kernel scale $\epsilon \approx 0.024 D_{\max}$ is chosen very small, such that only a few nearest neighbors are considered in the diffusion maps approach. Moreover, by investigating not only the first but also the following diffusion modes, one finds that ϕ_1 is the only independent direction, indicating that there exists only one spatial dimension in the system. This enables us to actually find the spatial order of the data set, as can be shown by shuffling the individual time series, c.f. Fig 4.4(c), before calculating the diffusion modes of the system. The first and only independent direction is then found to be nonmonotonic, as shown in Fig. 4.4(d). However, by sorting the entries of the diffusion mode in increasing order and then applying this arrangement to the corresponding time series, the spatial arrangement is recovered, see Fig. 4.4(e-f). Thus, we argue that the physical space is an intrinsic variability in this system. Nevertheless, the diffusion maps outcome is not unique. Due to the symmetry of the approach, the diffusion mode can either correspond to x or to $-x$. That is, it either parametrizes the left-to-right direction or vice versa. This can be observed in Fig. 4.4(f), where the sorted eigenvector ϕ_1 correlates with $-x$, and thus sorts the data in a mirrored way. Comparing the pictures 4.4(a) and (e), we observe that they correspond except of a left-right flip along the x-axis.

The approach above is not restricted to data with only one spatial axis. It is also applicable to data with periodic boundaries, that is, to systems located on a ring, and to systems with two spatial dimensions. For spatiotemporal intermittency in the complex Ginzburg-Landau equation with one spatial dimension and periodic boundary conditions, one finds that the first two diffusion modes span a circle. Shuffling, applying diffusion maps, and sorting the shuffled data along that circle, one obtains data that is, except for a rotation and/or reflection, equivalent to the original data. Note that the dynamics are not only incoherent in space, but also in time. Hence, the individual snapshots are, as the time series, mutually different. By comparing the snapshots instead of the time series, one can show that the time is also a heterogeneity in the system (not shown here). Furthermore, it is not surprising that by taking spatiotemporal patches, one can arrange them on a two dimensional plane, spanned by the variabilities space and time.
For a system with two spatial axes x and y, the data of spatiotemporal intermittency obtained with zero-flux boundaries is depicted in Fig. 4.5(a). By calculating the distances between the time trajectories and using the diffusion maps approach,

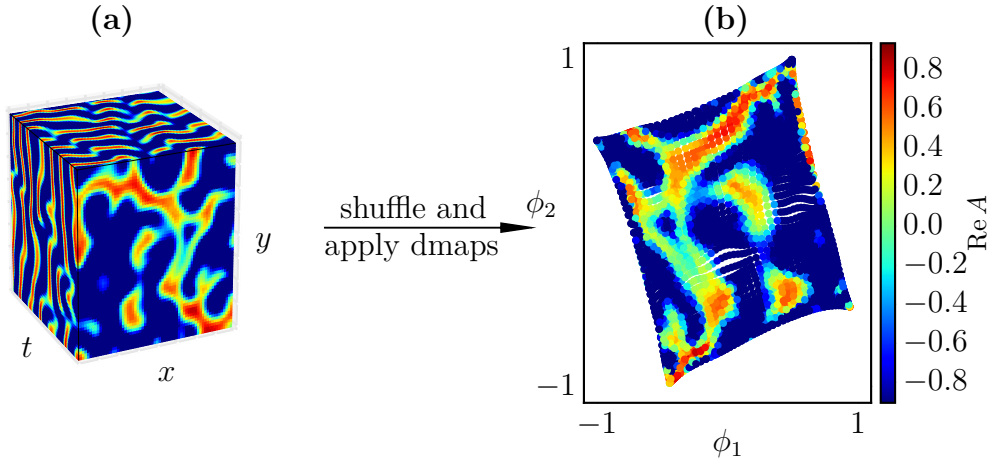

Figure 4.5: (a) Spatiotemporal data obtained from numerical simulations of the complex Ginzburg-Landau equation with two spatial dimensions. The data is colored with the real part of the complex amplitude W. (b) The first two independent diffusion modes ϕ_1 and ϕ_2, colored as in (a).

one finds two independent modes ϕ_1 and ϕ_2. When coloring these modes with W, one finds that the two modes indeed span a space that is one-to-one with the original physical space, as visually verified in Fig 4.5(b). Note that the ϕ_is contain $N_x \cdot N_y$ entries, that is, time series, with N_x and N_y being the respective number of grid points in the x- and y-direction, respectively. Therefore, when calculating the distances between the time series, we lose the spatial information inherent in the system. Nevertheless, due to the similarity of nearby time series, diffusion maps find that these are parametrized by two dimensions, and recover their actual two-dimensional order.

4.3 Recovering parameter space

In contrast to the complex Ginzburg-Landau equation and other reaction-diffusion systems, there are systems of oscillators that do not posses a spatial arrangement. Examples are globally coupled systems or networks with random connections. In this section we investigate a neural network, where each node of the network is modeled as a neuron from the pre-Bötzinger complex [131–133]. Each node of this network can be modeled using two variables, the potential V and the channel variable h,

$$\begin{aligned} C\frac{dV_i}{dt} &= -g_{\mathrm{Na}} m\left(V_i\right) h_i \left(V_i - V_{\mathrm{Na}}\right) - g_l \left(V_i - V_l\right) + I^i_{\mathrm{syn}} + I^i_{\mathrm{app}} \\ \frac{dh_i}{dt} &= \frac{h_\infty\left(V_i\right) - h_i}{\tau\left(V_i\right)}. \end{aligned}$$

with the coupling

$$I^i_{\text{syn}} = \frac{g_{\text{syn}}\left(V_{\text{syn}} - V_i\right)}{N} \sum_{j=1}^{N} A_{ij} s\left(V_j\right).$$

Here

$$\begin{aligned} m\left(V\right) &= \left(1 + \exp\left(-\left(V + 37\right)/6\right)\right)^{-1}, \\ h_\infty\left(V\right) &= \left(1 + \exp\left(\left(V + 44\right)/6\right)\right)^{-1}, \\ \tau\left(V\right) &= \left(\epsilon \cosh\left(\left(V + 40\right)/5\right)\right)^{-1}, \\ s\left(V\right) &= \left(1 + \exp\left(-\left(V + 40\right)/5\right)\right)^{-1} \end{aligned}$$

are nonlinear functions, whereas $C = 0.21$, $g_{Na} = 2.8$, $g_l = 2.4$, $g_{\text{syn}} = 0.3$, $V_{\text{syn}} = 0$, $V_{\text{Na}} = 50$, $V_l = -65$ and $\epsilon = 0.1$ are constants. As in previous studies [133], we take the intrinsic kinetic parameter I^i_{app} to vary across the ensemble ($I^i_{app} = 22 + 2\omega_i$, where ω_i is drawn from a uniform distribution on $[-1, 1]$), making the network kinetically heterogeneous.
We connect the neurons in the form of a Chung-Lu type network [134], where the network topology is given by a symmetric adjacency matrix $\mathbf{A}$. The entries A_{ij} are 1 if there is a coupling between oscillators i and j, and 0 otherwise. The algorithm for the creation of the A_{ij} uses a sequence of weights w_i for each oscillator i, defined as

$$w_i = pN(i/N)^r \quad , \quad i = 1, 2, ..., N \tag{4.1}$$

with parameters $p = 0.80$ and $r = 0.40$. From these weights, the entries P_{ij} of a matrix $\mathbf{P}$ of connection probabilities are defined as

$$P_{ij} = P_{ji} = \min\left(\frac{w_i w_j}{\sum_k w_k}, 1\right). \tag{4.2}$$

The matrix is then mirrored along the diagonal, and all diagonal entries are set to zero to avoid self-loops. As initial conditions, $V = -60.0$ and $h = 0.0$ are taken for all oscillators. We simulated our realization of a Chung-Lu network of $N = 1024$ oscillators, using lsode [135, 136]. The time series observations from each neuron were taken between $t_0 = 20$ and $t_1 = 40$ in the form of $T = 2001$ time steps. In particular, these Hodgkin-Huxley-type neurons oscillate periodically. The number of connections to a neuron i is the degree κ_i, which varies strongly between the neurons. That is, κ_i is another, structural heterogeneous parameter. The temporal evolution of a network of 1024 neurons is depicted in Fig. 4.6. There, one observes that the neurons oscillate clustered in the (V, h) plane, but with somewhat different phases and amplitudes. Due to the variabilities, their instantaneous values differ. Nevertheless, it has been shown that the dynamics of all neurons can be described as a smooth function of two the heterogeneous parameters I^i_{app} and κ_i [133]. This

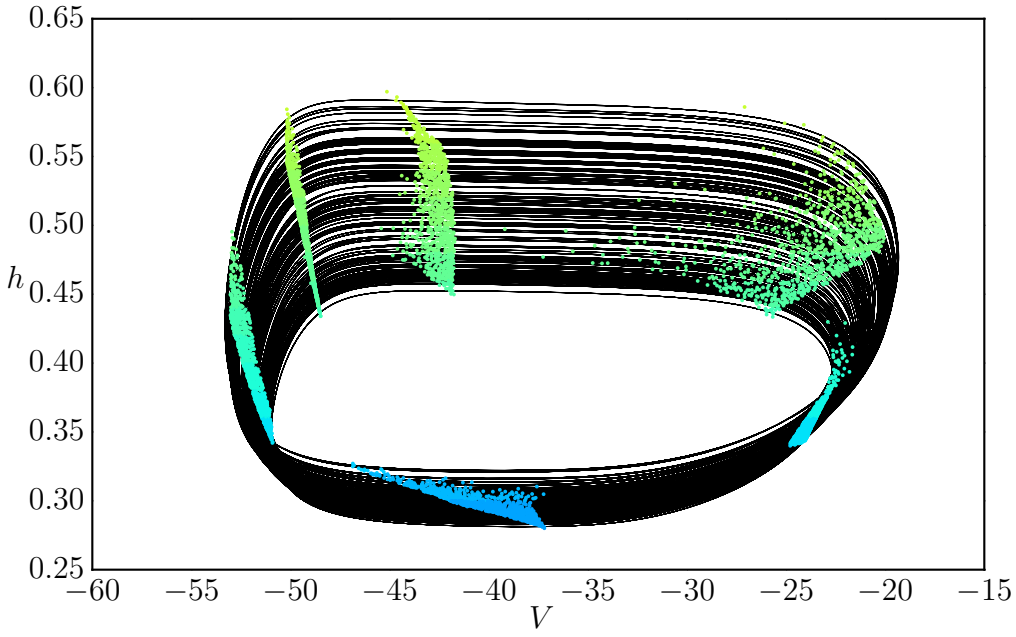

Figure 4.6: Temporal evolution of the two variables h and V of the individual oscillators in the Chung-Lu type network of pre-Bötzinger neurons.

is indicated by the color-code in Figs. 4.7(a) and (b). Note that there is a strong dependence of the dynamics on the intrinsic parameter I^i_{app}, whereas the dependence on the degree κ_i is rather week.

The parameter dependence in the network can also be recovered using diffusion maps. Calculating the pairwise distances between the time series and extracting the diffusion modes, yields that the first two diffusion modes parametrize a two-dimensional manifold. Hereby, $\epsilon = e^{10} \approx 93 D_{\max}$ was chosen large compared to the maximal distance in the data. By coloring the two diffusion modes with the heterogeneous parameter I^i_{app}, one observes a one-to-one correspondence between this parameter and the first mode, as depicted in Fig. 4.8(a). The second direction, perpendicular to the first mode, correlates with the degree κ_i, see Fig. 4.8(b). Note that the first few modes following ϕ_2 are harmonics, indicating that there are only two major directions that parametrize the dynamics. Comparing these results with the outcome from Sec. 4.2, an analogy between the two parameters in the heterogeneous neural network and the spatial axes in the reaction-diffusion system becomes apparent. It is worth mentioning that the diffusion maps approach enables us, even without knowing the spatial dimensions or the heterogeneous parameters in our system, to extract the dominant variabilities on which the dynamics depend.

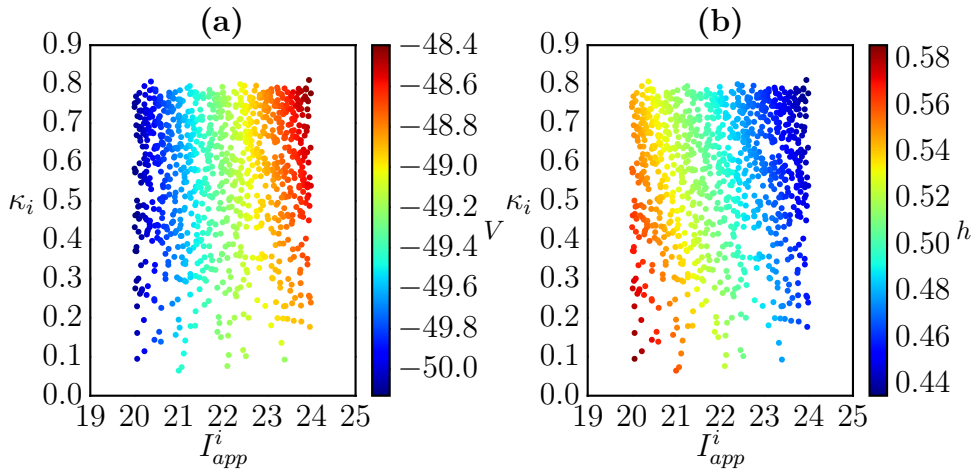

Figure 4.7: (a) Each oscillator as a function of the two heterogeneous parameters κ_i and I^i_{app}, colored with the voltages V at $t_0 = 20$. (b) Each oscillator as in (a), but colored with the variable h of the snapshot depicted in (a).

4.4 Tuning the scale parameter ϵ

In the example of the spatiotemporal chaos and the heterogeneous neural network, we used a specific choice of the kernel scale ϵ. In order to recover the spatial arrangement, we had to choose it very small, thereby considering only the nearest neighbors, that is, only very similar time series. In the case of the network, however, a larger ϵ revealed the dominant variabilities.
In this section, we vary ϵ in order to extract different features of our data. For a more thorough discussion of suitable choices for the kernel scale, see Ref. [137]. There, besides existing methods to chose appropriate scales [138–140], a new method based on the maximal edge weight in a reduced graph structure is discussed.
As a model example, we investigate a chimera state, that is, a dynamical hybrid state of coexisting coherence and incoherence [12, 19, 82, 103], see also Chapter 3. An example of such a state can be observed in the globally coupled version of the complex Ginzburg-Landau equation, Eq. 3.4. A simulation with one spatial dimension and $c_1 = 0.2$, $c_2 = -0.63$, $\nu = 0.1$ and $\eta = 0.65$ is depicted in Fig. 4.9(a). Note that here we take periodic boundaries, so that the spatial axis is in fact a ring. This chimera state, also called type II chimera, has an underlying two-cluster state, in which one of the two clusters develops incoherent dynamics while the other cluster remains synchronized [102]. By choosing the kernel scale $\epsilon = e^{-2.5} \approx 1.7 \cdot 10^{-3} D_{\max}$ very small compared to the maximal distance contained in the data, that is, again considering only very similar time series, we are able to reconstruct the spatial arrangement, as depicted in Fig. 4.9(b). Note that due to the periodicity of the spatial axis x, two diffusion modes are needed to embed the data. Furthermore, it is worth

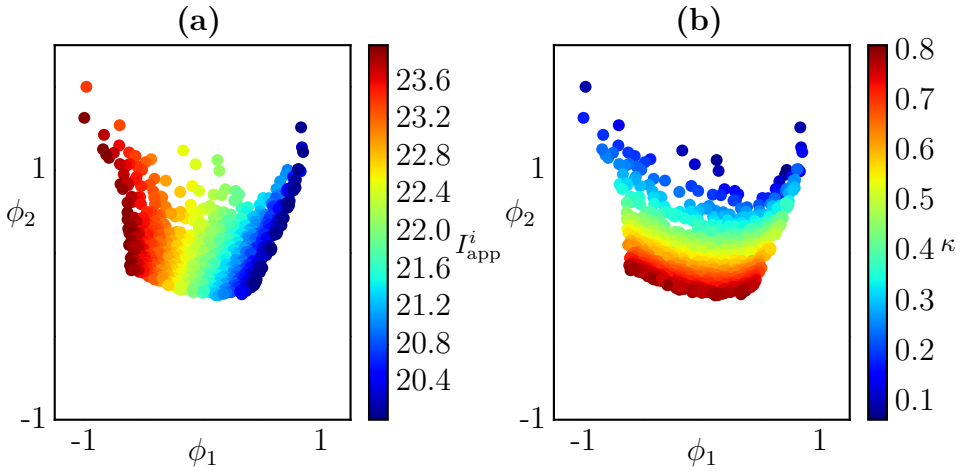

Figure 4.8: (a) The two independent diffusion modes ϕ_1 and ϕ_2, colored by applied heterogeneous current I^i_{app}. (b) The two diffusion modes ϕ_1 and ϕ_2 as in (a), colored by degree κ_i. Hereby, ϵ is taken as $\epsilon = e^{10} \approx 93 D_{\max}$

mentioning that the approach maps the coherent oscillations, which are, due to their synchrony, very similar, onto a very concentrated cluster in diffusion space. Nevertheless, by zooming in on this cluster, we find that the two diffusion modes are still able to differentiate between the synchronous series, see inset of Fig 4.9(b). This is possible since the diffusion in the system still preserves a slight drift in the coherent cluster and therefore allows for a discrimination of the coherent time series.
Tuning the scale parameter in the diffusion kernel alters the decay rate of the Gaussian function, practically allowing for the specification of how many 'similar' time series shall be considered by the diffusion maps algorithm. When using a very large ϵ, one therefore obtains a rather coarse description of the data.

For the network of preBötzinger neurons, a rather large ϵ revealed the heterogeneous parameters I^i_{app} and κ_i in the system. This can be explained by the fact that the heterogeneous parameters influence the overall coarse dynamics, but, in contrast to the spatiotemporal intermittency, points with similar variabilities are not necessarily similar in the sense that their mutual Euclidean distances are small, but rather their distances to all other points are similar. They have, so to say, similar coarse behavior. Thus, we in general expect to obtain the coarse variabilities in our data in the first diffusion modes for larger values of ϵ. In particular, we expect the most prominent coarse heterogeneity to be contained in the first independent diffusion mode. For the chimera state depicted in Fig. 4.9(a), the first eigenvectors for $\epsilon = e^{-2.5} \approx 1.7 \cdot 10^{-3} D_{\max}$ and $\epsilon = e^{7} \approx 22.5 D_{\max}$ are shown in Fig 4.9(d). Note that for large ϵ, ϕ_1 possesses approximately the same value in the whole coherent region and in the whole incoherent region, respectively, with a continuous connection linking the two plateaus due the diffusion boundary between them. Due to the choice

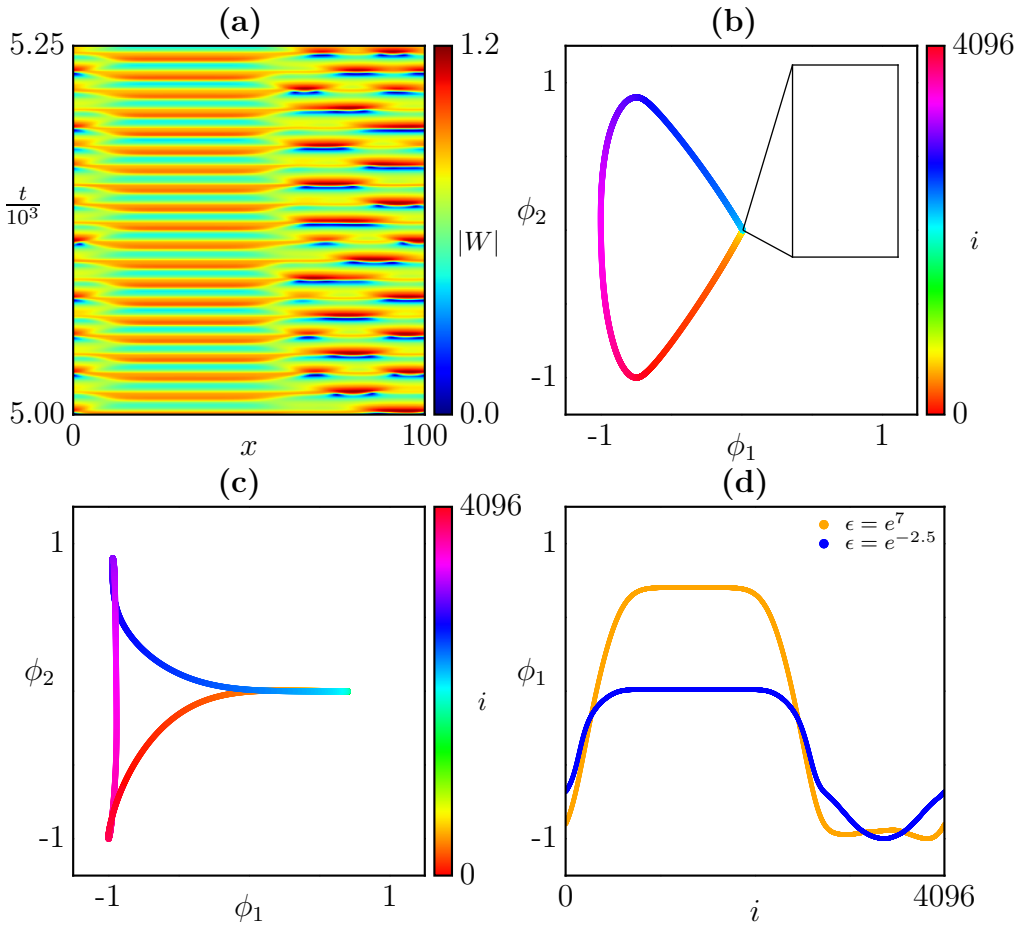

Figure 4.9: (a) Temporal evolution of the type II chimera state in a globally coupled version of the complex Ginzburg-Landau equation with one spatial dimension x and periodic boundary conditions. The pseudo-color corresponds to the modulus of the complex amplitude W. (b) The first two independent diffusion modes ϕ_1 and ϕ_2 for $\epsilon = e^{-2.5} \approx 1.7 \cdot 10^{-3} D_{\max}$, colored with the position i along the spatial coordinate x. (c) The first two independent diffusion modes ϕ_1 and ϕ_2 for $\epsilon = e^{7} \approx 22.5 D_{\max}$, colored with the position i along the spatial coordinate x. (d) First independent diffusion mode ϕ_1 for $\epsilon = e^{-2.5} \approx 1.7 \cdot 10^{-3} D_{\max}$ and $\epsilon = e^{7} \approx 22.5 D_{\max}$.

of ϵ, it contains the dominant heterogeneity of the data at a very coarse degree, yielding a one-dimensional coarse-grained description of the time series. In short, ϕ_1 seems to be clustered in the coherent and the incoherent region, respectively. This is in accordance with earlier studies, which have shown that the dynamics of the type-II chimera state are based on a modulated amplitude two-cluster state [30, 102]. Note that, like in the example of the preBötzinger neurons, the Euclidean distances between points with similar ϕ_1 are not necessarily small. In general, we argue that points being neighbors in ϕ_1 means that they share the same behavior. In this case, they correspond to the same underlying cluster. Furthermore, it is worth mentioning that for large ϵ diffusion maps no longer consider the physical space to be the dominant heterogeneity in the system. This becomes evident in Fig. 4.9(c), where the first two diffusion modes for $\epsilon = e^7 \approx 22.5 D_{\max}$ are plotted. These modes no longer form a circle, but have multiple loops and thus no longer parametrize physical space.

4.5 Embedding of chimera states

In order to gain a better understanding of the results obtained in the previous section, we investigate one of the first examples of a chimera state, reported by Kuramoto and Battogtokh in a system of nonlocally coupled phase oscillators [82]. There, the phase oscillators, located on a ring with unit length, split into a region of coherent and a regime of incoherent dynamics, c.f. Figs. 4.10(a,c). They were able to reduce the dynamics to a so-called order parameter, whose absolute value can be seen as a measure of coherence/incoherence. This space-dependent value, $R(x)$, is depicted in Fig. 4.10(b). Large values of R indicate synchronous dynamics, whereas the oscillators are desynchronized and incoherent where R is small. In general, the construction of order parameters for systems of phase oscillators can be achieved by following an ansatz proposed by Ott and Antonsen [141, 142]. However, for oscillators that show significant dynamics in additional variables, such as nonnegligible amplitude dynamics (e.g. the type II chimera in Sec. 4.4), this approach is no longer applicable. Hence, a different method for defining order parameters for these kinds of systems is desirable.

In this section, we propose a way to employ diffusion maps to define order parameters for chimera states. As already mentioned in the previous sections, by choosing the scale ϵ very small, the Gaussian kernel decays very fast with the Euclidean distance between time series, and thus one considers only pairs of time series with vanishing distances in the diffusion maps approach. For $\epsilon = e^4 \approx 0.32 D_{\max}$, the first nontrivial eigenvector ϕ_1 is depicted in Fig. 4.10(d). It is worth mentioning that, except for a change in its sign, ϕ_1 contains the same information as R. That is, ϕ_1 extracts the variability in the data that is also capture by R. Note that there is a major difference between ϕ_1 for the Kuramoto chimera state and ϕ_1 obtained from

the type II chimera discussed in Sec. 4.4. For the type II chimera, the order param-

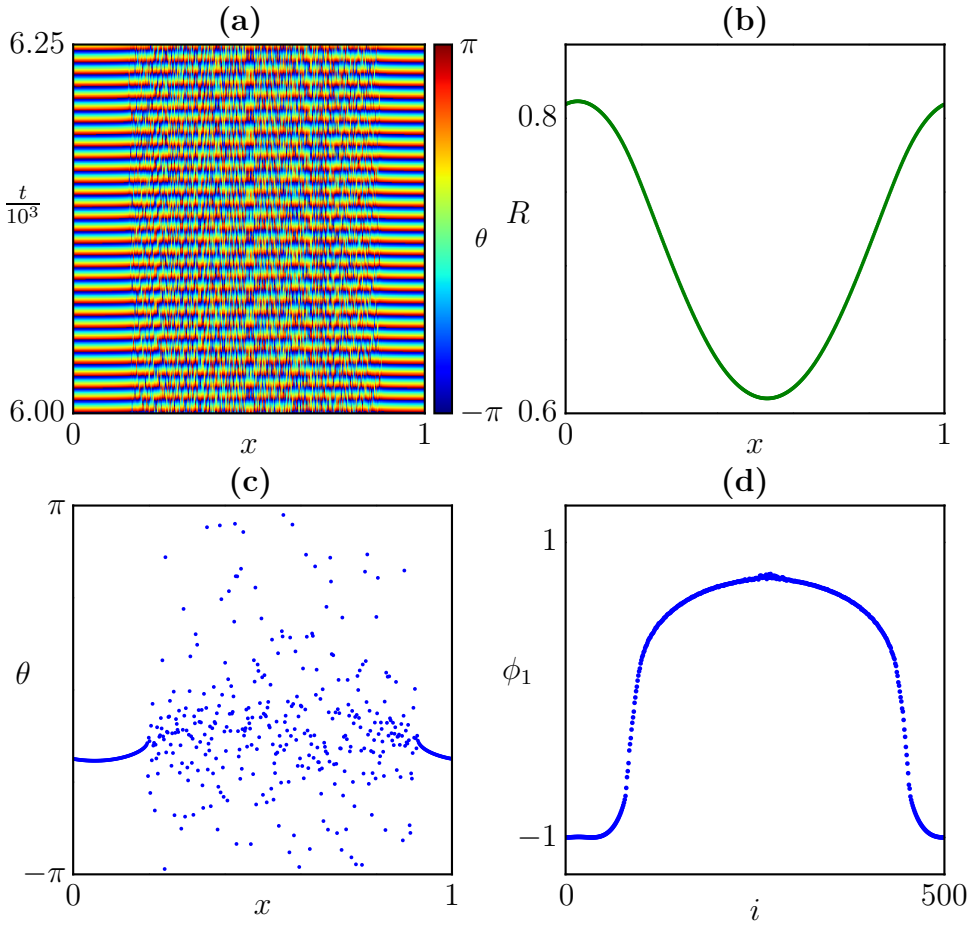

Figure 4.10: (a) Temporal evolution of the phases in a chimera state of nonlocally coupled phase oscillators. The color corresponds to the individual phases. (b) The absolute value of the order parameter, R. (c) Snapshot of the phases at $t = 6200$. (d) Eigenvector ϕ_1 for $\epsilon = e^4 \approx 0.32 D_{\max}$, corresponding the eigenvalue $\lambda_1 \approx 0.18$.

eter ϕ_1 is approximately constant in the individual clusters. This is, as discussed above, due to the underlying two-cluster state. But for the chimera state in the system of nonlocally coupled oscillators, the order parameter ϕ_1 varies continuously. We argue that this is due to the nonlocal coupling, which induces a continuous distribution of the frequency in the incoherent cluster. Due to this continuous frequency distribution, that is, due to different intrinsic properties of the oscillators, the incoherent oscillators are distinguishable, and thus the order parameter varies in the incoherent cluster. This variation is analogous to the first diffusion mode for the type II chimera with small ϵ, see Fig. 4.9(d). While for the Kuramoto chimera, the oscillators can be distinguished due to their different intrinsic frequencies, the

oscillators in the type II chimera can also be distinguished due to their position in space. This investigation of how diffusion maps are suited for the extraction of order parameters a first approach to the topic. It has been further elaborated in a master thesis [137], where a more thorough discussion of extracting order parameters for chimera states with diffusion maps can be found.

4.6 Reconstructing an attractor

In the previous examples, we compared time series to find variabilities which are intrinsic to the system, and used them as coordinates in which we regarded the data. But since we took entire time series as data points in the examples discussed above, the variabilities we could uncover were always perpendicular to the time direction and thus no variabilities along the time direction could be obtained.
In this section, we extend our analysis by cutting each time series into time chunks shorter than the available time interval in our data, and using these as data points. In addition, we let these pieces overlap, which ensures that their distances to neighbors in space and time are comparable. This approach enables us to find variabilities along directions in 'space-time', and will be illustrated in more detail on simulation data of the Kuramoto-Sivashinsky equation (KSE).
The KSE is a fourth-order partial differential equation

$$\partial_t u + \alpha \left(u \partial_x u + \partial_{xx} u \right) + 4 \partial_{xxxx} u = 0 \tag{4.3}$$

with the real variable $u = u(x,t)$ and the parameter α. For $\alpha = 53.3$ and $L = 2\pi$, with periodic boundaries, Eq. (4.3) shows modulated traveling waves [143], as shown in Fig. 4.11(a) for a 1d system with periodic boundary conditions. In this case, the dynamics are defined by two oscillations: that of the underlying traveling wave itself and that of the modulation. While the former is dominant when looking at the full dynamics, the nature of the latter becomes clear when moving to the co-rotating frame of the traveling wave, as depicted in Fig. 4.11(b). Here, each snapshot exhibits some periodic spatial profile. The amplitude of this profile oscillates in time such that every point in space oscillates with some constant modulation frequency. Altogether, the dynamics of each point in space and time are defined by its phase with respect to each of these two oscillations. In other words, the dynamics of the system lives on a 2-torus.
As a particular example, the dynamics shown in Fig. 4.11(a-b) are sampled in the form of $N = 100$ time series of length $T = 500$. Our first N time chunks are taken to consist of the first $l_{\text{Chunk}} = 200$ time steps at each point in space, respectively. The next N time chunks are similarly created by shifting the starting point to the nth time step of each time series and including the next $l_{\text{Chunk}} = 200$ steps from there. This process is repeated until the last N time chunks range from discrete time unit $T - l_{\text{Chunk}} = 300$ to $T = 500$. Therefore, each time chunk overlaps with the previous

one by $l_{\text{Chunk}} - n$ time steps.
For example, when obtaining time chunks of length $l_{\text{Chunk}} = 200$ from time series of length $T = 500$, a shift of $n = 8$ leads to the creation of $38 \cdot N$ overlapping time chunks. When performing diffusion maps on these time chunks the result, as in the previous sections, again depends on the value of the kernel scale ϵ. For $\epsilon = e^4$, a one-parameter dependence of the dynamics is detected, the diffusion coordinates of the time chunks forming a closed ring spanned by ϕ_1 and ϕ_2 (see Fig. 4.12(a); ϕ_3 hereby does not contain any additional information), and none of the at least 8 next diffusion modes being independent directions. As indicated by the smoothness of the coloring, the ring is parametrized by the spatial coordinates associated with the time chunks of the last snapshot, and thus by the phase of the traveling wave. (Most noticeable are those of the 100 time chunks sampled last in time, as these where plotted last.) Thus, the diffusion maps approach seems to have uncovered the underlying unmodulated traveling wave, the profile of which is also parametrized by space.
Decreasing the scale parameter, the ring in diffusion space partially unfolds into several rings, meaning that a third independent direction of the dynamics is gradually being detected. For $\epsilon = e^{3.5}$, this is shown in Fig. 4.12(b). Notably, each of the rings is still parametrized by space. A further decrease of ϵ leads to a further unfolding of the rings, see Figs. 4.12(c). At $\epsilon = e^{2.5}$ we get a full separation of the rings, as shown in Fig. 4.12(d). Together, these rings span a torus in diffusion space, one direction of which, the one along each of the rings, corresponds to the underlying traveling wave. The other direction, from one ring to the next, we argue to correspond to the modulating oscillation: When considering the period of one modulating oscillation

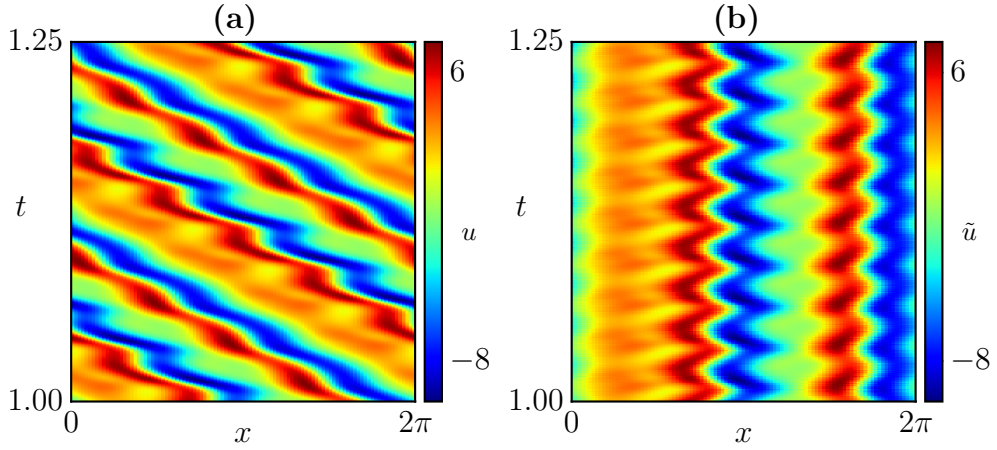

Figure 4.11: (a) Temporal evolution of u in the 1d Kuramoto-Sivashinsky equation with periodic boundaries, showing modulated traveling waves. (b) The dynamics in (a) in a co-rotating frame. The color corresponds to u.

in Fig. 4.11(b), its length is found to be 56 time steps in the $T = 500$ discretization described above. For an increment in the creation of time chunks of $n = 8$, the time chunks starting at $t_7 = 7n = 7 \cdot 8 = 56$ will thus have the same phase with respect to the modulating oscillation as the time chunks starting at $t_0 = 0$. Moreover, the profile of the underlying unmodulated traveling wave stays the same for all times, and is only shifted in space. Together, this assures that each of the time chunks starting at $t_0 = 0$ is identical to one of the time chunks, at another point in space, starting at $t_7 = 0$ (barring numerical sampling inaccuracy). As the same argument

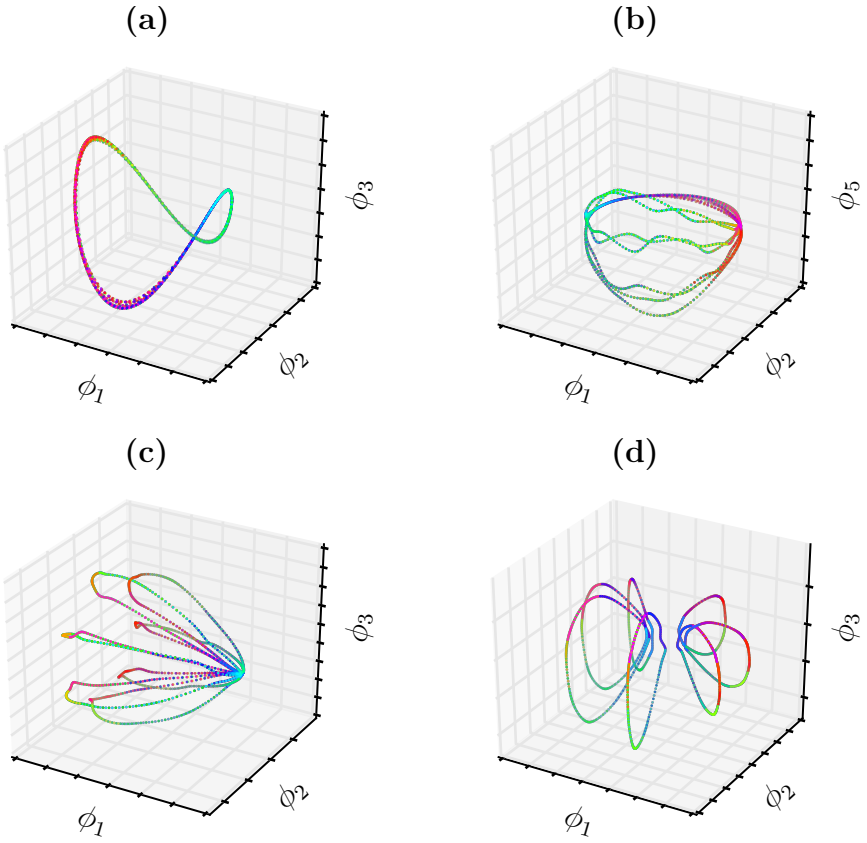

Figure 4.12: (a) First three independent diffusion modes obtained from overlapping time chunks created with a time shift of $n = 8$ and for $\epsilon = e^4$, colored by spatial position. (b-d) Equivalents to (a) for $\epsilon = e^{3.5}$, $\epsilon = e^3$, and $\epsilon = e^{2.5}$, respectively.

applies to any collection of time chunks starting at a given t_i, all these collections will thus occupy only seven distinct regions in diffusion space, and as each of them is represented by a ring, the result will be seven rings, arranged in a circle, exactly as in Fig. 4.12(d). Analogously, choosing a different increment of $n = 14$ when creating

the time chunks, leads to the diffusion modes (not shown here), where the torus is spanned by only four rings, just as predicted by our explanation. Moreover, the argumentation also holds for the choice of increments $n = 28$ and $n = 4$, leading to 2 and 14 rings spanning the torus in diffusion space, respectively (not shown here). Note that the toroidal direction corresponds to the phase of the modulation, whereas the poloidal direction corresponds to the phase of the traveling wave. Thus, those two directions are the dominant variabilities in this dynamical system, compare Fig. 4.12(d). In contrast to the spatial intermittency in the Ginzburg-Landau equation, the variabilities obtained by the modified approach described in this section are neither space nor time but the phases of the modulation and of the traveling wave, respectively.

4.7 Invariance to the Measrement Function

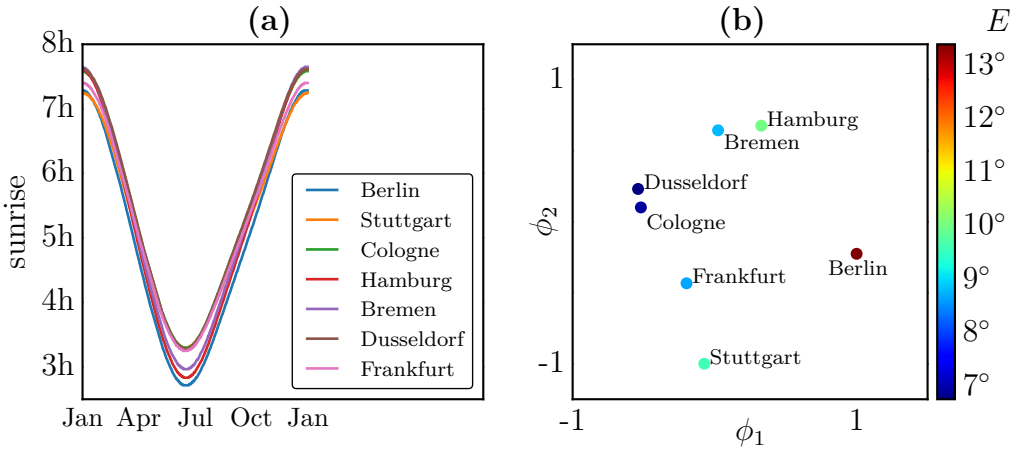

Figure 4.13: (a) Sunrise times in GMT of different German cities [128]. (b) The first two independent diffusion modes, ϕ_1 and $-\phi_2$ for $\epsilon = e^{15}$ of the data shown in (a), colored with their longitudinal geographic position. Note that by comparing with the actually locations in Fig. 4.2(b), it becomes obvious that ϕ_1 and ϕ_2 span a space in which the mutual arrangements of the cities reflect their actual positions. Additionally, due to the correspondence between the coloring and ϕ_1, one can visually verify that ϕ_1 parameterizes the west-east direction.

Embeddings of different sets of observations of the same system will, in general, be different, even if comparably informative. Consider the observation of sunrise/sunset in German cities not through the Boolean vectors of the daylight times of a particular day of the year, but rather through vectors containing the sunrise and sunset times of an entire year, as shown in Fig. 4.13(a). Here again, diffusion maps yield a similar (one could argue, homeomorphic) arrangement of the cities, as depicted in

Fig. 4.13(b). This is reminiscent of Koopman operator theory, with the Koopman operator being invariant to the measurement function [144–146].

4.8 Discussion

The individual examples discussed above highlight the utility of diffusion maps for the extraction of useful coordinates intrinsic to the data. Such coordinates may either be one-to-one with the spatial coordinate, the heterogeneous parameters or the underlying attracting manifold of the system. Hereby, the kernel scale plays an important role, since it effectively specifies the degree of coarsening we apply in our approach. For very small kernel scales, the data points effectively become disconnected, indicating that there are as many dimensions in the data as there are data points. Increasing the scale, data points become connected to their nearest neighbours. In this range of scales, we have seen that the emerging coordinates are one-to-one with the spatial arrangement of time series stemming from simulations of partial differential equations. For systems without a spatial coordinate, as in the case of the pre-Bötzinger neurons, one obtains an effective spatial representation which corresponds to the intrinsic heterogeneous parameters of the neurons. In both cases, that is for systems with and without a spatial dimension, the emerging coordinates may be used as coordinates to model the dynamics, using, for example, partial differential equations. For even larger values of ϵ, the diffusion modes become 'clumped' in the case of chimera states. This 'clumpedness' indicates that one might use a few ordinary differential equations to effectively describe the dynamics, opposed to partial differential equations on a smaller scale. For a more detailed discussion on the influence of the kernel scale on the embedding, see the master thesis, Ref. [137].
Finally, we briefly discussed that it is possible to extract coordinates which are independent of the measurement function. This then allows to fuse different observations of the 'same' dynamical phenomenon in a data driven way, or to map from one dynamical state to another. So far, such mappings have usually been obtained analytically, as, for example, the Cole-Hopf transformation between the the diffusion equation and the viscous Burgers equation [147]. There is, however, the condition that the measurement function yields 'enough' information of each data point. This directly links to the theorems of Whitney [148], Nash [149], and Takens [150], stating that an N-dimensional system can be embedded using $2N + 1$ coordinates. In the case of the Kuramoto-Sivashinsky equation, we have seen that taking time windows of lenght $l = 100$ contained sufficient delays to embed the dynamics on the torus.
Summarizing, we believe that such extracted variabilities may facilitate our understanding of complex dynamics. In particular for chimera states, the obtained one-dimensional representation of the dynamics may serve as an order parameter, allowing a distinction of different types of chimeras. The hope is that, not only for

chimera states, but for complex systems in general, the obtained coordinates may serve as a starting point for future modeling approaches, creating reduced equations in the new “emergent” or “equal” space.

Chapter 5

Summary and Conclusion

The main objective of this thesis is to shed light on dynamical phenomena occuring in networks of strongly coupled oscillators. In particular, we aimed at making a contribution to a better understanding of the mechanisms behind clustering and the formation of chimera states, states of coexisting coherence and incoherence.
We thus started from small ensembles of limit cycle oscillators, and showed how asymmetric (cluster) solutions can emerge in such small ensembles. Where such clusters exist thereby depends on the parameters of the system. Furthermore, stable cluster states may become unstable through Hopf bifurcations, creating cluster states that oscillate in their amplitudes and phase differences. We have seen that such oscillating clusters in ensembles of four oscillators may lead to chimera states through a sequence of symmetry breaking/period doubling bifurcations. Interestingly, two different types of chimera states appear along this sequence, which differ in the symmetry properties of the incoherent oscillators. This can be verified using symmetry detectives, which indeed suggest that asymmetric chimeras are invariant under the permutation of the two coherent oscillators, $\mathbf{S}_2^i$, only, whereas symmetric chimeras remain unchanged under operations of the symmetry group $\mathbf{S}_2^i \times \mathbf{S}_2^a$. Such a classification of minimal chimeras is applicable to not only the Stuart-Landau ensemble, but to general chimeras in sufficiently small networks. For too large networks, the amount of symmetry operations to test against, that is the cardinality of the equivariant symmetry group, usually becomes too excessive. However, we showed that one can draw conclusions from these minimal chimeras to their thermodynamic counterparts: asymmetric chimeras seem to form spatially coherent cluster, whereas symmetric chimeras manifest themselves as spatiotemporal incoherent dynamics in the incoherent cluster. In addition, asymmetric and symmetric chimera states are close in parameter space, with the asymmetric chimera forming a link between cluster states and symmetric chimeras. If such an arrangement also appears in other settings still remains unknown. Nevertheless, we are convinced that a classification according to the symmetry properties reveals deeper insights into chimera states in general.
The classification based on the symmetry of the incoherent oscillators is also applicable to systems larger than four oscillators, as long as the symmetry group of the

whole system does not become too large. For the case when there are more than two incoherent oscillators, under which symmetry operations are they invariant on average? As also pointed out by Dr. García-Morales, could there be symmetries on average different than $\mathbf{S}^a_{N_i}$, with N_i the number of incoherent oscillators? We believe that this is an important question which remains to be answered by future research. The answer to this question, however, may lead to an even more general classification of chimera states in small ensembles, and thus enhance our understanding of incoherent dynamics in systems of coupled agents in general.
Besides bifurcation into chimera states, balanced cluster states may also bifurcate from and to the synchronized solution in ensembles of mean-coupled Stuart-Landau oscillators. In particular, such transitions occurs via a hysteretic sequence of intermediate unbalanced clusters. This becomes especially clear when considering larger ensembles of globally coupled limit cycle oscillators. There, the cluster states become increasingly dense in phase space. In more detail, neighboring cluster states in phase space differ by the ratio of oscillators in each cluster: The closer the cluster curves are, the more similar in size are the individual clusters. Such properties can be exploited using the theory of persistence, allowing to extrapolate these results to any cluster distribution. In the course of our considerations, we found that the arrangement of such cluster states becomes singular at individual points in parameter space. There, the transition from balanced cluster states to the synchronous oscillations becomes continuous. We dubbed these co-dimension two points cluster singularities, and derived their position in parameter and phase space analytically. In our analytic derivation, however, we find two such points, of which we only investigate one in more detail. A detailed analysis of the second cluster singularity still remains to be done.
The generality of our model and our approach suggests that such singularities may also appear in different ensembles of globally coupled oscillators, and that an experimental validation should be possible. In particular, the existence of such points in normal forms may have far reaching implications for symmetry breaking in networks of coupled oscillators in general. Since small parameter variations close to this point can lead to a vast amount of different stable 2-cluster states, it might be favorable for biological as well as physical systems to operate close to such singular points. In especially for biological systems, this then allows for an efficient adaption and differentiation as a response to small changes in the environment.
Similar to their emergence in a small ensemble, chimera states may be born through symmetry increasing bifurcations from cluster states in larger networks. This is not only the case for globally coupled oscillators, but for a large variety of coupling topologies. Not surprisingly, the variety of qualitatively different chimera states observed in the literature is extensive, asking for a comprehensive classification. This led us to the development of two quantitative order parameters, one to characterize the spatial coherence in the chimera state, another to quantify the temporal correlations. In particular, we propose the order parameter g_0 describing the fraction of

spatially coherent oscillators. As shown in Chapter 3, it can be obtained by either applying the discrete Laplacian on simulation or experimental data with a spatial dimension, or by calculating the pairwise distances between the agents for systems without any spatial extension. This variable g_0 can then be used to distinguish three different types of chimeras: stationary chimeras, when g_0 is constant in time, breathing chimeras when g_0 is periodic and turbulent chimeras when g_0 behaves irregularly in time. Such a classification can be further refined using the second order parameter h_0, describing the fraction of temporally coherent oscillators. It can be calculated via pairwise correlation coefficients, and can be used to distinguish between moving chimera states, states where the coherent and incoherent clusters moves in space, and static chimeras, where the individual cluster remain stationary in space. A value of $h_0 < g_0$ indicates that more agents are spatially coherent than temporally coherent, and the chimera is moving, whereas $h_0 \approx g_0$ suggests that the chimera state is static. Finally, values of $g_0 = 1$ or $g_0 = 0$ indicate that the present state is either not a chimera state at all, or it is transient. In order to verify the usefulness of our approach, we tested and illustrated this classification on various examples from both experiments and simulations.

In addition to the classification of chimera states in small networks using symmetry detectives, the classification based on g_0 and h_0 allows the classification of chimeras also in large networks. The distinction between different kinds of these hybrid states is an important step towards comparing and eventually mapping chimera states in different systems. Furthermore, we published the functions calculating the above mentioned classification measures on GitHub under Python[1], which have been used in different fields dealing with chimeras [151–154], hopefully facilitating research along these directions.

It is worth mentioning that the two correlation measures are "hand-engineered" in the sense that they are specifically designed for this classification based on experience and thinking. Recent advances in machine and manifold learning, however, suggest that it should be possible to extract order parameters from data in an automated fashion. Here, we used a nonlinear manifold learning technique, diffusion maps, to extract intrinsic features of the data, which we call intrinsic variabilities. By comparing time series, we showed that such variabilities can either be spatial coordinates or heterogeneous parameters in the system, and argue that the representation through these coordinates may render the data in a more intelligible form. In particular, the extracted coordinates are implicitly contained in, or emerge from, the data, spanning what we call an 'emergent space'.

An important parameter of diffusion maps is the kernel scale, specifying the kernel width and thus the scale on which we want to approach the data. We therefore briefly discuss the influence of this parameter on the embedding of different chimera states. In the course of this, we argue that the first diffusion mode may, for a suit-

[1]The classify_chimera package is available under github.com/fkemeth/classify_chimeras.

able choice of the scale, allow conclusions about the underlying coarse dynamics and thus may serve as a suitable order parameter. Taking overlapping time chunks instead of whole time series, we explain how one can use diffusion maps to find the underlying attractor of a dynamical system. That is, the intrinsic variabilities extracted from the data parametrize the attracting manifold. We discuss how these various extracted coordinates may further help to understand complex dynamics, and may serve as suitable variables for the future development of reduced models.
The development of such reduced models, in particular finding equations in these extracted coordinates, is still an ongoing field of research. The vast number of publications dealing with chimera states suggests that this is also true for the dynamics of such states. In particular, the question if there is a universal mechanism through which chimera states, or hybrid states in general, are born, is still unsolved. Furthermore, the upcoming shift from phase oscillator systems, for which approaches proposed by Ott and Antonsen [141, 142] or Watanabe and Strogatz [155, 156] exist, to networks composed of amplitude oscillators where such approaches are no longer possible, requires the development of new methods. We believe that our considerations may serve as a starting point for the future development of such methods.
The question still remains of how the results presented here help us understand actual physical or biological problems, such as, for example, dynamical patterns in the brain. What can we indeed say about mechanism leading to uni-hemispheric sleep in certain animals?
Although a definite solution to these questions cannot be given at this point, we believe that the bifurcation scenarios and the chimera states explained in this thesis are of importance to the understanding of these problems. In particular, the ability to account for various chimera states observed in, for example, electro-chemical experiments using ensembles of coupled Stuart-Landau oscillators reassures that the study of normal forms indeed allows conclusions about actual physical processes.
Although the study of large networks of oscillators is not feasible, we showed that one can nevertheless learn a lot about large networks when starting from small ensembles. Finding regularities in systems of different sizes, that is, bifurcations occurring in large as well as in small ensembles, further indicates that the observed phenomena are generic. But understanding these phenomena even in normal forms is still a challenging task. This becomes especially obvious when considering how large the parameter space is even for networks of identical oscillators, and how vast the number of transitions is that occur even in very small parameter windows. Although we found regularities even in these small parameter windows, such as cluster transitions and singularities, a further exploration of parameter space may enhance our understanding of coupled oscillators.
Another evidence of the generality of our approach can be achieved when reducing normal form simulations as well as experimental data onto order parameters. Such order parameters, e.g. g_0 and h_0, or emergent coordinates obtained using diffusion maps, may indicate what kind of qualitative pattern, for example in the

brain, is observed, and if our simulations account for its qualitative behavior. These data-driven approaches then may further validate, or correct, our assumption that globally coupled ensembles of Stuart-Landau oscillators are a powerful model for describing distributed oscillatory behavior in nature.

Appendix A

Derivation of the Mean-Coupled Stuart-Landau Ensemble

Following Ref. [21], one can derive the complex Ginzburg-Landau equation in a rather generall way. Suppose you have a dynamical system with N variables

$$\partial_t x_i = F_i\left(x_1, \ldots, x_N, \boldsymbol{p}\right) \ , \ i = 1, \ldots, N,$$

with some parameters $\boldsymbol{p}$, which can be written in vectorized form as

$$\partial_t \boldsymbol{x} = \boldsymbol{F}\left(\boldsymbol{x}, \boldsymbol{p}\right). \tag{A.1}$$

Suppose Eq. (A.1) has a stationary point $\boldsymbol{x}_0$ such that

$$\boldsymbol{F}\left(\boldsymbol{x}_0, \boldsymbol{p}\right) = 0,$$

with $\boldsymbol{x}_0 = \boldsymbol{x}_0\left(\boldsymbol{p}\right)$ possibly dependent on the parameters $\boldsymbol{p}$. We can Taylor-expand around this fixed point by introducing the deviation $\boldsymbol{u} = \boldsymbol{x} - \boldsymbol{x}_0$ such that

$$\begin{aligned}\partial_t u_i &= \left.\frac{\partial F_i}{\partial x_j}\right|_{\boldsymbol{x}_0} u^j + \frac{1}{2}\left.\frac{\partial^2 F_i}{\partial x_j \partial x_k}\right|_{\boldsymbol{x}_0} u^j u^k + \frac{1}{6}\left.\frac{\partial^3 F_i}{\partial x_j \partial x_k \partial x_l}\right|_{\boldsymbol{x}_0} u^j u^k u^l + \ldots \\ &= \mathbf{L}_{ij} u^j + \frac{1}{2}\mathbf{H}_{ijk} u^j u^k + \frac{1}{6}\mathbf{D}_{ijkl} u^j u^k u^l + \ldots\end{aligned}$$

where we use the Einstein summation convention [157] and where $\mathbf{L}$ denotes the Jacobian matrix, $\mathbf{H}$ the Hessian matrix and $\mathbf{D}$ contains the third partial derivatives, whereas all are evaluated at the fixed point solution $\boldsymbol{x}_0$. Keeping in mind the correct summations described above, we can rewrite them in a more compact form as

$$\partial_t \boldsymbol{u} = \mathbf{L}\boldsymbol{u} + \mathbf{M}\boldsymbol{u}^2 + \mathbf{N}\boldsymbol{u}^3 + \ldots. \tag{A.2}$$

Suppose now that $\boldsymbol{x}_0$ is a stable steady state solution, that means the real parts of all eigenvalues of the Jacobian $\mathbf{J}$ are negative at this solution. Furthermore assume that by changing one parameter μ two complex conjugate eigenvalues cross the imaginary

axis transversally, such that $\boldsymbol{x}_0$ undergoes a supercritical Hopf bifurcation. Next, it is worth expanding the Jacobian at this bifurcation point such that

$$\mathbf{L} = \mathbf{L}_0 + \mu\mathbf{L}_1 + \mu^2\mathbf{L}_2 + \dots$$

and its eigenvalues

$$\lambda = \lambda_0 + \mu\lambda_1 + \mu^2\lambda_2 + \dots .$$

Let $\boldsymbol{v}^*$ and $\boldsymbol{v}$ be the left and right eigenvectors of $\mathbf{L}_0$, with

$$\begin{aligned} \mathbf{L}_0\boldsymbol{v} &= \lambda_0\boldsymbol{v} & \qquad \boldsymbol{v}^*\mathbf{L}_0 &= \lambda_0\boldsymbol{v}^* \\ \mathbf{L}_1\boldsymbol{v} &= \lambda_1\boldsymbol{v} & \qquad \boldsymbol{v}^*\mathbf{L}_1 &= \lambda_1\boldsymbol{v}^* \end{aligned}$$

and $\boldsymbol{v}^*\boldsymbol{v} = 1$. Since we are interested in a Hopf bifurcation of the stationary state,

$$\begin{aligned} \boldsymbol{v}^*\mathbf{L}_0\boldsymbol{v} &= \lambda_0 = i\omega_0 \\ \boldsymbol{v}^*\mathbf{L}_i\boldsymbol{v} &= \lambda_1 = \sigma_1 + i\omega_1. \end{aligned}$$

Furthermore, it is helpful to introduce a parameter $\epsilon > 0$ with $\mu = \epsilon^2\chi$ and $\chi = \operatorname{sign}\mu$. Using the fact that the amplitudes of the oscillations close to a Hopf bifurcation scale with $\sqrt{\mu}$, one can write

$$\boldsymbol{u} = \epsilon\boldsymbol{u}_1 + \epsilon^2\boldsymbol{u}_2 + \dots$$

and

$$\begin{aligned} \mathbf{L} &= \mathbf{L}_0 + \epsilon^2\chi\mathbf{L}_1 + \dots \\ \mathbf{M} &= \mathbf{M}_0 + \epsilon^2\chi\mathbf{M}_1 + \dots \\ \mathbf{N} &= \mathbf{N}_0 + \epsilon^2\chi\mathbf{N}_1 + \dots . \end{aligned}$$

Note that the real part of λ is of order ϵ^2 and thus slow compared to the rotations induced by $\lambda_0 = i\omega$. Therefore one may introduce a new time $\tau = \epsilon^2 t$ and write

$$dt \to \partial t + \epsilon^2\partial\tau.$$

This transformes Eq. (A.2) into

$$\begin{aligned} \left(\partial_t + \epsilon^2\partial_\tau\right)\left(\epsilon\boldsymbol{u}_1 + \epsilon^2\boldsymbol{u}_2 + \dots\right) = {} & \left(\mathbf{L}_0 + \epsilon^2\chi\mathbf{L}_1 + \dots\right)\left(\epsilon\boldsymbol{u}_1 + \epsilon^2\boldsymbol{u}_2 + \dots\right) \\ & + \left(\mathbf{M}_0 + \epsilon^2\chi\mathbf{M}_1 + \dots\right)\left(\epsilon\boldsymbol{u}_1 + \epsilon^2\boldsymbol{u}_2 + \dots\right)^2 \\ & + \left(\mathbf{N}_0 + \epsilon^2\chi\mathbf{N}_1 + \dots\right)\left(\epsilon\boldsymbol{u}_1 + \epsilon^2\boldsymbol{u}_2 + \dots\right)^3 \end{aligned}$$

which can be rewritten as

$$\left(\partial_t + \epsilon^2\partial_\tau - \mathbf{L}_0 - \epsilon^2\chi\mathbf{L}_1 + \dots\right)\left(\epsilon\boldsymbol{u}_1 + \epsilon^2\boldsymbol{u}_2 + \dots\right) = \epsilon^2\mathbf{M}_0\boldsymbol{u}_1^2$$

$$
\begin{aligned}
&+ \epsilon^3 \left(2\mathbf{M}_0 \boldsymbol{u}_1 \boldsymbol{u}_2 + \mathbf{N}_0 \boldsymbol{u}_1^3\right) \\
&+ O\left(\epsilon^4\right).
\end{aligned}
$$

Sorting this equation corresponding to the powers of ϵ yields

$$
\begin{aligned}
\left(\partial_t - \mathbf{L}_0\right) \boldsymbol{u}_1 &= 0 \\
\left(\partial_t - \mathbf{L}_0\right) \boldsymbol{u}_2 &= \mathbf{M}_0 \boldsymbol{u}_1^2 \\
\left(\partial_t - \mathbf{L}_0\right) \boldsymbol{u}_3 &= -\left(\partial_\tau - \chi \mathbf{L}_1\right) \boldsymbol{u}_1 + 2\mathbf{M}_0 \boldsymbol{u}_1 \boldsymbol{u}_2 + \mathbf{N}_0 \boldsymbol{u}_1^3 \\
&\vdots \\
\left(\partial_t - \mathbf{L}_0\right) \boldsymbol{u}_i &= \boldsymbol{B}_i
\end{aligned}
$$

This is a system of inhomogeneous differential equations. One can solve the homogeneous equation

$$
\begin{aligned}
\partial_t \boldsymbol{u}_1 &= \mathbf{L}_0 \boldsymbol{u}_1 \\
\rightarrow \boldsymbol{u}_1 &= \boldsymbol{u}_{\text{hom}} = W(\tau)\, \boldsymbol{v} e^{i\omega_0 t} + \bar{W}(\tau)\, \bar{\boldsymbol{v}} e^{-i\omega_0 t}.
\end{aligned}
$$

The inhomogeneous equation has a solution only if the Fredholm solvability condition is fulfilled, that is if

$$
\begin{aligned}
\langle \boldsymbol{B}_i, \boldsymbol{u}_{\text{hom}} \rangle &= 0 \\
\rightarrow \langle \boldsymbol{v}^* \cdot \boldsymbol{B}_i, \boldsymbol{v}^* \cdot \boldsymbol{u}_{\text{hom}} \rangle &= 0 \\
\rightarrow \int_{-\infty}^{+\infty} \boldsymbol{v}^* \cdot \boldsymbol{B}_i W(\tau)\, e^{i\omega_0 t} dt &= 0 \\
\rightarrow \int_0^{2\pi/\omega_0} \boldsymbol{v}^* \cdot \boldsymbol{B}_i e^{i\omega_0 t} dt &= 0
\end{aligned}
$$

where one can use the fact that $\boldsymbol{v}^* \cdot \bar{\boldsymbol{v}} = 0$, $W(\tau)$ is approximately constant and non-zero on the time scale of ωt and that the homogeneous solution is 2π periodic in $\omega_0 t$. In particular, one can thus infer that the $\boldsymbol{B}_i$ must also be 2π periodic in $\omega_0 t$ and hence one can write

$$
\boldsymbol{B}_i = \sum_l \boldsymbol{B}_i^{(l)}(\tau)\, e^{-il\omega_0 t}.
$$

The solvability condition then turns into

$$
\boldsymbol{v}^* \cdot \boldsymbol{B}_i^{(1)} = 0.
$$

The solution for $\boldsymbol{u}_2$ can be obtained by solving

$$
\left(\partial_t - \mathbf{L}_0\right) \boldsymbol{u}_2 = \mathbf{M}_0 \boldsymbol{u}_1^2,
$$

which has a solution of the form

$$\begin{aligned}\boldsymbol{u}_2 = &-\left(\mathbf{L}_0 - 2i\omega_0\right)^{-1}\mathbf{M}_0\boldsymbol{v}\,\boldsymbol{v}\,W^2 e^{2i\omega_0 t}\\ &-\left(\mathbf{L}_0 + 2i\omega_0\right)^{-1}\mathbf{M}_0\bar{\boldsymbol{v}}\,\bar{\boldsymbol{v}}\,\bar{W}^2 e^{-2i\omega_0 t}\\ &-2\mathbf{L}_0^{-1}\mathbf{M}_0\boldsymbol{v}\bar{\boldsymbol{v}}\,|W|^2 + c\boldsymbol{u}_1\end{aligned}$$

This leads to a $\boldsymbol{B}_3^{(1)}$ of

$$\begin{aligned}\boldsymbol{B}_3^{(1)} = &-\left(\partial_\tau - \chi\mathbf{L}_1\right)W\boldsymbol{v}\\ &+\left(4\mathbf{M}_0\boldsymbol{v}\,\mathbf{L}_0^{-1}\mathbf{M}_0\boldsymbol{v}\bar{\boldsymbol{v}} + 2\mathbf{M}_0\bar{\boldsymbol{v}}\left(\mathbf{L}_0 - 2i\omega_0\right)^{-1}\mathbf{M}_0\boldsymbol{v}\,\boldsymbol{v}\; + 3\mathbf{N}_0\boldsymbol{v}\,\boldsymbol{v}\,\bar{\boldsymbol{v}}\right)|W|^2 W\end{aligned}$$

and with the solvability condition

$$\begin{aligned}\partial_\tau W &= \boldsymbol{v}^*\chi\mathbf{L}_1 W\boldsymbol{v}\\ &\quad+\Big(4\boldsymbol{v}^*\mathbf{M}_0\boldsymbol{v}\,\mathbf{L}_0^{-1}\mathbf{M}_0\boldsymbol{v}\bar{\boldsymbol{v}}\\ &\quad+2\boldsymbol{v}^*\mathbf{M}_0\bar{\boldsymbol{v}}\;\left(\mathbf{L}_0 - 2i\omega_0\right)^{-1}\mathbf{M}_0\boldsymbol{v}\,\boldsymbol{v} + 3\boldsymbol{v}^*\mathbf{N}_0\boldsymbol{v}\,\boldsymbol{v}\,\bar{\boldsymbol{v}}\Big)\,|W|^2 W\\ &= \chi\lambda_1 W - g\,|W|^2 W\end{aligned}$$

with $g = g_1 + ig_2$. This is the general form of a Stuart-Landau oscillator. Suppose now that the variables $\boldsymbol{x}$ are fields over some spatial domain of length L coupled via diffusion, then the general dynamics can be described by

$$\partial_t\boldsymbol{x} = \boldsymbol{F}\left(\boldsymbol{x},\boldsymbol{p}\right) + \mathbf{D}\nabla^2\boldsymbol{x}$$

with a diffusion matrix $\mathbf{D}$. Furthermore, assume that some varibles have long range interactions such that they are influenced by the common mean. If we assume that this interaction is linear, then we get the following form for the dynamics

$$\partial_t\boldsymbol{x} = \boldsymbol{F}\left(\boldsymbol{x},\boldsymbol{p}\right) + \mathbf{D}\nabla^2\boldsymbol{x} + \mathbf{K}\frac{1}{L}\int_L\left(\boldsymbol{x}\left(r'\right) - \boldsymbol{x}\left(r\right)\right)dr'.$$

Follwoing Refs. [21–23], Eq. (A.2) turns into

$$\partial_t\boldsymbol{u} = \left(\mathbf{L} + \mathbf{D}\nabla^2\right)\boldsymbol{u} + \mathbf{K}\frac{1}{L}\int_L\left(\boldsymbol{u}\left(r'\right) - \boldsymbol{u}\left(r\right)\right)dr' + \mathbf{M}\boldsymbol{u}^2 + \mathbf{N}\boldsymbol{u}^3 + \ldots. \tag{A.3}$$

Rescaling space such that $s = \epsilon r$ and writing $\mathbf{K} \to \epsilon^2\mathbf{K}$[1], we get

$$\boldsymbol{B}_3 = -\left(\partial_\tau - \chi\mathbf{L}_1 - \mathbf{D}\nabla_s^2\right)\boldsymbol{u}_1$$

[1] We must assume the coupling to be weak, otherwise the center manifold theorem no longer applies, see Ref. [22]

$$+ \mathbf{K}\frac{1}{L}\int_L \left(u_1\left(s'\right) - u_1\left(s\right)\right) ds'$$
$$+ 2\mathbf{M}_0 \boldsymbol{u}_1\, \boldsymbol{u}_2 + \mathbf{N}_0 \boldsymbol{u}_1^3$$

such that

$$\begin{aligned}
\boldsymbol{B}_3^{(1)} = &- \left(\partial_\tau - \chi\mathbf{L}_1 - \mathbf{D}\nabla_s^2\right) W\boldsymbol{v} \\
&+ \mathbf{K}\boldsymbol{v}\frac{1}{L}\int_L \left(W\left(s'\right) - W\left(s\right)\right) ds' \\
&+ \Big(4\mathbf{M}_0\boldsymbol{v}\,\mathbf{L}_0^{-1}\mathbf{M}_0\boldsymbol{v}\bar{\boldsymbol{v}} + 2\mathbf{M}_0\bar{\boldsymbol{v}}\,\left(\mathbf{L}_0 - 2i\omega_0\right)^{-1}\mathbf{M}_0\boldsymbol{v}\,\boldsymbol{v} \\
&+ 3\mathbf{N}_0\boldsymbol{v}\,\boldsymbol{v}\,\bar{\boldsymbol{v}}\Big)\left|W\right|^2 W
\end{aligned}$$

or

$$\partial_\tau W = \chi\lambda_1 W + d\nabla_s^2 W - g\left|W\right|^2 W + k\frac{1}{L}\int \left(W\left(s'\right) - W\left(s\right)\right) ds'$$

with $d = d_1 + id_2 = \boldsymbol{v}^*\mathbf{D}\boldsymbol{v}$ and $k = k_1 + ik_2 = \boldsymbol{v}^*\mathbf{K}\boldsymbol{v}$. Introducting the rescaled time $\tau = at$, rescaled space $s = bx$ and $W = cW$, we have

$$\begin{aligned}
\frac{c}{a}\partial_t W &= c\chi\lambda_1 W + \frac{cd}{b^2}\nabla_x^2 W - gc^3\left|W\right|^2 W + ck\frac{1}{L}\int \left(W\left(s'\right) - W\left(s\right)\right) ds' \\
\Rightarrow \partial_t W &= a\chi\lambda_1 W + \frac{ad}{b^2}\nabla_x^2 W - gac^2\left|W\right|^2 W + ak\frac{1}{L}\int \left(W\left(s'\right) - W\left(s\right)\right) ds' \\
&= a\chi\left(\sigma_1 + i\omega_1\right) W + \frac{a}{b^2}\left(d_1 + id_2\right)\nabla_x^2 W \\
&- \left(g_1 + ig_2\right) ac^2\left|W\right|^2 W + a\left(k_1 + ik_2\right)\frac{1}{L}\int \left(W\left(s'\right) - W\left(s\right)\right) ds'
\end{aligned}$$

In the supercritical case, $\chi = 1$, and by taking $a = 1/(\sigma_1)$, $b = \sqrt{d_1/\sigma_1}$ and $c = \sqrt{\sigma_1/|g_1|}$ we get

$$\begin{aligned}
\partial_t W &= \left(1 + i\frac{\omega_1}{\sigma_1}\right) W + \left(1 + i\frac{d_2}{d_1}\right)\nabla_x^2 W \\
&- \left(1 + i\frac{g_2}{g_1}\right)\left|W\right|^2 W + \left(\frac{k_1}{\sigma_1} + i\frac{k_2}{\sigma_1}\right)\frac{1}{L}\int \left(W\left(s'\right) - W\left(s\right)\right) ds' \\
&= \left(1 + ic_0\right) W + \left(1 + ic_1\right)\nabla_x^2 W \\
&- \left(1 + ic_2\right)\left|W\right|^2 W + \left(\alpha + i\beta\right)\frac{1}{L}\int \left(W\left(s'\right) - W\left(s\right)\right) ds'
\end{aligned}$$

with $c_0 = \omega_1/\sigma_1$, $c_1 = d_2/d_1$, $c_2 = g_2/g_1$, $\alpha = k_1/\sigma_1$ and $\beta = k_2/\sigma_1$. Following Refs. [25, 31] and by moving to a co-moving frame $W \to W\exp ic_0 t$, we get that

$$\partial_t W e^{ic_0 t} = e^{ic_0 t}\partial_t W + ic_0 W e^{ic_0 t},$$

and thus one can further eliminate c_0 and obtain the rescaled version of the globally-coupled complex Ginzburg-Landau equation

$$\begin{aligned}\partial_t W = W + (1 + ic_1)\,\nabla_x^2 W - (1 + ic_2)\,|W|^2\,W \\ + (\alpha + i\beta)\,\frac{1}{L}\int (W(s') - W(s))\,ds',\end{aligned}$$

which is in fact Eq. (2.1) mentioned above.
Neglecting the diffusion term $(1 + ic_1)\,\nabla_x^2 W$, we can rewrite the integral as an ensemble average $\langle W \rangle = 1/N \sum_k W_k$, obtaining an ensemble of globally coupled oscillators,

$$\begin{aligned}\partial_t W_k = W_k - (1 + ic_2)\,|W_k|^2\,W_k \\ + (\alpha + i\beta)\left(\frac{1}{N}\sum_j W_j - W_k\right),\end{aligned}$$

with $k = 1, \ldots, N$, as already described in Eq. 2.2.

Appendix B

Equations in Polar Coordinates

The temporal evolution of four mean-coupled oscillators can be obtained using the full system Eq. (2.2)

$$\partial_t W_i = W_i - (1 + ic_2)\left|W_i\right|^2 W_i + \kappa\left(\langle W\rangle - W_i\right)\ ,\ i \in \{1,2,3,4\}\,,$$

with $\kappa = \alpha + \mathrm{i}\beta$. Replacing κ we get

$$\begin{aligned}
\partial_t W_1 &= W_1 - (1+ic_2)\left|W_1\right|^2 W_1 + \kappa\left(\frac{1}{4}\left(W_1+W_2+W_3+W_4\right) - W_1\right)\\
&= W_1 - (1+ic_2)\left|W_1\right|^2 W_1 + \kappa\left(\frac{1}{4}W_2 + \frac{1}{4}W_3 + \frac{1}{4}W_4 - \frac{3}{4}W_1\right)\\
&= \left(1 - \frac{3}{4}\kappa\right)W_1 - (1+ic_2)\left|W_1\right|^2 W_1 + \frac{\kappa}{4}\left(W_2+W_3+W_4\right)\\
&= \left(1 - 3\left(\alpha+i\beta\right)\right)W_1 - (1+ic_2)\left|W_1\right|^2 W_1 + \left(\alpha+i\beta\right)\left(W_2+W_3+W_4\right)
\end{aligned}$$

and in polar coordinates

$$\begin{aligned}
\dot{R}_i e^{i\phi_i} + iR_i\dot{\phi}_i e^{i\phi_i} &= \left(1 - 3\left(\alpha+i\beta\right)\right)R_i e^{i\phi_i} - (1+ic_2)R_i^3 e^{i\phi_i}\\
&\quad + \left(\alpha+i\beta\right)\left(R_j e^{i\phi_j} + R_k e^{i\phi_k} + R_l e^{i\phi_l}\right)\\
\dot{R}_i + iR_i\dot{\phi}_i &= \left(1 - 3\left(\alpha+i\beta\right)\right)R_i - (1+ic_2)R_i^3\\
&\quad + \left(\alpha+i\beta\right)\left(R_j e^{i(\phi_j-\phi_i)} + R_k e^{i(\phi_k-\phi_i)} + R_l e^{i(\phi_l-\phi_i)}\right)
\end{aligned}$$

The dynamics are given through the four amplitude equations

$$\begin{aligned}
\partial_t R_1 &= \left(1-3\alpha\right)R_1 - R_1^3\\
&\quad + \alpha\left[R_2\cos\left(\phi_2-\phi_1\right) + R_3\cos\left(\phi_3-\phi_1\right) + R_4\cos\left(\phi_4-\phi_1\right)\right]\\
&\quad - \beta\left[R_2\sin\left(\phi_2-\phi_1\right) + R_3\sin\left(\phi_3-\phi_1\right) + R_4\sin\left(\phi_4-\phi_1\right)\right]\\
\partial_t R_2 &= \left(1-3\alpha\right)R_2 - R_2^3\\
&\quad + \alpha\left[R_1\cos\left(\phi_1-\phi_2\right) + R_3\cos\left(\phi_3-\phi_2\right) + R_4\cos\left(\phi_4-\phi_2\right)\right]\\
&\quad - \beta\left[R_1\sin\left(\phi_1-\phi_2\right) + R_3\sin\left(\phi_3-\phi_2\right) + R_4\sin\left(\phi_4-\phi_2\right)\right]
\end{aligned}$$

$$
\begin{aligned}
\partial_t R_3 &= (1-3\alpha)\, R_3 - R_3^3 \\
&\quad + \alpha \left[R_1 \cos(\phi_1 - \phi_3) + R_2 \cos(\phi_2 - \phi_3) + R_4 \cos(\phi_4 - \phi_3) \right] \\
&\quad - \beta \left[R_1 \sin(\phi_1 - \phi_3) + R_2 \sin(\phi_2 - \phi_3) + R_4 \sin(\phi_4 - \phi_3) \right] \\
\partial_t R_4 &= (1-3\alpha)\, R_4 - R_4^3 \\
&\quad + \alpha \left[R_1 \cos(\phi_1 - \phi_4) + R_2 \cos(\phi_2 - \phi_4) + R_3 \cos(\phi_3 - \phi_4) \right] \\
&\quad - \beta \left[R_1 \sin(\phi_1 - \phi_4) + R_2 \sin(\phi_2 - \phi_4) + R_3 \sin(\phi_3 - \phi_4) \right]
\end{aligned}
$$

and the four phase equations

$$
\begin{aligned}
\partial_t \phi_1 &= -3\beta - c_2 R_1^2 \\
&\quad + \frac{\beta}{R_1} \left[R_2 \cos(\phi_2 - \phi_1) + R_3 \cos(\phi_3 - \phi_1) + R_4 \cos(\phi_4 - \phi_1) \right] \\
&\quad + \frac{\alpha}{R_1} \left[R_2 \sin(\phi_2 - \phi_1) + R_3 \sin(\phi_3 - \phi_1) + R_4 \sin(\phi_4 - \phi_1) \right] \\
\partial_t \phi_2 &= -3\beta - c_2 R_2^2 \\
&\quad + \frac{\beta}{R_2} \left[R_1 \cos(\phi_1 - \phi_2) + R_3 \cos(\phi_3 - \phi_2) + R_4 \cos(\phi_4 - \phi_2) \right] \\
&\quad + \frac{\alpha}{R_2} \left[R_1 \sin(\phi_1 - \phi_2) + R_3 \sin(\phi_3 - \phi_2) + R_4 \sin(\phi_4 - \phi_2) \right]
\end{aligned}
$$

$$
\begin{aligned}
\partial_t \phi_3 &= -3\beta - c_2 R_3^2 \\
&\quad + \frac{\beta}{R_3} \left[R_1 \cos(\phi_1 - \phi_3) + R_2 \cos(\phi_2 - \phi_3) + R_4 \cos(\phi_4 - \phi_3) \right] \\
&\quad + \frac{\alpha}{R_3} \left[R_1 \sin(\phi_1 - \phi_3) + R_2 \sin(\phi_2 - \phi_3) + R_4 \sin(\phi_4 - \phi_3) \right] \\
\partial_t \phi_4 &= -3\beta - c_2 R_4^2 \\
&\quad + \frac{\beta}{R_4} \left[R_1 \cos(\phi_1 - \phi_4) + R_2 \cos(\phi_2 - \phi_4) + R_3 \cos(\phi_3 - \phi_4) \right] \\
&\quad + \frac{\alpha}{R_4} \left[R_1 \sin(\phi_1 - \phi_4) + R_2 \sin(\phi_2 - \phi_4) + R_3 \sin(\phi_3 - \phi_4) \right]
\end{aligned}
$$

which can be reduced using the differences $\Delta\phi_{43} = \phi_4 - \phi_3$, $\Delta\phi_{32} = \phi_3 - \phi_2$ and $\Delta\phi_{21} = \phi_2 - \phi_1$

$$
\begin{aligned}
\partial_t \phi_1 &= -3\beta - c_2 R_1^2 \\
&\quad + \frac{\beta}{R_1} \left[R_2 \cos(\Delta\phi_{21}) + R_3 \cos(\Delta\phi_{32} + \Delta\phi_{21}) + R_4 \cos(\Delta\phi_{43} + \Delta\phi_{32} + \Delta\phi_{21}) \right] \\
&\quad + \frac{\alpha}{R_1} \left[R_2 \sin(\Delta\phi_{21}) + R_3 \sin(\Delta\phi_{32} + \Delta\phi_{21}) + R_4 \sin(\Delta\phi_{43} + \Delta\phi_{32} + \Delta\phi_{21}) \right] \\
\partial_t \phi_2 &= -3\beta - c_2 R_2^2
\end{aligned}
$$

$$
\begin{aligned}
&+ \frac{\beta}{R_2}\left[R_1\cos\left(\Delta\phi_{21}\right) + R_3\cos\left(\Delta\phi_{32}\right) + R_4\cos\left(\Delta\phi_{43}+\Delta\phi_{32}\right)\right] \\
&+ \frac{\alpha}{R_2}\left[R_1\sin\left(-\Delta\phi_{21}\right) + R_3\sin\left(\Delta\phi_{21}\right) + R_4\sin\left(\Delta\phi_{43}+\Delta\phi_{32}\right)\right]
\end{aligned}
$$

$$
\begin{aligned}
\partial_t\phi_3 &= -3\beta - c_2R_3^2 \\
&+ \frac{\beta}{R_3}\left[R_1\cos\left(\Delta\phi_{32}+\Delta\phi_{21}\right) + R_2\cos\left(\Delta\phi_{32}\right) + R_4\cos\left(\Delta\phi_{43}\right)\right] \\
&+ \frac{\alpha}{R_3}\left[R_1\sin\left(-\Delta\phi_{21}-\Delta\phi_{32}\right) + R_2\sin\left(-\Delta\phi_{32}\right) + R_4\sin\left(\Delta\phi_{43}\right)\right] \\
\partial_t\phi_4 &= -3\beta - c_2R_4^2 \\
&+ \frac{\beta}{R_4}\left[R_1\cos\left(\Delta\phi_{43}+\Delta\phi_{32}+\Delta\phi_{21}\right) + R_2\cos\left(\Delta\phi_{43}+\Delta\phi_{32}\right) + R_3\cos\left(\Delta\phi_{43}\right)\right] \\
&+ \frac{\alpha}{R_4}\left[R_1\sin\left(-\Delta\phi_{43}-\Delta\phi_{32}-\Delta\phi_{21}\right) + R_2\sin\left(-\Delta\phi_{43}-\Delta\phi_{32}\right) + R_3\sin\left(-\Delta\phi_{43}\right)\right]
\end{aligned}
$$

Reducing them to three yields

$$
\begin{aligned}
\partial_t\Delta\phi_{21} &= -c_2\left(R_2^2 - R_1^2\right) \\
&+ \frac{\beta}{R_2}\left[R_1\cos\left(\Delta\phi_{21}\right) + R_3\cos\left(\Delta\phi_{32}\right) + R_4\cos\left(\Delta\phi_{43}+\Delta\phi_{32}\right)\right] \\
&- \frac{\beta}{R_1}\left[R_2\cos\left(\Delta\phi_{21}\right) + R_3\cos\left(\Delta\phi_{32}+\Delta\phi_{21}\right) + R_4\cos\left(\Delta\phi_{43}+\Delta\phi_{32}+\Delta\phi_{21}\right)\right] \\
&+ \frac{\alpha}{R_2}\left[R_1\sin\left(-\Delta\phi_{21}\right) + R_3\sin\left(\Delta\phi_{32}\right) + R_4\sin\left(\Delta\phi_{43}+\Delta\phi_{32}\right)\right] \\
&- \frac{\alpha}{R_1}\left[R_2\sin\left(\Delta\phi_{21}\right) + R_3\sin\left(\Delta\phi_{32}+\Delta\phi_{21}\right) + R_4\sin\left(\Delta\phi_{43}+\Delta\phi_{32}+\Delta\phi_{21}\right)\right] \\
\partial_t\Delta\phi_{32} &= -c_2\left(R_3^2 - R_3^2\right) \\
&+ \frac{\beta}{R_3}\left[R_1\cos\left(\Delta\phi_{32}+\Delta\phi_{21}\right) + R_2\cos\left(\Delta\phi_{32}\right) + R_4\cos\left(\Delta\phi_{43}\right)\right] \\
&- \frac{\beta}{R_2}\left[R_1\cos\left(\Delta\phi_{21}\right) + R_3\cos\left(\Delta\phi_{32}\right) + R_4\cos\left(\Delta\phi_{43}+\Delta\phi_{32}\right)\right] \\
&+ \frac{\alpha}{R_3}\left[R_1\sin\left(-\Delta\phi_{21}-\Delta\phi_{32}\right) + R_2\sin\left(-\Delta\phi_{32}\right) + R_4\sin\left(\Delta\phi_{43}\right)\right] \\
&- \frac{\alpha}{R_2}\left[R_1\sin\left(-\Delta\phi_{21}\right) + R_3\sin\left(\Delta\phi_{32}\right) + R_4\sin\left(\Delta\phi_{43}+\Delta\phi_{32}\right)\right] \\
\partial_t\Delta\phi_{43} &= -c_2\left(R_4^2 - R_3^2\right) \\
&+ \frac{\beta}{R_4}\left[R_1\cos\left(\Delta\phi_{43}+\Delta\phi_{32}+\Delta\phi_{21}\right) + R_2\cos\left(\Delta\phi_{43}+\Delta\phi_{32}\right) + R_3\cos\left(\Delta\phi_{43}\right)\right] \\
&- \frac{\beta}{R_3}\left[R_1\cos\left(\Delta\phi_{32}+\Delta\phi_{21}\right) + R_2\cos\left(\Delta\phi_{32}\right) + R_4\cos\left(\Delta\phi_{43}\right)\right]
\end{aligned}
$$

$$
\begin{aligned}
&+ \frac{\alpha}{R_4}\left[R_1 \sin\left(-\Delta\phi_{43} - \Delta\phi_{32} - \Delta\phi_{21}\right) + R_2 \sin\left(-\Delta\phi_{43} - \Delta\phi_{32}\right) + R_3 \sin\left(-\Delta\phi_{43}\right)\right] \\
&- \frac{\alpha}{R_3}\left[R_1 \sin\left(-\Delta\phi_{21} - \Delta\phi_{32}\right) + R_2 \sin\left(-\Delta\phi_{32}\right) + R_4 \sin\left(\Delta\phi_{43}\right)\right]
\end{aligned}
$$

together with the amplitude equations

$$
\begin{aligned}
\partial_t R_1 &= \left(1 - 3\alpha\right) R_1 - R_1^3 \\
&\quad + \alpha\left[R_2 \cos\left(\Delta\phi_{21}\right) + R_3 \cos\left(\Delta\phi_{32} + \Delta\phi_{21}\right) + R_4 \cos\left(\Delta\phi_{43} + \Delta\phi_{32} + \Delta\phi_{21}\right)\right] \\
&\quad - \beta\left[R_2 \sin\left(\Delta\phi_{21}\right) + R_3 \sin\left(\Delta\phi_{32} + \Delta\phi_{21}\right) + R_4 \sin\left(\Delta\phi_{43} + \Delta\phi_{32} + \Delta\phi_{21}\right)\right] \\
\partial_t R_2 &= \left(1 - 3\alpha\right) R_2 - R_2^3 \\
&\quad + \alpha\left[R_1 \cos\left(\Delta\phi_{21}\right) + R_3 \cos\left(\Delta\phi_{32}\right) + R_4 \cos\left(\Delta\phi_{43} + \Delta\phi_{32}\right)\right] \\
&\quad - \beta\left[R_1 \sin\left(-\Delta\phi_{21}\right) + R_3 \sin\left(\Delta\phi_{32}\right) + R_4 \sin\left(\Delta\phi_{43} + \Delta\phi_{32}\right)\right] \\
\partial_t R_3 &= \left(1 - 3\alpha\right) R_3 - R_3^3 \\
&\quad + \alpha\left[R_1 \cos\left(\Delta\phi_{32} + \Delta\phi_{21}\right) + R_2 \cos\left(\Delta\phi_{32}\right) + R_4 \cos\left(\Delta\phi_{43}\right)\right] \\
&\quad - \beta\left[R_1 \sin\left(-\Delta\phi_{32} - \Delta\phi_{21}\right) + R_2 \sin\left(-\Delta\phi_{32}\right) + R_4 \sin\left(\Delta\phi_{43}\right)\right] \\
\partial_t R_4 &= \left(1 - 3\alpha\right) R_4 - R_4^3 \\
&\quad + \alpha\left[R_1 \cos\left(\Delta\phi_{43} + \Delta\phi_{32} + \Delta\phi_{21}\right) + R_2 \cos\left(\Delta\phi_{43} + \Delta\phi_{32}\right) + R_3 \cos\left(\Delta\phi_{43}\right)\right] \\
&\quad - \beta\left[R_1 \sin\left(-\Delta\phi_{43} - \Delta\phi_{32} - \Delta\phi_{21}\right) + R_2 \sin\left(-\Delta\phi_{43} - \Delta\phi_{32}\right) + R_3 \sin\left(-\Delta\phi_{43}\right)\right]
\end{aligned}
$$

Appendix C

CO-Oxidation Model with Global Coupling

For the CO-oxidation model, the dynamics of the coverage of carbon monoxide, c, is modeled by

$$\partial_t c = D\nabla^2 c + k_1 p_{\mathrm{co}} s_{\mathrm{c}} \left(1 - \left(\frac{c}{c_{\mathrm{s}}}\right)^3\right) - k_2 c - k_3 co \tag{C.1}$$

with the diffusion coefficient for CO, D, the rate of CO hitting the surface, k_1, the partial pressure of CO, p_{co}, the sticking coefficient of CO, s_{c}, the saturation coverage c_{s}, the CO-desorption rate k_2, the reaction rate k_3 and the oxygen coverage o. Unlike earlier studies [109], we assume that the diffusion process is isotropic and take the diffusion coefficient D as constant. The oxygen coverage o follows

$$\partial_t o = k_4 p_{\mathrm{o}_2} \left(\left(s_{\mathrm{o}_1} - s_{\mathrm{o}_2}\right) w + s_{\mathrm{o}_2}\right) \left(1 - \frac{c}{c_{\mathrm{s}}} - \frac{o}{o_{\mathrm{s}}}\right)^2 - k_3 co,$$

where k_4 is the rate of the oxygen molecules hitting the surface, p_{o_2} the partial pressure of these molecules in the gas phase, s_{o_1} and s_{o_2} are the sticking coefficients of oxygen on the 1×1 and 1×2 surface structure, respectively, and o_{s} is the saturation coverage of o. Notice that the adsorption of oxygen depends on the surface structure, w. This variable can be described by

$$\partial_t w = k_5 \left(g\left(\frac{c}{c_{\mathrm{s}}}\right) - w\right)$$

with the function $g(x)$,

$$g\left(x\right) = \begin{cases} 0 & \text{if } 0 \leq x < 0.2 \\ -\frac{x^3 - 1.05x^2 + 0.3x - 0.026}{0.0135} & \text{if } 0.2 \leq x \leq 0.5 \\ 1 & \text{if } 0.5 < x \leq 1.0. \end{cases}$$

Falcke and Engel introduced a global coupling through the gas phase through the partial pressure p_{co} [109]. The equation for changes of p_{co}, Eq. (C.2), results from

a constant inflow with p_{coe}, outflow with p_{co} and changes through adsorption and desorption. This can be summarized as shown in Eq. (C.2),

$$\partial_t p_{\mathrm{co}} = \frac{J}{V}\left(p_{\mathrm{coe}} - p_{\mathrm{co}}\left(1 + \frac{V_{\mathrm{ML}}}{JL}\int\left[k_1 p_{\mathrm{co}}\left(1 - \left(\frac{c}{c_{\mathrm{s}}}\right)^3\right) - k_2\frac{c}{c_{\mathrm{s}}}\right]dr\right)\right) \tag{C.2}$$

with J denoting the gas flow into the reactor, A the surface area, V the reactor volume and V_{ML} the volume of a mono-layer [109]. The parameters for this model are summarized in Table C.1 [109, 158]. Hereby the reaction rates k_i for $i = 2, 3, 5$ follow the Arrhenius equation

$$k_i = A_i e^{-E_i/(RT)}.$$

Integration parameters are $N = 3600$ and $L = 1800\,\mu$m. A fourth-order Runge-Kutta method with fixed time step $dt = 10^{-4}\,$s is used for integration.

Rate of CO hitting the surface	k_1	$4.18 \cdot 10^5\,\mathrm{s}^{-1}\mathrm{Torr}^{-1}$
CO sticking coefficient	s_{c}	1
CO saturation coverage	c_{s}	1
Rate of O_2 hitting the surface	k_4	$4.18 \cdot 10^5\,\mathrm{s}^{-1}\mathrm{Torr}^{-1}$
O_2 sticking coefficient on 1×1	s_{o_1}	0.6
O_2 sticking coefficient on 1×2	s_{o_2}	0.4
O_2 saturation coverage	o_{s}	0.8
Reaction rate	k_3	$A_3 = 3 \cdot 10^6\,\mathrm{s}^{-1}$, $E_3 = 10\,\mathrm{kcal/mol}$
CO desorption rate	k_2	$A_2 = 2 \cdot 10^{16}\,\mathrm{s}^{-1}$, $E_2 = 38\,\mathrm{kcal/mol}$
Surface structure transition rate	k_5	$A_5 = 10^2\,\mathrm{s}^{-1}$, $E_5 = 7\,\mathrm{kcal/mol}$
Diffusion coefficient	D	$10 \cdot 10^{-12}\,\mathrm{m}^2/\mathrm{s}$
Temperature	T	545 K
Partial pressure of CO in the gas inflow	p_{coe}	$3.992 \cdot 10^{-5}\,\mathrm{Torr}$
Reactor volume	V	50 l
Gas flow into the reactor	J	360 l/s
Partial pressure of O_2	p_{o_2}	$1.17 \cdot 10^{-4}\,\mathrm{Torr}$
Volume of a mono-layer	V_{ML}	0.3 l/ML
Length of the electrode	L	$L = 1800\,\mu$m

Table C.1: Parameters for the CO-oxidation model (C.1) to (C.2)

Bibliography

[1] D. H. Hubel and T. N. Wiesel. 'Receptive Fields of Single Neurones in the Cat's Striate Cortex'. In: *The Journal of Physiology* 148.3 (1959), pp. 574–591. DOI: 10.1113/jphysiol.1959.sp006308.

[2] M.A. Fischler and R.A. Elschlager. 'The Representation and Matching of Pictorial Structures'. In: *IEEE Transactions on Computers* C-22.1 (1973), pp. 67–92. DOI: 10.1109/t-c.1973.223602.

[3] David Marr. *Vision: A Computational Investigation into the Human Representation and Processing of Visual Information*. The MIT Press, 2010, p. 432. DOI: 10.7551/mitpress/9780262514620.001.0001.

[4] R.F. Thompson. *The Brain: A Neuroscience Primer*. Worth Publishers, 2000.

[5] *Human Brain Project - Brain Simulation Platform*. https://www.humanbrainproject.eu/en/brain-simulation/brain-simulation-platform/. Accessed: 2018-09-17.

[6] A L Hodgkin and A F Huxley. 'A quantitative description of membrane current and its application to conduction and excitation in nerve'. In: *The Journal of Physiology* 117.4 (1952), pp. 500–544.

[7] Richard FitzHugh. 'Impulses and Physiological States in Theoretical Models of Nerve Membrane'. In: *Biophysical Journal* 1.6 (1961), pp. 445–466.

[8] J. Nagumo, S. Arimoto and S. Yoshizawa. 'An Active Pulse Transmission Line Simulating Nerve Axon'. In: *Proceedings of the IRE* 50.10 (Oct. 1962), pp. 2061–2070. DOI: 10.1109/JRPROC.1962.288235.

[9] J L Hindmarsh and R M Rose. 'A model of neuronal bursting using three coupled first order differential equations'. In: *Proc R Soc Lond B Biol Sci* 221.1222 (1984), pp. 87–102.

[10] Gian Gastone Mascetti. 'Unihemispheric sleep and asymmetrical sleep: behavioral, neurophysiological, and functional perspectives'. In: *Nature and Science of Sleep* 8 (2016), pp. 221–238. DOI: 10.2147/NSS.S71970.

[11] Florian Mormann et al. 'Seizure prediction: the long and winding road'. In: *Brain* 130.2 (2007), pp. 314–333. DOI: 10.1093/brain/awl241.

[12] Daniel M. Abrams and Steven H. Strogatz. 'Chimera States for Coupled Oscillators'. In: *Phys. Rev. Lett.* 93 (17 Oct. 2004), p. 174102. DOI: 10.1103/PhysRevLett.93.174102.

[13] D. Golomb et al. 'Clustering in globally coupled phase oscillators'. In: *Phys. Rev. A* 45 (6 Mar. 1992), pp. 3516–3530. DOI: 10.1103/PhysRevA.45.3516.

[14] P. Ashwin and J. W. Swift. 'The dynamics of n weakly coupled identical oscillators'. In: *Journal of Nonlinear Science* 2.1 (Mar. 1992), pp. 69–108. DOI: 10.1007/BF02429852.

[15] Koji Okuda. 'Variety and Generality of Clustering in Globally Coupled Oscillators'. In: *Physica D: Nonlinear Phenomena* 63.3-4 (1993), pp. 424–436. DOI: 10.1016/0167-2789(93)90121-g.

[16] D. Battogtokh, A. Preusser and A. Mikhailov. 'Localized turbulence and cellular structures in systems with global coupling'. In: *Nonlinear Physics of Complex Systems*. Ed. by Jürgen Parisi, Stefan C. Müller and Walter Zimmermann. Berlin, Heidelberg: Springer Berlin Heidelberg, 1996, pp. 149–165. DOI: 10.1007/BFb0105436.

[17] Felix P. Kemeth, Sindre W. Haugland and Katharina Krischer. 'Symmetries of Chimera States'. In: *Phys. Rev. Lett.* 120 (21 May 2018), p. 214101. DOI: 10.1103/PhysRevLett.120.214101.

[18] F. P. Kemeth, S. W. Haugland and K. Krischer. 'Cluster singularities: the unfolding of clustering behavior in globally coupled oscillatory systems'. In: *ArXiv e-prints* (July 2018).

[19] Felix P. Kemeth et al. 'A classification scheme for chimera states'. In: *Chaos: An Interdisciplinary Journal of Nonlinear Science* 26.9 (2016), p. 094815. DOI: 10.1063/1.4959804.

[20] F. P. Kemeth et al. 'An Emergent Space for Distributed Data with Hidden Internal Order through Manifold Learning'. In: *IEEE Access* (Nov. 2018), pp. 1–1. DOI: 10.1109/ACCESS.2018.2882777.

[21] Y. Kuramoto. *Chemical Oscillations, Waves and Turbulence*. Vol. 19. Springer-Verlag Berlin Heidelberg, 1984, p. 158. DOI: 10.1007/978-3-642-69689-3.

[22] Vladimir García-Morales and Katharina Krischer. 'Normal-form approach to spatiotemporal pattern formation in globally coupled electrochemical systems'. In: *Phys. Rev. E* 78 (5 Nov. 2008), p. 057201. DOI: 10.1103/PhysRevE.78.057201.

[23] Vladimir García-Morales and Katharina Krischer. 'Nonlocal Complex Ginzburg-Landau Equation for Electrochemical Systems'. In: *Phys. Rev. Lett.* 100 (5 Feb. 2008), p. 054101. DOI: 10.1103/PhysRevLett.100.054101.

[24] D.G. Aronson, G.B. Ermentrout and N. Kopell. 'Amplitude Response of Coupled Oscillators'. In: *Physica D: Nonlinear Phenomena* 41.3 (1990), pp. 403–449. DOI: 10.1016/0167-2789(90)90007-c.

[25] D. Battogtokh and A. Mikhailov. 'Controlling turbulence in the complex Ginzburg-Landau equation'. In: *Physica D: Nonlinear Phenomena* 90.1 (1996), pp. 84–95. DOI: https://doi.org/10.1016/0167-2789(95)00232-4.

[26] D. Battogtokh, A. Preusser and A. Mikhailov. 'Controlling turbulence in the complex Ginzburg-Landau equation II. Two-dimensional systems'. In: *Physica D: Nonlinear Phenomena* 106.3 (1997), pp. 327–362. DOI: https://doi.org/10.1016/S0167-2789(97)00046-8.

[27] W. Ostwald. 'Über die vermeintliche Isomerie des roten und gelben Quecksilberoxyds und die Oberflächenspannung fester Körper'. In: *Zeitschrift für Physikalische Chemie* 37 (1900), pp. 495–503. DOI: 10.1515/zpch-1900-3431.

[28] A. Baldan. 'Review Progress in Ostwald ripening theories and their applications to nickel-base superalloys Part I: Ostwald ripening theories'. In: *Journal of Materials Science* 37.11 (June 2002), pp. 2171–2202. DOI: 10.1023/A:1015388912729.

[29] Gautam C. Sethia and Abhijit Sen. 'Chimera States: The Existence Criteria Revisited'. In: *Phys. Rev. Lett.* 112 (14 Apr. 2014), p. 144101. DOI: 10.1103/PhysRevLett.112.144101.

[30] Lennart Schmidt and Katharina Krischer. 'Chimeras in globally coupled oscillatory systems: From ensembles of oscillators to spatially continuous media'. In: *Chaos: An Interdisciplinary Journal of Nonlinear Science* 25.6 (2015), p. 064401. DOI: 10.1063/1.4921727.

[31] Vladimir García-Morales and Katharina Krischer. 'The complex Ginzburg-Landau equation: An introduction'. In: *Contemporary Physics* 53.2 (2012), pp. 79–95. DOI: 10.1080/00107514.2011.642554.

[32] Arkady Pikovsky, Michael Rosenblum and Jürgen Kurths. 'Mutual synchronization of two interacting periodic oscillators'. In: *Synchronization*. Synchronization. Cambridge University Press (CUP), 2001, pp. 222–235. DOI: 10.1017/cbo9780511755743.009.

[33] Martin Golubitsky and Ian Stewart. *The Symmetry Perspective: From Equilibrium to Chaos in Phase Space and Physical Space*. Basel, Boston, Berlin: Birkäuser Verlag, 2003.

[34] Yoshiki Kuramoto and Ikuko Nishikawa. 'Statistical Macrodynamics of Large Dynamical Systems. Case of a Phase Transition in Oscillator Communities'. In: *Journal of Statistical Physics* 49.3-4 (1987), pp. 569–605. DOI: 10.1007/bf01009349.

[35] Arkady Pikovsky and Michael Rosenblum. 'Dynamics of Globally Coupled Oscillators: Progress and Perspectives'. In: *Chaos: An Interdisciplinary Journal of Nonlinear Science* 25.9 (2015), p. 097616. DOI: 10.1063/1.4922971.

[36] Vincent Hakim and Wouter-Jan Rappel. 'Dynamics of the Globally Coupled Complex Ginzburg-Landau Equation'. In: *Physical Review A* 46.12 (1992), R7347–R7350. DOI: 10.1103/physreva.46.r7347.

[37] Wai Lim Ku, Michelle Girvan and Edward Ott. 'Dynamical Transitions in Large Systems of Mean Field-Coupled Landau-Stuart Oscillators: Extensive Chaos and Cluster States'. In: *Chaos: An Interdisciplinary Journal of Nonlinear Science* 25.12 (2015), p. 123122. DOI: 10.1063/1.4938534.

[38] Kwok Yeung Tsang et al. 'Dynamics of a Globally Coupled Oscillator Array'. In: *Physica D: Nonlinear Phenomena* 48.1 (1991), pp. 102–112. DOI: 10.1016/0167-2789(91)90054-d.

[39] D G Aronson, M Golubitsky and J Mallet-Paret. 'Ponies on a merry-go-round in large arrays of Josephson junctions'. In: *Nonlinearity* 4.3 (1991), p. 903.

[40] Lingfa Yang et al. 'Oscillatory clusters in a model of the photosensitive Belousov-Zhabotinsky reaction system with global feedback'. In: *Phys. Rev. E* 62 (5 Nov. 2000), pp. 6414–6420. DOI: 10.1103/PhysRevE.62.6414.

[41] Robert H. Clewley et al. *PyDSTool, a software environment for dynamical systems modeling*. URL http://pydstool.sourceforge.net. 2007.

[42] Robert H. Clewley. 'Hybrid Models and Biological Model Reduction with PyDSTool'. In: *PLoS Computational Biology* 8.8 (2012), e1002628. DOI: 10.1371/journal.pcbi.1002628.

[43] John Guckenheimer. 'Multiple Bifurcation Problems for Chemical Reactors'. In: *Physica D: Nonlinear Phenomena* 20.1 (1986), pp. 1–20. DOI: 10.1016/0167-2789(86)90093-x.

[44] Lennart Schmidt and Katharina Krischer. 'Two-cluster solutions in an ensemble of generic limit-cycle oscillators with periodic self-forcing via the mean-field'. In: *Phys. Rev. E* 90 (4 Oct. 2014), p. 042911. DOI: 10.1103/PhysRevE.90.042911.

[45] J M Gambaudo, P Glendinning and C Tresser. 'The gluing bifurcation: I. Symbolic dynamics of closed curves'. In: *Nonlinearity* 1.1 (1988), p. 203.

[46] Jianfu Ma and Jianhong Wu. 'Multistability and gluing bifurcation to butterflies in coupled networks with non-monotonic feedback'. In: *Nonlinearity* 22.6 (2009), p. 1383.

[47] Galina N. Borisyuk et al. 'Dynamics and bifurcations of two coupled neural oscillators with different connection types'. In: *Bulletin of Mathematical Biology* 57.6 (Nov. 1995), pp. 809–840. DOI: 10.1007/BF02458296.

[48] N. Nakagawa and Y. Kuramoto. 'Collective Chaos in a Population of Globally Coupled Oscillators'. In: *Progress of Theoretical Physics* 89.2 (1993), pp. 313–323. DOI: 10.1143/ptp/89.2.313.

[49] T. Brooke Benjamin and J. E. Feir. 'The Disintegration of Wave Trains on Deep Water Part 1. Theory'. In: *Journal of Fluid Mechanics* 27.03 (1967), p. 417. DOI: 10.1017/s002211206700045x.

[50] Mitchell J. Feigenbaum. 'Quantitative universality for a class of nonlinear transformations'. In: *Journal of Statistical Physics* 19.1 (July 1978), pp. 25–52. DOI: 10.1007/BF01020332.

[51] Mitchell J. Feigenbaum. 'The universal metric properties of nonlinear transformations'. In: *Journal of Statistical Physics* 21.6 (Dec. 1979), pp. 669–706. DOI: 10.1007/BF01107909.

[52] J. -P. Eckmann. 'Roads to turbulence in dissipative dynamical systems'. In: *Rev. Mod. Phys.* 53 (4 Oct. 1981), pp. 643–654. DOI: 10.1103/RevModPhys.53.643.

[53] S. Newhouse, D. Ruelle and F. Takens. 'Occurrence of strange Axiom A attractors near quasiperiodic flows on $T^m, m \geq 3$'. In: *Comm. Math. Phys.* 64.1 (1978), pp. 35–40.

[54] Lennart Schmidt et al. 'Coexistence of synchrony and incoherence in oscillatory media under nonlinear global coupling'. In: *Chaos: An Interdisciplinary Journal of Nonlinear Science* 24.1 (2014), p. 013102. DOI: 10.1063/1.4858996.

[55] Murad Banaji. 'Clustering in globally coupled oscillators.' In: *Dynamical Systems: An International Journal* 17.3 (2002), pp. 263–285. DOI: 10.1080/14689360210148485.

[56] Stephen H. Strogatz. *Nonlinear Dynamics and Chaos, 2nd Edition*. Oxford, UK: Routledge Tazlor & Francis Group, 2015, p. 532.

[57] Arkady Pikovsky and Antonio Politi. *Lyapunov Exponents - A Tool to Explore Complex Dynamics*. Cambridge: Cambridge University Press, 2016.

[58] Alan Wolf et al. 'Determining Lyapunov exponents from a time series'. In: *Physica D: Nonlinear Phenomena* 16.3 (1985), pp. 285–317. DOI: https://doi.org/10.1016/0167-2789(85)90011-9.

[59] Gene H. Golub and Charles F. Van Loan. *Matrix Computations, third edition*. London: The Johns Hopkins University Press, 1996.

[60] Ippei Shimada and Tomomasa Nagashima. 'A Numerical Approach to Ergodic Problem of Dissipative Dynamical Systems'. In: *Progress of Theoretical Physics* 61.6 (1979), pp. 1605–1616. DOI: 10.1143/PTP.61.1605.

[61] Giancarlo Benettin et al. 'Lyapunov Characteristic Exponents for smooth dynamical systems and for hamiltonian systems; a method for computing all of them. Part 1: Theory'. In: *Meccanica* 15.1 (Mar. 1980), pp. 9–20. DOI: 10.1007/BF02128236.

[62] Giancarlo Benettin et al. 'Lyapunov Characteristic Exponents for smooth dynamical systems and for hamiltonian systems; A method for computing all of them. Part 2: Numerical application'. In: *Meccanica* 15.1 (Mar. 1980), pp. 21–30. DOI: 10.1007/BF02128237.

[63] Michael T. Rosenstein, James J. Collins and Carlo J. De Luca. 'A practical method for calculating largest Lyapunov exponents from small data sets'. In: *Physica D: Nonlinear Phenomena* 65.1 (1993), pp. 117–134. DOI: https://doi.org/10.1016/0167-2789(93)90009-P.

[64] J. -P. Eckmann et al. 'Liapunov exponents from time series'. In: *Phys. Rev. A* 34 (6 Dec. 1986), pp. 4971–4979. DOI: 10.1103/PhysRevA.34.4971.

[65] Ernest Barany, Michael Dellnitz and Martin Golubitsky. 'Detecting the symmetry of attractors'. In: *Physica D: Nonlinear Phenomena* 67.1 (1993), pp. 66–87. DOI: https://doi.org/10.1016/0167-2789(93)90198-A.

[66] Michael Dellnitz, Martin Golubitsky and Matthew Nicol. 'Symmetry of Attractors and the Karhunen-Loève Decomposition'. In: *Trends and Perspectives in Applied Mathematics*. New York, NY: Springer New York, 1994, pp. 73–108. DOI: 10.1007/978-1-4612-0859-4_4.

[67] P. Chossat and M. Golubitsky. 'Symmetry-increasing bifurcation of chaotic attractors'. In: *Physica D: Nonlinear Phenomena* 32.3 (1988), pp. 423–436. DOI: https://doi.org/10.1016/0167-2789(88)90066-8.

[68] B. J. Gluckman et al. 'Time averaging of chaotic spatiotemporal wave patterns'. In: *Phys. Rev. Lett.* 71 (13 Sept. 1993), pp. 2034–2037. DOI: 10.1103/PhysRevLett.71.2034.

[69] David K. Campbell. 'Nonlinear Science-From Paradigms to Practicalities'. In: *Los Alamos Science* 15 (1987), pp. 218–262.

[70] G. I. Taylor. 'Stability of a Viscous Liquid Contained between Two Rotating Cylinders'. In: *Philosophical Transactions of the Royal Society of London. Series A, Containing Papers of a Mathematical or Physical Character* 223 (1923), pp. 289–343.

[71] C. David Andereck, S. S. Liu and Harry L. Swinney. 'Flow regimes in a circular Couette system with independently rotating cylinders'. In: *Journal of Fluid Mechanics* 164 (1986), pp. 155–183. DOI: 10.1017/S0022112086002513.

[72] A. Brandstäter et al. 'Low-Dimensional Chaos in a Hydrodynamic System'. In: *Phys. Rev. Lett.* 51 (16 Oct. 1983), pp. 1442–1445. DOI: 10.1103/PhysRevLett.51.1442.

[73] A. Brandstäter and Harry L. Swinney. 'Strange attractors in weakly turbulent Couette-Taylor flow'. In: *Phys. Rev. A* 35 (5 Mar. 1987), pp. 2207–2220. DOI: 10.1103/PhysRevA.35.2207.

[74] Yasushi Takeda. 'Quasi-periodic state and transition to turbulence in a rotating Couette system'. In: *Journal of Fluid Mechanics* 389 (1999), pp. 81–99. DOI: 10.1017/S0022112099005091.

[75] M. Field and M. Golubitsky. *Symmetry in Chaos*. Second. Society for Industrial and Applied Mathematics, 2009. DOI: 10.1137/1.9780898717709.

[76] Peter Ashwin and Jörg Tomes. 'Detection of symmetry of attractors from observations II. An experiment with S4 symmetry'. In: *Physica D: Nonlinear Phenomena* 100.1 (1997), pp. 71–84. DOI: https://doi.org/10.1016/S0167-2789(96)00176-5.

[77] V. Tchistiakov. 'Detecting symmetry breaking bifurcations in the system describing the dynamics of coupled arrays of Josephson junctions'. In: *Physica D: Nonlinear Phenomena* 91.1 (1996), pp. 67–85. DOI: https://doi.org/10.1016/0167-2789(95)00253-7.

[78] Martin Golubitsky and Ian Stewart. 'Recent advances in symmetric and network dynamics'. In: *Chaos: An Interdisciplinary Journal of Nonlinear Science* 25.9 (2015), p. 097612. DOI: 10.1063/1.4918595.

[79] Peter Ashwin and Oleksandr Burylko. 'Weak chimeras in minimal networks of coupled phase oscillators'. In: *Chaos: An Interdisciplinary Journal of Nonlinear Science* 25.1 (2015), p. 013106. DOI: 10.1063/1.4905197.

[80] J. P. van der Weele. 'Symmetry Breaking in the Period Doubling Route to Chaos'. In: *Chaotic Dynamics: Theory and Practice*. Ed. by T. Bountis. Boston, MA: Springer US, 1992, pp. 357–369. DOI: 10.1007/978-1-4615-3464-8_33.

[81] Joseph D. Hart et al. 'Experimental observation of chimera and cluster states in a minimal globally coupled network'. In: *Chaos: An Interdisciplinary Journal of Nonlinear Science* 26.9 (2016), p. 094801. DOI: 10.1063/1.4953662.

[82] Yoshiki Kuramoto and Dorjsuren Battogtokh. 'Coexistence of Coherence and Incoherence in Nonlocally Coupled Phase Oscillators'. In: *Nonlinear Phenom. Complex Syst.* 5 (2002), pp. 380–385.

[83] Yuri Maistrenko et al. 'Smallest chimera states'. In: *Phys. Rev. E* 95 (1 Jan. 2017), p. 010203. DOI: 10.1103/PhysRevE.95.010203.

[84] Louis M. Pecora et al. 'Cluster synchronization and isolated desynchronization in complex networks with symmetries'. In: *Nature Communications* 5 (June 2014), p. 4079. DOI: 10.1038/ncomms5079.

[85] Edward Ott and John C. Sommerer. 'Blowout bifurcations: the occurrence of riddled basins and on-off intermittency'. In: *Physics Letters A* 188.1 (1994), pp. 39–47. DOI: https://doi.org/10.1016/0375-9601(94)90114-7.

[86] Laurette S. Tuckerman and Dwight Barkley. 'Bifurcation analysis of the Eckhaus instability'. In: *Physica D: Nonlinear Phenomena* 46.1 (1990), pp. 57–86. DOI: 10.1016/0167-2789(90)90113-4.

[87] Carlo R. Laing and Carson C. Chow. 'Stationary Bumps in Networks of Spiking Neurons'. In: *Neural Computation* 13.7 (2001), pp. 1473–1494. DOI: 10.1162/089976601750264974.

[88] N.C Rattenborg, C.J Amlaner and S.L Lima. 'Behavioral, neurophysiological and evolutionary perspectives on unihemispheric sleep'. In: *Neuroscience and Biobehavioral Reviews* 24.8 (2000), pp. 817–842. DOI: http://dx.doi.org/10.1016/S0149-7634(00)00039-7.

[89] Dwight Barkley and Laurette S. Tuckerman. 'Computational Study of Turbulent Laminar Patterns in Couette Flow'. In: *Phys. Rev. Lett.* 94 (1 Jan. 2005), p. 014502. DOI: 10.1103/PhysRevLett.94.014502.

[90] Yohann Duguet and Philipp Schlatter. 'Oblique Laminar-Turbulent Interfaces in Plane Shear Flows'. In: *Phys. Rev. Lett.* 110 (3 Jan. 2013), p. 034502. DOI: 10.1103/PhysRevLett.110.034502.

[91] Grigory Bordyugov, Arkady Pikovsky and Michael Rosenblum. 'Self-emerging and turbulent chimeras in oscillator chains'. In: *Phys. Rev. E* 82 (3 2010), p. 035205.

[92] Iryna Omelchenko et al. 'Loss of Coherence in Dynamical Networks: Spatial Chaos and Chimera States'. In: *Phys. Rev. Lett.* 106 (23 June 2011), p. 234102. DOI: 10.1103/PhysRevLett.106.234102.

[93] Aaron M. Hagerstrom et al. 'Experimental observation of chimeras in coupled-map lattices'. In: *Nature Physics* 8 (2012), pp. 658–661. DOI: http://dx.doi.org/10.1038/nphys2372.

[94] Iryna Omelchenko et al. 'When Nonlocal Coupling between Oscillators Becomes Stronger: Patched Synchrony or Multichimera States'. In: *Phys. Rev. Lett.* 110 (22 May 2013), p. 224101. DOI: 10.1103/PhysRevLett.110.224101.

[95] Gautam C. Sethia, Abhijit Sen and George L. Johnston. 'Amplitude-mediated chimera states'. In: *Phys. Rev. E* 88 (4 Oct. 2013), p. 042917. DOI: 10.1103/PhysRevE.88.042917.

[96] Anna Zakharova, Marie Kapeller and Eckehard Schöll. 'Chimera Death: Symmetry Breaking in Dynamical Networks'. In: *Phys. Rev. Lett.* 112 (15 Apr. 2014), p. 154101. DOI: 10.1103/PhysRevLett.112.154101.

[97] Daniel M. Abrams et al. 'Solvable Model for Chimera States of Coupled Oscillators'. In: *Phys. Rev. Lett.* 101 (8 Aug. 2008), p. 084103. DOI: 10.1103/PhysRevLett.101.084103.

[98] Mark R. Tinsley, Simbarashe Nkomo and Kenneth Showalter. 'Chimera and phase-cluster states in populations of coupled chemical oscillators'. In: *Nature Physics* 8 (2012), p. 662. DOI: 10.1038/nphys2371.

[99] Azamat Yeldesbay, Arkady Pikovsky and Michael Rosenblum. 'Chimeralike States in an Ensemble of Globally Coupled Oscillators'. In: *Phys. Rev. Lett.* 112 (14 Apr. 2014), p. 144103. DOI: 10.1103/PhysRevLett.112.144103.

[100] Erik Andreas Martens et al. 'Chimera states in mechanical oscillator networks'. In: *Proceedings of the National Academy of Sciences* 110.26 (2013), pp. 10563–10567. DOI: 10.1073/pnas.1302880110.

[101] Matthias Wolfrum and Oleh E. Omel'chenko. 'Chimera states are chaotic transients'. In: *Phys. Rev. E* 84 (1 July 2011), p. 015201. DOI: 10.1103/PhysRevE.84.015201.

[102] Lennart Schmidt and Katharina Krischer. 'Clustering as a Prerequisite for Chimera States in Globally Coupled Systems'. In: *Phys. Rev. Lett.* 114 (3 Jan. 2015), p. 034101. DOI: 10.1103/PhysRevLett.114.034101.

[103] Mark J Panaggio and Daniel M Abrams. 'Chimera states: coexistence of coherence and incoherence in networks of coupled oscillators'. In: *Nonlinearity* 28.3 (2015), R67.

[104] R. Gopal et al. 'Observation and characterization of chimera states in coupled dynamical systems with nonlocal coupling'. In: *Phys. Rev. E* 89 (5 May 2014), p. 052914. DOI: 10.1103/PhysRevE.89.052914.

[105] S.M. Cox and P.C. Matthews. 'Exponential Time Differencing for Stiff Systems'. In: *Journal of Computational Physics* 176.2 (Mar. 2002), pp. 430–455. DOI: 10.1006/jcph.2002.6995.

[106] B.I. Shraiman et al. 'Spatiotemporal chaos in the one-dimensional complex Ginzburg-Landau equation'. In: *Physica D: Nonlinear Phenomena* 57.3 (1992), pp. 241–248. DOI: http://dx.doi.org/10.1016/0167-2789(92)90001-4.

[107] Sindre W. Haugland, Lennart Schmidt and Katharina Krischer. 'Self-organized alternating chimera states in oscillatory media'. In: *Scientific Reports* 5 (2015), p. 9883. DOI: 10.1038/srep09883.

[108] Sarah A. M. Loos et al. 'Chimera patterns under the impact of noise'. In: *Phys. Rev. E* 93 (1 Jan. 2016), p. 012209. DOI: 10.1103/PhysRevE.93.012209.

[109] M. Falcke and H. Engel. 'Influence of global coupling through the gas phase on the dynamics of CO oxidation on Pt(110)'. In: *Phys. Rev. E* 50.2 (1994), pp. 1353–1359. DOI: 10.1103/PhysRevE.50.1353.

[110] M. Falcke and H. Engel. 'Pattern formation during the CO oxidation on Pt(110) surfaces under global coupling'. In: *The Journal of Chemical Physics* 101.7 (1994), pp. 6255–6263. DOI: 10.1063/1.468379.

[111] M. Falcke. *Strukturbildung in Reaktions- Diffusionssystemen und globale Kopplung*. Berlin, Sebastianstr. 84: Wissenschaft und Technik Verlag Gross, 1995.

[112] Konrad Schönleber et al. 'Pattern formation during the oscillatory photoelectrodissolution of n-type silicon: turbulence, clusters and chimeras'. In: *New Journal of Physics* 16.6 (2014), p. 063024.

[113] Iryna Omelchenko et al. 'Transition from spatial coherence to incoherence in coupled chaotic systems'. In: *Phys. Rev. E* 85 (2 Feb. 2012), p. 026212. DOI: 10.1103/PhysRevE.85.026212.

[114] Joshua B. Tenenbaum, Vin de Silva and John C. Langford. 'A Global Geometric Framework for Nonlinear Dimensionality Reduction'. In: *Science* 290.5500 (2000), pp. 2319–2323. DOI: 10.1126/science.290.5500.2319.

[115] Sam T. Roweis and Lawrence K. Saul. 'Nonlinear Dimensionality Reduction by Locally Linear Embedding'. In: *Science* 290.5500 (2000), pp. 2323–2326. DOI: 10.1126/science.290.5500.2323.

[116] Mikhail Belkin and Partha Niyogi. 'Laplacian Eigenmaps for Dimensionality Reduction and Data Representation'. In: *Neural Computation* 15.6 (2003), pp. 1373–1396. DOI: 10.1162/089976603321780317.

[117] R. R. Coifman et al. 'Geometric diffusions as a tool for harmonic analysis and structure definition of data: Diffusion maps'. In: *Proceedings of the National Academy of Sciences of the United States of America* 102.21 (2005), pp. 7426–7431. DOI: 10.1073/pnas.0500334102.

[118] Boaz Nadler et al. 'Diffusion Maps, Spectral Clustering and Eigenfunctions of Fokker-Planck Operators'. In: *Proceedings of the 18th International Conference on Neural Information Processing Systems*. NIPS'05. Vancouver, British Columbia, Canada: MIT Press, 2005, pp. 955–962.

[119] Ronald R. Coifman and Stéphane Lafon. 'Diffusion maps'. In: *Applied and Computational Harmonic Analysis* 21.1 (2006). Special Issue: Diffusion Maps and Wavelets, pp. 5–30. DOI: https://doi.org/10.1016/j.acha.2006.04.006.

[120] Oskar Perron. 'Zur Theorie der Matrices'. German. In: *Mathematische Annalen* 64.2 (1907), pp. 248–263. DOI: 10.1007/BF01449896.

[121] A. Singer and H.-T. Wu. 'Vector diffusion maps and the connection Laplacian'. In: *Communications on Pure and Applied Mathematics* 65.8 (2012), pp. 1067–1144. DOI: 10.1002/cpa.21395.

[122] Amit Singer and Ronald R. Coifman. 'Non-linear independent component analysis with diffusion maps'. In: *Applied and Computational Harmonic Analysis* 25.2 (2008), pp. 226–239. DOI: 10.1016/j.acha.2007.11.001.

[123] R. Talmon and R. R. Coifman. 'Empirical Intrinsic Geometry for Nonlinear Modeling and Time Series Filtering'. In: *Proceedings of the National Academy of Sciences* 110.31 (2013), pp. 12535–12540. DOI: 10.1073/pnas.1307298110.

[124] Carmeline J. Dsilva et al. 'Data-Driven Reduction for a Class of Multiscale Fast-Slow Stochastic Dynamical Systems'. In: *SIAM Journal on Applied Dynamical Systems* 15.3 (2016), pp. 1327–1351. DOI: 10.1137/151004896.

[125] Roy R. Lederman and Ronen Talmon. 'Learning the Geometry of Common Latent Variables Using Alternating-Diffusion'. In: *Applied and Computational Harmonic Analysis* 44.3 (2015), pp. 509–536. DOI: 10.1016/j.acha.2015.09.002.

[126] Ofir Lindenbaum et al. 'MultiView Diffusion Maps'. In: *CoRR* abs/1508.05550 (2015).

[127] Ronald R. Coifman and Matan Gavish. 'Harmonic Analysis of Digital Data Bases'. In: *Wavelets and Multiscale Analysis*. Wavelets and Multiscale Analysis. Birkhäuser Boston, 2011, pp. 161–197. DOI: 10.1007/978-0-8176-8095-4_9.

[128] *Reproduced from The Astronomical Almanac Online and produced by the U.S. Naval Observatory and H.M. Nautical Almanac Office*. 2017.

[129] *Boundary borders reproduced from thematicmapping.org under a Creative Common Attribution-Share Alike License, https://creativecommons.org/licenses/by-sa/3.0/*. 2009.

[130] Hugues Chaté and Paul Manneville. 'Dynamics of Complex Systems Phase diagram of the two-dimensional complex Ginzburg-Landau equation'. In: *Physica A: Statistical Mechanics and its Applications* 224.1 (1996), pp. 348–368. DOI: http://dx.doi.org/10.1016/0378-4371(95)00361-4.

[131] Jonathan Rubin and David Terman. 'Synchronized Activity and Loss of Synchrony Among Heterogeneous Conditional Oscillators'. In: *SIAM Journal on Applied Dynamical Systems* 1.1 (2002), pp. 146–174. DOI: 10.1137/S111111110240323X.

[132] Carlo R. Laing et al. 'Managing heterogeneity in the study of neural oscillator dynamics'. In: *The Journal of Mathematical Neuroscience* 2.1 (2012), pp. 1–22. DOI: 10.1186/2190-8567-2-5.

[133] M. Choi et al. 'Dimension reduction in heterogeneous neural networks: Generalized Polynomial Chaos (gPC) and ANalysis-Of-VAriance (ANOVA)'. In: *The European Physical Journal Special Topics* 225.6 (Sept. 2016), pp. 1165–1180. DOI: 10.1140/epjst/e2016-02662-3.

[134] Carlo R. Laing, Karthikeyan Rajendran and Ioannis G. Kevrekidis. 'Chimeras in random non-complete networks of phase oscillators'. In: *Chaos* 22.1, 013132 (2012), p. 013132. DOI: 10.1063/1.3694118.

[135] A.C. Hindmarsh. *LSODE. Ordinary Differential Equation System Solver.* Dec. 1986.

[136] K Radhakrishnan and A C Hindmarsh. 'Description and use of LSODE, the Livemore Solver for Ordinary Differential Equations'. In: (Dec. 1993). DOI: 10.2172/15013302.

[137] Kevin Höhlein. 'Extensive Chaos and Collective Order in Chimera States'. MA thesis. James-Franck-Str. 1, 85748 Garching: TU München, Oct. 2018.

[138] Tyrus Berry and John Harlim. 'Iterated diffusion maps for feature identification'. In: *Applied and Computational Harmonic Analysis* 45.1 (2018), pp. 84–119. DOI: 10.1016/j.acha.2016.08.005.

[139] Bubacarr Bah. 'Diffusion Maps: Analysis and Applications'. MA thesis. Linton Road, Oxford OX2 6UD: University of Oxford, Sept. 2008.

[140] R. R. Coifman et al. 'Graph Laplacian Tomography From Unknown Random Projections'. In: *IEEE Transactions on Image Processing* 17.10 (Oct. 2008), pp. 1891–1899. DOI: 10.1109/TIP.2008.2002305.

[141] Edward Ott and Thomas M. Antonsen. 'Low dimensional behavior of large systems of globally coupled oscillators'. In: *Chaos: An Interdisciplinary Journal of Nonlinear Science* 18.3 (2008), p. 037113. DOI: 10.1063/1.2930766.

[142] Edward Ott and Thomas M. Antonsen. 'Long time evolution of phase oscillator systems'. In: *Chaos: An Interdisciplinary Journal of Nonlinear Science* 19.2 (2009), p. 023117. DOI: 10.1063/1.3136851.

[143] H. S. Brown and I. G. Kevrekidis. 'Modulated traveling waves for the Kuramoto-Sivashinsky equation'. In: *Pattern Formation: Symmetry Methods and Applications (Fields Institute Communication).* Vol. 5. American Mathematical Society. Providence, RI, 1996.

[144] B. O. Koopman. 'Hamiltonian Systems and Transformation in Hilbert Space'. In: *Proceedings of the National Academy of Sciences* 17.5 (1931), pp. 315–318. DOI: 10.1073/pnas.17.5.315.

[145] P. J. Schmid et al. 'Applications of the Dynamic Mode Decomposition'. In: *Theoretical and Computational Fluid Dynamics* 25.1-4 (2010), pp. 249–259. DOI: 10.1007/s00162-010-0203-9.

[146] Peter J. Schmid. 'Dynamic mode decomposition of numerical and experimental data'. In: *Journal of Fluid Mechanics* 656 (2010), pp. 5–28. DOI: 10.1017/S0022112010001217.

[147] Eberhard Hopf. 'The partial differential equation $u_t + uu_x = \mu u_{xx}$'. In: *Communications on Pure and Applied Mathematics* 3.3 (1950), pp. 201–230. DOI: 10.1002/cpa.3160030302.

[148] Hassler Whitney. 'Differentiable Manifolds'. In: *Annals of Mathematics* 37.3 (1936), pp. 645–680. DOI: 10.2307/1968482.

[149] John Nash. 'C^1 Isometric Imbeddings'. In: *Annals of Mathematics* 60.3 (1954), pp. 383–396. DOI: 10.2307/1969840.

[150] Floris Takens. 'Detecting strange attractors in turbulence'. In: *Dynamical Systems and Turbulence, Warwick 1980: Proceedings of a Symposium Held at the University of Warwick 1979/80*. Ed. by David Rand and Lai-Sang Young. Berlin, Heidelberg: Springer Berlin Heidelberg, 1981, pp. 366–381. DOI: 10.1007/BFb0091924.

[151] Nikos E. Kouvaris et al. 'Chimera states in a network-organized public goods game with destructive agents'. In: *Chaos: An Interdisciplinary Journal of Nonlinear Science* 26.12 (2016), p. 123108. DOI: 10.1063/1.4971974.

[152] J. Shena et al. 'Turbulent chimeras in large semiconductor laser arrays'. In: *Scientific Reports* 7 (Feb. 2017), p. 42116. DOI: 10.1038/srep42116.

[153] Sarika Jalan, Saptarshi Ghosh and Bibhabasu Patra. 'Is repulsion good for the health of chimeras?' In: *Chaos: An Interdisciplinary Journal of Nonlinear Science* 27.10 (2017), p. 101104. DOI: 10.1063/1.5005576.

[154] Teresa Chouzouris et al. 'Chimera states in brain networks: Empirical neural vs. modular fractal connectivity'. In: *Chaos: An Interdisciplinary Journal of Nonlinear Science* 28.4 (2018), p. 045112. DOI: 10.1063/1.5009812.

[155] Shinya Watanabe and Steven H. Strogatz. 'Integrability of a globally coupled oscillator array'. In: *Phys. Rev. Lett.* 70 (16 Apr. 1993), pp. 2391–2394. DOI: 10.1103/PhysRevLett.70.2391.

[156] Shinya Watanabe and Steven H. Strogatz. 'Constants of motion for superconducting Josephson arrays'. In: *Physica D: Nonlinear Phenomena* 74.3 (1994), pp. 197–253. DOI: https://doi.org/10.1016/0167-2789(94)90196-1.

[157] Einstein A. 'Die Grundlage der allgemeinen Relativitätstheorie'. In: *Annalen der Physik* 354.7 (1916), pp. 769–822. DOI: 10.1002/andp.19163540702.

[158] K. Krischer, M. Eiswirth and G. Ertl. 'Oscillatory CO oxidation on Pt(110): Modeling of temporal self-organization'. In: *The Journal of Chemical Physics* 96.12 (1992), pp. 9161–9172. DOI: 10.1063/1.462226.